

ISSN 2071-4726
2071-0305

Инженерно-строительный журнал

НАУЧНОЕ ИЗДАНИЕ

№6(90) 2019





ПОЛИТЕХ
Санкт-Петербургский
политехнический университет
Петра Великого

Инженерно-строительный институт
Центр дополнительных профессиональных программ
195251, г. Санкт-Петербург, Политехническая ул., 29,
тел/факс: 552-94-60, www.stroikursi.spbstu.ru,
stroikursi@mail.ru

**Приглашает специалистов организаций, вступающих в СРО,
на курсы повышения квалификации (72 часа)**

Код	Наименование программы	Виды работ*
Курсы по строительству		
БС-01-04	«Безопасность и качество выполнения общестроительных работ»	п.1,2, 3, 5, 6, 7, 9, 10, 11, 12, 13, 14
БС-01	«Безопасность и качество выполнения геодезических, подготовительных и земляных работ, устройства оснований и фундаментов»	1,2,3,5
БС-02	«Безопасность и качество возведения бетонных и железобетонных конструкций»	6,7
БС-03	«Безопасность и качество возведения металлических, каменных и деревянных конструкций»	9,10,11
БС-04	«Безопасность и качество выполнения фасадных работ, устройства кровель, защиты строительных конструкций, трубопроводов и оборудования»	12,13,14
БС-05	«Безопасность и качество устройства инженерных сетей и систем»	15,16,17,18,19
БС-06	«Безопасность и качество устройства электрических сетей и линий связи»	20,21
БС-08	«Безопасность и качество выполнения монтажных и пусконаладочных работ»	23,24
БС-12	«Безопасность и качество устройства мостов, эстакад и путепроводов»	29
БС-13	«Безопасность и качество выполнения гидротехнических, водолазных работ»	30
БС-14	«Безопасность и качество устройства промышленных печей и дымовых труб»	31
БС-15	«Осуществление строительного контроля»	32
БС-16	«Организация строительства, реконструкции и капитального ремонта. Выполнение функций технического заказчика и генерального подрядчика»	33
Курсы по проектированию		
БП-01	«Разработка схемы планировочной организации земельного участка, архитектурных решений, мероприятий по обеспечению доступа маломобильных групп населения»	1,2,11
БП-02	«Разработка конструктивных и объемно-планировочных решений зданий и сооружений»	3
БП-03	«Проектирование внутренних сетей инженерно-технического обеспечения»	4
БП-04	«Проектирование наружных сетей инженерно-технического обеспечения»	5
БП-05	«Разработка технологических решений при проектировании зданий и сооружений»	6
БП-06	«Разработка специальных разделов проектной документации»	7
БП-07	«Разработка проектов организации строительства»	8
БП-08	«Проектные решения по охране окружающей среды»	9
БП-09	«Проектные решения по обеспечению пожарной безопасности»	10
БП-10	«Обследование строительных конструкций и грунтов основания зданий и сооружений»	12
БП-11	«Организация проектных работ. Выполнение функций генерального проектировщика»	13
Э-01	«Проведение энергетических обследований с целью повышения энергетической эффективности и энергосбережения»	
Курсы по инженерным изысканиям		
И-01	«Инженерно-геодезические изыскания в строительстве»	1
И-02	«Инженерно-геологические изыскания в строительстве»	2,5
И-03	«Инженерно-гидрометеорологические изыскания в строительстве»	3
И-04	«Инженерно-экологические изыскания в строительстве»	4
И-05	«Организация работ по инженерным изысканиям»	7

*(согласно приказам Минрегионразвития РФ N 624 от 30 декабря 2009 г.)

**По окончании курса слушателю выдается удостоверение о краткосрочном повышении
квалификации установленного образца (72 ак. часа)**

Для регистрации на курс необходимо выслать заявку на участие, и копию диплома об образовании по телефону/факсу: 8(812) 552-94-60, 535-79-92, , e-mail: stroikursi@mail.ru.

Инженерно-строительный журнал

НАУЧНОЕ ИЗДАНИЕ

ISSN 2071-4726, 2071-0305

Свидетельство о государственной регистрации: ПИ №ФС77-38070, выдано Роскомнадзором

Специализированный научный журнал. Выходит с 09.2008.

Включен в Перечень ведущих периодических изданий ВАК РФ

Периодичность: 8 раз в год

Учредитель и издатель:

Санкт-Петербургский политехнический университет Петра Великого

Адрес редакции:

195251, СПб, ул. Политехническая, д. 29, Гидрокорпус-2, ауд. 245

Главный редактор:

Екатерина Александровна Линник

Научный редактор:

Николай Иванович Ватин

Выпускающий редактор:

Анастасия Крупина

Редакционная коллегия:

д.ф.-м.н., доцент Р.А. Абдикаримов;
 д.т.н., проф. В.В. Бабков;
 к.т.н., проф. А.И. Боровков;
 д.т.н., проф. А. Бородинец;
 д.т.н., проф. Н.И. Ватин;
 PhD, проф. М. Вельжкович;
 к.т.н., М.Р. Гарифуллин;
 д.т.н., проф. Э.К. Завадскас;
 д.ф.-м.н., проф. М.Н. Кирсанов;
 D.Sc., проф. М. Кнежевич;
 д.т.н., проф. В.В. Лалин;
 д.т.н., проф. Б.Е. Мельников;
 д.т.н., академик М.М. Мирсаидов;
 д.т.н., проф. Р.Б. Орлович;
 Dr. Sc. Ing., professor
 Л. Пакрастиньш;
 Dr.-Ing. Habil., professor
 Х. Пастернак;
 д.т.н., проф. А.В. Перельмутер;
 д.т.н., проф. М.Р. Петриченко;
 д.т.н., проф. В.В. Сергеев;
 д.ф.-м.н., проф. М.Х. Стрелец;
 д.т.н., проф. О.В. Тараканов;
 д.т.н., проф. Б.Б. Телтаев;
 д.т.н., проф. В.И. Травуш;
 д.т.н., проф. Д. Унгерман;
 д.т.н., проф. С.В. Федосов

Дата выхода: 30.10.2019

Содержание

Ерофеев В.Т., Родин А.И., Якунин В.В., Тувин М.Н. Структура, состав и свойства геополимеров из отходов минеральной ваты	3
Дворкин Л.И., Житковский В.В. Метод расчета цементно-водного отношения пропариваемого бетона	15
Юсуф М.О. Микроструктурные и прочностные характеристики портландцемента с металлическим наполнением	28
Масталыгина Е.Е., Овчинников В.А., Чухланов В.Ю. Легкие жаростойкие полимербетоны на основе олигооксигидридсилметиленилосилоксисилана и полых сферических наполнителей	37
Ибрагим Я, Набил М. Риск внешней взрывной нагрузки на свайные фундаменты	47
Аль-Рушан Р. Поведение двухсторонних плит, подвергнутых падению груза	62
Строкова В.В., Нелюбова В.В., Рыкунова М.Д. Стойкость цементного камня в растворах санационных средств	72
Бородинец А., Проземент А., Заяц А., Земитис Ю. Реновация пожарных депо в условиях холодного климата	85
Утепов Е.Б., Анискин А., Ибрашов А., Тулебекова А. Размещение датчиков зрелости в зависимости от границ температурного перехода	93
Эхсани Р., Шарбатдар М.К., Хайруддин А. Пластичность и способность перераспределения моментов двухпролётных железобетонных балок	104
Фироозфар А., Доусти М. Керманская просадочная глина, модифицированная оксидом кальция, бентонитом и нанокремнеземом	119

© ФГАОУ ВО СПбПУ, 2019

© Иллюстрация на обложке: Илья Смагин

Контакты:E-mail: mce@spbstu.ruWeb: <http://www.engstroy.spbstu.ru>

Magazine of Civil Engineering

SCHOLAR JOURNAL

ISSN 2071-4726, 2071-0305

Peer-reviewed scientific journal

Start date: 2008/09

8 issues per year

Publisher:Peter the Great St. Petersburg
Polytechnic University**Indexing:**Scopus, Russian Science Citation
Index (WoS), Compendex, DOAJ,
EBSCO, Google Academia, Index
Copernicus, ProQuest, Ulrich's Serials
Analysis System, CNKI**Corresponding address:**245 Hydro Building, 29
Polytechnicheskaya st., Saint-
Petersburg, 195251, Russia**Editor-in-chief:**

Ekaterina A. Linnik

Science editor:

Nikolay I. Vatin

Technical editor:

Anastasia Krupina

Editorial board:R.A. Abdikarimov, D.Sc., associate
professor

V.V. Babkov, D.Sc., professor

A.I. Borovkov, PhD, professor

A. Borodinecs, Dr.Sc.Ing., professor

M. Veljkovic, PhD, professor

M. Garifullin, PhD, postdoctorant

E.K. Zavadskas, D.Sc., professor

M.N. Kirsanov, D.Sc., professor

M. Knezevic, D.Sc., professor

V.V. Lalin, D.Sc., professor

B.E. Melnikov, D.Sc., professor

M.M. Mirsaidov, D.Sc., professor

R.B. Orlovich, D.Sc., professor

L. Pakrastinsh, Dr.Sc.Ing., professor

H. Pasternak, Dr.-Ing.habil.,
professor

A.V. Perelmuter, D.Sc., professor

M.R. Petrichenko, D.Sc., professor

V.V. Sergeev, D.Sc., professor

M.Kh. Strelets, D.Sc., professor

O.V. Tarakanov, D.Sc., professor

B.B. Teltayev, D.Sc., professor

V.I. Travush, D.Sc., professor

S.V. Fedosov, D.Sc., professor

Date of issue: 30.10.2019

Contents

Erofeev, V.T., Rodin, A.I., Yakunin, V.V., Tuvin, M.N. Structure, composition and properties of geopolymers from mineral wool waste	3
Dvorkin, L.I., Zhitkovsky, V.V. Method of proportioning the cement-water ratio of steam-cured concrete	15
Yusuf, M.O. Microstructure and strength of iron-filing Portland cement paste and mortar	28
Mastalygina, E.E., Ovchinnikov, V.A., Chukhlanov, V.Yu. Light heat-resistant polymer concretes based on oligoxyhydridesilmethylensiloxysilane and hollow spherical fillers	37
Ibrahim, Y.E-H., Nabil, M. Risk of surface blast load on pile foundations	47
Al-Rousan, R. Behavior of two-way slabs subjected to drop- weight	62
Stroková, V.V., Nelubova, V.V., Rykunova, M.D. Resistance of cement stone in sanitation solutions	72
Borodinecs, A., Prozuments, A., Zajacs, A., Zemitis, J. Retrofitting of fire stations in cold climate regions	85
Uteпов, Ye.B., Aniskin, A., Ibrashov, A.P., Tulebekova, A. Maturity sensors placement based on the temperature transitional boundaries	93
Ehsani, R., Sharbatdar, M.K., Kheyroddin, A. Ductility and moment redistribution capacity of two-span RC beams	104
Firoozfar, A., Dousti, M. Kerman collapsible clay amendment by lime, bentonite, and nano silica	119

© Peter the Great St. Petersburg Polytechnic University. All rights reserved.

© Coverpicture – Ilya Smagin

E-mail: mce@spbstu.ruWeb: <https://engstroy.spbstu.ru/en/>



DOI: 10.18720/MCE.90.1

Structure, composition and properties of geopolymers from mineral wool waste

V.T. Erofeev, A.I. Rodin*, V.V. Yakunin, M.N. Tuvin

Ogarev Mordovia State University, Saransk, Respublika Mordoviya, Russia

* *E-mail: al_rodin@mail.ru*

Keywords: geopolymers, slags, mineral wool, mechanical properties, X ray diffraction analysis, thermoanalysis, microstructure

Abstract. The waste generated during the mineral wool production makes up to 30 % of the finished product mass. These wastes can be used for producing building materials, in particular as raw materials for the production of geopolymers (alkali-activated binders). The research aim was to determine the influence of the chemical composition of mineral wool production wastes (MWPW) on the phase composition, structure, and physico-mechanical properties of geopolymers. Five types of MWPW with various chemical compositions and specific surfaces were hydrated in the presence of NaOH (from 2 to 4 wt. %). The experimental results were obtained using the methods of X ray diffraction (XRD), differential thermal (DTA) and thermogravimetric (DTG) analyses. Moreover, scanning electron microscopy (SEM) and physical and mechanical tests were used. The main hydration product of MWPW in the NaOH presence is determined to be calcium hydrosilicates of the C–A–S–H fiber texture type. The largest amount of C–A–S–H was detected in geopolymer samples made of wastes with an acidity modulus between 1.4 and 1.6. The compressive strength of the obtained materials reaches 80 MPa. They are also characterized by high water resistance. The Al_2O_3 content in the waste should be about 10 % in order to obtain geopolymers with stable properties. The obtained results made it possible to define the correlation between the structure, composition, and physico-mechanical properties of geopolymers made of MWPW. The practical effect of the research results lies in the possibility of obtaining higher strength classes concrete.

1. Introduction

One of the most popular material types in modern construction are cement binders. Alkali-activated binders (geopolymers) can become a good alternative to them. Materials based on them possess high strength and chemical resistance. Implementing such materials also helps to solve environmental problems; it helps to reduce CO_2 emissions into the atmosphere, reduces pollution of surface waters and groundwater, atmosphere, soil and plants [1–6]. The technology for producing geopolymers is as follows. Slags of metallurgical industries are milled to the specific surface of Portland cement and tempered with alkaline solutions. The most of construction products and structures based on alkali-activated binders are obtained using blast furnace slag of iron industry. Slags of non-ferrous metallurgy, furnace clinkers (ashes), chemical and a number of others are also widely used [7–13]. A special category of slag includes mineral wool production waste (MWPW). Up to 30 % of such waste from the mass of finished products is generated during production process [14]. The possibility of using MWPW in order to obtain geopolymers was described before [14].

Analyzing the mineral wool chemical composition of the most famous world manufacturers (ROCKWOOL, Knauf, etc.) showed that the CaO content in most samples is between 20 and 30 %, and the total amount of Al_2O_3 and MgO is more than 20 %. Understanding the correlation between the chemical composition of MWPW and physico-mechanical properties of hardened composites is possible only through a comprehensive study of the hydration processes in waste activated by alkaline solutions. Such studies are almost absent in the literature. However, hydration processes of blast furnace slag with various chemical compositions, tempered with silicate or alkali metal hydroxide solutions, have been studied quite extensively [2, 15–19]. It is known that the main product of this interaction is a calcium hydrosilicate gel of the C–A–S–H type. The structure of this gel is similar to tobermorite with a partial replacement of Ca by Al. According to studies [15, 18], this structure is characterized by a higher polymerization degree, as well as a greater degree

Erofeev, V.T., Rodin, A.I., Yakunin, V.V., Tuvin, M.N. Structure, composition and properties of geopolymers from mineral wool waste. Magazine of Civil Engineering. 2019. 90(6). Pp. 3–14. DOI: 10.18720/MCE.90.1

Ерофеев В.Т., Родин А.И., Якунин В.В., Тувин М.Н. Структура, состав и свойства геополимеров из отходов минеральной ваты // Инженерно-строительный журнал. 2019. № 6(90). С. 3–14. DOI: 10.18720/MCE.90.1



This open access article is licensed under CC BY 4.0 (<https://creativecommons.org/licenses/by/4.0/>)

of crosslinking between tobermorite chains. Many researchers [2, 15, 18, 20–26] argue that secondary phases, such as zeolites and the N–A–S–H gel, are formed in the composition of CaO and MgO when hydrated, in addition to the C–A–S–H gel; hydrotalcite is formed in case of high CaO and MgO content; sterlinghillite is formed in case of high Al₂O₃ and CaO content; and etc.

The ratio of oxides in the slag is of particular importance for the formation of both the C–A–S–H phase and secondary phases during hydration of alkali-activated binders: CaO/SiO₂, MgO/Al₂O₃ and Al₂O₃/SiO₂. According to studies [2, 18, 19, 22, 25, 27], the increased CaO content in the composition of the alkali-activated binder promotes its rapid setting, the formation of C–A–S–H phase with a low Al content, and AFm type phases in small quantities. Bernal, S.A. and Haha, M.B. et al. determined [16, 20] that a C–A–S–H gel with a large substitution of Ca for Al is formed in the composition upon hydration of alkali-activated binders with a small MgO amount. Increasing the Al content in the C–A–S–H gel above a certain value leads to a deterioration in the physico-mechanical properties of composites with this structure. In another research [15] Haha, M.B. with colleagues found that the high content of Al₂O₃ in the slag composition increases the amount of Al₂O₃ in the hydrotalcite formed during the alkaline reaction, which subsequently leads to recrystallization and deterioration of the physico-mechanical properties of the composites.

The goal of the paper is to determine the effect of the mineral wool production waste (MWPW) chemical composition on the phase composition, structure, and physico-mechanical properties of geopolymers.

The following tasks were solved:

- the phase composition of the geopolymer samples made of MWPW was established using the of X-ray diffraction and thermal analyzing methods;
- the surface microstructure of the samples was studied using scanning electron microscopy method;
- the influence of the microstructure and phase composition of the composites on the values of their average density, compressive strength, water adsorption and water resistance has been established.

2. Methods

2.1. Materials

The main criterion for the chemical composition of mineral wool is the acidity modulus M_a , which is calculated according to the following formula:

$$M_a = \frac{\text{SiO}_2 + \text{Al}_2\text{O}_3}{\text{CaO} + \text{MgO}}, \quad (1)$$

where the numerator and denominator are the total contents of these oxides, % by weight.

Throughout the research, five types of MWPW with an acidity modulus from 1 to 2 were tested. The chemical composition of the waste is given in Table 1.

Table 1. Chemical composition of MWPW.

Comp. No	Chemical composition, % by weight.											
	CaO	SiO ₂	Al ₂ O ₃	MgO	Na ₂ O	K ₂ O	TiO ₂	Fe ₂ O ₃	MnO	SO ₃	P ₂ O ₅	
	2	3	4	5	6	7	8	9	10	11	12	
w1	40.995	36.336	10.306	8.201	1.058	0.883	0.815	0.547	0.295	0.248	0.033	
w2	25.284	41.135	10.655	11.556	1.951	0.875	1.287	5.753	0.263	0.094	0.091	
w3	26.228	41.800	13.257	11.412	1.171	0.383	0.297	2.392	0.227	0.277	0.013	
w4	25.451	40.548	15.421	9.358	2.163	0.456	0.741	4.615	0.183	0.130	0.012	
w5	19.772	46.362	11.249	8.565	1.967	1.082	1.131	7.739	0.156	0.091	0.139	

The end of the Table 1

Chemical composition, % by weight.							Ratio of oxides				
Cl	CuO	Cr ₂ O ₃	ZnO	Co ₃ O ₄	NiO	Loss on ignition	CaO/SiO ₂	Al ₂ O ₃ /SiO ₂	MgO/Al ₂ O ₃	M_a	
13	14	15	16	17	18	19	20	21	22	23	
0.026	0.014	0.013	0	0	0	0.230	1.128	0.284	0.796	0.948	
0	0.020	0.033	0.011	0.012	0.007	0.973	0.615	0.259	1.085	1.406	
0.009	0.010	0.096	0	0.008	0.024	2.396	0.627	0.317	0.861	1.463	
0.009	0.017	0.099	0.017	0.010	0.008	0.762	0.628	0.380	0.607	1.608	
0.004	0.015	0.040	0.005	0.014	0.014	1.655	0.426	0.243	0.761	2.033	

Granular NaOH dissolved in water was used as an alkaline activator. Mass fraction of the main substance is not less than 99.5 %.

2.2. Compositions and sample manufacturing technology

Alkali-activated binders and composites based on them were manufactured according to the following technology. Five types of MWPW (see Table 1 for chemical compositions) were dried to constant weight at a temperature of 105 °C. Then the waste was milled to a specific surface area from 125.12 to 377.23 m²/kg using the dry method and up to almost 1,500 m²/kg using the wet method. The water was poured into a working mixer with an alkaline activator (NaOH) previously dissolved in it. Ground MWPW were gradually loaded and mixed for 5–7 minutes. The water/slag (W/S) ratio allowed achieving equal fluidity of the mortar mix. Cube-shaped samples with a face of 20 mm were made from the resulting mixture by vibration molding. Samples in the molds were kept at a temperature of 50 °C and a relative humidity of at least 85 % for 5 hours. Then, samples outside the molds were steamed at atmospheric pressure according to the regime of 3+6+2 h at an isothermal heating temperature of 85±5 °C. The steamed products were dried to constant weight at a temperature of 30 °C and a relative humidity of not more than 50 %, after which further tests were carried out.

The compositions tested in the study are presented in Table 2.

Table 2. The compositions tested in the study.

Comp. No	Binder composition, %					NaOH	Dimensional indicators of waste		W/S ratio
	MWPW (see Table 1 for chemical composition)						Average particle diameter, μm	The specific surface of the powders, m ² /kg	
	w1	w2	w3	w4	w5				
C1	98	–	–	–	–	2			
C2	97	–	–	–	–	3	18.096	125.12	0.27
C3	96	–	–	–	–	4			
C4	–	98	–	–	–	2			
C5	–	97	–	–	–	3	6.605	342.79	0.287
C6	–	96	–	–	–	4			
C7	–	–	98	–	–	2			
C8	–	–	97	–	–	3	6.482	349.3	0.267
C9	–	–	96	–	–	4			
C10	–	–	–	98	–	2			
C11	–	–	–	97	–	3	14.962	151.33	0.357
C12	–	–	–	96	–	4			
C13	–	–	–	–	98	2			
C14	–	–	–	–	97	3	6.002	377.23	0.327
C15	–	–	–	–	96	4			
C16	98	–	–	–	–	2			
C17	97	–	–	–	–	3	1.533	1,476.94	0.303
C18	96	–	–	–	–	4			
C19	–	–	–	98	–	2			
C20	–	–	–	97	–	3	3.096	731.32	0.332
C21	–	–	–	96	–	4			

2.3. Analytical techniques

Geopolymer samples were tested using X ray diffraction (XRD), differential thermal (DTA) and thermogravimetric (DTG) analyses, as well as scanning electron microscopy (SEM):

– XRD of samples was carried out using an ARL X'tra diffractometer (Switzerland). Samples of hydrated alkali-activated binders were ground in an agate mortar with an agate pestle with acetone before passing through a sieve with a 90 μm screen opening. The diffraction patterns were recorded on CuK α_{1+2} radiation in the range of angles $2\theta = 4-70^\circ$ with a speed of 1.2 °/min, in increments of 0.02 °, integration time 1 sec. Using the Hanawalt method with the ICDD PDF-2 database, the qualitative phase composition of the samples was determined.

– DTA and DTG of samples was carried out using a TGA/DSC1 device (Switzerland). MWPW samples and hydrated alkali-activated binders were prepared as for the XRD. 0.025 g of the crushed sample was weighed to the nearest 0.0001 g and poured into an alundum crucible with a volume of 150 μl. Next, the sample was condensed by tapping the crucible on the table. The crucible was mounted on a holder and placed in an oven. The sample was heated from 30 to 1000 °C at a rate of 10 °C/min.

– surface SEM of geopolymer samples was carried out using a Quanta 200 i 3D device (USA) in the low vacuum mode (10⁻³ Pa) with 20 kV accelerating voltage and a working distance of 15 mm.

The average density and compressive strength of geopolymer samples was determined by testing at least 10 cube samples with a 20 mm face of each composition.

The water adsorption of the samples in percent by weight was determined by the ratio of water mass absorbed by the sample at full saturation to the dry sample mass.

Water resistance (W) of samples activated by NaOH MWPW was determined by the following formula:

$$W = \frac{R_{ws}}{R_d}, \quad (2)$$

where R_{ws} is the compressive strength of the samples after aging in water for 90 days;

R_d is the compressive strength of dried samples according to the method described in section 2.2.

3. Results and Discussion

3.1. X ray diffraction

The results of X ray diffraction analysis of MWPW samples after alkaline activation are presented in Figure 1.

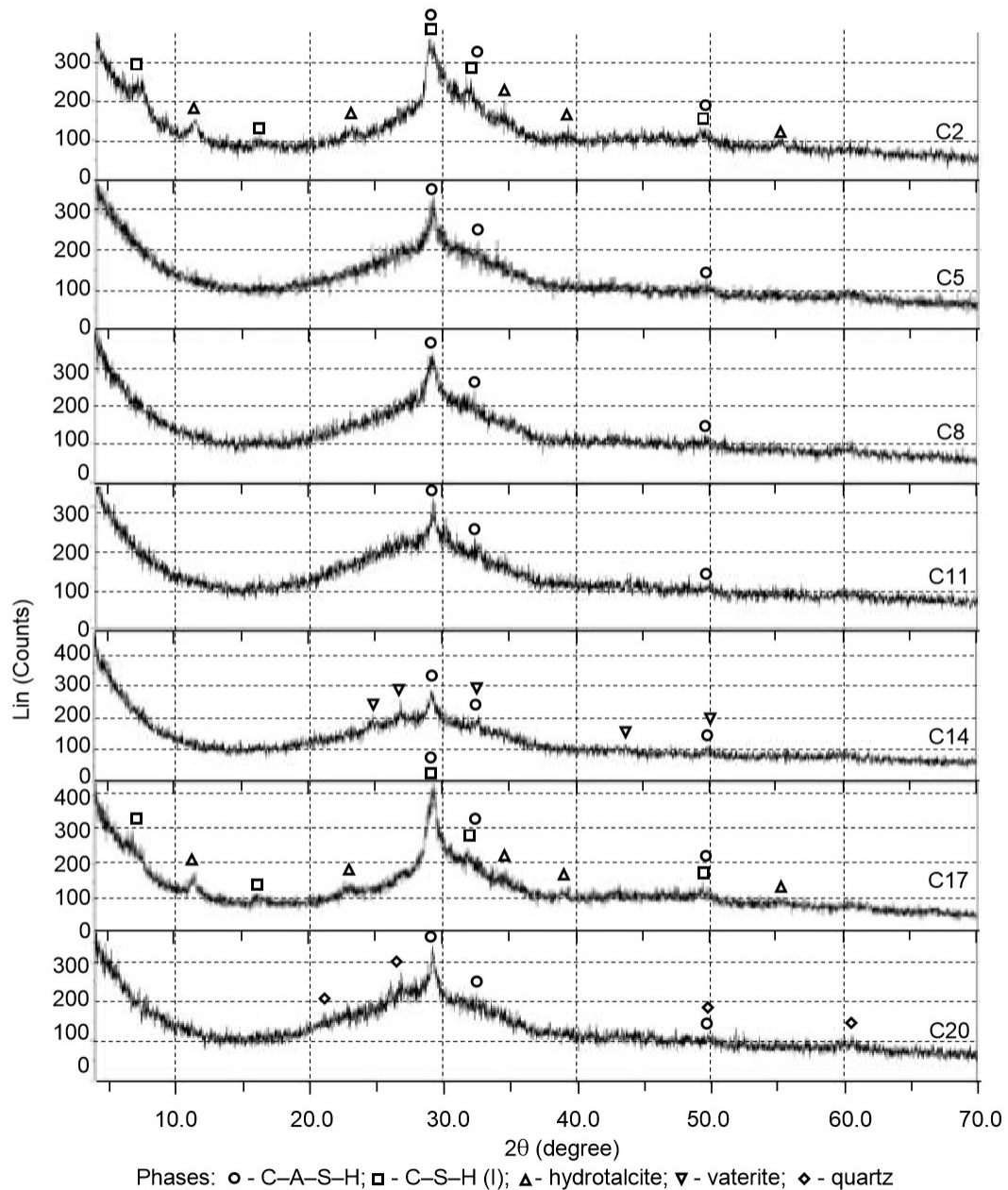


Figure 1. XRD samples of hydrated slag alkaline binders: C2, C5, C8, C11, C14, C17, C20 – see Table 2.

Definitive peaks for tobermorite-like calcium hydrosilicates with a partial replacement of Ca by Al C–A–S–H (PDF 00-033-0306) and C–S–H (I) (PDF 00-034-0002) were registered on X ray diffraction patterns of MWPW samples with an approximate CaO/SiO₂ ratio of 1.1, MgO/Al₂O₃ – 0.8 and Al₂O₃/SiO₂ – 0.3 (acid modulus M_a is approximately 1) after alkaline activation with an aqueous NaOH solution (compositions C2 and C17). Also, a significant amount of the secondary phase hydrotalcite (Mg₆Al₂(CO₃)(OH)₁₆·4H₂O, PDF 01-89-0460), was detected in the composition of these samples. An increase in the specific surface of the waste from 125.12 to almost 1,500 m²/kg led to a change in the X ray diffraction pattern of peak intensity at 2θ of about 29.5°, which indicates the formation of larger amounts of calcium hydrosilicates. The peaks on X ray diffraction patterns C2 and C17 related to hydrotalcite are almost identical, which indicates a slight effect of changes in the specific surface of the waste (from 125.12 to almost 1,500 m²/kg) on the formation of this phase.

The presence of peaks related to the C–A–S–H phase (PDF 00-033- 0306) was registered on X ray diffraction patterns C5 and C8 of hydrated alkali-activated binder samples made of MWPW with practically equal M_a (1.4–1.46) and CaO/SiO₂ ratio (0.6). The absence of secondary phases of the crystalline structure is determined. The main difference between these wastes lies in the MgO/Al₂O₃ ratio (about 0.26 for C5 and 0.32 for C8) and Al₂O₃/SiO₂ (about 0.26 for C5 and 0.32 for C8). Similar data was obtained by analyzing X ray diffraction patterns of activated NaOH waste with a M_a of about 1.6 and an equal CaO/SiO₂ and MgO/Al₂O₃ ratio of about 0.6 and Al₂O₃/SiO₂ of about 0.4 (compositions C11 and C20). Reflections related to quartz were additionally recorded on the X ray diffraction pattern C20 (PDF 00-046-1045), as well as an increase in peak intensity at 2θ of about 29.5°. An increase in the hydration degree of the C20 composition compared to C11.

X ray diffraction patterns of waste samples activated with NaOH with M_a of approximately 2 (composition C14) are characterized by the presence of peaks related to the C–A–S–H phase (PDF 00-033-0306), the absence of hydrotalcite peaks, and the occurrence of reflexes common for vaterite (PDF 00-024-0030).

3.2. Thermoanalysis

Thermoanalysis of the MWPW samples is presented in Figure 2 and in Table 3.

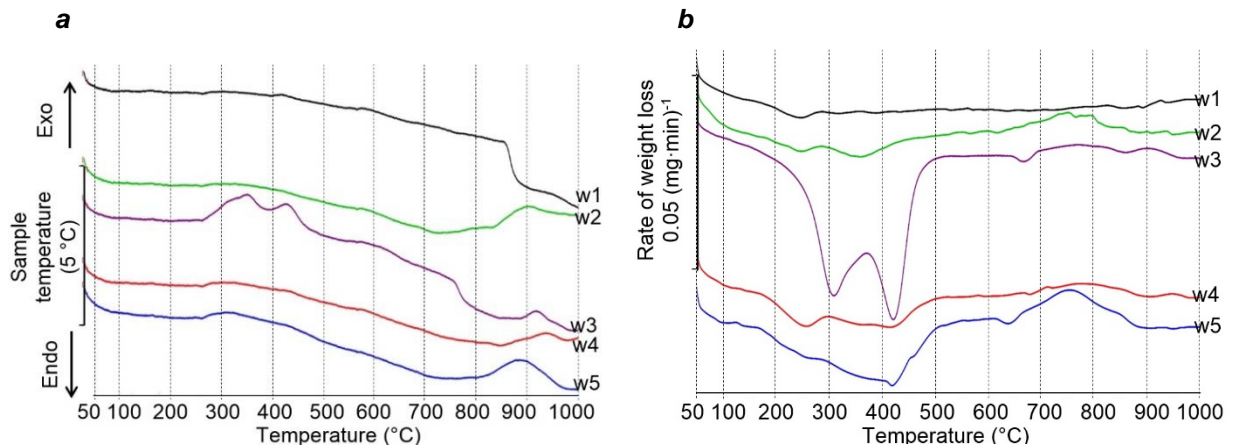


Figure 2. DTA (a) and DTG (b) MWPW curves: w1–w5 – see Table 1.

Table 3. Mass losses (in wt. %) of MWPW samples for various temperature ranges (°C).

Sample	30–250/°C	250–500/°C	500–600/°C	600–750/°C	750–1000/°C	30–1000/°C
w1	–0.099	–0.134	0.010	0.025	0.202	0.004
w2	–0.386	–0.585	–0.055	0.078	0.060	–0.888
w3	–0.083	–2.357	0.044	0.125	0.302	–1.969
w4	–0.183	–0.589	0.032	0.150	0.276	–0.314
w5	–0.486	–1.206	0.005	0.229	0.212	–1.246

According to the data obtained (Figure 2 and Table 3), the following main phase transformations occurring in the MWPW during heating were exposed. The first exothermic effect and sample mass loss in the temperature range from 250 to 500 °C corresponds to burning out of organic compounds used in bonding mineral wool to mats. The greatest mass loss and intensity of this effect are in the compositions w3 and w5. An insignificant endothermic effect with a peak at a temperature of about 570 °C without mass loss, observed on the DTA curves of all tested wastes, corresponds to the transition of β-quartz to α-quartz. The endothermic effect on the DTA curve (sample w3) at a temperature between 750 and 800 °C (the sample mass has not changed) corresponds to a softening of the glass phase in the waste. The exothermic effect with a peak at a temperature of about 850 °C, which was registered on the DTA curve w1, without mass loss by the sample refers to wollastonite crystallization. This exothermic effect for w2–w5 compositions is shifted to the area of

higher temperatures (peaks with maxima from 880 to 920 °C), which corresponds to the crystallization of melilite minerals. The results obtained correlate with the data of many researchers [2, 15–18, 22, 25, 27].

Thermoanalysis of geopolymer samples made of MWPW is presented in Figure 3 and in Table 4.

Table 4. Mass losses (wt. %) of geopolymers samples in various temperature ranges (°C).

Sample	30–250/°C	250–500/°C	500–600/°C	600–750/°C	750–1000/°C	30–1000/°C
C2	-6.560	-2.120	-0.319	-0.270	-0.120	-9.389
C5	-13.375	-2.049	-0.241	-0.180	0.040	-15.805
C8	-12.861	-3.561	-0.217	-0.163	0.097	-16.705
C11	-6.770	-2.206	-0.292	-0.347	0.126	-9.489
C14	-13.640	-2.057	-0.240	-0.136	0.171	-15.902
C17	-13.393	-2.677	-0.332	-0.256	-0.020	-16.678
C20	-17.760	-2.282	-0.347	-0.316	0.007	-20.698

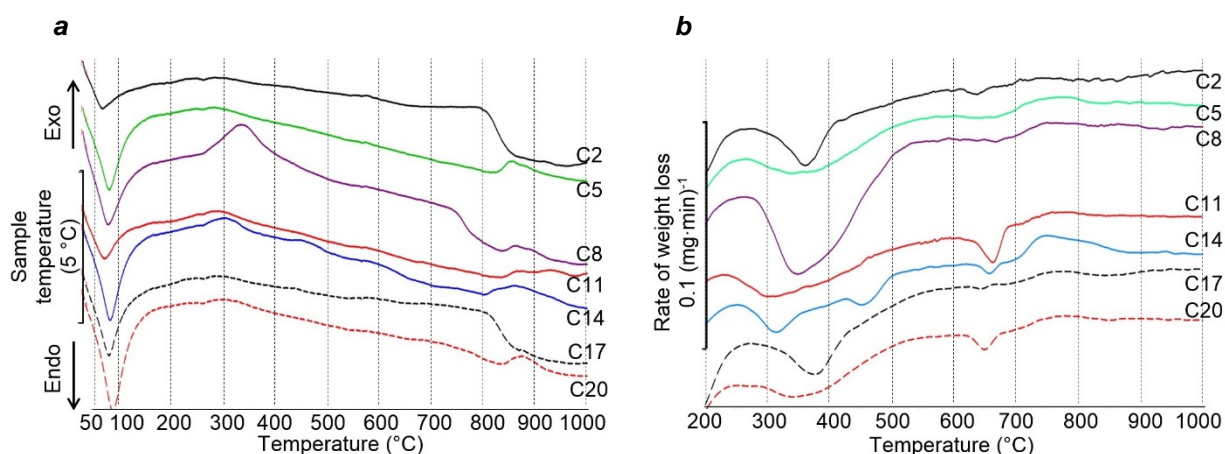


Figure 3. DTA (a) and DTG (b) curves of geopolymer samples: C2, C5, C8, C11, C14, C17, C20 – see Table 2.

According to the data presented in Table 4 and Figure 3, the main phase transformations during heating, occurring in hydrated alkaline-activated binder samples made of MWPW are as follows. The large endothermic effect on the DTA curves and the significant weight loss by all samples in the temperature range from 30 to 250 °C are associated with the dissociation of crystalline unbound water and the dehydration of calcium hydrosilicates. The presence of calcium hydrosilicates in all the samples is also indicated by the shift of exothermic effects with peaks at temperatures from 850 to 950 °C (Figure 2, a) to lower temperatures (Figure 3, a). The exothermic effect for compositions C2 and C17 with a peak at a temperature of about 810 °C is associated with crystallization of wollastonite made of calcium hydrosilicates with a CaO/SiO₂ ratio of approximately 1. The peak of this exothermic effect in the other compositions is shifted to the 860–870 °C temperature range, which is explained by the content of C–A–S–H phase in the sample composition. The presence of the C–A–S–H phase in the composition of samples obtained by MWPW alkaline activation with M_a between 1.4 and 2 can also be determined by the wide depression in the DTG curves and the mass loss of the samples in the temperature range from 250 to 500 °C (Table 4 and Figure 3, b). In this temperature range, the organic compounds used for bonding mineral wool mats burnt out also. The reaction is accompanied by an exothermic effect in the DTA curves and mass loss of the samples.

A slight endothermic effect and almost equal weight loss of samples C2 and C17 in the temperature range from 300 to 430 °C confirm the XRD data on the insignificant effect of changes in the specific surface of the waste from 125.12 to 1,476.94 m²/kg on the formation of hydrotalcite.

A small endothermic depression in the TA curves of all compositions with a peak at about 570 °C corresponds to the transition of β -quartz to α -quartz. The depressions in the DTG curves for sample C14, accompanied by insignificant endothermic effects in the temperature range from 260 to 350 °C and from 420 to 490 °C, probably correspond to the dehydration of calcium hydroaluminates and hydrogranates.

The mass losses of the MWPW samples activated with NaOH with M_a from 1.6 to 2, as well as the distinct depressions in the DTG curves at the temperature of about 650 °C, are associated with the dehydration of sodium-calcium aluminosilicate hydrates. The reaction is accompanied by a slight endothermic effect. The area of this depression for compositions with $M_a = 1.6$ decreases with an increase in the specific surface of the waste. This is most likely caused by an increase in the amount of the C–A–S–H phase binding Al, which is required for the formation of sodium-calcium aluminosilicate hydrates.

In the DTA curve for composition C14, two endothermic effects are additionally observed with maxima at temperatures around 430 and 700 °C. The appearance of these effects is associated with the formation of vaterite. The presence of this phase confirms the mass loss and depression in the DTG curve in the temperature range from 650 to 750 °C, as well as the results of XRD.

3.3. SEM

Comparative surface microstructure characteristics of the geopolymer samples made of MWPW with M_a equal to 1 and 1.4 are presented in Figure 4.

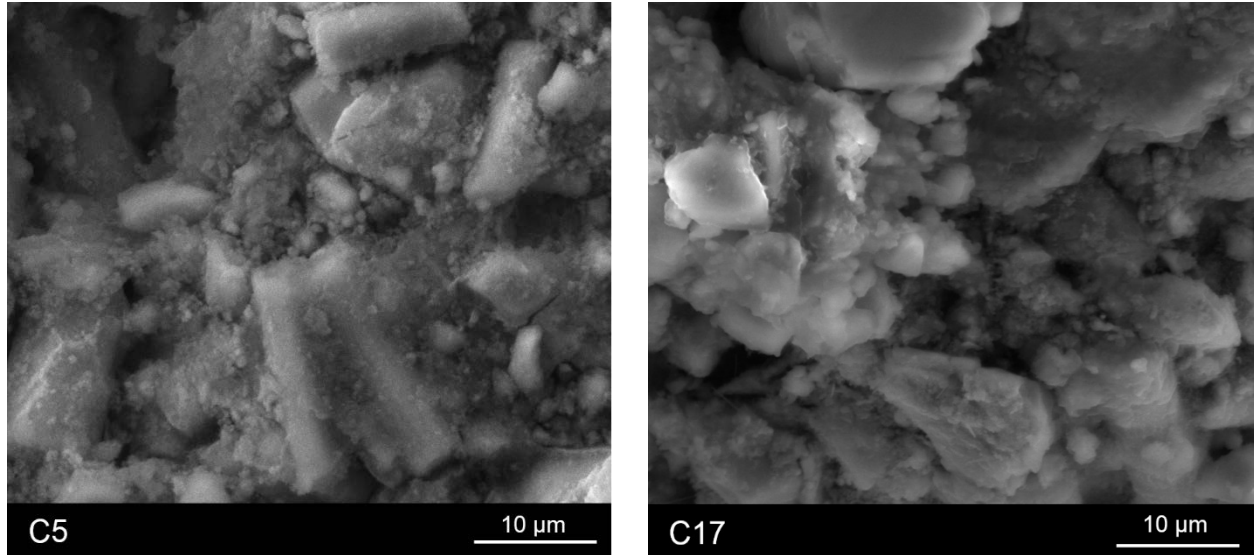


Figure 4. SEM-micrographs of geopolymer sample surfaces (compositions C5 and C17).

According to SEM-micrographs, the needle-shaped waste particles are visible on the surface of a geopolymer sample made of MWPW with $M_a = 1.4$ (C5). Almost the entire surface of the waste particles is covered with fibrous neoplasms, which most likely relate to tobermorite calcium hydrosilicates of C–A–S–H type. There are no clear boundaries between the particles. In the middle of Figure 4, the intergrowth of two needle-shaped particles of the C5 waste is clearly visible.

The microstructure of the geopolymer sample surface made of MWPW with $M_a = 1$ (C17) is as follows. The waste particles have a granular angular shape. Almost the entire surface of the particles is covered with neoplasms, mostly with a scaly structure, which is most likely relevant for the C–S–H (I) phase. Needle-shaped neoplasms representative for hydrotalcite crystals are also visible in the pores. In some places, neoplasms of the fibrous structure (C–A–S–H) are visible.

3.4. Average density and compressive strength

The average density values and compressive strength of geopolymer samples made of MWPW are presented in Figure 5.

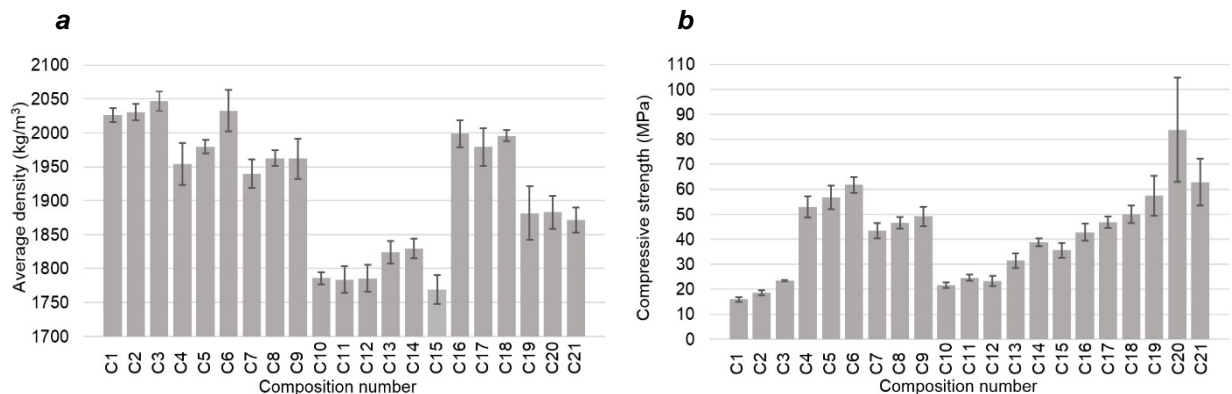


Figure 5. Average density (a) and compressive strength (b) of geopolymer samples.

While studying the hydration processes of MWPW activated with NaOH, it was found that only C1–C3 and C16–C18 compositions set and gain strength at a temperature of about 20 °C and a relative air humidity of at least 85 %. All compositions were obtained using MWPW with $M_a \approx 1$. The inability of the remaining compounds to self-set is associated with a low CaO content. This feature is described in the researches of

various authors [22, 25, 27]. It was previously determined [14], that geopolymer samples made of MWPW must be isothermally heated in molds for 5 hours at a temperature of at least 50 °C and a relative humidity of at least 85 %, in order to ensure the formwork strength. Based on these studies, a methodology for the manufacture of samples was developed, which is described in section 2.2. of the article.

Analyzing the average density values of the samples (Figure 5, a) allowed defining that this indicator decreases from 2,030 to about 1,800 kg/m³ on average with an increase of the waste M_a value from 1 to 2. Such an effect can be explained by a decrease in the true density of MWPW, as well as by the increase of the W/S ratio value of the mortar mixture.

According to the data (Figure 5, b), and also based on the results of previous studies [14], the compressive strength of geopolymer samples made of MWPW increases by 2.5–3 times with an increase in the waste M_a from 1 to 1.4. A further increase in the acid modulus to 2 leads to a decrease in compressive strength by almost 40%. In addition to M_a , the compressive strength of the samples depends on the specific surface of the waste. With an increase in the w1 specific waste surface from 125.12 to 1,476.94 m²/kg, the compressive strength of the samples increased by more than 2 times. An increase in the NaOH amount in the composition of the mortar mixture from 2 to 4 % slightly increases the compressive strength of the geopolymer MWPW samples with M_a between 1 and 1.46. Waste geopolymers with an acidity modulus of 1.6 and 2 have maximum compressive strength when activated with a 3 % NaOH.

The compressive strength of geopolymer samples is significantly affected by the Al₂O₃ content in the composition of MWPW. The effect is observed with an increase in the specific surface of the waste. The compressive strength values obtained for MWPW geopolymer samples with Al₂O₃ content of more than 15 % (w4) (specific waste surface is 731.32 m²/kg) were not stable. The spread between the maximum and minimum values of various samples was about 50 MPa, which is more than 40 % of the average value of this indicator. Such an effect was not observed when testing MWPW geopolymer samples with an Al₂O₃ content of about 10 %. Even with an increase in the specific surface of the waste to 1,500 m²/kg, the spread between the maximum and minimum compressive strength values of samples did not exceed 10 % of the average value.

3.5. Water absorption and water resistance

According to studies [2, 6, 14, 28, 29], the water resistance of geopolymers depends on the chemical composition of the initial slag. For example, glass-fiber composites with a CaO content of less than 6 % are not waterproof ($W < 0.8$), and NaOH-activated blast furnace slags continue to gain strength in water. The results of studies aimed at determining the water adsorption and water resistance of NaOH-activated MWPW samples with different acid modulus are presented in Figure 6.

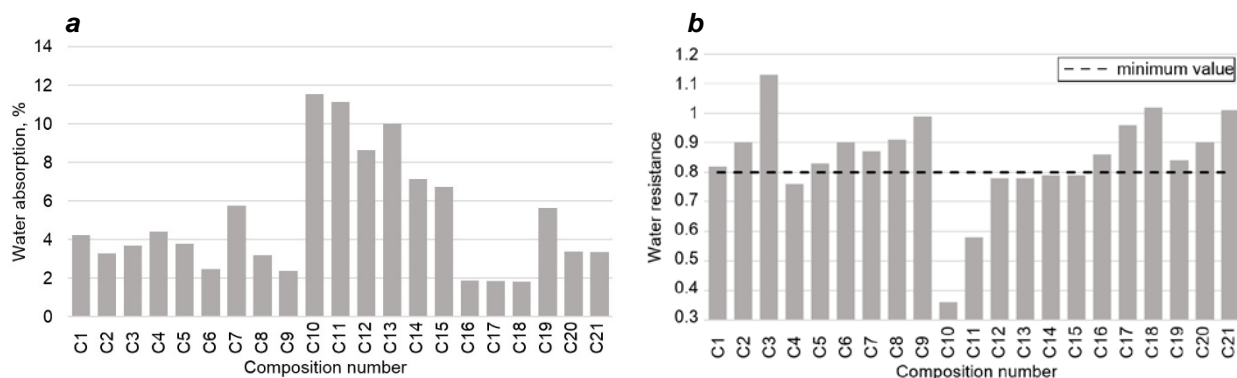


Figure 6. Water adsorption (a) and water resistance (b) of geopolymer samples.

According to the data obtained (Figure 6), the water adsorption of geopolymers depends on at least two following MWPW characteristics: chemical composition and fineness of grinding. The chemical composition of MWPW and the glue used in the preparation of mineral wool mats affect the amount of water required to obtain a mortar mixture of the equal mobility (W/S ratio). With an increase in the amount of water in the mortar mixture, the number of pores in the hardened composite increases. As a result, water adsorption increases. So, at almost equal specific MWPW surface area of the compositions w3 and w5, the W/S ratio of the mortar mixture is 0.06 lower for w3 waste (see Table 2), and the water adsorption of the hardened composite is almost 2 times less. Features of water adsorption by thermal insulation materials made of mineral wool are described in detail [30].

With increasing the MWPW specific surface, the W/S ratio of the mortar mixture increases, but the water adsorption of the hardened composite decreases. This feature can be explained by the filling of pores in the geopolymer with hydration products. According to XRD and TA data, NaOH-activated waste with a higher specific surface area has a greater degree of hydration. For example, when the specific surface area of w1 composition MWPW increases from 125.12 to 1,476.94 m²/kg, the W/S ratio of the mortar mixture increases from 0.27 to 0.303. At the same time, water adsorption of the geopolymer decreases by almost 2 times (from 3.8 to 1.9 % on average).

Resistance of MWPW geopolymers aged in water for 90 days depends on at least three following factors: the chemical composition of the waste, its specific surface, and the amount of alkaline component. With increasing M_a waste from 1 to 2, the water resistance of hardened composites decreases. For example, C8 geopolymers ($M_a = 1.46$) are water resistant ($W = 0.9$), and C14 ($M_a = 2$) are not waterproof ($W = 0.79$). It is possible to increase the water resistance of geopolymers by increasing the specific surface area of MWPW. Significant effect is achieved when using waste with $M_a > 1$. With an increase in the specific surface area of w4 waste composition from 377.23 (C11) to 731.32 m²/kg (C20), the samples of geopolymers became waterproof (water resistance increases from 0.58 to 0.9). An increase in the amount of alkaline component in the composition of the mortar mixture also increases the water resistance of the geopolymer. This effect decreases with increasing of waste M_a . So, with an increase of NaOH from 2 to 4 % in the composition of mortar mixture based on the waste w1 ($M_a = 1$), the water resistance increases from 0.82 to 1.13. However, it practically does not change if based on the w5 waste ($M_a = 2$) (W about 0.79).

4. Conclusion

1. The chemical composition impact of mineral wool production wastes (MWPW) on the phase composition, structure, and physico-mechanical properties of geopolymer samples has been determined.

2. It was defined using the methods of X ray differential and thermal analyses, that following tobermorite-like phases of calcium hydrosilicates are formed during hydration of NaOH-activated MWPW with $M_a = 1$: C–S–H (I) and C–A–S–H, as well as the secondary hydrotalcite phase. When waste M_a is activated from 1.4 to 2, neoplasms are represented mainly by the C–A–S–H phase. With an increase of M_a to more than 1.46, the presence of phases of sodium-calcium aluminosilicate hydrates, calcium hydroaluminates, and hydrogranates can also be detected in the geopolymer samples.

3. According to the SEM data, the C–A–S–H phase in the samples of hydrated MWPW with $M_a = 1.4$ has a fibrous structure, which covers almost the entire surface of the needle-shaped waste particles. Neoplasms in MWPW geopolymers with $M_a = 1$ are represented mostly by a scaly structure (probably the C–S–H (I) phase). In certain spots, needle-shaped neoplasms (hydrotalcite crystals) and fibrous structure (C–A–S–H phase) are observed.

4. It was established that the compressive strength of MWPW geopolymers samples strongly depends on the amount of the formed C–A–S–H phase of the fibrous structure. The water resistance of geopolymers is depends more on the amount of CaO in the initial waste composition. With its decrease, water resistance decreases. However, this indicator can be boosted by increasing the specific surface of the waste and by changing the amount of alkaline activator.

5. Water-resistant geopolymers (W is approximately 1) with a compressive strength of at least 80 MPa can be obtained by MWPW activation with 3–4 % of NaOH (in terms of dry matter). The acidity modulus of the waste should be in the range from 1.4 to 1.6, the Al₂O₃ content should be about 10 %, the specific surface area of at least 700 m²/kg.

6. The established regularities of structure formation processes of MWPW composites allow us to simulate their course in real conditions and select rational compositions of composites for use in specific areas of construction.

5. Acknowledgments

The work was carried out within the framework of the Grant of the President of the Russian Federation MK-6416.2018.3.

References

1. Bagheri, A., Nazari, A., Hajimohammadi, A., Sanjayan, J.G., Rajeev, P., Nikzad, M., Ngo, T., Mendis, P. Microstructural study of environmentally friendly boroaluminosilicate geopolymers. *Journal of Cleaner Production*. 2018. 189. Pp. 805–812. DOI: 10.1016/j.jclepro.2018.04.034.
2. Huseien, G.F., Sam, A.R.M., Shah, K.W., Asaad, M.A., Tahir, M.M., Mirza, J. Properties of ceramic tile waste based alkali-activated mortars incorporating GBFS and fly ash. *Construction and Building Materials*. 2019. 214. Pp. 355–368. DOI: 10.1016/j.conbuildmat.2019.04.154.
3. Kang, S.-H., Kwon, Y.-H., Hong, S.-G., Chun, S., Moon, J. Hydrated lime activation on byproducts for eco-friendly production of structural mortars. *Journal of Cleaner Production*. 2019. 231. Pp. 1389–1398. DOI: 10.1016/j.jclepro.2019.05.313.
4. Provis, J.L., Bernal, S.A. Geopolymers and related alkali-activated materials. *Annual Review of Materials Research*. 2014. 44. Pp. 299–327. DOI: 10.1146/annurev-matsci-070813-113515.
5. Provis, J.L., Palomo, A., Shi, C. Advances in understanding alkali-activated materials. *Cement and Concrete Research*. 2015. 78. Pp. 110–125. DOI: 10.1016/j.cemconres.2015.04.013.
6. Rafeet, A., Vinai, R., Soutsos, M., Sha, W. Effects of slag substitution on physical and mechanical properties of fly ash-based alkali activated binders (AABs). *Cement and Concrete Research*. 2019. 122. Pp. 118–135. DOI: 10.1016/j.cemconres.2019.05.003.
7. Erofeev, V., Korotaev, S., Bulgakov, A., Tretiakov, I., Rodin, A. Getting Fired Material with Vitreous Binder Using Frame Technology. *Procedia Engineering*. 2016. 164. Pp. 166–171. DOI: 10.1016/j.proeng.2016.11.606.

8. Fediuk R.S., Lesovik V.S., Svintsov A.P., Mochalov A.V., Kulichkov S.V., Stoyushko N.Y., Gladkova N.A., Timokhin R.A. Self-compacting concrete using pretreated rice husk ash. *Magazine of Civil Engineering*. 2018. 79(3). Pp. 66–76. DOI: 10.18720/MCE.79.7.
9. Heah, C.Y., Kamarudin, H., Mustafa Al Bakri, A.M., Bnhussain, M., Luqman, M., Khairul Nizar, I., Ruzaidi, C.M., Liew, Y.M. Study on solids-to-liquid and alkaline activator ratios on kaolin-based geopolymers. *Construction and Building Materials*. 2012. 35. Pp. 912–922. DOI: 10.1016/j.conbuildmat.2012.04.102.
10. Liew, Y.-M., Heah, C.-Y., Li, L.-Y., Jaya, N.A., Abdullah, M.M.A.B., Tan, S.J., Hussin, K. Formation of one-part-mixing geopolymers and geopolymer ceramics from geopolymer powder. *Construction and Building Materials*. 2017. 156. Pp. 9–18. DOI: 10.1016/j.conbuildmat.2017.08.110.
11. Nematollahi, B., Sanjayan, J. Effect of different superplasticizers and activator combinations on workability and strength of fly ash based geopolymer. *Materials and Design*. 2014. 57. Pp. 667–672. DOI: 10.1016/j.matdes.2014.01.064.
12. Shang, J., Dai, J.-G., Zhao, T.-J., Guo, S.-Y., Zhang, P., Mu, B. Alternation of traditional cement mortars using fly ash-based geopolymer mortars modified by slag. *Journal of Cleaner Production*. 2018. 203. Pp. 746–756. DOI: 10.1016/j.jclepro.2018.08.255.
13. Xie, J., Wang, J., Rao, R., Wang, C., Fang, C. Effects of combined usage of GGBS and fly ash on workability and mechanical properties of alkali activated geopolymer concrete with recycled aggregate. *Composites Part B: Engineering*. 2019. 164. Pp. 179–190. DOI: 10.1016/j.compositesb.2018.11.067.
14. Erofeev, V.T., Rodin, A.I., Yakunin, V.V., Bogatov, A.D., Bochkina, V.S., Chegodajkin, A.M. Alkali-activated slag binders from rock-wool production wastes. *Magazine of Civil Engineering*. 2018. 82(6). Pp. 219–227. DOI: 10.18720/MCE.82.20.
15. Haha, M.B., Lothenbach, B., Le Saout, G., Winnefeld, F. Influence of slag chemistry on the hydration of alkali-activated blast-furnace slag – Part II: Effect of Al_2O_3 . *Cement and Concrete Research*. 2012. 42(1). Pp. 74–83. DOI: 10.1016/j.cemconres.2011.08.005.
16. Haha, M.B., Lothenbach, B., Le Saout, G., Winnefeld, F. Influence of slag chemistry on the hydration of alkali-activated blast-furnace slag – Part I: Effect of MgO. *Cement and Concrete Research*. 2011. 41(9). Pp. 955–963. DOI: 10.1016/j.cemconres.2011.05.002.
17. Ismail, I., Bernal, S.A., Provis, J.L., San Nicolas, R., Hamdan, S., Van Deventer, J.S.J. Modification of phase evolution in alkali-activated blast furnace slag by the incorporation of fly ash. *Cement and Concrete Composites*. 2014. 45. Pp. 125–135. DOI: 10.1016/j.cemconcomp.2013.09.006.
18. Myers, R.J., Bernal, S.A., San Nicolas, R., Provis, J.L. Generalized structural description of calcium-sodium aluminosilicate hydrate gels: The cross-linked substituted tobermorite model. *Langmuir*. 2013. 29(17). Pp. 5294–5306. DOI: 10.1021/la4000473.
19. Tänzer, R., Buchwald, A., Stephan, D. Effect of slag chemistry on the hydration of alkali-activated blast-furnace slag. *Materials and Structures/Materiaux et Constructions*. 2014. 48(3). Pp. 629–641. DOI: 10.1617/s11527-014-0461-x.
20. Bernal, S.A., San Nicolas, R., Myers, R.J., Mejía De Gutiérrez, R., Puertas, F., Van Deventer, J.S.J., Provis, J.L. MgO content of slag controls phase evolution and structural changes induced by accelerated carbonation in alkali-activated binders. *Cement and Concrete Research*. 2014. 57. Pp. 33–43. DOI: 10.1016/j.cemconres.2013.12.003.
21. Geng, G., Myers, R.J., Li, J., Maboudian, R., Carraro, C., Shapiro, D.A., Monteiro, P.J.M. Aluminum-induced dreierketten chain cross-links increase the mechanical properties of nanocrystalline calcium aluminosilicate hydrate. *Scientific Reports*. 2017. 7. Article number 44032. DOI: 10.1038/srep44032.
22. Li, C., Sun, H., Li, L. A review: The comparison between alkali-activated slag (Si + Ca) and metakaolin (Si + Al) cements. *Cement and Concrete Research*. 2010. 40(9). Pp. 1341–1349. DOI: 10.1016/j.cemconres.2010.03.020.
23. Marsh, A., Heath, A., Patureau, P., Evernden, M., Walker, P. Alkali activation behaviour of un-calcined montmorillonite and illite clay minerals. *Applied Clay Science*. 2018. 166. Pp. 250–261. DOI: 10.1016/j.clay.2018.09.011.
24. Ogundiran, M.B., Kumar, S. Synthesis and characterisation of geopolymer from Nigerian Clay. *Applied Clay Science*. 2015. 108. Pp. 173–181. DOI: 10.1016/j.clay.2015.02.022.
25. Walkley, B., San Nicolas, R., Sani, M.-A., Rees, G.J., Hanna, J.V., van Deventer, J.S.J., Provis, J.L. Phase evolution of C-(N)-A-S-H/N-A-S-H gel blends investigated via alkali-activation of synthetic calcium aluminosilicate precursors. *Cement and Concrete Research*. 2016. 89. Pp. 120–135. DOI: 10.1016/j.cemconres.2016.08.010.
26. Węgrzyn, A., Rafalska-Lasocha, A., Majda, D., Dziembaj, R., Papp, H. The influence of mixed anionic composition of Mg-Al hydrotalcites on the thermal decomposition mechanism based on in situ study. *Journal of Thermal Analysis and Calorimetry*. 2010. 99(2). Pp. 443–457. DOI: 10.1007/s10973-009-0190-5.
27. Garcia-Lodeiro, I., Aparicio-Rebollo, E., Fernández-Jimenez, A., Palomo, A. Effect of calcium on the alkaline activation of aluminosilicate glass. *Ceramics International*. 2016. 42(6). Pp. 7697–7707. DOI: 10.1016/j.ceramint.2016.01.184.
28. Erofeev, V.T., Fedortsov, A.P., Bogatov, A.D., Fedortsov, V.A., Gusev, B.V. Evaluation of corrosion of alkaliglass composites, predicting their physico-chemical resistance and ways to improve it. *Proceedings of Higher Education Institutions: Textile Industry Technology*. 2018. 374(2). Pp. 238–246.
29. Hanjitsuwan, S., Phoo-ngernkham, T., Li, L.-Y., Damrongwiriyanupap, N., Chindapasirt, P. Strength development and durability of alkali-activated fly ash mortar with calcium carbide residue as additive. *Construction and Building Materials*. 2018. 162. Pp. 714–723. DOI: 10.1016/j.conbuildmat.2017.12.034.
30. Vatin, N.I., Pestryakov, I.I., Sultanov, Sh.T., Ogidan, T.O., Yarunicheva, Y.A., Kiryushina, A.P. Water vapour by diffusion and mineral wool thermal insulation materials. *Magazine of Civil Engineering*. 2018. 81(5). Pp. 183–192. DOI: 10.18720/MCE.81.18.

Contacts:

Vladimir Erofeev, +7(8342)47-40-19; a_l_rodin@mail.ru

Alexander Rodin, +7(951)051-45-28; a_l_rodin@mail.ru

Vladislav Yakunin, +7(953)029-70-58; vladisjakunin@yandex.ru

Maksim Tuvin, +7(987)691-35-09; maxim.tuvin@yandex.ru



DOI: 10.18720/MCE.90.1

Структура, состав и свойства геополимеров из отходов минеральной ваты

В.Т. Ерофеев, А.И. Родин*, В.В. Якунин, М.Н. Тувин

Мордовский государственный университет им. Н.П. Огарёва, г. Саранск, Республика Мордовия, Россия

* E-mail: al_rodin@mail.ru

Ключевые слова: геополимеры, отходы, минеральная вата, механические свойства, рентгенофазовый анализ, термический анализ, микроструктура

Аннотация. При производстве минеральной ваты образуются отходы в количестве до 30 % от массы готовой продукции. Данные отходы можно использовать при изготовлении строительных материалов, в частности в качестве сырья для получения геополимеров (шлакощелочных вяжущих). Цель исследования состояла в установлении влияния химического состава отходов производства минеральной ваты (ОПМВ) на фазовый состав, структуру и физико-механические свойства геополимеров. Пять видов ОПМВ с различным химическим составом и удельной поверхностью гидратировали в присутствии NaOH (от 2 до 4 мас. %). Экспериментальные результаты получены с применением методов рентгенофазового (РФА), дифференциально-термического (ДТА) и дифференциально-термогравиметрического (ДТГ) анализа, сканирующей электронной микроскопии (СЭМ), физико-механических испытаний. Установлено, что основным продуктом гидратации ОПМВ в присутствии NaOH являются гидросиликаты кальция типа C–A–S–H волокнистой структуры. Наибольшее количество C–A–S–H зафиксировано в образцах геополимеров из отходов с модулем кислотности от 1,4 до 1,6. Прочность при сжатии полученных материалов достигает 80 МПа. Они также характеризуются высокой водостойкостью. Для получения геополимеров со стабильными свойствами содержание Al_2O_3 в отходе должно быть около 10 %. Выявленные результаты позволили установить взаимосвязь между структурой, составом и физико-механическими свойствами геополимеров из ОПМВ. Практическая значимость результатов исследования заключается в возможности получения бетонов более высоких классов по прочности.

Литература

1. Bagheri A., Nazari A., Hajimohammadi A., Sanjayan J.G., Rajeev P., Nikzad M., Ngo T., Mendis P. Microstructural study of environmentally friendly boroaluminosilicate geopolymers // *Journal of Cleaner Production*. 2018. 189. Pp. 805–812. DOI: 10.1016/j.jclepro.2018.04.034.
2. Huseien G.F., Sam A.R.M., Shah K.W., Asaad M.A., Tahir M.M., Mirza J. Properties of ceramic tile waste based alkali-activated mortars incorporating GBFS and fly ash // *Construction and Building Materials*. 2019. 214. Pp. 355–368. DOI: 10.1016/j.conbuildmat.2019.04.154.
3. Kang S.-H., Kwon Y.-H., Hong S.-G., Chun S., Moon J. Hydrated lime activation on byproducts for eco-friendly production of structural mortars // *Journal of Cleaner Production*. 2019. 231. Pp. 1389–1398. DOI: 10.1016/j.jclepro.2019.05.313.
4. Provis J.L., Bernal S.A. Geopolymers and related alkali-activated materials // *Annual Review of Materials Research*. 2014. 44. Pp. 299–327. DOI: 10.1146/annurev-matsci-070813-113515.
5. Provis J.L., Palomo A., Shi C. Advances in understanding alkali-activated materials // *Cement and Concrete Research*. 2015. 78. Pp. 110–125. DOI: 10.1016/j.cemconres.2015.04.013.
6. Rafeet A., Vinai R., Soutsos M., Sha W. Effects of slag substitution on physical and mechanical properties of fly ash-based alkali activated binders (AABs) // *Cement and Concrete Research*. 2019. 122. Pp. 118–135. DOI: 10.1016/j.cemconres.2019.05.003.
7. Erofeev V., Korotaev S., Bulgakov A., Tretiakov I., Rodin A. Getting Fired Material with Vitreous Binder Using Frame Technology // *Procedia Engineering*. 2016. 164. Pp. 166–171. DOI: 10.1016/j.proeng.2016.11.606.
8. Федюк Р.С., Лесовик В.С., Свинцов А.П., Мочалов А.В., Куличков С.В., Стоюшко Н.Ю., Гладкова Н.А., Тимохин Р.А. Самоуплотняющийся бетон с использованием предварительно подготовленной золы рисовой шелухи // *Инженерно-строительный журнал*. 2018. № 3(79). С. 66–76. doi: 10.18720/MCE.79.7
9. Heah C.Y., Kamarudin H., Mustafa Al Bakri A.M., Bnhussain M., Luqman M., Khairul Nizar I., Ruzaidi C.M., Liew Y.M. Study on solids-to-liquid and alkaline activator ratios on kaolin-based geopolymers // *Construction and Building Materials*. 2012. 35. Pp. 912–922. DOI: 10.1016/j.conbuildmat.2012.04.102.
10. Liew Y.-M., Heah C.-Y., Li L.-Y., Jaya N.A., Abdullah M.M.A.B., Tan S.J., Hussin K. Formation of one-part-mixing geopolymers and geopolymer ceramics from geopolymer powder // *Construction and Building Materials*. 2017. 156. Pp. 9–18. DOI: 10.1016/j.conbuildmat.2017.08.110.

11. Nematollahi B., Sanjayan J. Effect of different superplasticizers and activator combinations on workability and strength of fly ash based geopolymer // *Materials and Design*. 2014. 57. Pp. 667–672. DOI: 10.1016/j.matdes.2014.01.064.
12. Shang J., Dai J.-G., Zhao T.-J., Guo S.-Y., Zhang P., Mu B. Alternation of traditional cement mortars using fly ash-based geopolymer mortars modified by slag // *Journal of Cleaner Production*. 2018. 203. Pp. 746–756. DOI: 10.1016/j.jclepro.2018.08.255.
13. Xie J., Wang J., Rao R., Wang C., Fang C. Effects of combined usage of GGBS and fly ash on workability and mechanical properties of alkali activated geopolymer concrete with recycled aggregate // *Composites Part B: Engineering*. 2019. 164. Pp. 179–190. DOI: 10.1016/j.compositesb.2018.11.067.
14. Ерофеев В.Т., Родин А.И., Якунин В.В., Богатов А.Д., Бочкин В.С., Чеодайкин А.М. Шлакощелочные вяжущие из отходов производства минеральной ваты // *Инженерно-строительный журнал*. 2018. № 6(82). С. 219–227. doi: 10.18720/МСЕ.82.20
15. Haha M.B., Lothenbach B., Le Saout G., Winnefeld F. Influence of slag chemistry on the hydration of alkali-activated blast-furnace slag – Part II: Effect of Al_2O_3 // *Cement and Concrete Research*. 2012. 42(1). Pp. 74–83. DOI: 10.1016/j.cemconres.2011.08.005.
16. Haha M.B., Lothenbach B., Le Saout G., Winnefeld F. Influence of slag chemistry on the hydration of alkali-activated blast-furnace slag – Part I: Effect of MgO // *Cement and Concrete Research*. 2011. 41(9). Pp. 955–963. DOI: 10.1016/j.cemconres.2011.05.002.
17. Ismail I., Bernal S.A., Provis J.L., San Nicolas R., Hamdan S., Van Deventer J.S.J. Modification of phase evolution in alkali-activated blast furnace slag by the incorporation of fly ash // *Cement and Concrete Composites*. 2014. 45. Pp. 125–135. DOI: 10.1016/j.cemconcomp.2013.09.006.
18. Myers R.J., Bernal S.A., San Nicolas R., Provis J.L. Generalized structural description of calcium-sodium aluminosilicate hydrate gels: The cross-linked substituted tobermorite model // *Langmuir*. 2013. 29(17). Pp. 5294–5306. DOI: 10.1021/la4000473.
19. Tänzer R., Buchwald A., Stephan D. Effect of slag chemistry on the hydration of alkali-activated blast-furnace slag. *Materials and Structures // Materiaux et Constructions*. 2014. 48(3). Pp. 629–641. DOI: 10.1617/s11527-014-0461-x.
20. Bernal S.A., San Nicolas R., Myers R.J., Mejía De Gutiérrez, R., Puertas, F., Van Deventer, J.S.J., Provis, J.L. MgO content of slag controls phase evolution and structural changes induced by accelerated carbonation in alkali-activated binders // *Cement and Concrete Research*. 2014. 57. Pp. 33–43. DOI: 10.1016/j.cemconres.2013.12.003.
21. Geng G., Myers R.J., Li J., Maboudian R., Carraro C., Shapiro D.A., Monteiro P.J.M. Aluminum-induced dreierketten chain cross-links increase the mechanical properties of nanocrystalline calcium aluminosilicate hydrate // *Scientific Reports*. 2017. 7. Article number 44032. DOI: 10.1038/srep44032.
22. Li C., Sun H., Li L. A review: The comparison between alkali-activated slag (Si + Ca) and metakaolin (Si + Al) cements // *Cement and Concrete Research*. 2010. 40(9). Pp. 1341–1349. DOI: 10.1016/j.cemconres.2010.03.020.
23. Marsh A., Heath A., Patureau P., Evernden M., Walker P. Alkali activation behaviour of un-calcined montmorillonite and illite clay minerals // *Applied Clay Science*. 2018. 166. Pp. 250–261. DOI: 10.1016/j.clay.2018.09.011.
24. Ogundiran M.B., Kumar S. Synthesis and characterisation of geopolymer from Nigerian Clay // *Applied Clay Science*. 2015. 108. Pp. 173–181. DOI: 10.1016/j.clay.2015.02.022.
25. Walkley B., San Nicolas R., Sani M.-A., Rees G.J., Hanna J.V., van Deventer J.S.J., Provis J.L. Phase evolution of C-(N)-A-S-H/N-A-S-H gel blends investigated via alkali-activation of synthetic calcium aluminosilicate precursors // *Cement and Concrete Research*. 2016. 89. Pp. 120–135. DOI: 10.1016/j.cemconres.2016.08.010.
26. Węgrzyn A., Rafalska-Lasocha A., Majda D., Dziembaj R., Papp H. The influence of mixed anionic composition of Mg-Al hydrotalcites on the thermal decomposition mechanism based on in situ study // *Journal of Thermal Analysis and Calorimetry*. 2010. 99(2). Pp. 443–457. DOI: 10.1007/s10973-009-0190-5.
27. Garcia-Lodeiro I., Aparicio-Rebollo E., Fernández-Jimenez A., Palomo A. Effect of calcium on the alkaline activation of aluminosilicate glass // *Ceramics International*. 2016. 42(6). Pp. 7697–7707. DOI: 10.1016/j.ceramint.2016.01.184.
28. Ерофеев В.Т., Федорцов А.П., Богатов А.Д., Федорцов В.А., Гусев Б.В. Оценка коррозии стеклощелочных композитов, прогнозирование их физико-химического сопротивления и способы его повышения // *Известия высших учебных заведений: Технология текстильной промышленности*. 2018. № 2(374). Pp. 238–246.
29. Hanjitsuwan S., Phoo-ngernkham T., Li L.-Y., Damrongwiriyanupap N., Chindaprasirt P. Strength development and durability of alkali-activated fly ash mortar with calcium carbide residue as additive // *Construction and Building Materials*. 2018. 162. Pp. 714–723. DOI: 10.1016/j.conbuildmat.2017.12.034.
30. Ватин Н.И., Пестряков И.И., Султанов Ш.Т., Огидан О.Т., Яруничева Ю.А., Кирюшина А. Диффузионное влагопоглощение теплоизоляционных изделий и минеральной ваты // *Инженерно-строительный журнал*. 2018. № 5(81). С. 183–192. doi: 10.18720/МСЕ.81.18.

Контактные данные:

Владимир Трофимович Ерофеев, +7(8342)47-40-19; эл. почта: al_rodin@mail.ru
Александр Иванович Родин, +7(951)051-45-28; эл. почта: al_rodin@mail.ru
Владислав Васильевич Якунин, +7(953)029-70-58; эл. почта: vladisjakunin@yandex.ru
Максим Николаевич Тувин, +7(987)691-35-09; эл. почта: maxim.tuvin@yandex.ru

© Ерофеев В.Т., Родин А.И., Якунин В.В., Тувин М.Н., 2019



DOI: 10.18720/MCE.90.2

Method of proportioning the cement-water ratio of steam-cured concrete

L.I. Dvorkin, V.V. Zhitkovsky

National University of Water and Environmental Engineering, Rivne, Ukraine

* E-mail: dvorkin.leonid@gmail.com

Keywords: cement-water ratio, strength, temperature, steam-curing, hardening, modes

Abstract. The article presents the results of experimental studies that made it possible to substantiate the calculated dependences of the steam-cured concrete strength and the required values of the cement-water ratio (C/W) to ensure the specified strength values. For this purpose, dependences are obtained that are valid when using Portland cement and slag Portland cement, as well as a change in the wide range of regime parameters of heat treatment: temperature and duration of curing. To calculate the required values of C/W , a formula is justified, which allows determining the strength of cement under steaming when the temperature changes in the range of 60...95 C and the duration of isothermal heating during steaming from 4 to 18 hours. To calculate the strength of cement during steaming, the coefficients are recommended, which allow taking into account the content of aluminates and mineral additives in cement. Taking into account the calculated dependencies, an algorithm is proposed for calculating the C/W of steam-cured concrete and an example of its implementation.

1. Introduction

Wide experimental data on the effect of various steaming regimes [1–10], as well as the compositions of concrete mixtures, mineral and chemical additives [11–18] on the strength and other properties of concrete have been obtained in the works by many researchers, including those performed in recent years. However, the design method of proportioning of steam-cured concrete with a given strength, both instantly after steam curing and for certain duration of their subsequent hardening, considering a set of basic technological factors, has not been proposed in these studies. It leads in practice to the need for a sufficiently large amount of additional experiments in the proportioning of concrete mixes with required properties. The main task of the concrete mixes proportioning is determination the required cement-water ratio as the main parameter of the composition of concrete mixtures.

A number of calculated equations for the steam-curing concrete compositions design was proposed in the works [2–4]. These equations, obtained in the form of regression equations, are valid, but have a local character. Such equations are valid only in a certain interval of change of the factors taken into account.

S. Mironov and L. Malinina had showed [18] that at constant C/W concrete strength depends on the temperature, duration of the total heat cycle and subsequent curing. However, the required calculated dependencies had not been obtained by them, considering the activity of cements, steaming mode, and other technological factors. Concrete strength forecast after 4 h upon steaming (R_c^{st}) according to the normalized mode (2+3+6+2 h at 80 °C) with a certain cement activity after steaming (R_{cem}^{st}) was offered by L. Kaiser and R. Chekhova [19] using an empirical equation:

$$R_c^{st} = 0.41(R_{cem}^{st} + 9)C/W - 0.83(C/W)^2 - 0.35R_{cem}^{st} - 7. \quad (1)$$

Dvorkin, L.I., Zhitkovsky, V.V. Method of proportioning the cement-water ratio of steam-cured concrete. Magazine of Civil Engineering. 2019. 90(6). Pp. 15–27. DOI: 10.18720/MCE.90.2

Дворкин Л.И., Житковский В.В. Метод расчета цементно-водного отношения пропариваемого бетона // Инженерно-строительный журнал. 2019. № 6(90). С. 15–27. DOI: 10.18720/MCE.90.2



This open access article is licensed under CC BY 4.0 (<https://creativecommons.org/licenses/by/4.0/>)

It is difficult to apply equation (1) for the design of concrete compositions. This equation does not take into account the duration of hardening of concrete after steaming, the possible deviations of the steaming mode from the nominal one.

The dependence of the strength of cement concrete (R_c) based on cements of different mineralogical composition and the heat treatment time in hours at an isothermal aging temperature of 80° C was also established [19]. The samples were subjected to heat treatment with 3 + n + 2 hours modes and a preliminary exposure of 2 hours. They were tested 6 h after removal from the chamber. The established dependence is expressed by the formula:

$$R_c = A_{cem} (\lg \tau - \lg \tau_0), \quad (2)$$

where A_{cem} is parameter characterizing the influence of cement and test conditions, MPa;

τ is the heat treatment time in hours, including the isothermal exposure period n and part of the warm-up and cooling periods, during which the temperature of the samples exceeds 60 °C, on average $\tau = n + 3$;

τ_0 is induction hardening period i.e. the beginning of the formation of a solid structure.

The parameters of equation (2) for cements of different mineralogical composition are given in Table 1.

Table 1. Equation parameters (2) [19].

Cement group	Cement number	Mineralogical characteristic cement	A, MPA	τ_0 , h	Limit of function linearity in h
I – low aluminate	1	$C_3A = 2...3 \%$; $C_3S = 60 \%$	12.5	0.6	20...25
	2	$C_3A = 2...3 \%$; $C_3S = 50 \%$	9.5	0.45	20
II – medium aluminate	3	$C_3A = 8 \%$; $C_3S = 60...65 \%$	10.0	0.15	9...10
	4	$C_3A = 8 \%$; $C_3S = 50 \%$	9.5	0.2	9...10
III – high aluminate	5	$C_3A = 11...12 \%$; $C_3S = 55 \%$	8.5	0.15	9
	6	$C_3A = 11...12 \%$; $C_3S = 40...50 \%$	7.0	0.18	7...8

As it can be seen from the Table 1, at an equal amount of C_3A , the strength characteristics of used cements (A) increase with increasing C_3S content in clinker. It grows with the decrease of the C_3A content at the equal amount of alite; the more C_3A content is, the shorter is the induction period. Cements of the I group have the minimal hardening rate of the steam cured concrete, the cement of the III group has the maximum one.

The optimal duration of isothermal exposure of concrete at 80...90 °C for the cements of all groups, above which the increase in strength becomes minimal, is 4...12 hours.

Recommended optimal modes of heat treatment of concrete (temperature rise – isothermal exposure, cooling in hours) on cements of various mineralogical groups [19] are given below:

Group I – 3 + 12 + 2;

Group II – 3 + 6 + 2;

Group III – 3 + 4 + 2;

Ordinary slag Portland cement – 3 + 14 + 2

Rapid hardening slag Portland cement – 3 + 8 + 2.

Most cements (except of the III group) provides intensive strength increase up to 28 days when steam cured in optimal conditions.

The strength of the steam cured concrete, considering the subsequent hardening up to 1 day (R_{cl}^{st}), can be determined from the equation proposed by V.I. Shein [20]:

$$R_{cl}^{st} = R_c^{st} + K_t I \lg(\tau_1 / \tau_0) R_c^{28}, \quad (3)$$

where I is the intensity of hardening of concrete after steam curing;

τ_1 is duration of hardening of concrete after steam curing (0.5...24 h);

$\tau_0 = 4$ h;

R_c^{28} is concrete compressive strength in 28 days;

K_t is temperature coefficient (at average temperature of curing concrete 20 °C – $K_t = 1.0$; 30...40 °C – $K_t = 1.1...1.2$; 10 °C – $K_t = 0.8$).

Effective technological method of the increasing yield strength in the initial periods of hardening after steam curing is the introduction hardening accelerating additives into the fresh concrete [21].

Equations (2) and (3) should be used to predict the effect of the hardening duration of the steam-curing concrete, taking into account the steaming mode and the chemical and mineralogical composition of the cement. However, they do not allow to solve the main task of designing concrete mixes composition – finding the required C/W with the complex effect of cement strength in the conditions of steaming, steaming mode and the duration of following curing.

Obtaining the dependencies required to determine the compositions of the steam-curing concrete by the calculated-experimental method was the goal of this work. The creation of such dependencies develops as a theoretical understanding of the influence of the main technological factors on the properties of concrete. The development of such equations contributes to the creation of a calculation base for an express and practical available determination of concrete mixes composition that provide specified properties.

2. Materials and Methods

The studies were performed on cubic samples of concrete with dimensions 10×10×10 cm, which hardened both under normal conditions and steam curing. For the manufacture of concrete concrete mixes with slump 10...15 cm and stiffness $V_b = 30...50$ s have been used. Medium aluminate Portland cement CEM II/A-S ($C_3A = 6...8$ %, $C_3S = 58...61$ %), as well as slag Portland Cement CEM III/A were used as a binders. Both cements had a strength class of 42.5 N in accordance to European norms EN 197-1. The composition of cements and their physical-mechanical properties are given in Table 2.

Table 2. Composition and properties of used cements.

Cement	Cement composition, %		Setting time hour-min		Normal consistency, %	Compressive strength, MPa	
	clinker	slag	initial	final		7 days	28 days
Portland Cement	80	20	1-20	3-45	24.6	28.5	48.2
Slag Portland Cement	55	45	1-40	4-20	26.2	24.3	45.4

Quartz sand with a modulus of fineness $M_f = 2.1$ and granite crushed stone fraction 5–20 mm were aggregates of concrete. As a hardening accelerator sodium sulfate was added to concrete mixtures in an amount of 1 % by weight of cement.

Steaming of concrete samples was carried out in laboratory steaming chamber, which allows to regulate the temperature and duration of heat treatment within the required limits. The steaming temperature changed from 60 to 95 °C, the duration of isothermal heating from 2 to 18 h. After steaming, the samples were cooled for 2 hours.

3. Results and Discussion

Strength after thermal treatment (R_c^{st}) should be provided besides 28 days strength (R_c^{28}) for steam-cured concrete at proportioning, unlike normal hardening concrete. Given strength parameters can be achieved either at equal or at different C/W (Table 3). In the second case it is necessary to select C/W providing achievement of two given strength parameters. As shown in Table 3, C/W can vary, depending on the values of R_c^{28} and R_c^{st} , ratio between them, steaming period, duration of further hardening.

As it follows from Table 3, if the steaming period and duration of further curing is shorter, increase of strength after thermal treatment and prerequisites are created to R_c^{st} become the dominating strength parameter and vice versa. Applying high-early-strength cement, hardening accelerating admixtures and optimization the thermal treatment mode lead to narrowing the required C/W interval [19].

It is convenient to use the general equation for compressive strength 28 days to obtain required C/W :

$$R_c^{28} = pA_t R_{cem} \left(\frac{C}{W} - 0.5 \right), \quad (4)$$

where R_{cem} is cement compressive strength at 28 days of curing under normal conditions.

Table 3. Parameters, determining strength of steam-cured concrete.

No.	Steaming period, hours	Post-steaming period under normal conditions, hours	Design strength parameters/required C/W	
			Compressive strength after steam-curing and further curing, R_c^{st} , MPa	Design concrete strength, R_c^{28} , MPa
1	7	4	$\frac{14^*}{1.8}$	$\frac{20}{1.4}$
2	16	4	$\frac{14}{1.4}$	$\frac{20}{1.4}$
3	7	4	$\frac{21^*}{2.3}$	$\frac{30}{1.8}$
4	16	4	$\frac{21}{1.8}$	$\frac{30}{1.8}$
5	16	4	$\frac{15}{1.5}$	$\frac{30^*}{1.8}$
6	16	4	$\frac{25}{2.4}$	$\frac{40}{2.4}$
7	7	4	$\frac{35^*}{3.1}$	$\frac{50}{2.9}$
8	7	4	$\frac{25}{2.9}$	$\frac{50}{2.9}$
9	7	24	$\frac{35}{2.9}$	$\frac{50}{2.9}$
10	16	4	$\frac{25}{2.3}$	$\frac{50^*}{2.9}$

Notes: 1. The data is obtained for Portland cement with tricalcium silicate $C_3A = 6...8\%$, quartz sand of medium fineness and crushed granite stone size 5...20 mm. Concrete was steam cured at 80° according to the following mode 1+2+3.5+0.5 (total duration – 7 h) and 2+3+9+2 hours (total duration is 16 hours).

2. Required C/W values are given under the line.

3. * – dominant strength parameter.

For steam-cured concrete $pA_i = AA_1A_2...A_n$ is a multiplicative coefficient, describing the initial materials features' influence (A), thermal treatment (A_1), hardening accelerating admixtures (A_2), etc.

The influence of various factors on A coefficient was widely investigated [21–23]. According to results of experimental data processing [17, 22, 23], coefficient A_1 for steam-cured concrete with compressive strength R_c^{28} up to 30 MPa varies from 0.85 to 0.95, for $R_c^{28} > 30$ MPa it is from 0.95 to 1.05. The lower values of A_1 are characteristic for shortened thermal treatment cycles and concrete mixtures with high water demand. The value of coefficient A_2 can be assumed according to known recommendations [22, 23].

We obtained the equations given below as the result of statistical processing of experimental data [17] for concrete with:

– 28-day compressive strength within the range of 20...30 MPa using Portland cement with strength of 40 MPa:

$$A_{\tau,t} = 0.242 \ln(\tau) + 0.0115t + 0.008; \quad (5)$$

– 28-day compressive strength within the range of 30...40 MPa using Portland cement with strength 50...60 MPa:

$$A_{\tau,t} = 0.2179 \ln(\tau) + 0.0134t + 0.063; \quad (6)$$

– 28-day compressive strength in the range of 20...30 MPa using blast-furnace slag cement with strength of 40 MPa:

$$A_{\tau,t} = 0.2395 \ln(\tau) + 0.0111t - 0.06, \quad (7)$$

where τ is the hardening duration of hardening, days;

t is the average concrete temperature, $^\circ\text{C}$ ($t = 5...40$ $^\circ\text{C}$).

The system of coefficients A_i can be specified by statistical processing of experimental data for a certain industrial enterprise. Table 4 presents an example of coefficients, characterizing effects of raw materials quality (A), hardening duration (A_τ), thermal treatment ($A_{t,t}$) and hardening accelerating admixtures (A_{ac}) on compressive strength of concrete, as well as calculated (R_c) and real (R_r) concrete strength values at $C/W = 1.4$ for Portland cement with strength 40 MPa.

Table 4. Values of coefficients A_i , calculated (R_c) and real (R_r) concrete strength values ($R_{cem} = 40$ MPa, $C/W = 1.4$).

Type of concrete	Age of hardening	Coefficients					R_c , MPa	R_r , MPa
		A	A_τ	$A_{t.t.}$	A_{ac}	pA		
Normally hardened concrete	7 days	0.53	0.65	–	–	0.34	12.4	14.5
	28 days	0.53	–	–	–	0.53	19.1	15.3
	90 days	0.53	1.20	–	–	0.64	22.9	25.2
	180 days	0.53	1.35	–	–	0.72	25.8	21.9
Concrete steam-cured at 80 °C, steam-curing mode (2+3+6+2 h)	4 h	0.53	–	0.63	–	0.33	12	13.9
	12 h	0.53	–	0.71	–	0.38	13.5	11.5
	24 h	0.53	–	0.75	–	0.4	14.3	12.7
Same, with hardening accelerating admixture of sodium sulfate	4 h	0.53	–	0.63	1.3	0.43	15.4	17.5
	12 h	0.53	–	0.71	1.25	0.47	17	19
	24 h	0.53	–	0.75	1.2	0.48	17.3	19.7

Deviations of calculated strength values from average experimental ones do not exceed 17 %, which is acceptable for the calculations at the design stage of the mix's compositions.

Strength of concrete after steaming (R_c^{st}) varies in a wide range, thus the dominant factors, are cement-water ratio (C/W) and cement strength at the given thermal treatment cycle (R_{cem}^{st}).

it is rational to express the steam-cured concrete strength R_c^{st} as well as R_c^{28} using Bolomey formula for porportioning:

$$R_c^{st} = \rho K R_{cem}^{st} (C/W - b), \quad (8)$$

where $K = K_1 K_2 K_3 \dots K_n$ is a multiplicative coefficient, considering the influence of various factors on strength of steam-cured concrete (K is the basic coefficient, characterizing the impact of R_{cem}^{st} ;

K_1 is coefficient, depending on concrete mixture workability;

K_2 is coefficient, taking into account the impact of steam-cured concrete aggregates;

K_3 is coefficient, considering strength growth due to hardening accelerators addition).

It is acceptable to use Equation (8) for approximating the data, calculated according to Equation (1), (see Table 5). The values of basic coefficient K vary depending on R_{cem}^{st} within the range 0.5–0.67. By applying average values of the coefficient $K = 0.66$ for $R_{cem}^{st} = 20$ –25 MPa and $K = 0.53$ for $R_{cem}^{st} = 30$ –40 MPa [19] the deviations in the values of R_{cem}^{st} calculated according Equations (1), (8) were below 10 %.

Table 5. Calculated values of R_c^{st} , MPa.

R_{cem}^{st} , MPa	Equation	C/W						
		1.55	1.80	2.00	2.30	2.60	2.80	3.00
20	(1)	10.7	14.3	17.1	21.2	25.1	27.6	30.1
	(8) $K = 0.66; b = 0.74$	10.6	13.9	16.6	20.5	24.5	27.1	29.8
25	(1)	12.1	16.2	19.4	24.1	28.7	31.6	34.5
	(8) $K = 0.66; b = 0.74$	13.3	17.4	20.7	25.7	30.6	33.9	37.2
30	(1)	13.5	18.2	21.8	27.1	32.3	35.6	38.9
	(8) $K = 0.53; b = 0.74$	12.9	16.9	20.1	25.0	29.8	33.0	36.2
40	(1)	16.4	22.0	26.5	33.0	39.4	43.6	47.7
	(8) $K = 0.53; b = 0.74$	17.2	22.6	26.9	33.3	39.7	44.0	48.3

Note: Coefficients K and b have been obtained by analyzing linear dependencies $R_c^{st} = f(R_{cem}^{st}, C/W)$ following the data given in [19].

Coefficient b in Equation (8) varies insignificantly for the entire range of R_c^{st} values of the concrete compositions (Table 5) and it is equal to 0.74. Coefficient K decreases as the steamed cement strength increases (Table 5), it shows that the influence of the last one on concrete strength is nonlinear. This conclusion follows also from Equation (1).

The values of coefficient K , given in Table 5, are valid for low-slump fresh concrete, based on crushed stone and medium grained sand. Water content and correspondingly workability, which can be considered in Equation (8) by coefficient K_1 have significant impact on strength of steam-cured concrete at constant C/W . For concrete with slump $Sl = 1-4$ cm the value of $K_1 = 1$, and with $Sl \geq 9$ cm – $K_1 = 0.9$, if Vebe time $V_b = 30-50$ sec then $K_1 = 1.1$ (Table 6).

Table 6. Experimental and calculated values of concrete strength after steaming.

No.	Concrete strength R_c^{st} , MPa	C/W						
		1.55	1.80	2.00	2.30	2.60	2.80	3.00
$R_{cem}^{st} = 20$ MPa; $Sl = 10-15$ Cm								
1	Experimental values	9.9	13.4	14.5	19.1	22.7	23.8	27.3
2	Calculated according to Equation (8) at $K_1 = 0.9$	9.6	12.6	15.0	18.5	22.1	24.5	26.8
$R_{cem}^{st} = 40$ MPa; $Sl = 10-15$ Cm								
3	Experimental values	16.7	20.6	24.4	31.9	36.7	41.8	45.9
4	Calculated according to Equation (8) at $K_1 = 0.95$	16.3	21.3	25.4	31.4	37.5	41.5	45.5
$R_{cem}^{st} = 20$ MPa; $V_b = 30-50$ sec.								
5	Experimental values	10.5	14.8	17.7	23.5	27.6	28.5	31.1
6	Calculated according to Equation (8) at $K_1 = 1.1$	11.8	15.4	18.3	22.7	27.0	29.9	32.8
$R_{cem}^{st} = 40$ MPa; $V_b = 30-50$ sec.								
7	Experimental values	17.4	23.8	29.8	35.7	42.8	48.8	52.1
8	Calculated according to Equation (8) at $K_1 = 1.1$	18.9	24.7	29.4	36.4	43.4	48.0	52.7

Notes: 1. Experimental data have been obtained using Portland cement (tricalcium aluminate content $C_3A = 6...8$ %), medium grained quartz sand and crushed granite stone 5...20 mm. Concrete was steamed at 80 °C according to cycle (2)+3+6+2 h.

2. The average deviation of calculated values K_1 from the experimental ones does not exceed 5 %.

The steam-cured concrete aggregates features can make influence on water-content variation and directly on the change of C/W to achieve required strength. In the last case coefficient K_2 is added to Equation (8). For ordinary aggregates $K_2 = 1$. However, it can be assumed that $K_2 = 0.95$ if crushed stone or gravel has reduced strength as well as if the content of weak grains or clay, silt and dust content is rather high; $K_2 = 0.9$ for sand with fineness modulus below 1.5.

The essential reserve for C/W reduction of steam-cured concrete can be provided by strength growth due to hardening accelerators, considered by coefficient K_3 in Equation (8), and further hardening after thermal treatment.

Processing the experimental results obtained when the concrete samples were kept at 20 °C for 0.5–24 hours after steaming ($\tau_{p,p}$) using the 2 + 3 + τ_{iz} + 2 mode (τ_{iz} is the isothermal aging per hour) at $t = 80$ °C allowed us to calculate the nomogram for determination the change in the concrete strength after the heat treatment (Figure 1) within the range 0.5–24 h after steaming at different duration from equation:

$$R_{c1}^{st} = R_c^{st} + \Delta R_c R_c^{28}. \quad (9)$$

At $\tau_{p,p} = 1 - 28$ days the intensity of concrete strength growth is practically independent of steaming mode parameters. Concrete strength at this hardening interval can be found according to the following formula:

$$R_{c2}^{st} = R_{c1}^{st} + K_t \frac{R_c^{28} - R_{c1}^{st}}{\lg 28} \lg \tau_{p,p}. \quad (10)$$

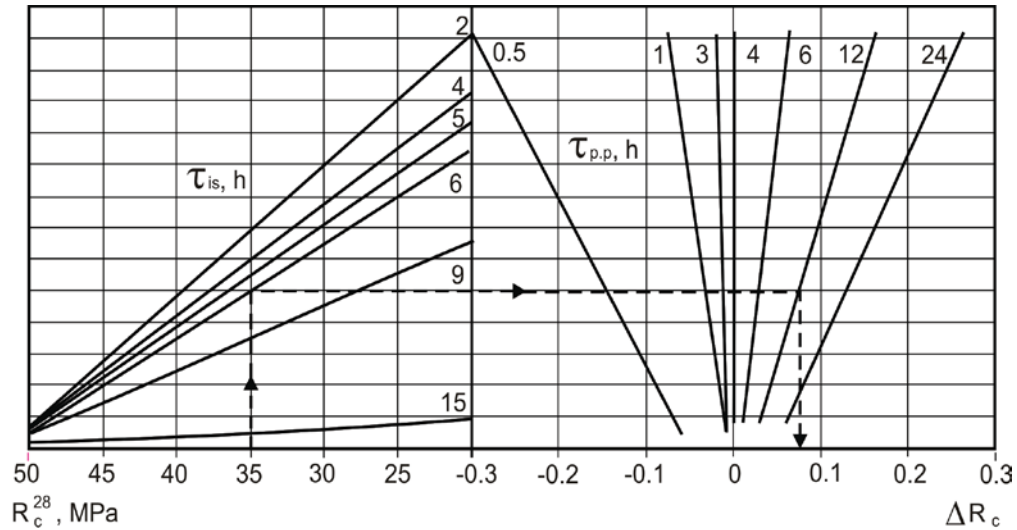


Figure 1. Nomogram for calculation of increase in relative concrete strength ΔR_c^{st} after steaming and post-steaming period up to 1 day.

Cement strength at steaming (R_{cem}^{st}) can be expressed as:

$$R_{cem}^{st} = R_{cem} K_e, \quad (11)$$

where K_e is efficiency coefficient, characterizing the influence of different technological factors on strength of standard cement – sand specimens at $W/C = 0.4$ after thermal treatment.

The K_e value determined for steaming standard cement – sand mortar specimens varies depending on the applied cement from 0.55 to 0.75.

Corresponding graphs (Figure 2) of basic efficiency coefficient K_e^0 depending on isothermal heating duration τ_{is} and temperature $t_{t,t}$ for Portland cement with strength of 50 MPa ($K_{e_{p.c}}^0$) and blast furnace slag cement with strength of 40 MPa ($K_{e_{s.p.c}}^0$), obtained by experimental data processing are given below [19].

Cements have been made of typical medium aluminate clinker (tricalcium aluminate $C_3A = 6.2-7.1\%$, tricalcium silicate $C_3S = 58.5-61.3\%$) and additionally included: Portland cement – 5% of gypsum, blast furnace slag cement – 5% of gypsum and 50% of blast furnace slag. Cement strength at steam curing was obtained 4 h after thermal treatment (steam-curing cycle 2 + 3 + τ_{is} + 2). The steam curing temperature was varied from 60 to 95 °C, τ_{is} from 2 to 18 h. The value of K_e^0 was found from the condition that $K_e^0 = R_{cem}^{st} / R_{cem}$.

Table 7 presents the experimental and calculated values of K_e^0 , obtained according to Figure 2. Analysis of the calculated and experimental values of K_e^0 shows their high convergence.

The most influential factors, effecting K_e , are chemical-mineralogical composition, mineral admixtures content and cement strength:

$$K_e = K_A K_D K_{R_{cem}} K_e^0, \quad (12)$$

where K_e^0 is the basic efficiency coefficient value that can be found using Figure 2;

K_A , K_D , $K_{R_{cem}}$ are correcting coefficients, depending correspondingly on aluminate content in cement, mineral admixtures content and cement strength.

Considering the data given in [18, 19], there are following values of K_A : for high aluminate cements at $\tau_{is} \leq 3$ h $K_A = 0.9$; $\tau_{is} \geq 6$ h; $K_A = 0.8$ for low aluminate cements at $\tau_{is} \leq 3$ h $K_A = 0.8$; $\tau_{is} \geq 6$ h $K_A = 0.95$; $\tau_{is} \geq 9$ h; $K_A = 1 - 1.1$.

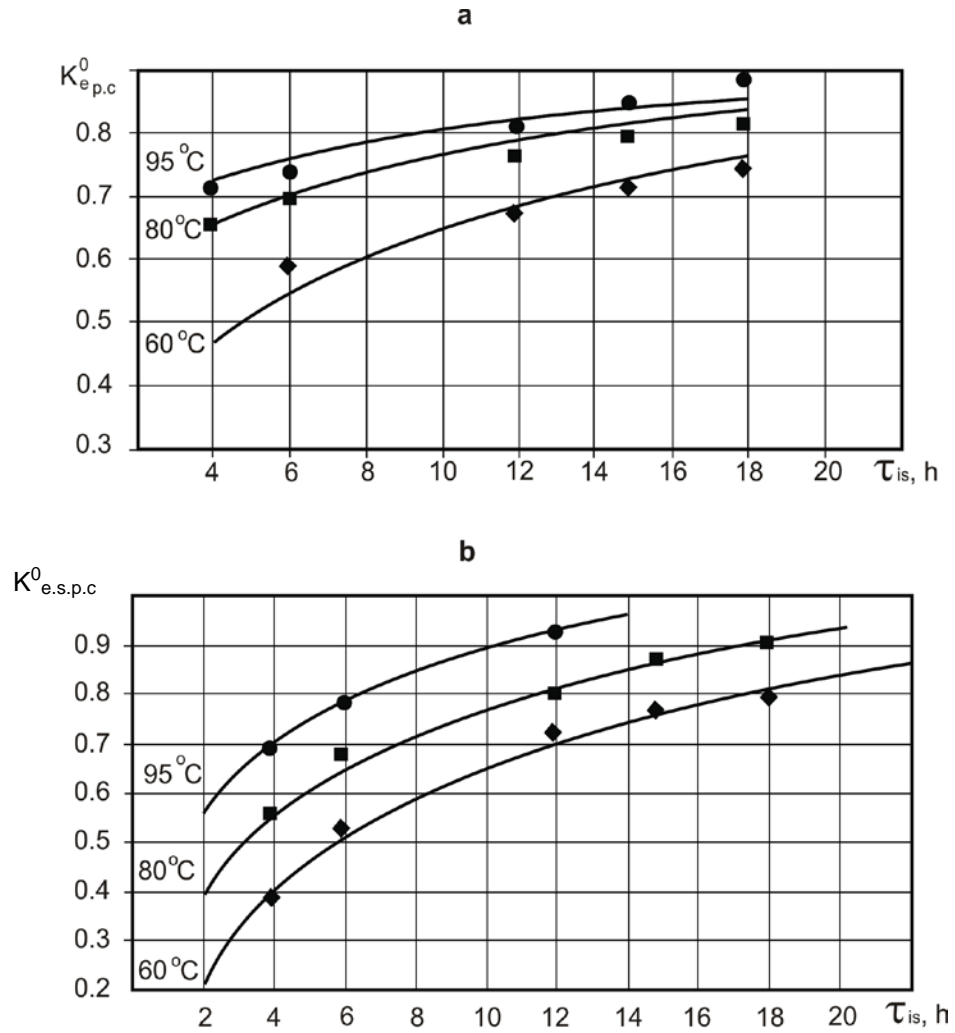


Figure 2. Graphs for determining coefficients K_e^0 : a – Portland cement; b – blast furnace slag cement; $\diamond - t_{t,t} = 60^\circ\text{C}$; $\square - t_{t,t} = 80^\circ\text{C}$; $\circ - t_{t,t} = 95^\circ\text{C}$.

Table 7. Calculated and experimental values of K_e^0 and relative strength values.

K_e^0 and relative strength values	Steam curing temperature, °C, $t_{t,t}$	Isothermic heating duration τ_{is} , h.				
		4	6	12	15	18
Portland cement with tricalcium aluminate content $C_3A = 6...8\%$ (authors data)						
Calculated values of K_e^0	60	0.48	0.56	0.70	0.74	0.78
	80	0.63	0.69	0.78	0.81	0.83
	95	0.75	0.78	0.84	0.86	0.87
Experimental values of K_e^0	60	0.51	0.59	0.67	0.72	0.75
	80	0.63	0.69	0.76	0.78	0.81
	95	0.71	0.74	0.81	0.86	0.89
Blast furnace slag cement (authors data)						
Calculated values of K_e^0	60	0.40	0.51	0.70	0.76	0.81
	80	0.55	0.65	0.82	0.87	0.92
	95	0.67	0.75	0.91	0.95	–
Experimental values of K_e^0	60	0.39	0.52	0.71	0.76	0.8
	80	0.55	0.66	0.81	0.87	0.91
	95	0.69	0.78	0.94	0.97	–
Portland cement with tricalcium aluminate content $C_3A = 6...8\%$ [18]						
Experimental values for relative strength of concrete at $W/C = 0.4 (R_c^{st} / R_c^{28})$	60	0.5	0.6	0.76	0.8	0.83
	80	0.67	0.76	0.87	0.88	0.88
	100	0.70	0.72	–	–	–
Blast furnace slag cement [18]						
Same	60	0.4	0.49	0.67	0.74	0.8
	80	0.55	0.64	0.84	0.9	0.92
	100	0.7	0.8	–	–	–

The value of coefficient K_D depends on mineral admixtures' type and content. If the mineral admixtures' content is up to 10 % the cement strength at steam curing is usually constant. At a 20 % mineral admixtures' content a certain reduction of R_{cem}^{st} is observed at shortened steam-curing cycles. At $\tau_{is} \leq 4$ h adding 20 % of blast furnace slag and fly ash to cement leads to average strength decrease at 10 % ($K_D = 0.9$), pozzolanic admixtures – 15 % ($K_D = 0.85$) [24]. At $\tau_{is} > 4$ h – $K_D = 1.0$.

For cement with 28-day strength of 50 MPa $K_{Rcem} = 1$, 40 MPa $K_{Rcem} = 1.05$; 30 MPa $K_{Rcem} = 1.15$; 55 MPa $K_{Rcem} = 0.95$.

The scheme of the algorithm for calculation C/W of steam-cured concrete is presented in Figure 3. The described set of calculation dependencies enables to obtain the required cement-water ratio (C/W) at different requirements to concrete under thermal treatment and different hardening duration, as well as estimate the efficiency of technological solutions, related to varying the temperature, isothermal duration, hardening after steaming, etc.

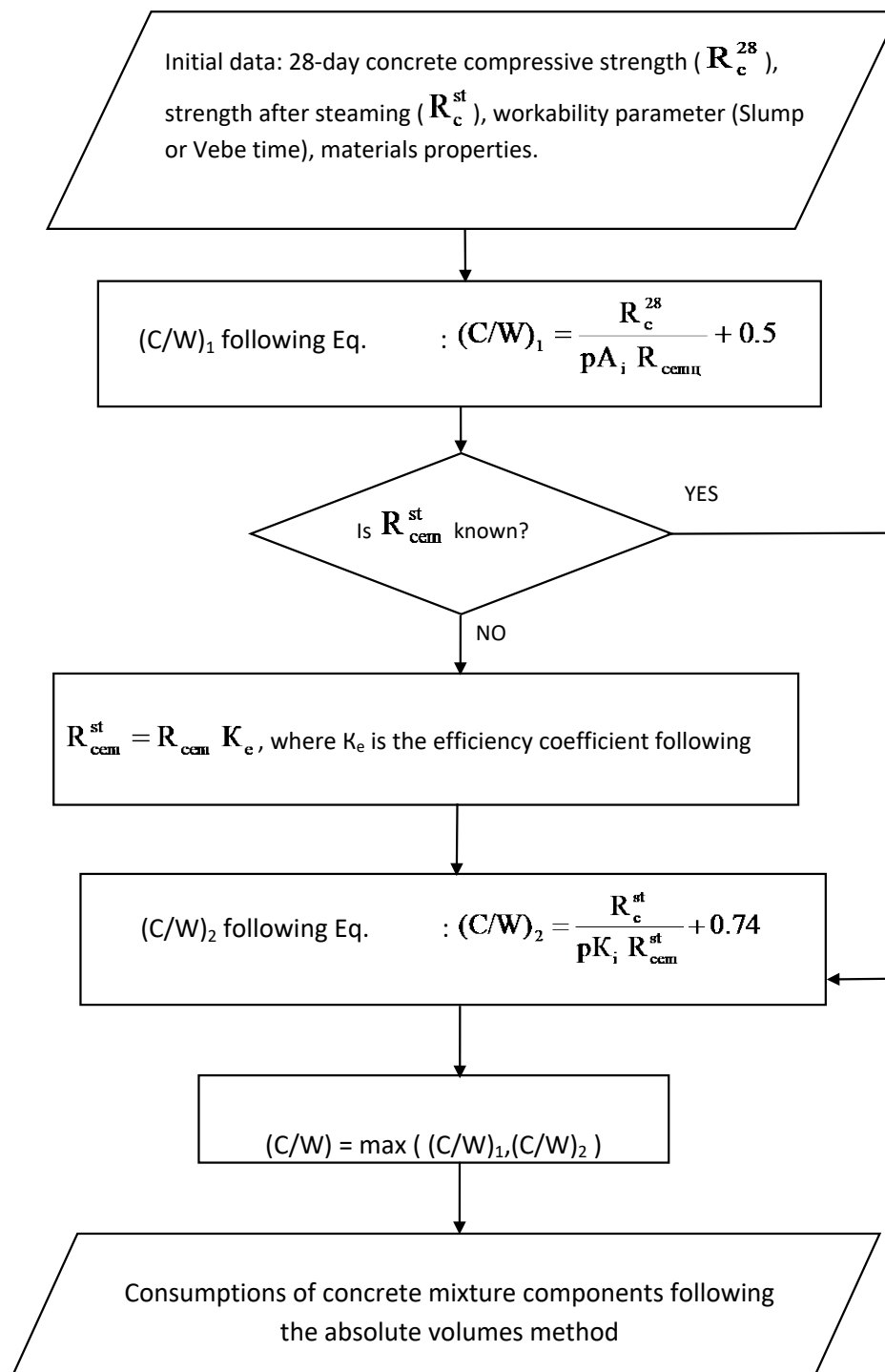


Figure 3. Algorithm for calculation of steam-cured concrete C/W .

Example

To determine C/W and achieve compressive strength of concrete 28 MPa after steaming and further hardening of 1 day, while ensuring design strength of 28 days 40 MPa.

Initial data: slump of fresh concrete – 10–15 cm, steaming mode – 2+3+6+2 at 80 °C.

Materials: Portland cement CEM II/A-S ($C_3A = 8\%$, $C_3S = 60\%$) strength class 42.5 N (design strength 50 MPa), crushed stone 5–20 mm, sand with fineness modulus 2.1.

Accept $A = 0.55$ in the Equation (4) and determine $(C/W)_1$, to achieve given concrete strength in 28 days:

$$C/W_1 = \frac{R_c^{28}}{AA_1 R_{cem}} = \frac{40}{0.55 \cdot 1 \cdot 50} + 0.5 = 1.95.$$

The value of the basic coefficient of steaming efficiency is taken according to Figure 2.

$$K_0^e = 0.7.$$

Values of correction coefficients:

$$K_A = K_D = K_{R_{cem}} = 1.$$

Calculate the value K_e considering the influence of the mineralogical composition of cement, the content of mineral additives and the activity of the cement according to the formula (12):

$$K_e = K_A K_D K_{R_{cem}} K_e^0 = 1 \cdot 1 \cdot 1 \cdot 0.7 = 0.7.$$

Cement strength after steaming, according to (11):

$$R_{cem}^{st} = R_{cem} K_e = 50 \cdot 0.7 = 35 \text{ MPa}.$$

Value of ΔR according to Figure 1:

$$\Delta R = 0.1.$$

Strength of concrete in 4 h after steaming Equation (9):

$$R_c^{st} = 28 - 0.1 \cdot 40 = 24 \text{ MPa}.$$

Find $(C/W)_2$ according to the Equation (8) to achieve of necessary concrete strength after steam curing:

$$(C/W)_2 = \frac{R_c^{st}}{pKR_{cem}^{st}} + 0.74 = \frac{24}{0.53 \cdot 1 \cdot 1 \cdot 35} + 0.74 = 2.03.$$

Since $(C/W)_2 > (C/W)_1$ we accept $C/W = 2.03$ for further calculations of the concrete composition.

4. Conclusions

1. The equations of concrete strength are experimentally substantiated, which allow taking into account the steaming mode and the duration of the subsequent hardening up to 28 days.

2. Multiplicative coefficients, taking into account the complex of basic technological factors, proposed quantitative dependencies and recommendations for calculating these coefficients are included in the equation of strength of concrete immediately after steaming and after 28 days of hardening.

3. As a result of processing the experimental data, a nomogram was drawn to calculate the strength of concrete at the age of 0.5–24 h after steam curing. Equation for calculation of the increase in concrete strength after steam curing at the age of 1–28 days was also suggested.

4. The equation for determination the activity of Portland cement and blast furnace slag cement developed during steam curing has been substantiated, taking into account cement activity during normal hardening and the coefficient reflecting the effect of temperature and the duration of isothermal holding of concrete during steaming (coefficient of steaming efficiency). Graphical dependencies are recommended to find this coefficient.

5. The combination of the obtained quantitative dependencies and recommendations allows to find the values of the required cement-water ratio for steam-cured concrete in accordance with the suggested algorithm, under given conditions.

References

1. Lui, B., Xie, Y., Li, X. Influence of steam curing on the compressive strength of concrete containing supplementary cementing materials. *Cement and Concrete Research*. 2005. 35. Pp. 994–998. DOI: 10.1007/s13369-015-1952-y.
2. Asad, Hanif, Yongjae, Kim, Muhammad, Usman, Cheolwoo, Park. Optimization of Steam-Curing Regime for Recycled Aggregate Concrete Incorporating High Early Strength Cement – A Parametric Study [Online]. *Materials*. 2018. No. 11(12). Pp. 2487–2501. URL: <https://doi.org/10.3390/ma11122487>
3. Nakajima, N., Maruyana, T., Koyama, N., Date, S. Effect of Steam Curing on Initial Strength Development of Mortar. *International Journal of Engineering and Technology*. 2017. 9. Pp. 468–473. DOI: 10.7763/IJET.2017.V9.1018.
4. Gambhir, M.L. *Concrete Technology. Theory and Practice* [Online]. Tata Mc. Graw-Hill Education. 1986. Pp. 318. URL: <https://www.abebooks.com/servlet/BookDetailsPL?bi=4814294016>
5. Neville, A.M. *Properties of Concrete* [Online]. 5th ed. Wiley, New York. 1995. URL: <https://igitgeotech.files.wordpress.com/2014/10/properties-of-concrete-by-a-m-neville.pdf>
6. Benammar, B., Mezghiche, B., Guettala, S. Influence of atmospheric steam curing by solar energy on the compressive and flexural strength of concretes. *Construction and Building materials*. 2013. 49. Pp. 511–518. DOI: 10.1016/j.conbuildmat.2013.08.085.
7. Ramezani-pour, A., Khazali, M., Vosoughi, P. Effect of steam curing cycles on strength and durability of SCC: a case study in precast concrete [Online]. *Construction and Building Materials*. 2013. 49. Pp. 807–813. URL: https://www.researchgate.net/publication/273451175_Effect_of_steam_curing_cycles_on_strength_and_durability_of_SCC_A_case_study_in_precast_concrete
8. Ba, M., Qian, C., Guoc, X. Effects of steam curing on strength and porous structure of concrete with low water/binder ratio [Online]. *Construction and Building Materials*. 2011. 25. Pp. 123–128. URL: <https://doi.org/10.1016/j.conbuildmat.2010.06.049>
9. Kim, S., Moon, Y., Eo, S. Compressive strength development of concrete with different curing time and temperature [Online]. *Cement Concrete Research*. 1998. 28. Pp. 1761–1773. URL: [https://doi.org/10.1016/S0008-8846\(98\)00164-1](https://doi.org/10.1016/S0008-8846(98)00164-1)
10. Hwang, S., Khatib, R., Lee, H., Lee, S. Optimization of Steam-curing regime for high-strength self-consolidation concrete for precast, prestressed concrete application. *PCJ Journal*. 2012. 57. Pp. 48–62. DOI: 10.15554/pcj.06012012.48.62.
11. Bingol, F., Tohumcu, I. Effects of different curing regimes on the compressive strength properties of self-compacting concrete incorporating fly ash and silica fume. *Materials and Design*. 2013. 51. Pp. 12–18. DOI: 10.1016/j.matdes.2013.03.106.
12. Toutanji, H., Bayasi, Z. Effect of curing procedures on properties of silica fume concrete. *Cement Concrete Research*. 1999. 29. Pp. 497–501. DOI: 10.1016/S0008-8846(98)00197-5.
13. Baosu, L., Yousun, X., Shiqiong, Z., Sian, L. Some factors affecting early compressive strength of steam-curing concrete with ultra-fine fly ash. *Cement Research*. 2001. 31. Pp. 1455–1458. URL: [https://doi.org/10.1016/S0008-8846\(01\)00559-2](https://doi.org/10.1016/S0008-8846(01)00559-2)
14. Ramezani-pour, A., Esmaeli, K., Gahari, S. Influence of initial steam curing and different types of mineral additives on mechanical and durability properties of self-compacting concrete [Online]. *Construction and Building Materials*. 2014. 73. Pp. 187–194. URL: <https://doi.org/10.1016/j.conbuildmat.2014.09.072>
15. Popovics, S. *Strength and Related Properties of Concrete. A Quantitative Approach* [Online]. John Wiley and Sons. Inc, New York, 1998. 122 p. URL: https://www.researchgate.net/publication/255222981_Strength_and_related_properties_of_concrete_A_quantitative_approach
16. Smirnova, O. Sovmestimost portlandtsementa i superplastifikatorov na polikarboksilatnoy osnove dlya polucheniya vysokoprochnogo betona sbornyykh konstruktsiy. *Inzhenerno-stroitelnyy zhurnal*. 2016. No. 6(66). Pp. 12–22. DOI: 10.5862/MCE.66.2. (rus)
17. Mironov, S. *Teoriya i metody zimnego betonirovaniya* [Online]. M.: Stroyizdat, 1975. 700 p. URL: <https://dwg.ru/dnl/10628> (rus)
18. Mironov, S., Malinina, L. *Uskoreniye tverdeniya betona* [Online]. M.: Stroyizdat, 1964. 346 p. URL: <http://elima.ru/books/index.php?id=4625> (rus)
19. Kayser, L., Chekhova, R. *Tsementy i ikh ratsionalnoye ispolzovaniye pri proizvodstve sbornyykh zhelezobetonnykh elementov*. M.: Stroyizdat, 1972. 80 p. (rus)
20. Shein, V. *Fiziko-khimicheskiye osnovy optimizatsii tekhnologii betona*. M.: Stroyizdat, 1977. 271 p. (rus)
21. Dvorkin, O. *Proyektirovaniye betonnykh kompozitsiy. (Osnovy teorii i metodologii)* [Online]. Rovno: NUVGP, 2003. 265 p. URL: <https://www.twirpx.com/file/1071563/> (rus)
22. Dvorkin, L., Dvorkin, O. *Raschetnoye prognozirovaniye svoystv i proyektirovaniye sostavov betona*. M.: Infra-Inzheneriya, 2016. 386 p. (rus)
23. Dvorkin, L., Dvorkin, O. *Osnovy betonovedeniya* [Online]. St. Peterburg: Stroy Beton, 2006. 682 p. URL: <https://elibrary.ru/i tem.asp?id=19626303> (rus)
24. Kayser, L. *Kinetika tverdeniya portlandtsementov v usloviyakh preparirvaniya*. Trudy. RILEM. M.: Stroyizdat, 1968. Pp. 65–74. (rus)

Contacts:

Leonid Dvorkin, +38(068)353-33-38; dvorkin.leonid@gmail.com

Vadim Zhitkovsky, +38(096)564-00-27; zhitk@ukr.net



DOI: 10.18720/MCE.90.2

Метод расчета цементно-водного отношения пропариваемого бетона

Л.И. Дворкин, В.В. Житковский

Национальный университет водного хозяйства и природопользования, г. Ровно, Украина

* E-mail: dvorkin.leonid@gmail.com

Ключевые слова: цементно-водное отношение, прочность, температура, пропаривание, твердение, режимы

Аннотация. В статье приведены результаты экспериментальных исследований, позволившие обосновать расчетные зависимости прочности пропаренного бетона и необходимых значений цементно-водного отношения (Ц/В) для обеспечения заданных значений прочности. С этой целью получены зависимости, справедливые при применении портландцемента и шлакопортландцемента, а также изменении в широком диапазоне режимных параметров тепловой обработки: температуры и длительности последующего твердения. Для расчетов необходимых значений Ц/В обоснована формула, позволяющая определить активность цемента в условиях пропаривания при изменении температуры в диапазоне 60...95 °С и длительности изотермического прогрева при пропаривании от 4 до 18 часов. Для расчета активности цемента рекомендованы для условий пропаривания также коэффициенты, позволяющие учитывать алюминатность цемента, вид и содержание в цементе минеральных добавок. С учетом полученных расчетных зависимостей предложен алгоритм для расчета Ц/В пропаренных бетонов и пример его реализации.

Литература

1. Lui B., Xie Y., Li X. Influence of steam curing on the compressive strength of concrete containing supplementary cementing materials // *Cement and Concrete Research*. 2005. 35. Pp. 994–998. DOI: 10.1007/s13369-015-1952-y.
2. Asad Hanif, Yongjae Kim, Muhammad Usman, Cheolwoo Park. Optimization of Steam-Curing Regime for Recycled Aggregate Concrete Incorporating High Early Strength Cement – A Parametric Study [Электронный ресурс] // *Materials*. 2018. No. 11(12). Pp. 2487–2501. URL: <https://doi.org/10.3390/ma11122487>
3. Nakajima N., Maruyana T., Koyama N., Date S. Effect of Steam Curing on Initial Strength Development of Mortar // *International Journal of Engineering and Technology*. 2017. 9. Pp. 468–473. DOI: 10.7763/IJET.2017.V9.1018.
4. Gambhir M.L. *Concrete Technology. Theory and Practice* [Электронный ресурс]. Tata Mc. Graw-Hill Education. 1986. Pp. 318. URL: <https://www.abebooks.com/servlet/BookDetailsPL?bi=4814294016>
5. Neville A.M. *Properties of Concrete* [Электронный ресурс]. 5th ed. Wiley, New York. 1995. URL: <https://igitgeotec.h.files.wordpress.com/2014/10/properties-of-concrete-by-a-m-neville.pdf>
6. Benammar B., Mezghiche B., Guettala S. Influence of atmospheric steam curing by solar energy on the compressive and flexural strength of concretes // *Construction and Building materials*. 2013. 49. Pp. 511–518. DOI: 10.1016/j.conbuildmat.2013.08.085.
7. Ramezani-pour A., Khazali M., Vosoughi P. Effect of steam curing cycles on strength and durability of SCC: a case study in precast concrete [Электронный ресурс] // *Construction and Building Materials*. 2013. 49. Pp. 807–813. URL: https://www.researchgate.net/publication/273451175_Effect_of_steam_curing_cycles_on_strength_and_durability_of_SCC_A_case_study_in_precast_concrete
8. Ba M., Qian C., Guoc X. Effects of steam curing on strength and porous structure of concrete with low water/binder ratio [Электронный ресурс] // *Construction and Building Materials*. 2011. 25. Pp. 123–128. URL: <https://doi.org/10.1016/j.conbuildmat.2010.06.049>
9. Kim S., Moon Y., Eo S. Compressive strength development of concrete with different curing time and temperature [Электронный ресурс] // *Cement Concrete Research*. 1998. 28. Pp. 1761–1773. URL: [https://doi.org/10.1016/S0008-8846\(98\)00164-1](https://doi.org/10.1016/S0008-8846(98)00164-1)
10. Hwang S., Khatib R., Lee H., Lee S. Optimization of Steam-curing regime for high-strength self-consolidation concrete for precast, prestressed concrete application // *PCJ Journal*. 2012. 57. Pp. 48–62. DOI: 10.15554/pcj.06012012.48.62.
11. Bingol F., Tohumcu I. Effects of different curing regimes on the compressive strength properties of self-compacting concrete incorporating fly ash and silica fume // *Materials and Design*. 2013. 51. Pp. 12–18. DOI: 10.1016/j.matdes.2013.03.106.
12. Toutanji H., Bayasi Z. Effect of curing procedures on properties of silica fume concrete // *Cement Concrete Research*. 1999. 29. Pp. 497–501. DOI: 10.1016/S0008-8846(98)00197-5.
13. Baosu L., Yousun X., Shiqiong Z., Sian L. Some factors affecting early compressive strength of steam-curing concrete with ultra-fine fly ash [Электронный ресурс] // *Cement. Concrete Research*. 2001. 31. Pp. 1455–1458. URL: [https://doi.org/10.1016/S0008-8846\(01\)00559-2](https://doi.org/10.1016/S0008-8846(01)00559-2).
14. Ramezani-pour A., Esmaeli K., Gahari S. Influence of initial steam curing and different types of mineral additives on mechanical and durability properties of self-compacting concrete [Электронный ресурс] // *Construction and Building Materials*. 2014. 73. Pp. 187–194. URL: <https://doi.org/10.1016/j.conbuildmat.2014.09.072>

15. Popovics S. Strength and Related Properties of Concrete. A Quantitative Approach [Электронный ресурс]. John Wiley and Sons. Inc, New York. 1998. 122 p. URL: https://www.researchgate.net/publication/255222981_Strength_and_related_properties_of_concrete_A_quantitative_approach
16. Смирнова О. Совместимость портландцемента и суперпластификаторов на поликарбоксилатной основе для получения высокопрочного бетона сборных конструкций // Инженерно-строительный журнал. 2016. № 6(66). С. 12–22. DOI: 10.5862/MCE.66.2.
17. Миронов С. Теория и методы зимнего бетонирования [Электронный ресурс]. М.: Стройиздат, 1975. 700 с. URL: <https://dwg.ru/dnl/10628>
18. Миронов С., Малинина Л. Ускорение твердения бетона [Электронный ресурс]. М.: Стройиздат, 1964. 346 с. URL: <http://elima.ru/books/index.php?id=4625>
19. Кайсер Л., Чехова Р. Цементы и их рациональное использование при производстве сборных железобетонных элементов. М.: Стройиздат, 1972. 80 с.
20. Шеин В. Физико-химические основы оптимизации технологии бетона. М.: Стройиздат, 1977. 271 с.
21. Дворкин О. Проектирование бетонных композиций. (Основы теории и методологии) [Электронный ресурс]. Ровно: НУВГП. 2003. 265 с. URL: <https://www.twirpx.com/file/1071563/>
22. Дворкин Л., Дворкин О. Расчетное прогнозирование свойств и проектирование составов бетона. М.: Инфра-Инженерия, 2016. 386 с.
23. Дворкин Л., Дворкин О. Основы бетоноведения [Электронный ресурс]. СПб.: Строй Бетон, 2006. 682 с. URL: <https://elibrary.ru/item.asp?id=19626303>
24. Кайсер Л. Кинетика твердения портландцементов в условиях пропаривания // Труды. RILEM. М.: Стройиздат, 1968. С. 65–74.

Контактные данные:

Леонид Иосифович Дворкин, +38(068)353-33-38; эл. почта: dvorkin.leonid@gmail.com

Вадим Владимирович Житковский, +38(096)564-00-27; эл. почта: zhitk@ukr.net

© Дворкин Л.И., Житковский В.В., 2019



DOI: 10.18720/MCE.90.3

Microstructure and strength of iron-filing Portland cement paste and mortar

M.O. Yusuf

University of Hafr Al Batin, Saudi Arabia

* E-mail: moruff@gmail.com

Keywords: iron-filing, strength, microstructure, Fourier transform, carbonation, workability

Abstract. This study investigated the role played by iron-filing in the strength and microstructural characteristic of high ordinary Portland cement (OPC) based paste and mortar at substitution levels that ranged from 0 to 15 wt.%. It was found that, iron-filing mainly comprised Fe_2O_3 , reduced the workability, influence carbonation, early strength development and impacted the nature of the product formed especially if prepared within the w/c ratio of 0.25 and 0.35–0.4 for paste and mortar, respectively. Moreover, iron-filing also induced and enhanced belite hydration, and influenced the crack-bridging effect within the microstructural matrix, while substitution level less than 5 % affected not the early strength. Besides, iron-filing could also influence the formation of calcium ferrosilicate hydrate as revealed in the microstructural analysis or elemental analysis from energy-dispersive X-ray spectrometer. The 28-day strength of 114 MPa and 61 MPa were achievable in paste and mortar, respectively for iron-filing replacement level within 5–10 %, even substitution up to 15 % could perform better than the sample prepared with OPC only. The study promotes waste valorization and the use of iron-filing in mass-concrete production.

1. Introduction

Iron filings (IF) are mostly byproduct obtained from metal cutting, grinding, filing, or milling of finished iron products especially in workshops and foundry. Their history largely tracks the development of iron, and it is another waste generated by steel production other than blast furnace slag. They are fine powder of small pieces of iron, and often used in science demonstrations to show the direction of a magnetic field [1]. Consumption of IF through contamination by grinding or milling could be dangerous to human health due to the tendency to cause chronic diseases like hemochromatosis, and siderosis [2]. There has been an attempt to re-design food grinding machines to reduce contamination due to IF by [2] in order to emphasize its danger on public health. However, among other benefits of iron-filing is their use in the removal of chloride contamination of groundwater [3] even though this fact still remains controversial among other pro-environmental researchers.

There have been several attempts towards utilizing IF and other ore related materials replacement for fine aggregates (sand) or paste in concrete production such as silicomanganese fume [4], volcanic pumice[5], coal gangue [6] and copper mine tailing [7]. For instance, Adeyanju and Manohar [8] had reported that using enough quantity of IF and steel fibers could enhance thermal and mechanical properties of energy storage plant due to increase in its capacity in comparison with the plain concrete. Alserai et al. [9] also asserted that an increase in IF composition up to 1 % of the mixture could increase the compressive, tensile and flexural strength of geopolymer concrete when used with recycled aggregates. Alzaed [1] also reported that the contribution of iron-filings to concrete strengths could be up to 10 % of the mixture beyond which the insignificant contribution could be observed. Their findings were also correlated with the results obtained by other researchers [10].

Yusuf, M.O. Microstructure and strength of iron-filing Portland cement paste and mortar. Magazine of Civil Engineering. 2019. 90(6). Pp. 28–36. DOI: 10.18720/MCE.90.3

Юсуф М.О. Микроструктурные и прочностные характеристики портландцемента с металлическим наполнением // Инженерно-строительный журнал. 2019. № 6(90). С. 28–36. DOI: 10.18720/MCE.90.3



This open access article is licensed under CC BY 4.0 (<https://creativecommons.org/licenses/by/4.0/>)

Moreover, Kumar et al. [11] replaced sand with iron-ore tailing and there was no significant change in the strength of the resultant beam due to sand replacement. Similarly, Familusi et al. [12] reported that quarry-dust can be used in binary with iron-filing to produce concrete of comparable strength with conventional concrete strength such that the waste combinations were 37.5 and 50 % of the mixture. The increase in strength has been reported to be from pore blockage such that 2 % of iron powder inclusion could reduce the total porosity by 50 % [13]. Olutoge et al. [14] also reported that the optimum sand replacement for IF was 20 % with 13.5 % gain in the recordable compressive strength.

Further, Ghannam et al. [15] reported the optimum performance of iron-filing in terms of compressive and flexural strengths for sand replacement to be 20 % whereas Noori and Ibrahim [16] asserted that 12 % sand replacement by IF gave the optimum in terms of mechanical strengths characteristics. In the contrary, Vasudevan [17] reported decreasing slump value with the addition of 5 % iron-filing in replacement for sand while the maximum compressive strength was only 3.2 % greater than the control. The difference in the percentage reported could be due to difference in the water/c ratio, sizes of the IF and contaminations such as carbon content or other elements used in the alloy. However, just a few authors presented the oxide composition of the IF used in their studies.

Meanwhile, none of these studies captures the microstructural interaction of IF within the binder matrix, likewise, its performance in paste strength, and bond characteristics within the mixture. These points are very important and serve as the aims of this present study with a view to establishing the actual roles being played by IF in OPC paste and mortar production through sand partial replacements, respectively. It is expected that this study will also provide more information towards understanding the IF interaction within the microstructure and to provide an empirical fact towards the promotion of green environments, and its excessive utilization in mass concrete structures such as walk ways and blinding to foundation of reinforced concrete structures among other applications.

2. Materials and Methods

2.1. Materials

2.1.1. Ordinary Portland cement.

The cement used in the study satisfies the requirement of ASTM C 150 [18] and the oxide compositions determined by x-ray fluorescence technique is as shown in Table 1 with particle size distribution as shown in Figure 1.

Table 1. Oxides composition of Ordinary Portland and iron-filing Oxides.

Oxides	OPC, %	Iron filing (IF), %
SiO ₂	19.01	1.38
Al ₂ O ₃	4.68	0.61
Fe ₂ O ₃	3.20	96.5
CaO	66.89	0.02
MgO	0.81	–
Na ₂ O	0.09	–
TiO ₂	0.22	0.03
K ₂ O	1.17	0.13
P ₂ O ₅	0.08	0.05
SO ₃	3.66	0.23
MnO	0.19	0.5
Cl	–	0.05
Cr ₂ O ₃	–	0.11
ZnO	–	0.07
SnO	–	0.08
SrO ₂	–	0.02
CuO	–	0.22
LOI	2.48	–
SiO ₂ + Al ₂ O ₃ + Fe ₂ O ₃	26.89	98.49

2.1.2. Iron-filing powder

It is collected at mechanical lathe machine workshop at Senaiya Hafr Al Batin in the Eastern Province of Saudi Arabia with the fineness modulus of 2.89. The particle size distribution of the material is as shown in Figure 2 while the oxide composition (Table 1) reflects the dominance of iron oxide.

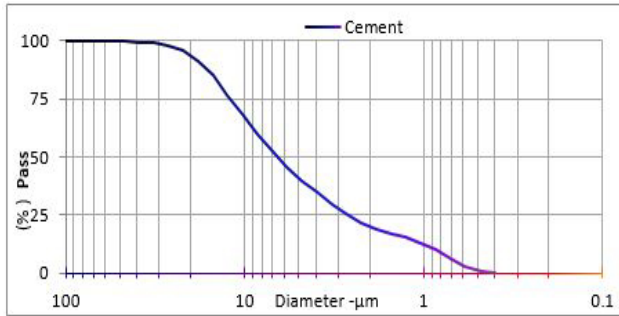


Figure 1. Particle size distribution of the ordinary Portland cement.

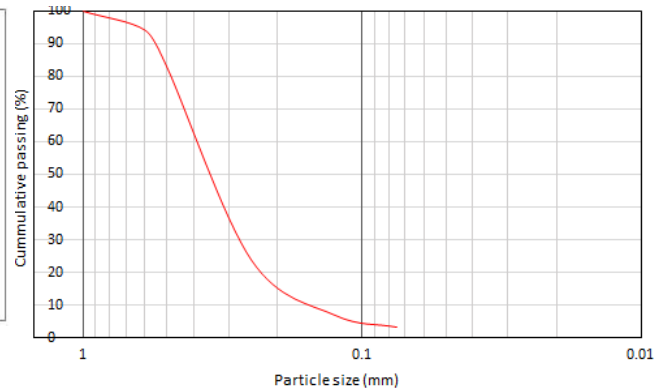


Figure 2. Particle size distribution curve of iron-filing powder.

2.1.3. Fine aggregate

It comprised dune sand with fineness modulus of 1.85, specific gravity in saturated dry condition was 2.62 while its absorption capacity was 0.65 %. The physical properties of OPC, iron-filing (IF) powder and fine aggregates are as shown in Table 2.

Table 2. Physical properties of fine aggregates and iron filing.

Physical Properties	Sand	Iron Filing	cement
Bulk Density	1699	1932	3100
Specific gravity	2.67	6.85	3.41
Fineness modulus	3.3	2.89	–
Average diameter, D_{50} (μm)	–	250	6.69

2.2. Research methodology

The research methodology involved development of experimental design for paste and mortar at w/c ratios of 0.25 and 0.35, respectively. The proportion of IF varied from 0–15 % in both cases while the compressive strengths were determined at 7, 14 and 28 days. The microstructural analysis of the paste was determined to understand the micrograph of the sample matrix while Fourier transform infra-red spectroscopy (FTIR) was used to determine the impact of iron-filing (IF) on the bond characteristics of the binders.

2.2.1. Microstructural and Fourier infrared analysis

The JEOL scanning electron microscopy coupled with energy dispersive spectroscopy (SEM + EDS) model 5800 LV, was used to test the morphology of the 28 days sample paste obtained from compressive strength sample by first coating it in gold film [19, 20]. The pulverized paste was used for the Fourier transform infra-red (FTIR) spectroscopy bond characterization within the sample matrix by using Perking Elmer 880 spectrometer that is based on the attenuated total reflection (ATR) technique.

2.2.2. Mix proportion

Mix design was conducted such that the percentage composition of the IF was used in partial replacement for ordinary Portland cement (OPC) in paste ($w/b = 0.25$) and sand in mortar ($w/b = 0.35$) in varied quantities as 0, 5, 10 and 15 % as shown in Table 3 and 4. The superplasticizers used (Glenum®) was 0.63 wt.% in paste and 1 wt.% in mortar, respectively to achieve the required consistency. The Sand/OPC ratio was maintained at approximately 2.5.

Table 3. Paste constituent materials in kg/m^3 .

Sample ID	OPC (kg/m^3)	Iron filing (kg/m^3)	Water (kg/m^3)	SP (kg/m^3)	Unit weight (kg/m^3)
M _{0.35} F ₀	1872	0	477	12	2361
M _{0.35} F ₅	1819	95	477	12	2403
M _{0.35} F ₁₀	1730	193	477	12	2412
M _{0.35} F ₁₅	1630	289	477	12	2409

Table 4. Mortar Material composition.

Sample ID	OPC (kg/m^3)	Sand (kg/m^3)	Water (kg/m^3)	SP (kg/m^3)	Iron filing (kg/m^3)	Unit weight (kg/m^3)
M _{0.35} F ₀	625	1569	221	6.3	0	2421.0
M_{0.35}F₅	625	1519	221	6.3	80	2450.8
M _{0.35} F ₁₀	625	1449	221	6.3	162	2463.2
M _{0.35} F ₁₅	625	1410	221	6.3	245	2507.2

2.2.3. Mixing of the specimen

OPC was first placed in Hobart planetary mixer after which the iron-filing (IF) powder was added, and then mixed for 3 mins. Water (70 %) together with superplasticizer was added and then further mixed for 2 mins. Sand was then added and the whole mixture was mixed continuously for additional 3 mins before adding the remaining water (30 %) to ensure homogeneous mixture. The paste and mortar were then cast into 50×50×50 mm mould in 3 layers on the table vibrator to vibrate for 15 secs. The samples were demoulded after 12 hrs and then lowered into curing tank at the room temperature of 25 ± 2 °C.

2.2.4. Workability

The workability of the specimen was determined by flow table in accordance with ASTM C 1437 [21]. The slump value was expressed as a percentage:

$$\text{Slump}(\%) = \frac{\text{measured flow} - 100}{100} \times 100.$$

2.2.5. Compressive strength

Compressive strength of the specimen prepared in triplicate were tested using universal testing machine at the loading rate of 2.4 kN/s. The compressive strength test was conducted upon removing the samples from curing tank and drained for 6 hrs. The samples were tested after 7, 14 and 28 days.

3. Results and Discussions

3.1. The physical characteristics of iron filing

Iron-filing (IF) has a bulk density lower than ordinary Portland cement (OPC) and greater than sand particles (Table 2). Its specific gravity is almost twice that of OPC. Therefore, its inclusion increases the density of the resultant paste or mortar as applicable. Therefore, concrete produced with iron-filing based paste or mortar can be used for providing adequate thrust for underground buried pipes. The average size D_{50} is around 250 μm which could be categorized into fine aggregates by virtue of its being less than 4.75 mm (No. 4) in accordance with ASTM C33 [22]. Figure 3 shows the increment of resultant mortar density as the quantity of iron-filing increases. The initial density of OPC mortar for w/c ratio of 0.4 increases by 3.5 %, 7.4 % and 10.34 % for increment level of IF by 0, 5, 10 and 15 %, respectively. These values slightly reduced when the w/c ratio reduced to 0.35. The decrease observed could be due to self-desiccation phenomenon that led to autogenous shrinkage in the sample of lower w/c ratio [23–25].

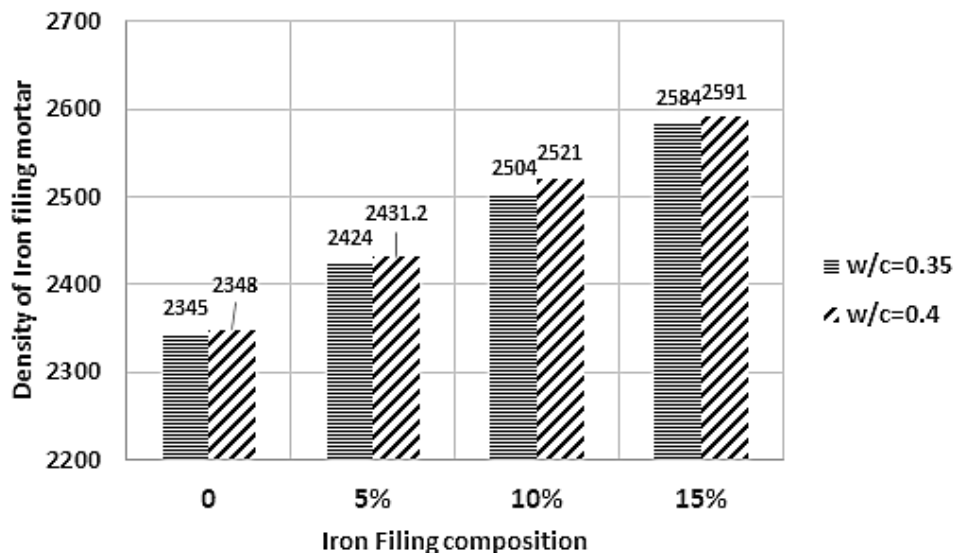


Figure 3. Density of mortars at different iron-filing substitution levels.

3.2. Workability of the samples

From Figure 4, the consistency of the iron-filing (IF) mortar decreases with lower water-cement ratio. There is improvement in the workability as the w/c ratio increases from 0.35 to 0.4 due to decrease in the slope of the curve as shown in Figure 4. This suggests that inclusion of IF could increase the consistency of the mixture especially when the mixture is workable. The workability of the control mortar (OPC only) decreased by 63.6 % upon reducing the w/c ratio from 0.4 to 0.35. This further decreased to 68.6 %, 94.4 % and 97.6 % upon replacing sand with IF in the percentages of 5 %, 10 %, and 15 %. Therefore, with adequate consistency (fluidity) of the mixture, inclusion of IF could be used successfully to improve the workability of the mortar.

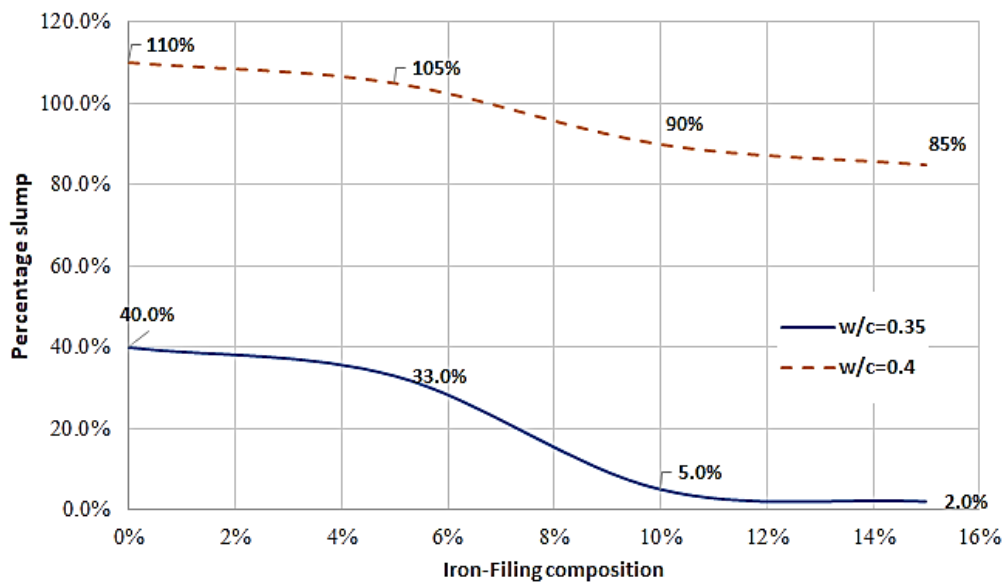


Figure 4. Slump values at different iron-filing substitution level.

3.3. Impacts of iron-filing on the compressive strength of paste and mortar

From Figure 5, addition of 5 % of iron-filing has the highest 7-day compressive strength in comparison with other mixtures. The compressive strengths compared to the control (0 %) at 7, 14 and 28 days for 5 % replacement were 1.7 %, 2.1 % and 2.94 %, respectively. As replacement increases to 10 %, the early (7-day) strength decreases by 14 % due to an increase in the interfacial transition zones (ITZ) between the IF particles and the paste matrix. The rate of strength development at 14 days noticed to be 37.5 % at 10 % replacement became 4.2 and 6.1 % in 5 % and 15 % substitutions, respectively. As the hydration process continues, belite (C_2S) hydration was significantly aided by the presence of IF thereby leading to denser C-S-H in comparison with IF-free sample. The possibility of the reaction shown in Equation (1) indicates that IF at optimum quantity could influence hydration reaction to form calcium ferrosilicate hydrate (CAFSH) or a complex mineral of modified CSH configuration. However, this requires further investigation to determine the extent of possibility and stoichiometry of this reaction.



The maximum 14- and 28-day strengths at 10 % level substitution were 12.2 and 13.8 %, respectively of the control while that of 15 % cement replacement performed less as the percentage reduced to 7.3 %. Contribution of iron-filing to strength development could be due to micro-reinforcement, microstructural stability, pore-filling or crack-bridging effects within the microstructure as shown in SEM (Figure 6). The micrograph shows a localized crack-bridging effect in IF paste in comparison with the interconnected cracks of OPC (control) paste.

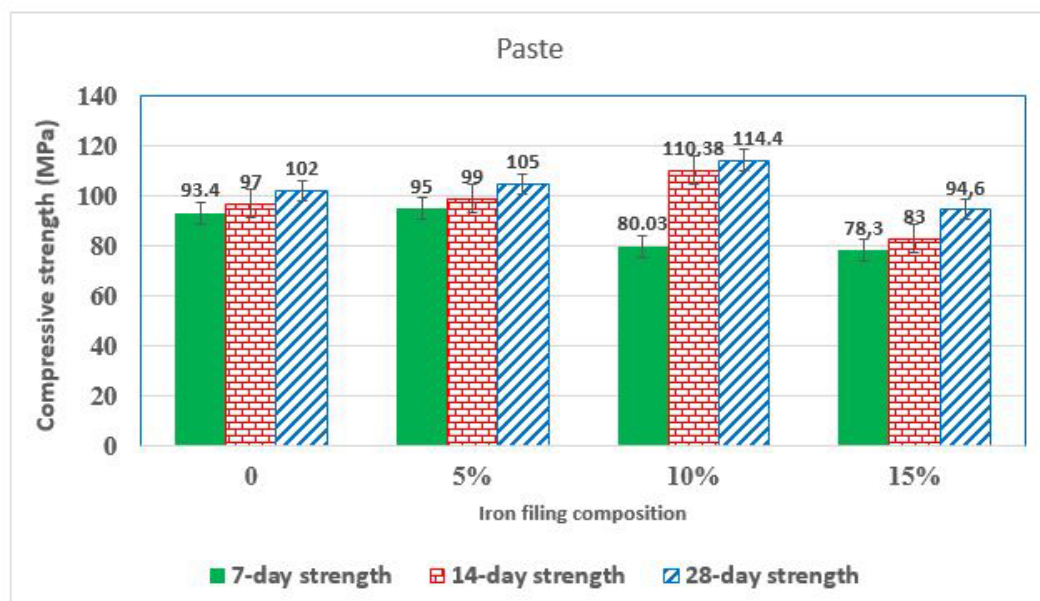


Figure 5. Compressive strength of ironfiling-OPC pastes.

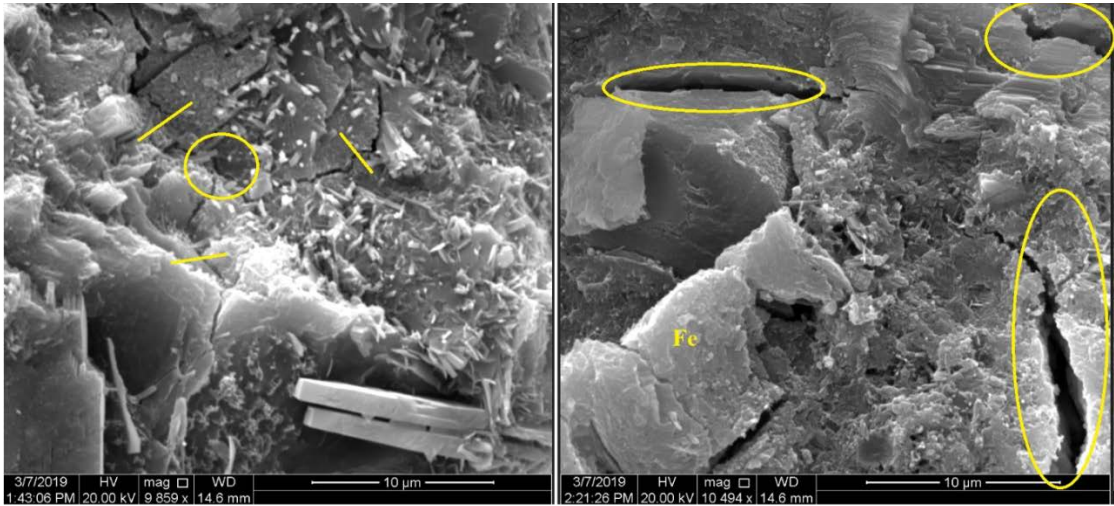


Figure 6. Micrographs of OPC paste (left) and OPC-Iron filing paste (right).

Be that as it may, the introduction of iron-filing (IF) into mortar increases the heterogeneity of the mixture (mortar) compare to the paste sample. There was a formation of two ITZs which exist in-between the paste/iron-filing and sand/paste. Besides, the frictional interaction between IF and sand particle could also improve the compressive strength compared to IF-free sample. More ITZ paste/iron filing in 10 % sand replacement could be responsible for the slowing down the hydration of tricalcium silicate (alite- C_3A) and tricalcium silicate (C_3S). For instance, the lower 14-day strength and the subsequent higher strength gain between 14–28 day in 10 % sand replacement compared to that of 5 % and 15 % substitution as shown in Figure 7. This could indicate that IF at its optimum percentage hinders the rate of strength development at early hydration process. The resultant strength improved due to frictional resistant between sand particle, paste, and IF. Therefore, IF/Paste ratios play a significant role in determining the maximum achievable strength. The maximum strength of 61 MPa can be achieved with OPC replacement of 5–10 % as also observed in the paste samples.

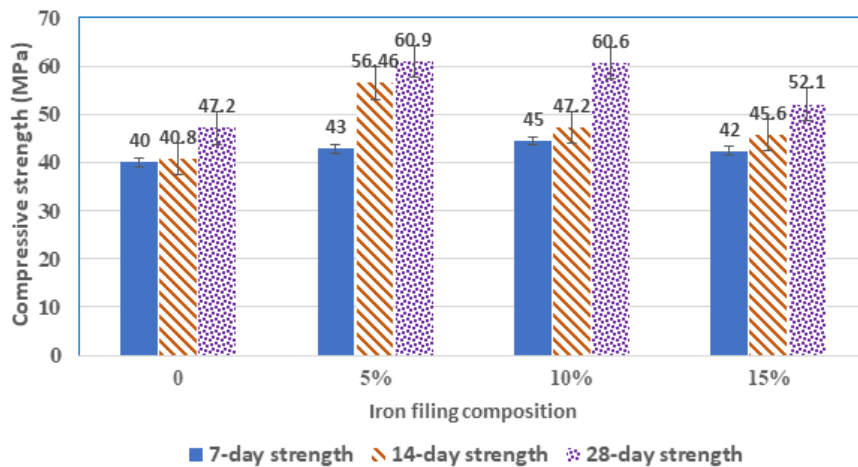


Figure 7. Compressive strength of OPC-iron filling mortar.

In addition, 15 % sand substitution level also performed better than OPC control mortar. There was 28.4 % higher strength gain between 14 and 28 days in mortar sample with 10 % IF ($M_{0.35}F_{10}$) when compared to 7.9 % in the 5 % replacement ($M_{0.35}F_5$).

3.4. Effect of iron-filing on the carbonation of the product

From Figure 8, inclusion of iron-filing has no significant effects on the asymmetric stretching of Si-O-T as the frequencies of vibrations remain 958 cm^{-1} . However, the asymmetric stretching of C-O (CO_3^{2-}) shown by a deeper trough at the wavenumber 1418 cm^{-1} is more apparent in IF sample compared to the OPC only sample [20, 26, 27]. Therefore, there is a possibility for the formation of $\text{Fe}(\text{CO}_3)_2$ that could oxidize to form $\text{Fe}(\text{CO}_3)_3$ due to the following two-stage reactions of the interaction of Fe with portlandite that formed during the primary hydration reaction.



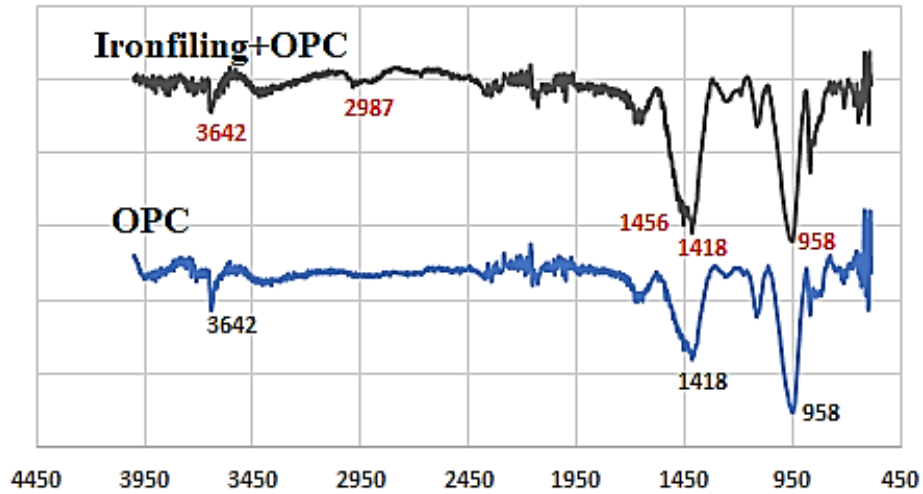


Figure 8. FTIR of the iron filing-OPC and OPC pastes.

Similarly, the vibration of water molecule is observed at 2987 cm^{-1} which indicates the asymmetric stretching or hydrogen bonding within H-O-H molecules [20, 28, 29]. This is possible because of the proliferation of hydroxyl ion in the proximity to one another as shown in the Equations 2 and 3 thereby leading to hydrogen bonding.

Figure 9 shows the presence of CSH (regions 3 and 4) and Fe-based compound (C-F-S-H) or FeCO_3 as shown in the Equations 1 and 4. The IF-free sample predominantly contains Ca, Si and O that depict the dominance of CSH in the two distinctive regions (3 and 4). The sample containing IF is heterogeneous in nature when compared C-(A)-S-H region 1 to C-A/F-S-H region 2 within the micrograph as shown in the EDS result (Figure 9).

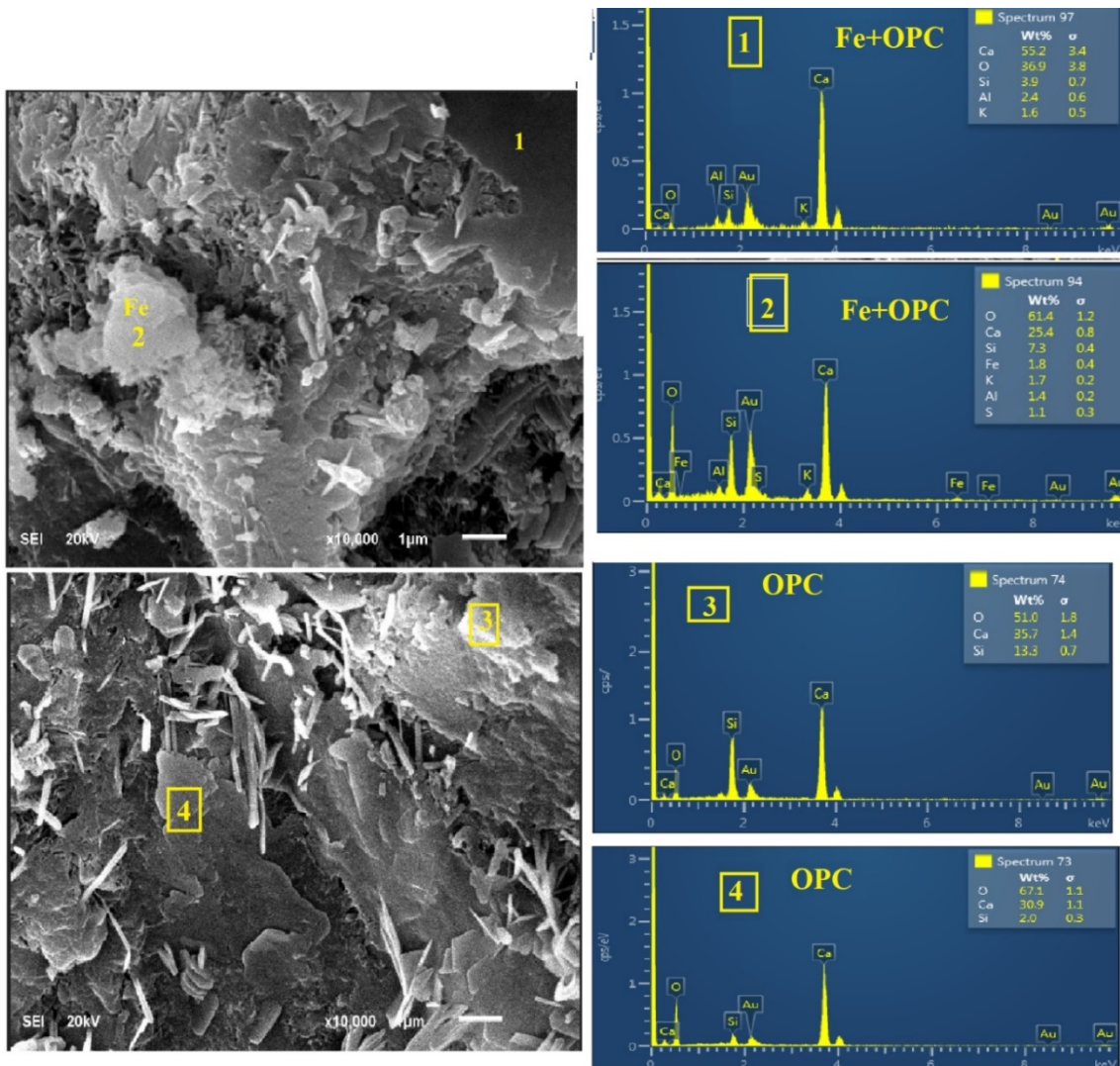


Figure 9. Micrographs of Iron-filing+OPC (top) and OPC paste only (bottom).

4. Conclusions

Iron-filing (IF) powder was used in partial substitution for cement and sand in ordinary Portland cement based paste and mortar with a view to understanding its roles in terms of workability, strength, bonds and microstructural characteristics of the samples. The following are the conclusions:

- At lower water cement ratio up to 0.35, iron-filing decreases the workability of the mixture of mortar. It could however enhance the consistency of the mixture at higher water-cement ratio due to IF low water absorptive tendency.
- Iron-filing substitution level in moderate quantity in mortar could increase the compressive strength of paste and mortar specimens considerably. However, excessive substitution could have a debilitating effect on workability and strength performance.
- Substituting sand with iron-filing at very low quantity has no significant effect on the early hydration of OPC.
- Iron-filing influenced the formation calcium ferrosilicate hydrate intertwined with the calcium silicate hydrate within the microstructures.
- From the C-O bond vibration as noted in FTIR, iron-filing could influence the carbonation of the paste and mortar due to the propensity of the formation of iron carbonate.

5. Acknowledgement

The author appreciates the University of Hafr Al Batin for the supports and facilities provided to carry out the relevant tests required for this study.

References

1. Alzaed, A.N. Effect of Iron Filings in Concrete Compression and Tensile Strength. *International Journal of Recent Development in Engineering and Technology*. 2014. Vol. 3. No. 4, October.
2. Normanyo, E., Asiam, E.K., Amankwa-Poku, K., Adetunde, I.A. Redesign of a grinding mill for the minimisation of Iron filings production. *European Journal of Scientific Research*. 2009. 36(3). Pp. 418–436.
3. Goodlaxson, J.D., Agrawal, A., Muftikian, R., Grittini, C., Fernando, Q., Clausen, J. Modified iron filings remove contaminants from groundwater. Oak Ridge National Laboratory, 1996.
4. Najamuddin, S.K., Megat Johari, M.A., Maslehuddin, M., Yusuf, M.O. Synthesis of low temperature cured alkaline activated silicomanganese fume mortar. *Construction and Building Materials*. 2019. 200. Pp. 387–397.
5. Zeyad, A.M., Bassam, A.T., Yusuf, M.O. Strength and transport characteristics of volcanic pumice powder based high strength concrete. *Construction and Building Materials*. 2019. 216. Pp. 314–324.
6. Yao, Y., Sun, H. A novel silica alumina-based backfill material composed of coal refuse and fly ash. *Journal of Hazardous Materials*. 2012. 213–214. Pp. 71–82.
7. Ahmari, S., Zhang, L., Zhang, J. Effect of activator type/concentration and curing temperature on alkaline activated binder based on copper mine tailings. *Material science*. 2012. 47. Pp. 5933–5945.
8. Adeyanju, A.A., Manohar, K. Effects of Steel Fibers and Iron Filings on Thermal and Mechanical Properties of Concrete for Energy Storage Application. *Journal of Minerals & Materials Characterization & Engineering*. 2011. 10(15). Pp. 1429–1448.
9. Alserai, S.J., Alsaraj, W.K., Abass, Z.W. Effect of Iron Filings on the Mechanical Properties of Different Types of Sustainable Concrete. *The Open Civil Engineering Journal*. 2018. 12. Pp. 441–457.
10. Tayeh, B.A., Al Saffar, D.M. Utilization of Waste Iron Powder as Fine Aggregate in Cement Mortar. *Journal of engineering Research and Technology*. 2018. 5(2).
11. Prema Kumar, W.P., Ananthayya, M.B., Vijay, K. Effect of Replacing Sand by Iron Ore Tailings on the Compressive Strength of Concrete and Flexural Strength of Reinforced Concrete Beams. *International Journal of Engineering Research & Technology (IJERT)*. 2014. 3(7). Pp. 1374–1376.
12. Familusi, A.O., Ogundare, D.A., Adewumi, B.E., Alao, M.O. Use of quarry dust and iron filings in concrete production. 5th National Conference on Engineering Technology Held at Federal Polytechnic Offa, February 2018., 2018.
13. Kim, J., Heo, Y., Noguchi, T. Effect of Iron Powder on Inhibition of Carbonation Process in Cementitious Materials. *ISIJ International*. 2015. 55(7). Pp. 1522–1530.
14. Olutoge, F.A., Onugba, M.A., Oholi, A. Strength Properties of Concrete Produced With Iron Filings as Sand Replacement. *British Journal of Applied Science & Technology*. 2016. 18(3).
15. Ghannam, S.N., Vasconez, H.R. Experimental study of concrete made with granite and iron powder as partial replacement of sand. *Sustainable Materials and Technology*. 2016. 9. Pp. 1–9.
16. Noori, K.M.G., Ibrahim, H.I. Mechanical Properties of Concrete Using Iron Waste as a Partial Replacement of Sand. 4th International Engineering Conference on Developments in Civil & Computer Engineering. 2018.
17. Vasudevan, G. Performance on Used Iron Sand as Concrete Admixture, 3rd International Conference on Civil, Biological and Environmental Engineering (CBEE-2016) Feb. 4–5, 2016 Bali (Indonesia), 2016.
18. ASTM C150 / C150M-16e1, Standard Specification for Portland Cement [Online]. ASTM International, West Conshohocken, PA, 2016. URL: www.astm.org
19. Yusuf, M.O., Megat Johari, M.A., Ahmad, Z.A., Maslehuddin, M. Effects of the addition of Al(OH)₃ on the strength of alkaline activated ground blast furnace slag-ultrafine palm oil fuel ash (AAGU) based binder. *Construction and Building Materials*. 2014. 50(0). Pp. 361–367.
20. Yusuf, M.O., Megat Johari, M.A., Ahmad, Z.A., Maslehuddin, M. Effects of H₂O/Na₂O molar ratio on the Strength of Alkaline Activated Ground Blast Furnace Slag-Ultrafine Palm Oil Fuel Ash Based Concrete. *Materials & Design*. 2014. 56(0). Pp. 158–164.

21. ASTM C-1437, Standard Test Method for Flow of Hydraulic Cement Mortar, American Society for Testing and Materials [Online]. ASTM International, West Conshohocken, PA, 2013. URL: www.astm.org
22. ASTM C-33, Standard specification for concrete aggregate, American Society for Testing and Materials [Online]. ASTM International, West Conshohocken, PA, 2001. URL: www.astm.org
23. Atis, C.D., Bilim, C., Celik, O., Karahan, O. Influence of Activator on the Strength and Drying Shrinkage of Alkali-Activated Slag Mortar. *Construction and Building Materials*. 2009. 23. Pp. 548–555.
24. Collins, F., Sanjayan, J.G. Effect of pore size distribution on drying shrinkage of alkali-activated slag concrete. *Cement and Concrete Research*. 2000. 30. Pp. 1401–1406.
25. Yusuf, M.O., Megat Johari, M.A., Ahmad, Z.A., Maslehuddin, M. Shrinkage and strength of alkaline activated ground steel slag/ultrafine palm oil fuel ash pastes and mortars. *Materials & Design*. 2014. 63. Pp. 710–718.
26. García Lodeiro, I., Macphee, D.E., Palomo, A., Fernández-Jiménez, A. Effect of alkalis on fresh C–S–H gels. FTIR analysis. *Cement and Concrete Research*. 2009. 39(3). Pp. 147–153.
27. Lecomte, I., Henrist, C., Liégeois, M., Maseri, F., Rulmont, A., Cloots, R. (Micro)-structural comparison between geopolymers, alkali-activated slag cement and Portland cement. *Journal of the European Ceramic Society*. 2006. 26(16). Pp. 3789–3797.
28. Swapna, K., Mahamuda, S.K., Rao, A.S., Shakya, S., Sasikala, T., Haranath, D., Prakash, G.V., Optical studies of Sm³⁺ ions doped Zinc Alumino Bismuth Borate glasses. *Spectrochimica Acta Part A: Molecular and Biomolecular Spectroscopy*. 2014. 125. Pp. 53–60.
29. Coates, J. Interpretation of Infrared Spectra. A Practical Approach, *Encyclopedia of Analytical Chemistry*, 2006.

Contacts:

Moruf Yusuf, +966598373550; moruff@gmail.com

© Yusuf, M.O., 2019



DOI: 10.18720/MCE.90.4

Light heat-resistant polymer concretes based on oligooxyhydridesilmethylsiloxysilane and hollow spherical fillers

E.E. Mastalygina^{a*}, V.A. Ovchinnikov^a, V.Yu. Chukhlanov^b

^a Plekhanov Russian University of Economics, 36, Stremyanny pereulok, Moscow, 117997, Russia

^b Vladimir State University named after Alexander and Nikolay Stoletovs, Vladimir, Russia

* E-mail: elena.mastalygina@gmail.com

Keywords: polymer concrete, reinforced concrete, silicon-organic binder, hollow spherical filler, glass microspheres, ceramic microspheres

Abstract. Novel type of light heat-resistant polymer concretes was developed on the basis of oligooxyhydridesilmethylsiloxysilane with hollow glass or ceramic microspheres. Adding hollow glass and ceramic microspheres being waste products from thermal power plants operating on solid fuels allowed developing reasonably priced materials and reducing potential environmental pollution. For optimization of production technology, the curing and molding conditions of materials were studied. According to impact strength changes, the optimal curing mode for the composites was at 480–515 K for 4.25–4.5 hours depending on the filler type and binder content. It was stated that used organic-silicon binder provided thermal resistance and high strength characteristics of the composite material. In comparison with traditional silicone resins, the compressive strength value of the developed materials increased by almost two times and the modulus of elasticity increased by almost an order of magnitude. Due to the interaction of aluminum hydroxide groups of ceramic microspheres with organosilicon polymer, Young's modulus of the materials filled by ceramic microspheres was higher by 20–30 % than that of the concretes with glass microspheres. Consequently, enhanced physical and mechanical properties expand possibilities of using these materials under exposure of significant external static loads.

1. Introduction

Many recent studies have focused on physical, mechanical and thermal properties of different types of concrete [1–4]. Fiber reinforcement is commonly used in order to increase strength and tensile-deformation properties of concretes [5]. Introduction of hydrosilicates additives [6] allows to increase the water and frost resistance of materials. Lightweight concretes containing fillers or pores are characterized by improved heat-insulating properties [7, 8].

The filling of mineral binders with hollow microspheres with particle ranging in size from units to several hundred micrometers has been known for a relatively long time. Despite low density and acceptable thermal conductivity, they are characterized by low impact strength. In addition, a major drawback of such materials is their low chemical resistance to aggressive natural and technogenic factors, such as acid rain and carbon dioxide, which limits their use in construction. The polymeric binders can be a promising alternative to the mineral binders.

Light polymer concretes (LPC) comprised of hollow microspheres fastened by mineral or organic bindings are promising materials for thermal insulation with enhanced physical-mechanical properties, in particular, increased impact strength. Most polymeric materials are resistant to acid and alkaline reagents,

Mastalygina, E.E., Ovchinnikov, V.A., Chukhlanov, V.Yu. Light heat-resistant polymer concretes based on oligooxyhydridesilmethylsiloxysilane and hollow spherical fillers. Magazine of Civil Engineering. 2019. 90(6). Pp. 37–46. DOI: 10.18720/MCE.90.4

Масталыгина Е.Е., Овчинников В.А., Чухланов В.Ю. Легкие жаростойкие полимербетоны на основе олигооксигидридсилметиленилсилоксисилана и полых сферических наполнителей // Инженерно-строительный журнал. 2019. № 6(90). С. 37–46. DOI: 10.18720/MCE.90.4



characterized by high adhesive characteristics to the filler particles surface. However, they have several disadvantages, such as low thermal stability and susceptibility to degradation by ultraviolet radiation. In this regard, much attention is drawn to the polymer concretes based on siloxane binders.

The composites based on the hollow inorganic microspheres and silicone polymeric binders with a siloxane main chain were described in the previous works [9–12]. The weaknesses of these thermal insulation materials are their relatively low tensile strength and low thermal stability. The long-term operation temperature of composites with the most common polymethylphenylsiloxane binder does not exceed 250°C, after which a catastrophic loss of tensile strength is observed [13–15]. Fundamentally, new silicon-organic binders containing siloxane and carbosilane units in the main chain are used to increase tensile strength and thermal stability of ceramic microspheres (CM) [16–18]. Under heating, such polymer changes into the ladder structure characterized by the increased tensile strength and thermal stability up to 400°C. Considering that the initial polymer contains a heat-resistant filler, as a result of heat treatment a composite material with high strength characteristics is formed.

This work was devoted to the novel light polymer concretes based on a novel class of silicon-organic polymer oligooxyhydridesilmethylenesiloxysilan (OHSMS) with hollow glass and ceramic microspheres. Based on the fact that ceramic microspheres are the products of smoke emissions of solid-fuel power plants, using waste products as the fillers for the composites under investigation allowed to develop a reasonably priced material and to reduce potential environmental pollution. The materials of this type can be used in the construction of facilities operating at elevated temperatures under aggressive environment and exposure of ionizing radiation, for example, in the construction of conventional and nuclear power plants, chemical production facilities.

The main goal of this research was to study the mechanism of interaction of the binder and the polymer, as well as to examine the physical-mechanical properties and behavior of the developed materials under deformation. The results of this research can be used for developing a new group of polymer concretes with high strength characteristics and resistance to shock loads, thermal effects, chemicals and all types of radiation.

2. Materials and Methods

Hollow glass microspheres (HGM) and hollow ceramic microspheres (HCM), referred to cenospheres, obtained by the flotation processing of fume emissions from the thermal power plants operating on solid fuels, specifically on the Kuzbass coal, were used as fillers. The cenospheres had the following composition: 57 % SiO₂, 28 % Al₂O₃, the rest oxides CaO, MgO, Na₂O, Fe₂O₃. In comparison with HGM filler, the fractional composition of HCM is characterized by the larger fractions. Taking into account the low content of HCM float fraction and the necessity of the further utilization of the separated small fractions, the additional fraction separation of HCM is not economically and environmentally justifiable. For this research, HCM were used as a filler without additional fractionation.

Varnish VKL-1 TU 6-05-64-101–85 was used as a binding agent. The main component of this agent is oligooxyhydridesilmethylenesiloxysilan (OHSMS), which contains carbosilane and silane bonds in addition to siloxane bonds. OHSMS was obtained by the esterification reaction of the high-boiling fraction of the direct synthesis of methylchlorosilanes and was used as a solution in the organic solvents [19].

The technology of sample preparation included several stages. At the first stage, in order to achieve the consistency of “wet sand” mixing the binding agent with HGM or HCM was conducted with a rotation speed of 45 rpm by an open low-speed laboratory mixer with a capacity of 0.1 m³ and a frame mixer. In the cases of mixing at elevated temperatures, the mixer with the composite content was placed in an oil bath. Temperature control and adjustments were carried out by the PEX controller REX100. Mixing modes temperature and time are given in Table 1. Then, the composite samples were molded under pressure from 0.05 to 0.5 MPa in the metal molds with an internal sizes of 30×30×30 mm for compression tests and 80×10×4 for impact tests, followed by heat treatment according to the modes indicated by the Box–Behnken design.

The complex of physical and mechanical properties of the obtained composite samples were investigated according to the standard methods. Analysis of compression strength and modulus of elasticity was carried out by a specialized machine Instron Model 4206 (Germany) in accordance with standard ISO 604:2002 at room temperature on cubic samples with a loading speed of 1 mm/min. Izod impact strength of the materials was determined by a pendulum machine GOTECH GT-7045-MDL (Taiwan) in accordance with standard ISO 1268-4:2005.

3. Results and Discussion

The properties of polymer concretes are determined by a set of factors, including chemical composition and structure of polymer matrix (binding agent) [20]. Oligooxyhydridesilmethylenesiloxysilan (OHSMS) used as a binding agent has the following chemical formula:

$$\begin{aligned} & \left[(\text{OH})_{n_1} (\text{CH}_3)_{3-n_1} \text{SiO}_2 \right]_n \times \left[(\text{CH}_3)_{m_1} \text{H}_{2-m_1} \text{SiO}_{m_2} \right]_m \times \left[(\text{CH}_3)_{k_1} \text{H}_{2-k_1} \text{SiCH}_2 \right]_k \times \\ & \times \left[(\text{CH}_3)_{l_1} \text{H}_{2-l_1} \text{SiSiH}_{2l_2} (\text{CH}_3)_{l_2} \right]_l \times \left[\text{O}_{p_2} \text{Si} (\text{CH}_3)_{p_1} \right]_p \times \left[\text{O}_{q_2} \text{Si} (\text{CH}_3)_{3-q_1} (\text{OH})_{q_1} \right]_q \end{aligned} \quad (1)$$

where $n, m, k, l, p, q = 1 \div 4$; $m_1, k_1, l_1, l_2, p_1 = 1 \div 2$; $m_2, p_2 = 1 \div 1.5$; $n_2, q_2 = 1$; $n_1, q_1 = 0 \div 1$.

To determine the optimal technological conditions of obtaining materials, the processes of curing and molding were studied comprehensively. Curing of OHSMS apparently occurs due to the presence of both reactive hydroxyl groups and hydride radicals. Considering the chemical structure of OHSMS, it can be assumed that intensive processes of oligomer curing take place only under the conditions of increased temperatures. The kinetics of the OHSMS curing was defined by the degree of the oligomer curing.

The degree of OHSMS crosslinking (Figure 1) was determined by a residual amount of the fraction dissolved in organic solvent by means of a Soxhlet apparatus. It was stated that nearly 100 % of the oligomer crosslinking was occurred at a temperature of 513 K and a curing time of 6 hours.

After primary investigation, the selection of optimal processing modes of curing was performed. The scheme of obtaining LPC based on OHSMS as a binder was as follows: mixing of OHSMS and microspheres to the consistency of "wet sand", molding of products under pressure, at which the required packing density of microspheres of approximately 60 % is achieved, and subsequent heat treatment. The developed processing method allows to obtain LPC with a volume fraction of the binder not more than 25 vol.%. This is associated with a sharp decrease in the number of open pores in the material and the subsequent hindered penetration of organic solvent.

Table 1 gives the modes of obtaining products from LPC by molding materials under low pressure. The relatively long time and increased temperature during the process of components mixing were determined by a poor solubility of OHSMS in organic solvents (12.5 %) and by the necessity for their subsequent removal to achieve "wet sand" consistency.

Table 1. Modes of obtaining LPC filled by HGM and HCM (curing temperature 423 K, time 2 hours).

Filler type	Composition (wt.%)		Volume fraction of binding agent (%)	Blending mode		Exposure to air (hours)	Packed density (kg/m ³)
	Filler	Binding agent (solid residue)		Time (min)	Temperature (K)		
HGM	65	35	5	10	289	1	257
HGM	60	40	10	20	333	3	294
HGM	55	45	15	40	353	6	372
HGM	50	50	20	60	353	24	401
HGM	45	55	25	90	353	48	462
HCM	75	25	5	10	289	1	361
HCM	70	30	10	20	333	3	416
HCM	65	35	15	40	353	6	474
HCM	60	40	20	60	353	24	514
HCM	55	45	25	90	353	48	578

As the composition reached the consistency of «wet sand», it was placed in a mold and was subjected to layer-by-layer molding under low pressure until the maximum packed density of microspheres was reached (0.6 for HGM and 0.66 for HCM). The maximum packed density was controlled by the values of constant packed density of the material regardless of the molding pressure (Figure 2).

The results of this study showed that a minimal pressure for achieving the required fullness volume coefficient was 0.4 MPa for the composites with HCM and 0.25 MPa for the composites with HGM. Further increase in pressure could cause destruction of the hollow shells of microspheres.

After molding and before heat treating composite materials were kept in an open mold block in accordance with the modes given in Table 1. This operation allowed to foam concrete during heat treatment due to an excessive unextracted solvent. The preliminary curing temperature of 423 K was not optimal, since it was obviously insufficient for the complete crosslinking of OHSMS.

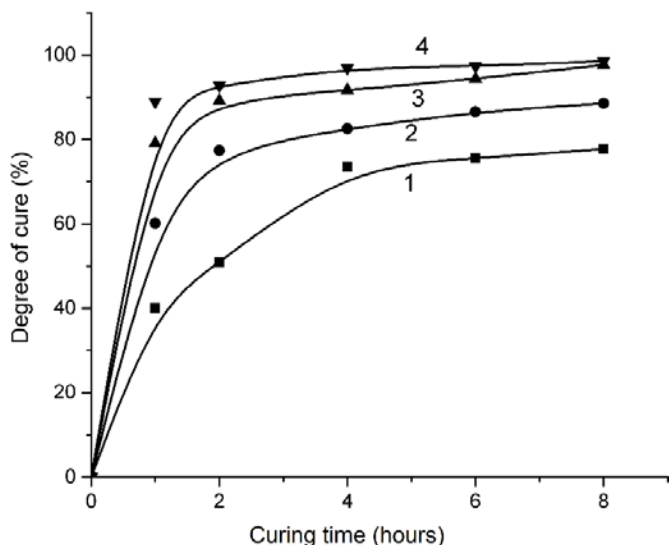


Figure 1. Dependence of the bonding agent (OHSMS) curing degree on the curing time and temperature: 1 – 433 K, 2 – 473 K, 3 – 513 K, 4 – 553 K.

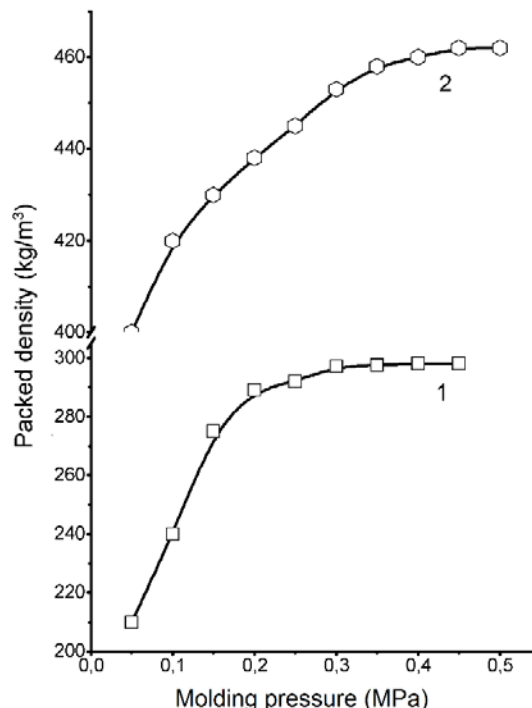


Figure 2. Dependence of the packed density of LPC on molding pressure: 1 – glass microspheres filler (HGM); 2 – ceramic microspheres filler (HCM).

Determination of the optimal temperature conditions of heat treatment is a considerable task, since many factors have an effect on the final performance properties of LPC. However, the dominant factors are temperature, curing time and binding agent content [21]. Therefore, in this study the full three-factor experiment planning was conducted in order to select the optimal modes (Table 2).

The impact resistance was used as a response function, since with increasing temperature and time LPC can completely lose plastic properties and resistance to impact, which is extremely undesirable for protective materials. The impact strength value depends on the degree of macromolecules crosslinking and it can decrease at a certain stage, when a certain crosslinking frequency is exceeded [22]. The purpose of Box–Behnken design was to find the corresponding optimal technological parameters, in particular temperature and time. Figures 3 and 4 show lines of equal levels of impact strength values depending on time and temperature of heat treatment for LPC filled by HGM and HCM with a binder content of 10 vol.% and 20 vol.%, correspondingly.

Table 2. Box–Behnken Design.

No.	Trial No.	Input data of experiment					
		Coded variable levels			Natural variable levels		
		X_1	X_2	X_3	X_1 (Time, hours)	X_2 (Temperature, K)	X_3 (Binding agent, %)
1	6	+	+	0	8	553	15
2	2	+	-	0	8	473	15
3	5	-	+	0	2	553	15
4	1	-	-	0	2	473	15
5	10	+	0	+	8	513	20
6	12	+	0	-	8	513	10
7	11	-	0	+	2	513	20
8	9	-	0	-	2	513	10
9	8	0	+	+	5	553	20
10	7	0	+	-	5	553	10
11	4	0	-	+	5	473	20
12	3	0	-	-	5	473	10
13	13	0	0	0	5	513	15
14	14	0	0	0	5	513	15
15	15	0	0	0	5	513	15
16	16	0	0	0	5	513	15
17	17	0	0	0	5	513	15

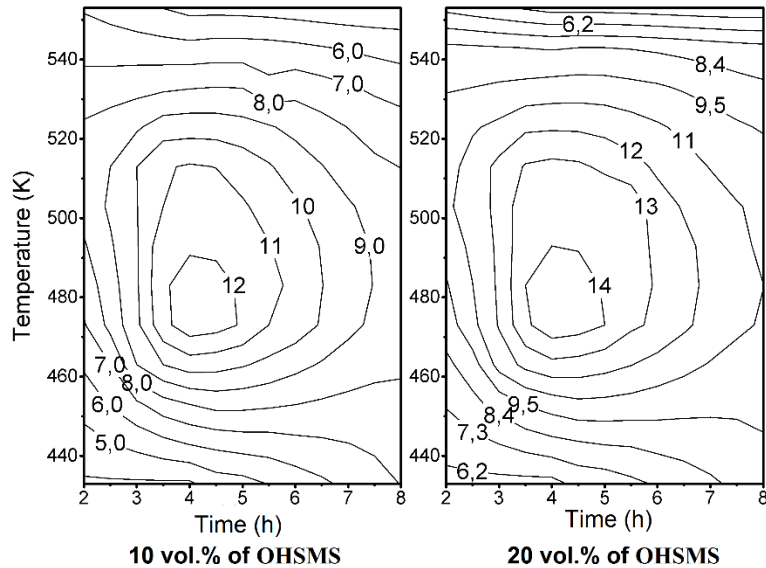


Figure 3. Lines of impact resistance equal levels f or LPC with HGM (10 vol.% and 20 vol.% of OHSMS).

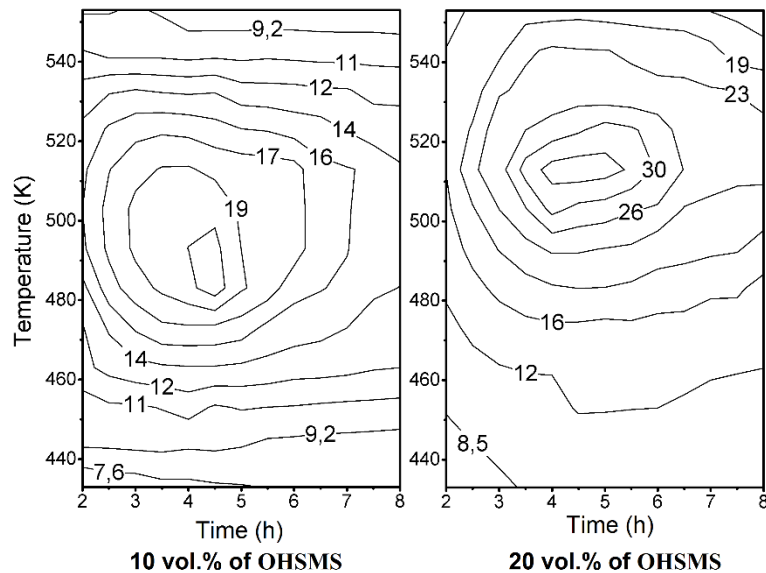


Figure 4. Lines of impact resistance equal levels for LPC with HCM (10 vol.% and 20 vol.% of OHSMS).

According to the obtained experimental data, as the binding content increased, the impact strength value shifted towards higher temperatures. As expected, an optimum impact value zone was found in all the cases. When HGM was used as a filler, the optimum impact strength was achieved at OHSMS content of 10 vol.% at a temperature of 480 K and curing time of 4.25 hours.

With an increase in the binder content up to 20 vol.%, no significant changes in the optimum character were observed. For this composition, the impact strength of the building material increased by no more than 20 %, owing to the low reactivity of HGM surface with OHSMS at the given temperatures.

When HCM was used as a filler, another behavior was observed. For composites filled by HCM, the optimal curing mode was 515 K at the curing time of 4.5 hours (20 vol.% of OHSMS). The impact strength increased significantly to about 36 kJ/m at OHSMS content of 20 vol.%, which is a very significant value for building materials with the similar density.

Automated implementation of the Box-Behnken Design allowed to obtain the following regressions that describe the dependence of impact strength value on curing time, temperature and binding agent content.

For LPC filled by HGM:

$$\sigma_{sp} = 20.87 + 0.674X_1 + 2.123X_2 + 1.585X_3 - 3.299X_1^2 - 7.844X_2^2 - 2.434X_3^2 - 0.995X_1X_2 + 1.282X_1X_3 + 1.942X_2X_3. \quad (2)$$

For LPC filled by HCM:

$$\sigma_{sp} = 21.44 + 0.701X_1 + 2.122X_2 + 1.559X_3 - 3.561X_1^2 - 7.158X_2^2 - 2.694X_3^2 - 0.994X_1X_2 + 1.23X_1X_3 + 1.942X_2X_3, \quad (3)$$

where X_1 is curing time; X_2 is curing temperature; X_3 is binding agent content in LPC.

The results presented above indicate that there is an active interaction of the filler with the binding agent due to the presence of active functional groups on the HCM surface. By virtue of the chemical composition, there are aluminum hydroxide groups with an increased reactivity on the surface of HCM. The interaction of aluminum hydroxide groups of HCM with functional groups of the organosilicon polymer located along the main chain apparently occurs.

OHSMS used as a binder differs from commonly used organosilicon materials in not only chemical nature (silane and carbosilane bonds in the main polymer chain appear in addition to siloxane bond), but also in a high frequency of OHSMS macromolecules cross-linking limiting their mobility after curing [23]. Thus, the developed composite materials based on OHSMS have lower plastic properties than commonly used LPC. However, the analysis of physical and mechanical properties under compression showed compression strength and modulus of elasticity increased in comparison to these values of commonly used LPC (Figure 5).

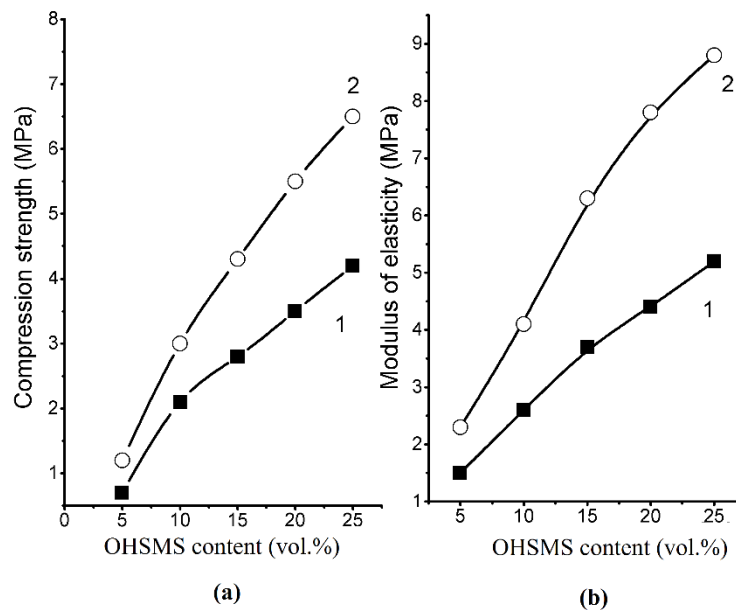


Figure 5. Dependence of mechanical strength characteristics of LPC filled by HGM (curve 1) and HCM (curve 2) on bonding agent content (OHSMS): (a) compression strength, (b) modulus of elasticity.

Apart from the nature and the content of a binder, the chemical composition and the size distribution of fillers have a significant impact on the physical and mechanical properties of LPC. In this study the use of HCM filler led to a significant increase in compressive strength as compared to LPC with HGM filler. The modulus of elasticity of LPC with HCM as a filler is 20–30 % higher than that of LPC with HGM. This could be explained by a difference in the fractional composition and the chemical interaction between the binder and the filler surface. Apparently, chemical reaction occurred between the surface functional groups of HCM and the reactive groups of OHSMS [24]. Moreover, in comparison with traditional silicone resins (polyphenyl and polymethylphenyl siloxane), the compressive strength value increased by almost two times and the modulus of elasticity increased by almost an order of magnitude. The properties of the developed concrete expand possibilities of using the material under exposure of significant external static loads.

4. Conclusions

Novel type of light heat-resistant polymer concrete was developed on the basis of oligooxyhydridesilmethylenesiloxysilan with hollow glass and ceramic microspheres. Organic-silicon binder provided thermal resistance and high strength characteristics of the composite material. Adding hollow glass and ceramic microspheres being waste products from the thermal power plants operating on solid fuels allowed to develop reasonably priced materials and to reduce potential environmental pollution.

The minimum molding pressure of light polymer concrete depends on the type of microspheres: 0.4 MPa for compositions with hollow ceramic microspheres and 0.25 MPa for compositions with hollow glass microspheres. The difference is explained by a more significant deviation of the shape of ceramic microspheres

from a spherical one, which makes it difficult to achieve maximum packing density of the filler. A further increase in pressure is impractical due to the possibility of destruction of the microspheres shells.

For lightweight polymer concrete with oligooxyhydridesilmethylenesiloxysilan content of 10 vol.% and filled with hollow glass microspheres, the optimum curing mode monitored by the toughness function was achieved at a temperature of 480 K and a cure time of 4.25 hours. When using ceramic microspheres with an organosilicon polymer, the optimum temperature and the cure time were increased by about 5 %. This is apparently due to the difference in the concentration of silanol groups on the surface of glass and ceramic microspheres and the difference in heat-conducting characteristics. At the same time, with an increase in the binder content to 20 vol.%, no significant changes in the behavior of the composites were observed.

The compressive strength and elastic modulus of the developed composites significantly exceeds the strength of the materials with traditional organosilicon binders, in particular polymethylphenylsiloxane. This is due to a number of factors, such as the spatial ladder structure of the polymer, the presence of a significant number of reactive groups in the binder, and their interaction with hydroxyl groups on the surface of the filler with the formation of physical and chemical bonds.

The use of hollow ceramic microspheres as a filler led to a significant increase in compressive strength compared to materials with hollow glass microspheres. The elastic modulus of lightweight polymer concrete with ceramic microspheres was 20–30 % higher than that of materials with glass microspheres, which is due to both higher strength characteristics of the filler shells and the difference in the interaction between the binder and the filler surface.

To sum up the obtained results, it could be concluded that using oligooxyhydridesilmethylenesiloxysilan as a binding agent provides the possibility to obtain construction materials, which can be used in various industries, particularly in ferrous and nonferrous-metals industries, conventional and nuclear power industries. Increased physical- mechanical properties, high thermal resistance and resistant to aggressive technogenic and natural factors expand possibilities of using these materials under exposure of significant external static loads.

References

1. Fediuk, R.S., Lesovik, V.S., Liseitsev, Yu.L., Timokhin, R.A., Bituyev, A.V., Zaiakhanov, M.Ye., Mochalov, A.V. Composite binders for concretes with improved shock resistance. *Magazine of Civil Engineering*. 2019. 85(1). Pp. 28–38. DOI: 10.18720/MCE.85.3.
2. Hezhev, T.A., Zhurtov, A.V., Tspinov, A.S., Klyuev, S.V. Fire resistant fibre reinforced vermiculite concrete with volcanic application. *Magazine of Civil Engineering*. 2018. 80(4). Pp. 181–194. DOI: 10.18720/MCE.80.16.
3. Barabanshchikov, Yu.G., Belyaeva, S.V., Arkhipov, I.E., Antonova, M.V., Shkol'nikova, A.A., Lebedeva, K.S. Influence of superplasticizers on the concrete mix properties. *Magazine of Civil Engineering*. 2017. 74(6). Pp. 140–146. DOI:10.18720/MCE.74.11.
4. Nizina, T.A., Balykov, A.S., Volodin, V.V., Korovkin, D.I. Fiber fine-grained concretes with polyfunctional modifying additives. *Magazine of Civil Engineering*. 2017. 72(4). Pp. 73–83. DOI: 10.18720/MCE.72.9.
5. Klyuev, S.V., Klyuev, A.V., Vatin, N.I. Fiber concrete for the construction industry. *Magazine of Civil Engineering*. 2018. 84(8). Pp. 41–47. DOI: 10.18720/MCE.84.4.
6. Loganina, V.I., Pyshkina, I.S., Martyashin, G.V. Effect of the supplement based on calcium hydrosilicates on the resistance of lime coatings. *Magazine of Civil Engineering*. 2017. 72(4). Pp. 20–27. DOI: 10.18720/MCE.72.3.
7. Steshenko, A.B., Kudyakov, A.I. Cement based foam concrete with aluminosilicate microspheres for monolithic construction. *Magazine of Civil Engineering*. 2018. 84(8). Pp. 86–96. DOI: 10.18720/MCE.84.9.
8. Kudyakov, A.I., Kopanitsa, N.O., Sarkisov, J.S., Kasatkina, A.V., Prischepa, I.A. Foam concrete of increased strength with the thermomodified peat additives. *IOP Conference Series: Materials Science and Engineering*. 2015. 71(1). Pp. 012012. DOI: 10.1088/1757-899X/71/1/012012.
9. Li, G., Wang, L., Ni, H., Pittman Jr., C.U. Polyhedral oligomeric silsesquioxane (POSS): a review. *Journal of Inorganic and Organometallic Polymers*. 2001. 11(3). Pp. 123–154. DOI: 10.1023/A:1015287910502.
10. Wu, Y.C., Kuo, S.W. Synthesis and characterization of polyhedral oligomeric silsesquioxane (POSS) with multifunctional benzoxazine groups through click chemistry. *Polymer*. 2010. 51(17). Pp. 3948–3955. DOI: 10.1016/j.polymer.2010.06.033.
11. Fina, A., Abbenhuis, H.C.L., Tabuani, D., Camino, G. Metal functionalized POSS as fire retardants in polypropylene. *Polymer Degradation and Stability*. 2006. 91(10). Pp. 2275–2281. DOI: 10.1016/j.polymdegradstab.2006.04.014.
12. Baldi, F., Bignotti, F., Fina, A., Tabuani, D., Riccò, T. Mechanical characterization of polyhedral oligomeric silsesquioxane/polypropylene blends. *Journal of Applied Polymer Science*. 2007. 105(2). Pp. 935–943. DOI: 10.1002/app.26142.
13. Chukhlanov, V.Yu., Selivanov, O.G. Electrical properties of syntactic foams based on hollow carbon microspheres and polydimethylsiloxane. *Russian Physics Journal*. 2016. 59(7). Pp. 944–948. DOI: 10.1007/s11182-016-0858-9.
14. Carniato, F., Fina, A., Tabuani, D., Boccaleri, E. Polypropylene containing Ti- and Al-polyhedral oligomeric silsesquioxanes: crystallization process and thermal properties. *Nanotechnology*. 2008. Vol. 19. No. 47. Pp. 475701. DOI: 10.1088/0957-4484/19/47/475701.
15. Fina, A., Tabuani, D., Peijs, T., Camino, G. POSS grafting on PPgMA by one-step reactive blending. 2009. *Polymer*. 50(1). Pp. 218–226. DOI: 10.1016/j.polymer.2008.11.002.
16. Yarullin, A.F., Kuznetsova, L.E., Yarullina, A.F., Stoyanov, O.V. Electrophysical properties of oligomer-polymer complexes based on heat-resistant oligoaryleneamines. *Polymer Science Series D*. 2013. 6(2). Pp. 109–115. DOI: 10.1134/S1995421213020172.
17. Smirnova, N.N. Pervaporation properties of film and composite membranes based on an interpolyelectrolyte complex of sulfonate-containing aromatic copolyamide. *Russian Journal of Applied Chemistry*. 2018. 91(3). Pp. 404–411. DOI: 10.1134/S1070427218030102.

18. Bardella, L., Genna, F. On the elastic behavior of syntactic foams. *International Journal of Solids and Structures*. 2001. 38(40–41). Pp. 7235–7260. DOI: 10.1016/S0020-7683(00)00228-6.
19. Skachkova, V.K., Lyubimov, A.V., Lyubimova, G.V., Gusev, M.N., Grachev, A.V., Lalayan, V.M., Shaulov, A.Yu., Berlin, A.A. Optically transparent heat-resistant nanocomposites based on epoxy resin and silicon dioxide. *Nanotechnologies in Russia*. 2013. 8(1–2). Pp. 92–98. DOI: 10.1134/S199507801301014X.
20. Chukhlanov, V.Yu., Selivanov, O.G. The thermophysical properties of syntactic plastic foams based on polydimethylsiloxane binder. *International Polymer Science and Technology*. 2016. 43(3). Pp. 39–42. DOI: 10.1177/0307174X1604300308.
21. Chen, L., Chai, S., Liu, K., Ning, N., Gao, J., Liu, Q., Chen, F., Fu, Q. Enhanced epoxy/silica composites mechanical properties by introducing graphene oxide to the interface. *ACS Applied Materials & Interfaces*. 2012. Vol. 4. No. 8. Pp. 4398–4404. DOI: 10.1021/am3010576.
22. Wouterson, E.M., Boey, F.Y.C., Hu, X., Wong, S.C. Specific properties and fracture toughness of syntactic foam: Effect of foam microstructures. *Composites Science and Technology*. 2005. 65(11–12). Pp. 1840–1850. DOI: 10.1016/j.compscitech.2005.03.012.
23. O'Lenick, A.J. Silicone polymers: new possibilities in nanotechnology. *American Chemical Society. Symposium series*. 2007. Vol. 961. Pp. 165–175. DOI: 10.1021/bk-2007-0961.ch009.
24. Kamar, N.T., Hossain, M.M., Khomenko, A., Haq, M., Drzal, L.T., Loos, A. Interlaminar reinforcement of glass fiber/epoxy composites with graphene nanoplatelets. *Composites Part A: Applied Science and Manufacturing*. 2015. Vol. 70. Pp. 82–92. DOI: 10.1016/j.compositesa.2014.12.010.

Contacts:

Elena Mastalygina, +7(910)444-23-64; elena.mastalygina@gmail.com

Vasily Ovchinnikov, +7(926)834-28-98; fizhim@rambler.ru

Vladimir Chukhlanov, +7(904)039-86-91; krypton0@mail.ru

© Mastalygina, E.E., Ovchinnikov, V.A., Chukhlanov, V.Yu., 2019



DOI: 10.18720/MCE.90.4

Легкие жаростойкие полимербетоны на основе олигооксигидридсилметиленилосилоксисилана и полых сферических наполнителей

Е.Е. Масталыгина^а, В.А. Овчинников^а, В.Ю. Чухланов^б

^а *Российский экономический университет им. Г.В. Плеханова, г. Москва, Россия*

^б *Владимирский государственный университет имени Александра Григорьевича и Николая Григорьевича Столетовых, г. Владимир, Россия*

* E-mail: elena.mastalygina@gmail.com

Ключевые слова: полимербетон, армированный бетон, кремнийорганическое связующее, полый сферический наполнитель, стеклянные микросферы, керамические микросферы

Аннотация. Новый тип легких полимербетонов был разработан на основе олигооксигидридсилметиленилосилоксисилана с полыми стеклянными или керамическими микросферами. Добавление полых стеклянных и керамических микросфер, являющихся отходами тепловых электростанций, позволило уменьшить себестоимость материалов и снизить потенциальное загрязнение окружающей среды. Для оптимизации технологии производства изучены технологические условия отверждения и формования материалов. В соответствии с изменениями ударной вязкости был установлен оптимальный режим отверждения для композитов при 480–515 К в течение 4,25–4,5 часа в зависимости от типа наполнителя и содержания связующего. Было установлено, что использованное кремнийорганическое связующее обеспечивает термическую устойчивость и высокие прочностные характеристики композиционного материала. По сравнению с традиционными кремнийорганическими смолами, предел прочности при сжатии разработанных материалов увеличился почти в два раза, а модуль упругости увеличился почти на порядок. Благодаря взаимодействию алюмогидрооксидных групп керамических микросфер с кремнийорганическим полимером, модуль упругости материалов с керамическими микросферами на 20–30 % выше, чем модуль упругости полимербетонов со стеклянными микросферами. Высокие физико-механические свойства расширяют возможности использования этих материалов при воздействии значительных внешних статических нагрузок.

Литература

1. Федюк Р.С., Лесовик В.С., Лисейцев Ю.Л., Тимохин Р.А., Битуев А.В., Заяханов М.Е., Мочалов А.В. Композиционные вяжущие для бетонов повышенной ударной стойкости // Инженерно-строительный журнал. 2019. № 1(85). С. 28–38. DOI: 10.18720/MCE.85.3
2. Жежев Т.А., Журтов А.В., Ципинов А.С., Ключев С.В. Огнезащитные фибровемикулитобетоны с вулканическими добавками // Инженерно-строительный журнал. 2018. № 4(80). С. 181–194. doi: 10.18720/MCE.80.16.
3. Барабанщиков Ю.Г., Беляева С.В., Архипов И.Е., Антонова М.В., Школьников А.А., Лебедева К.С. Влияние суперпластификаторов на свойства бетонной смеси // Инженерно-строительный журнал. 2017. № 6(74). С. 140–146. doi: 10.18720/MCE.74.11
4. Низина Т.А., Балыков А.С., Володин В.В., Коровкин Д.И. Дисперсно-армированные мелкозернистые бетоны с полифункциональными модифицирующими добавками // Инженерно-строительный журнал. 2017. № 4(72). С. 73–83. doi: 10.18720/MCE.72.9
5. Ключев С.В., Ключев А.В., Ватин Н.И. Фибробетон для строительной индустрии // Инженерно-строительный журнал. 2018. № 8(84). С. 41–47. doi: 10.18720/MCE.84.4.
6. Логанина В.И., Пышкина И.С., Мартяшин Г.В. Влияние добавки на основе гидросиликатов кальция на стойкость известковых покрытий // Инженерно-строительный журнал. 2017. № 4(72). С. 20–27. doi: 10.18720/MCE.72.3
7. Стешенко А.Б., Кудяков А.И. Цементный пенобетон с алюмосиликатной микросферой для монолитного домостроения // Инженерно-строительный журнал. 2018. № 8(84). С. 86–96. doi: 10.18720/MCE.84.9
8. Kudyakov A.I., Kopanitsa N.O., Sarkisov J.S., Kasatkina A.V., Prischepa I.A. Foam concrete of increased strength with the thermomodified peat additives // IOP Conf. Ser. Mater. Sci. Eng. IOP Publishing. 2015. Vol. 71. No. 1. Pp. 012012.
9. Li G., Wang L., Ni H., Pittman Jr. C.U. Polyhedral oligomeric silsesquioxane (POSS) : a review // J. Inorg. Organomet. Polym. Kluwer Academic Publishers-Plenum Publishers. 2001. Vol. 11. No. 3. Pp. 123–154.
10. Wu Y.C., Kuo S.W. Synthesis and characterization of polyhedral oligomeric silsesquioxane (POSS) with multifunctional benzoxazine groups through click chemistry // Polymer (Guildf). Elsevier. 2010. Vol. 51. No. 17. Pp. 3948–3955.

11. Fina A., Abbenhuis H.C.L., Tabuani D., Camino G. Metal functionalized POSS as fire retardants in polypropylene // *Polym. Degrad. Stab.* Elsevier. 2006. Vol. 91. No. 10. Pp. 2275–2281.
12. Baldi F., Bignotti F., Fina A., Tabuani D., Riccò T. Mechanical characterization of polyhedral oligomeric silsesquioxane/polypropylene blends // *J. Appl. Polym. Sci.* John Wiley & Sons, Ltd. 2007. Vol. 105. No. 2. Pp. 935–943.
13. Chukhlanov V.Yu., Selivanov O.G. Electrical properties of syntactic foams based on hollow carbon microspheres and polydimethylsiloxane // *Russ. Phys. J.* Springer US. 2016. Vol. 59. No. 7. Pp. 944–948.
14. Carniato F., Fina A., Tabuani D., Boccaleri E. Polypropylene containing Ti- and Al-polyhedral oligomeric silsesquioxanes: crystallization process and thermal properties // *Nanotechnology*. 2008. Vol. 19. No. 47. Pp. 475701.
15. Fina A., Tabuani D., Peijs T., Camino G. POSS grafting on PPgMA by one-step reactive blending // *Polymer (Guildf)*. Elsevier. 2009. Vol. 50. No. 1. Pp. 218–226.
16. Yarullin A.F., Kuznetsova L.E., Yarullina A.F., Stoyanov O.V. Electrophysical properties of oligomer-polymer complexes based on heat-resistant oligoaryleneamines // *Polym. Sci. Ser. D*. 2013. Vol. 6. No. 2. Pp. 109–115.
17. Smirnova N.N. Pervaporation properties of film and composite membranes based on an interpolyelectrolyte complex of sulfonate-containing aromatic copolyamide // *Russ. J. Appl. Chem.* Pleiades Publishing, 2018. Vol. 91. No. 3. Pp. 404–411.
18. Bardella L., Genna F. On the elastic behavior of syntactic foams // *Int. J. Solids Struct.* 2001. Vol. 38. No. 40–41. Pp. 7235–7260.
19. Skachkova V.K., Lyubimov A.V., Lyubimova G.V., Gusev M.N., Grachev A.V., Lalayan V.M., Shaulov A.Yu., Berlin A.A. Optically transparent heat-resistant nanocomposites based on epoxy resin and silicon dioxide // *Nanotechnologies Russ.* SP MAIK Nauka/Interperiodica. 2013. Vol. 8. No. 1–2. Pp. 92–98.
20. Chukhlanov V.Yu., Selivanov O.G. The thermophysical properties of syntactic plastic foams based on polydimethylsiloxane binder // *Int. Polym. Sci. Technol.* SAGE PublicationsSage UK: London, England. 2016. Vol. 43. No. 3. Pp. 39–42.
21. Chen L., Chai S., Liu K., Ning N., Gao J., Liu Q., Chen F., Fu Q. Enhanced epoxy/silica composites mechanical properties by introducing graphene oxide to the interface // *ACS Appl. Mater. Interfaces*. 2012. Vol. 4. No. 8. Pp. 4398–4404.
22. Wouterson E.M., Boey F.Y.C., Hu X., Wong S.C. Specific properties and fracture toughness of syntactic foam: Effect of foam microstructures // *Compos. Sci. Technol.* Elsevier. 2005. Vol. 65. No. 11–12. Pp. 1840–1850.
23. O'Lenick A.J. Silicone polymers: new possibilities in nanotechnology // *Am. Chem. Soc. Symp. Ser.* 2007. Vol. 961. Pp. 165–175.
24. Kamar N.T., Hossain M.M., Khomenko A., Haq M., Drzal L.T., Loos A. Interlaminar reinforcement of glass fiber/epoxy composites with graphene nanoplatelets // *Compos. Part A Appl. Sci. Manuf.* Elsevier. 2015. Vol. 70. Pp. 82–92.

Контактные данные:

Елена Евгеньевна Масталыгина, +7(910)444-23-64; эл. почта: elena.mastalygina@gmail.com

Василий Андреевич Овчинников, +7(926)834-28-98; эл. почта: fizhim@rambler.ru

Владимир Юрьевич Чухланов, +7(904)039-86-91; эл. почта: krypton0@mail.ru

© Масталыгина Е.Е., Овчинников В.А., Чухланов В.Ю., 2019



DOI: 10.18720/MCE.90.5

Risk of surface blast load on pile foundations

Y.E-H. Ibrahim^{a,b*}, M. Nabil^b,

^a Prince Sultan University, Riyadh, Saudi Arabia

^b Zagazig University, Zagazig, Egypt

* E-mail: yibrahim@vt.edu

Keywords: soil, buildings, blast load, finite element, pile foundation, expanded polystyrene

Abstract. Recent terrorist attacks have raised the importance of studying the structural response under blast loads. Most of the past research has focused on the superstructure performance without considering the foundation behavior under blast loads. In this research, a pile foundation system was analyzed using detailed finite element analysis using ABAQUS under blast load to investigate the effectiveness of different mitigation techniques. The foundation system includes nine concrete piles encased in steel pipes with external diameters of 0.6 m. The piles have a length of 20 m in silty clay and stiff clay layers. The piles are connected using a reinforced concrete raft with dimensions of 10 m×10 m and a thickness of 1 m. The blast load considered resulted from a surface explosive charge of 457 kg of TNT at a standoff distance 2.5 m from raft and at a height of 0.56 m above ground surface. The raft was loaded by 200 kN/m² to represent the load transferred from the structure. Barrier walls from different materials including aluminum, rubber, Thermoplastic polyurethane (TPU) and Expanded Polystyrene (EPS) were considered to mitigate the blast load effect on the pile foundation. Also, an open trench before the raft was considered and compared to the used wall barriers. It was observed that the open trench and a wall barrier from Expanded Polystyrene showed the best mitigation to the blast effect compared to the original case and other wall barriers from different materials. A parametric study was conducted to optimize the selected EPS wall barrier in terms of thickness and depth.

1. Introduction

After the recent attacks on many iconic buildings, many researchers have focused in their research on the structural response of buildings when subjected to blast loads and possible solutions to mitigate the risk of this threat [1–6]. Due to the complexity of the problem and the severe damage occurring in the superstructures, most of the research conducted in this area focused on the analysis and response of the superstructure without taking in consideration the effect of the foundation. Dynamic waves resulting from surface blast explosions can severely damage the foundation and underground structures through dynamic loads exerted from reflected waves after hitting the ground [7–9].

Most of the research work addressing the soil and structural response of foundations and underground structures under blast loads was conducted through finite element analysis using powerful packages such as ABAQUS [10], LS-Dyna [11] and ANSYS [12] to consider the nonlinearity of materials, soil block modeling with its boundary conditions and dynamic loads exerted on soil and underground structures and foundations [13–18]. The finite element analysis provides well representation of the problem without the need for experimental work, which is hard to perform and this explains the limited research work in this area [19–20].

Representing the blast loads in the finite element analysis needs careful consideration in order to obtain accurate results and real simulation. Based on spherical explosive charges, most of empirical equations were developed in order to calculate the pressure that is generated by air, surface, subsurface or under water explosives on structures [7–9, 21–26]. The calculated pressure exerted by blast loads through these empirical equations is affected by different parameters such as the weight of explosive charge, its duration, time of wave

Ibrahim, Y.E-H., Nabil, M. Risk of surface blast load on pile foundations. Magazine of Civil Engineering. 2019. 90(6). Pp. 47–61. DOI: 10.18720/MCE.90.5

Ибрагим Я, Набил М. Риск внешней взрывной нагрузки на свайные фундаменты // Инженерно-строительный журнал. 2019. № 6(90). С. 47–61. DOI: 10.18720/MCE.90.5



This open access article is licensed under CC BY 4.0 (<https://creativecommons.org/licenses/by/4.0/>)

arrival at the structure and particle displacement, velocity, and acceleration. The pressure generated on soils depends on soil properties such as void ratio and water content, especially in cohesive soils compared to granular soils with high relative density [21, 26].

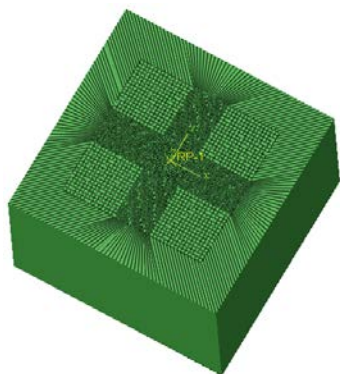
The shape of the crater developed in soils due to blast explosions is significantly affected by the weight of explosive charge. Explosives with higher weights lead to significant increase in energy dissipation. Pile foundations subjected to surface blast loads may not be used to support superstructure after the blast because of the high horizontal stresses developed in the top portions of piles close to the explosive charge [27].

Many researchers investigated ways to mitigate the risk of blast loads on underground structures using barriers. The studied solutions included using barriers from different materials between the surface explosion and the underground structure as well as using trenches filled with polystyrene foam. It was concluded that these solutions had great influence on reducing the blast risk on underground structures especially using compressible geofom barrier made of polyurethane [28–31].

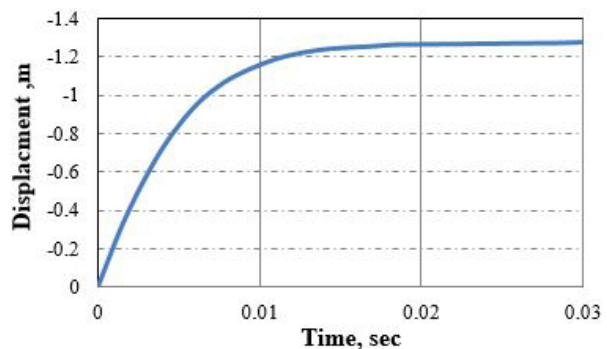
In this research, the effectiveness of using different techniques to mitigate the blast load effect on pile foundation and surrounding soil was investigated using detailed finite element analysis using ABAQUS. The pile foundation includes nine piles connected with a raft foundation. The mitigation techniques included the using open trench or wall barrier from different materials such as aluminum, rubber, thermoplastic polyurethane (TPU) and expanded polystyrene (EPS). The blast load effect was considered through an explosive charge of 457 kg of TNT placed at a standoff distance of 2.5 m from the edge of the raft and at a height of 0.56 m above ground surface. All barrier walls are assumed to have 0.25 m thickness and placed at the edge of the raft foundation. The walls extended to 5.0 m below the ground surface. After comparing the effectiveness of using these techniques, a parametric study was conducted to optimize the use of the most effective mitigation technique in order to obtain the best protection of the pile foundation under blast load.

2. Methods

First, in order to verify the representation of blast load on soil block and its effect on the formation of the soil crater in terms of its radius and depth, a soil model was created using ABAQUS with its CONWEP representation of blast load. The results were compared to that obtained from previous empirical equations provided by Cooper [9] and Gould [32] and previous finite element model [33]. The developed finite element model is shown in Figure (1.a). The soil block had the dimensions of 100 m×100 m×50 m and 10 m of non-reflected boundaries in both X and Y directions and used a fixed boundary in Z direction. A 100-kg spherical charge with a density of 1630 kg/m³ was used. The scale distance R from the surface of the earth to the center of the charge was 0.50 m to confirm that the CONWEP will work well with the target surface X-Y surface.



a) Finite Element Model



b) Time history of vertical displacement at center of crater

Figure 1. Finite element model of soil block used for verification.

An elastic–plastic analysis using the Drucker-Prager Cap model was conducted. The apparent crater radius and depth, which were measured relative to the original surface, were compared to the empirical equations and previous finite element model (Table 1). Figure 1.b shows the time history of the vertical displacement of the center of crater after the soil block was subjected to the blast load.

Table 1. Crater depth and width from numerical analysis, empirical equations.

Method	Apparent Crater Radius (m)	Apparent Crater Depth (m)
Cooper [9]	1.80	–
Gould [32]	2.85	1.19
Previous Finite Element Model [33]	1.37	1.20
Developed Finite Element Model	1.69	1.27

According to the results obtained, the developed finite element model provided results with acceptable accuracy in terms of the radius and depth of the soil crater. Accordingly the finite element model was used in this research.

The pile foundation considered in this study consisted of 9 reinforced concrete piles with a diameter of 600 mm each encased in 15 mm thick steel casing with a total length of 20 m. The piles are 4.2 m (center to center) apart from each other. The piles are connected with a raft foundation with the dimensions of 10 m x 10 m with a total thickness of 1.0 m. A uniform load with an intensity of 200 kN/m² was applied on the raft to represent the load transferred from the structure. Blast charge of 457 kg of TNT was placed at a standoff distance 2.5 m from closest raft edge and at a height of 0.56 m above ground surface. The soil block considered had the dimensions of 100 m x 100 m in plan with a depth of 50 m. Standard elements were used for soil block surrounding the raft and pile foundations followed by infinite elements in order to provide quiet boundary conditions to the finite element model. The soil profile consisted of upper layer of silty clay with a total thickness of 10 m. This layer was followed by 40-m thick stiff clay. The soil properties are given in the following Table 2 [34]:

Table 2. Properties of soil layers [34].

Soil Property	silty clay	stiff clay
Young's Modulus (MPa)	51.7	328
Poisson Ratio	0.45	0.17
Density kg/m ³	1920	1920
Material Cohesion (MPa)	0.036	1.38
Material angle of friction (degrees)	24	36.9
Cap eccentricity parameter	0.3	0.33
Initial cap yield surface position	0.02	0.02
Transition surface radius parameter	0.05	0.01
Cap hardening behavior [Stress (MPa), plastic volumetric strain]	[2.75, 0] [4.83, 0.02] [5.15, 0.04] [6.20, 0.08]	[2.75, 0] [4.14, 0.02] [5.51, 0.05] [6.20, 0.09]

A wall barrier was used at closer edge of the raft with a length equals to the length of the raft (10.0 m). The depth of wall barrier was 5.0 m with its top at the ground surface. The thickness of the wall was 0.25 m. Figure 2 shows the arrangement of the piles, wall location and blast charge position.

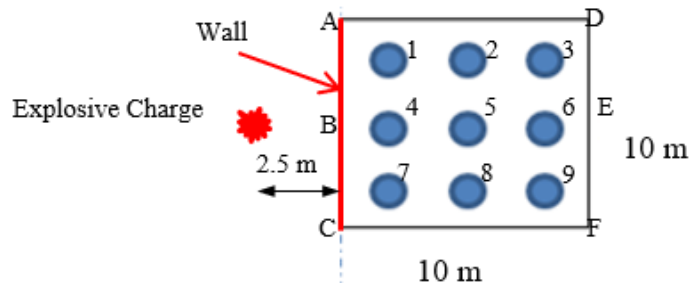


Figure 2. Pile foundation arrangement and wall location.

Different types of wall barriers were considered including:

- No barrier (original case)
- Open trench
- Barrier from different materials (Aluminum, Thermoplastic polyurethane TPU, Rubber and Expanded Polystyrene EPS)

Table 3 shows the different physical properties of materials used.

Table 3. Different physical properties of materials used.

Material	Modulus of Elasticity E (MPa)	Poisson Ratio ν	Specific Weight γ (kN/m ³)
Aluminum	73.09 * 10 ³	0.33	27.4
Thermoplastic polyurethane (TPU)	158	0.40	11.5
Rubber	76.53	0.45	1.1
Expanded Polystyrene (EPS)	7.5	0.00	1.0

Soil block was modeled in ABAQUS using Lagrangian three-dimensional solid continuum elements. ABAQUS CONWEP empirical model was used to model the blast load on soil and foundations through defining the equivalent TNT explosive charge and its location. The objective of the analysis was to consider the soil behavior including crater formation and pile foundation performance [33]. In order to represent the soil behavior, Drucker-Prager Cap model in ABAQUS was used. This model considers soil hardening/softening and stress path dependence [35]. CIN3D8 elements were used to model the infinite elements and the boundary conditions of the considered soil block. These elements are 3D 8-nodes solid continuum finite elements. C3D8R elements were used to model the concrete elements of raft and piles. These elements are 8-node solid elements with reduced integration. In order to model the inelastic behavior of concrete material of raft and piles, concrete damage plasticity model was used. This model considers the concept of isotropic damaged elasticity in combination with isotropic tensile and compressive plasticity. Based on the material properties of Chopra and Chakrabarti [36], stress-strain curve was developed by Martin [37], which was used in this study. Values of yielding and failure strains of concrete were 0.002 and 0.004, respectively. In order to model the plasticity in ABAQUS, true stress and logarithmic plastic strain were used. Figure 3 shows the finite element model of the soil and pile foundation.

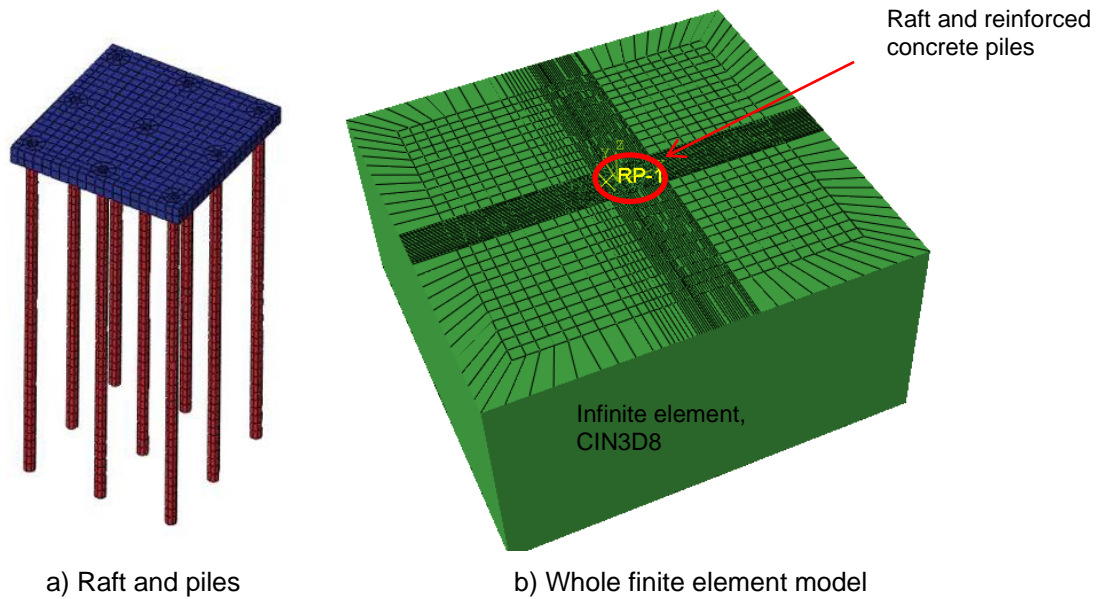


Figure 3. Finite element model of pile foundation and soil block.

Aluminum is modeled using Johnson-Cook constitutive model [38], which provides simple mathematical relationship of stress-strain-temperature using material parameters; A, B, C and m as shown in Table 4.

Table 4. Johnson-Cook parameters for Aluminum [38]

A (MPa)	B (MPa)	C	M
349	426	0.0083	1

Ductile failure criterion in ABAQUS was used to model TPU. The parameters needed to model the isotropic hardening are given in Table 5 [38]

Table 5. Isotropic hardening stress-strain values for TPU [39]

Yield stress (MPa)	11.05	25.92	45.36	119.02	265.26	295.43	390.17
Plastic strain	0	0.36	0.76	1.42	1.90	2.18	2.97

The strain rate of TPU, fracture strain for ductile damage and Stress triaxiality were assumed to be 0.001 S^{-1} , 2.9 and 0.33, respectively [39].

Hyperelastic and viscoelastic properties of rubber were modeled using ABAQUS. Neo-Hookean model for hyperelastic behavior was used. The material constants C_{10} , C_{01} and D_1 were 1 MPa, 0 and $5.085 \cdot 10^{-3} \text{ Pa}$, respectively. Prony series was used to model the viscoelastic behavior of the rubber. The material constants used were g_i , K_i and τ_i with values of 0.3, 0 and 0.1, respectively. These parameters can be obtained from shear or relaxation test [40].

To model the hyperfoam material properties of EPS, ABAQUS default parameters were used to define the strain energy function. The hyperfoam material is different from the regular hyperelastic material in terms of its high compressibility (ABAQUS Manual). Viscoelastic behavior of the material was modeled through

assigning values for the parameters used to define the prony series. The values used for this material were 0.5, 0.5 and 0.003 for g_i , K_i and τ_i , respectively

Note that the dimensions of the barrier wall used were kept the same for all materials during this study, even though it might not be practically accepted. This was decided in order to compare different responses of these materials and to decide on the most effective one. Then the final selected material can be more investigated to get the best enhancement can be obtained for the mitigation of blast load effect considering the cost and availability.

3. Results and Discussions

The finite element analysis of the pile foundations, soil block and wall barrier was conducted under blast load of 457 kg of TNT at a standoff distance 2.5 m from closest raft edge and at a height of 0.56 m above ground surface. The effect of wall barrier used was considered through using different wall materials as well as open trench and comparing the results with the original case, where the pile foundations are not protected. Figures from 3 to 18 show the effect of different wall barrier from different materials and open trench on the response of soil and pile foundation under the effect of blast load.

Figure 4 shows the soil crater developed after the blast in the original case. A typical crater shape was obtained. The maximum vertical downward displacement in soil was 0.75 m at distance of 2.5 m from raft edge. The soil profile was almost not affected at a distance of around 6.0 m from the raft edge in front of the explosion. Figure 4 shows the lateral displacement of the soil for the original case. The maximum lateral displacement was 0.17 m at 3.0 m from the raft edge in front of the explosion.

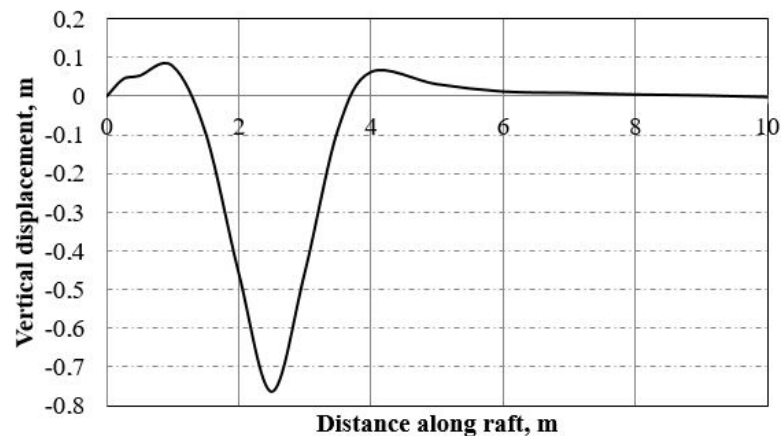


Figure 4. Crater shape (Distance measured from B).

In the first part of the analysis, the wall barrier had a thickness of 0.25 m and a total depth of 5.0 m with its top at the same level with the top level of the raft foundation, which is at the ground surface. Figures 6 and 7 show the vertical and lateral displacement at the middle axis of the raft foundation (line BE) for different cases considered. The maximum vertical displacement at the original case was 0.6 cm at point B. Using open trench resulted in much reduction of the vertical displacement to around 0.1 cm, while the wall barrier resulted in reduction of the value in most of the cases. Similarly, the lateral displacement of the middle axis of the raft was around 0.9 cm at point B at the original case and it was reduced significantly upon using the open trench to around 0.1 cm. EPS wall barrier resulted in considerable reduction of the lateral displacement to around 0.36 cm, and the EPS wall barrier was considered the best barrier used, in this regard.

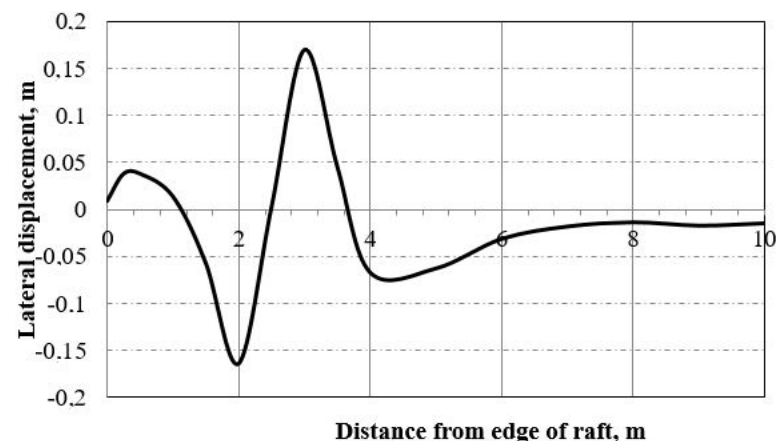


Figure 5. Lateral displacement in the soil (Distance measured from B).

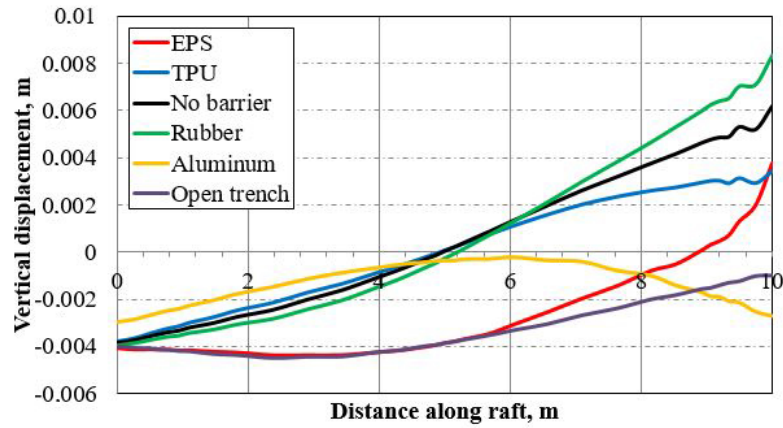


Figure 6. Vertical displacement at raft foundation (E at zero and B at 10 m) at $t = 0.03$ seconds.

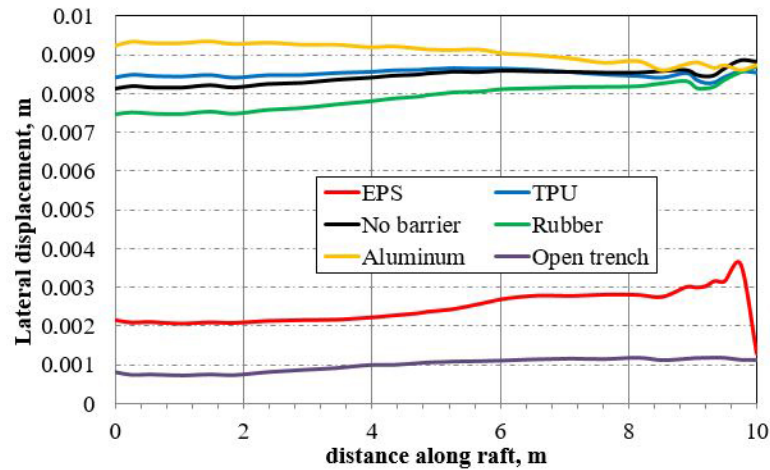


Figure 7. Lateral displacement at raft foundation (E at zero and B at 10 m) at $t = 0.03$ seconds.

Figure 8 shows the deformation of the set of piles due to the blast load in the original case. It is clear that the most deformed pile was the pile close to the explosive charge (number 4) and the large deformations occurred at the top part of the piles. Figure 9 to Figure 13 show the response of the edge pile (pile number 4); while Figure 14 to Figure 19 show the response of the central pile (pile number 5). According to Figure 9, TPU and rubber barriers had no considerable effect on the vertical displacement at the top of the edge pile while the vertical displacement at its top was increased in the case of open trench, EPS and Aluminum barrier wall. The pile foundations experienced the largest residual vertical displacement of the edge pile (0.25 cm) at its top in the Aluminum barrier case. Figures 10 and 11 show the lateral and vertical displacements over the length of the edge pile (number 4) in all cases, respectively.

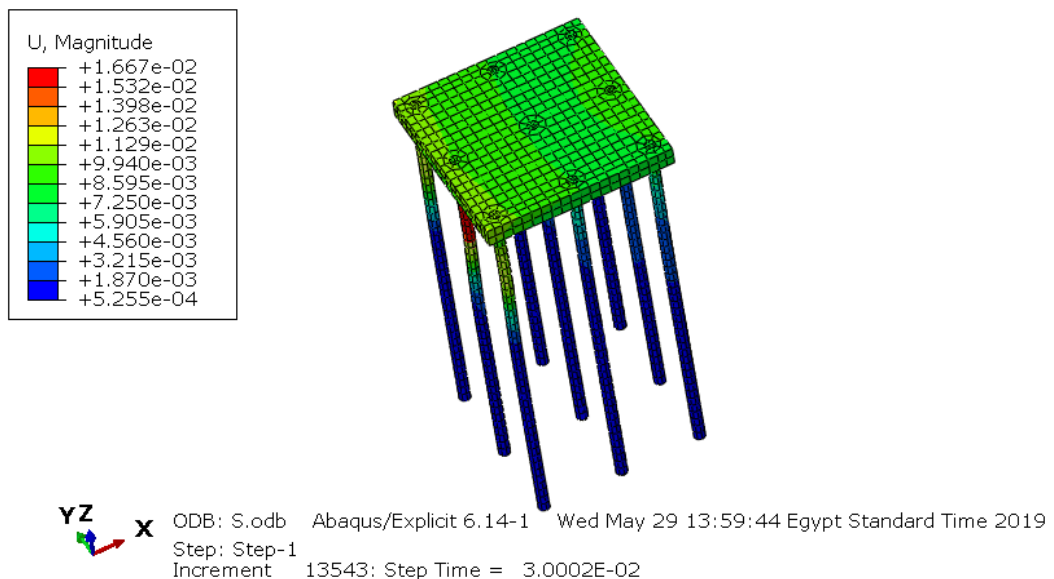


Figure 8. Deformed shape of pile foundation at $t = 0.03$ seconds in the original case (no wall barrier).

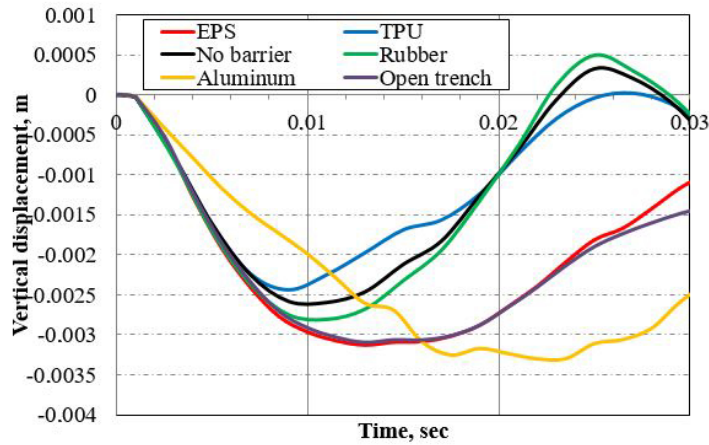


Figure 9. Vertical displacement at central of edge pile (Pile No. 4) at $t = 0.03$ seconds.

The maximum lateral displacement of the pile occurred at depth of 3.0 m in all cases, except for the open trench case, where the maximum lateral displacement was at depth of 5.0 m. Open trench and EPS barrier wall resulted in significant reduction of the lateral displacement, especially in the open trench case, compared to the original case. Rubber barrier wall has no effect on the lateral displacement, while more lateral displacement was obtained when using TPU and Aluminum walls. Similar results were obtained regarding the vertical displacement of the edge pile with the occurrence of maximum downward displacement at depth of 7.0 m for most of the cases and maximum upward displacement at its top as shown in Figure 11.

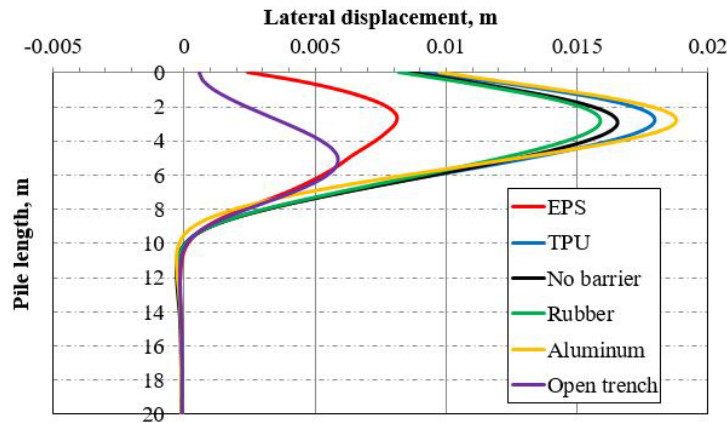


Figure 10. Lateral displacement at edge pile (Pile No. 4) at $t = 0.03$ seconds.

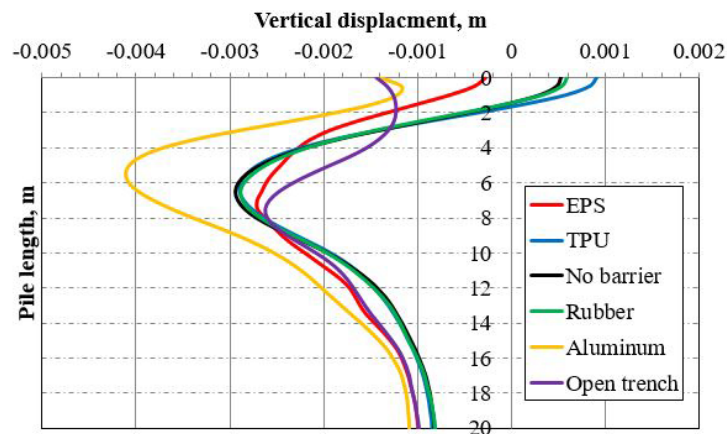


Figure 11. Vertical displacement at edge pile at $t = 0.03$ seconds.

Figures 12 and 13 show the vertical and lateral stresses developed in the pile number 4. Values of vertical stresses did not show big variances in most of the cases, however, the lateral stresses were much reduced in the open trench case. Higher vertical stresses were received in the top part of the edge pile with the maximum vertical stress at depth of 3.0 m from the pile top. The maximum lateral stresses were experienced at the top of the pile with much less stresses in lower parts of the edge pile. The open trench had

better effect on the vertical and lateral displacements and stresses on the edge pile when subjected to blast loads.

Considering pile number 5, which is located under the center of the raft, the lateral and vertical displacement at the top of the pile are shown in Figures 14 and 15. By the end of the blast load duration, significant reduction in lateral displacements was obtained in both cases; open trench and EPS wall barrier.

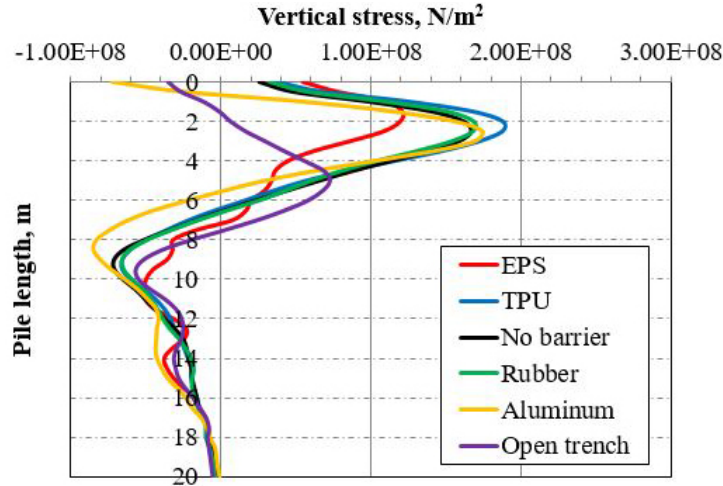


Figure 12. Vertical stress at edge pile (Pile No. 4) at $t = 0.03$ seconds.

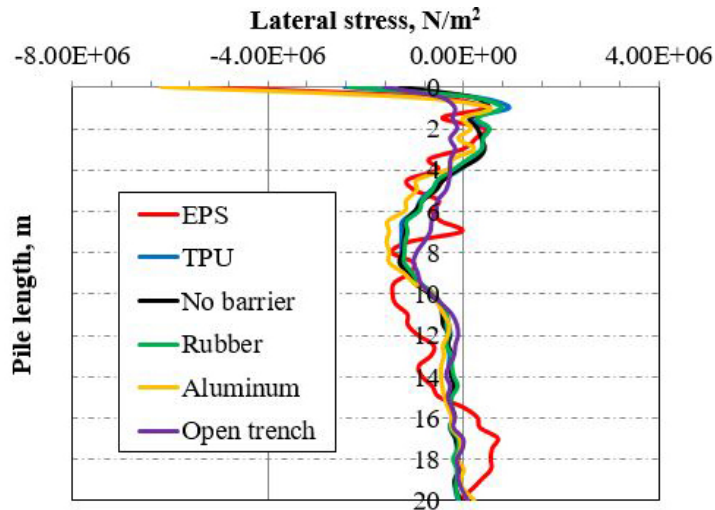


Figure 13. Lateral stress at edge pile (Pile No. 4) at $t = 0.03$ seconds.

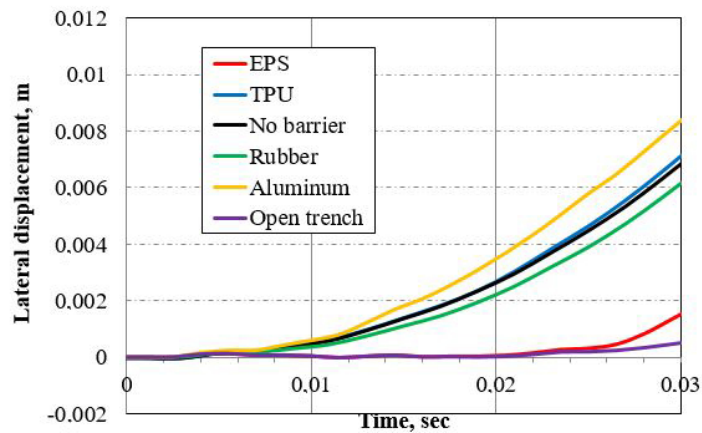


Figure 14. Lateral displacement at central pile (Pile No. 5).

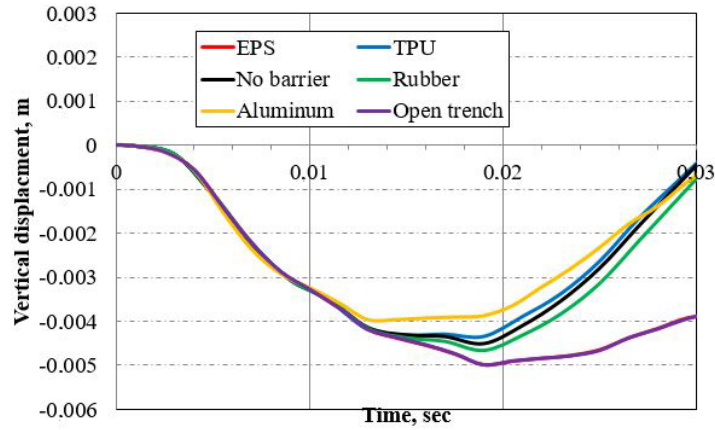


Figure 15. Vertical displacement at central pile (Pile No. 5).

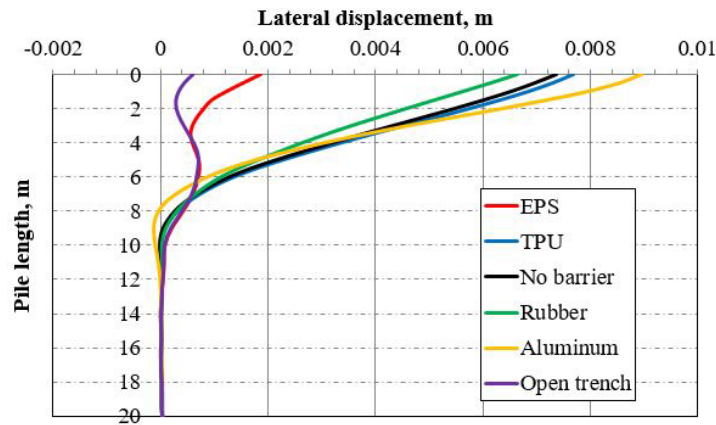


Figure 16. Lateral displacement at center pile (Pile No. 5) at $t = 0.03$ seconds.

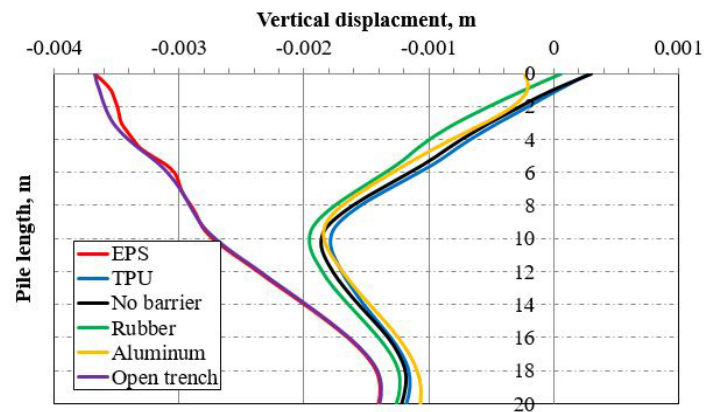


Figure 17. Vertical displacement at center pile (Pile No. 5) at $t = 0.03$ seconds.

After reaching a conclusion that the EPS wall barrier is the best wall barrier in terms of mitigating the blast load risk on the pile foundation, a parametric study was conducted to optimize the effectiveness of this wall barrier in this regard. Three cases were considered to study the effect of the wall thickness of EPS wall barrier including using thickness of 50 cm and 100 cm besides the case considered earlier (25 cm) and comparing these cases with the original case that has no wall barrier. The results of this parametric study are shown in Figures 20 to 27. According to the results, considerable enhancement was obtained upon increasing the wall thickness in terms of the lateral and vertical displacements over the pile length (Figures 20 and 21, respectively for edge pile), time history of lateral and vertical displacement at the top of the central pile (Figures 22 and 23, respectively), lateral displacement over the length of the central pile and finally the vertical displacement along the central X-axis of the raft. The top half of the edge pile experienced large lateral displacements in all cases while no noticeable lateral displacements were spotted in the lower part. The maximum vertical displacements were obtained at a depth of 8 to 10 m in all cases. Increasing the wall barrier thickness from 50 cm to 100 cm has a negligible effect on the enhancement of the pile foundations under blast loads. According to the importance of the building and the possibility of being targeted in a terrorist attack, the designer and the owner may choose the thickness of the wall barrier to mitigate the blast load risk on the foundation. According to the results obtained, the maximum recommended wall barrier thickness is 50 cm.

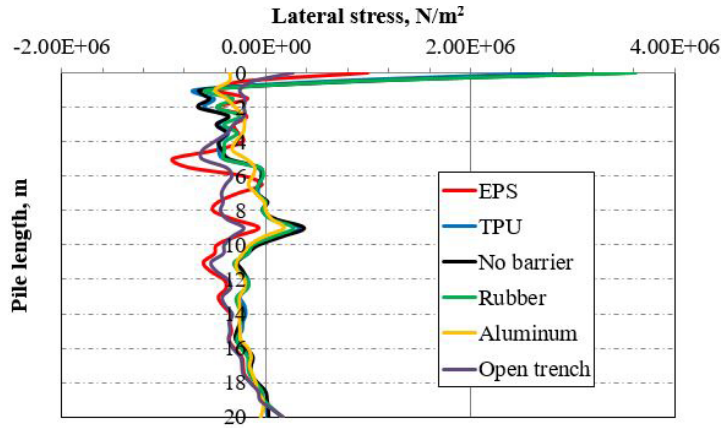


Figure 18. Lateral stress at center pile (Pile No. 5) at $t = 0.03$ seconds.

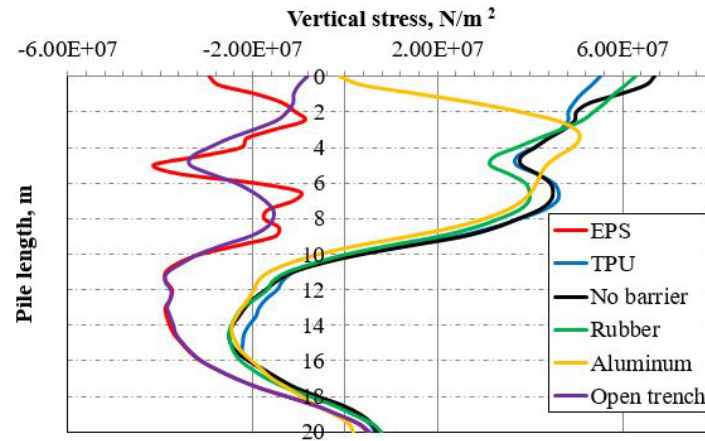


Figure 19. Vertical stress at center pile (Pile No. 5) at $t = 0.03$ seconds.

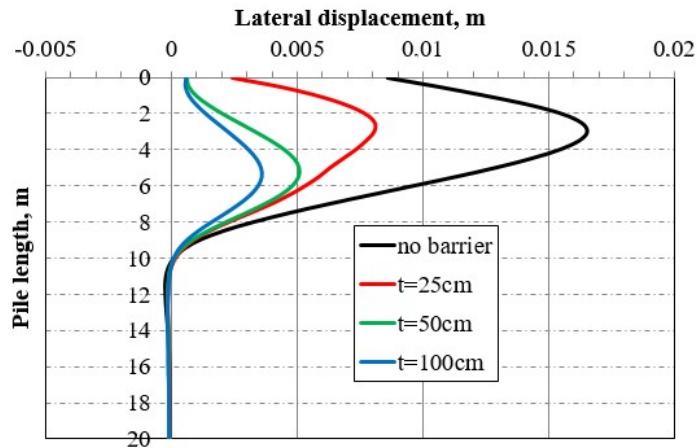


Figure 20. Lateral displacement of Pile No. 4 at $t = 0.03$ seconds.

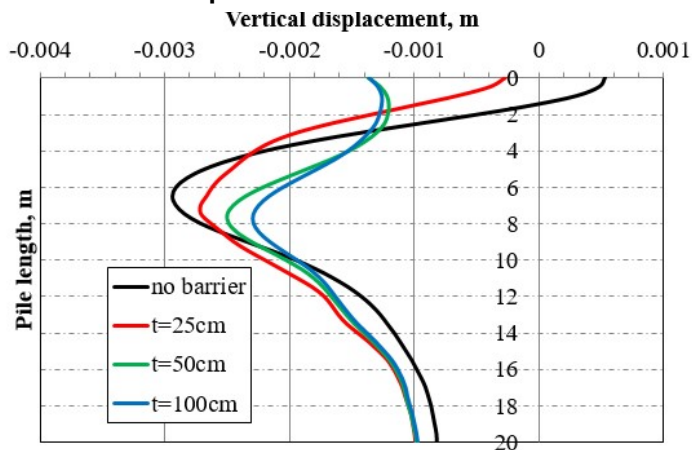


Figure 21. Vertical displacement of Pile No. 4 at $t = 0.03$ seconds.

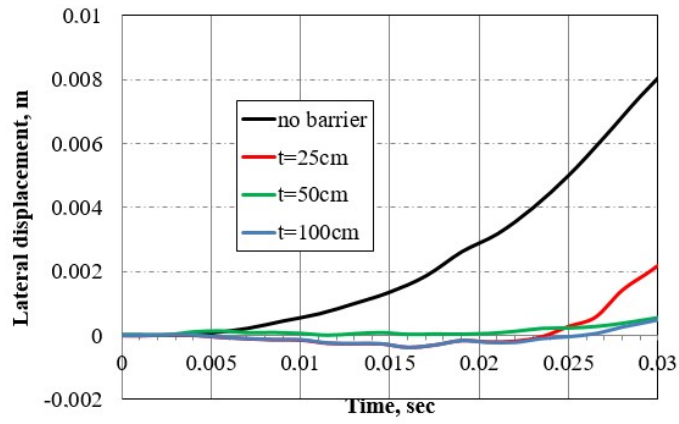


Figure 22. Lateral displacement at central of Pile No. 4.

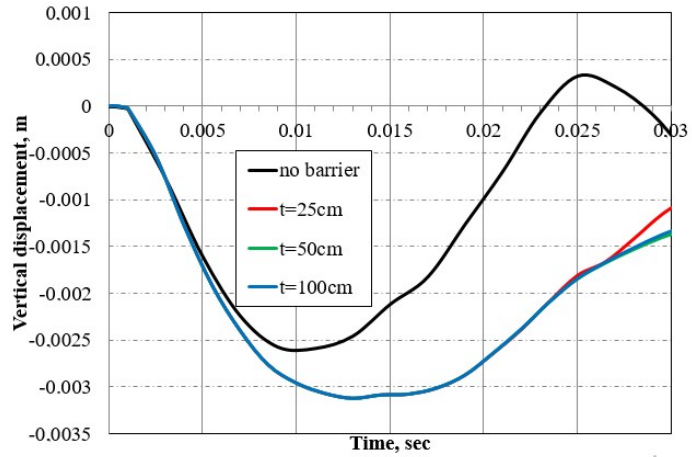


Figure 23. Vertical displacement at central of Pile No. 4.

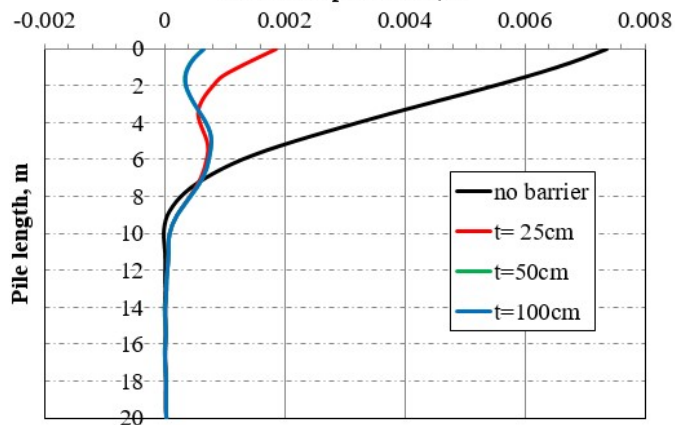


Figure 24. Lateral displacement at central of Pile No. 5 at $t = 0.03$ seconds.

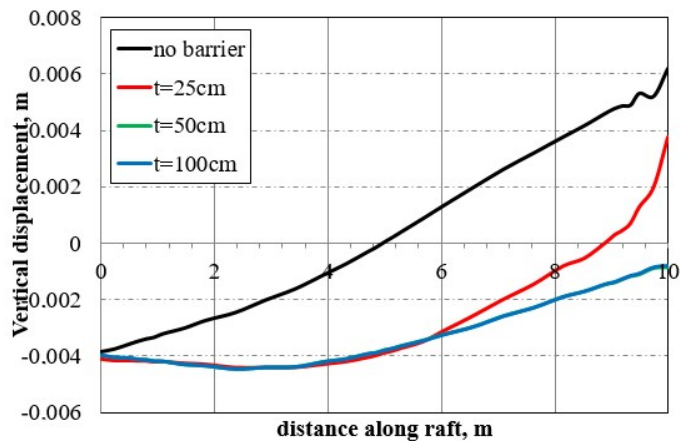


Figure 25. Vertical displacement along line BE at raft at $t = 0.03$ seconds.

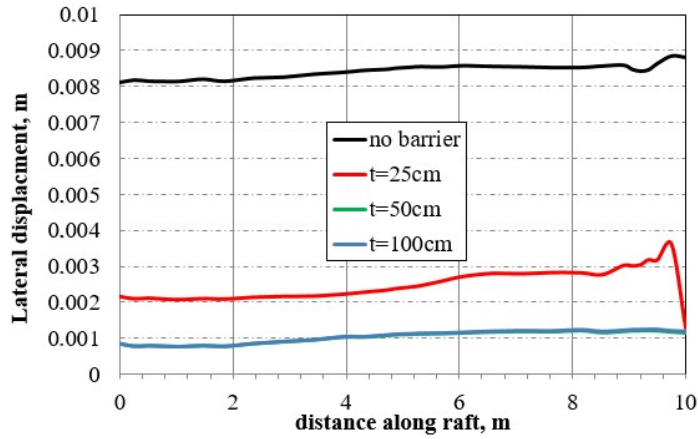


Figure 26. Lateral displacement along line BE at raft.

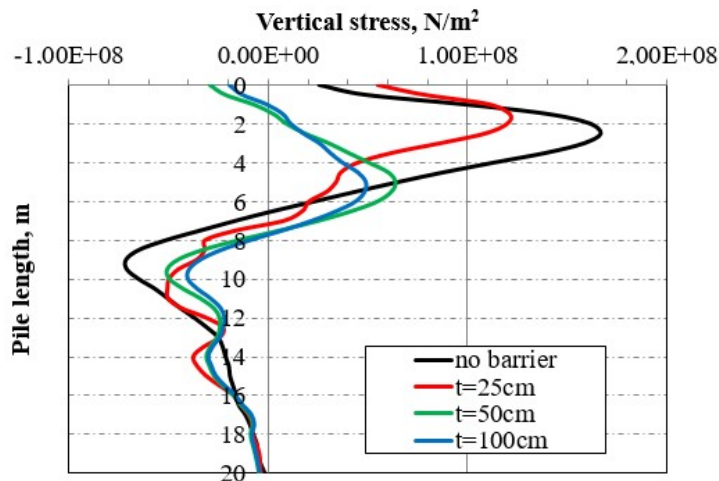


Figure 27. Vertical stress along Pile No. 4.

On the other hand, it might be considered to increase the depth of the wall barrier to provide better protection for the pile foundation system. The original case considered had wall barrier with a total depth of 5.0 m. Most of the large deformations obtained in piles were observed in top 5.0 m of the pile length. Accordingly, another parametric study was conducted to investigate the effect of having different depths of wall barrier including 10.0 and 15.0 m and the results were compared to the case considered earlier (depth of 5.0 m) and the original case that had no wall barrier. The results are shown in Figures 28 to 31. According to the results obtained, increasing the wall depth had no significant enhancement on the pile and foundation performance under blast load. There was no considerable protection obtained upon increasing the depth of the wall barrier to 10.0 or 15.0 m against the surface blast load. A depth of 5.0 m of EPS wall barrier was considered the optimal wall barrier in all cases considered.

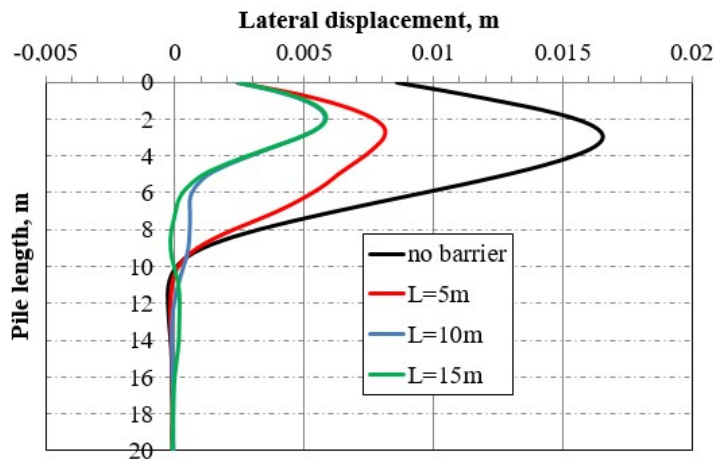


Figure 28. Lateral displacement of Pile No. 4 at $t = 0.03$ seconds.

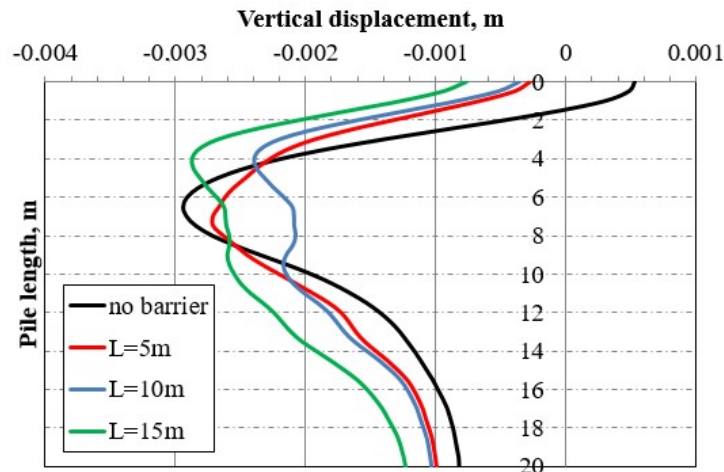


Figure 29. Vertical displacement of Pile No. 4 at $t = 0.03$ seconds.

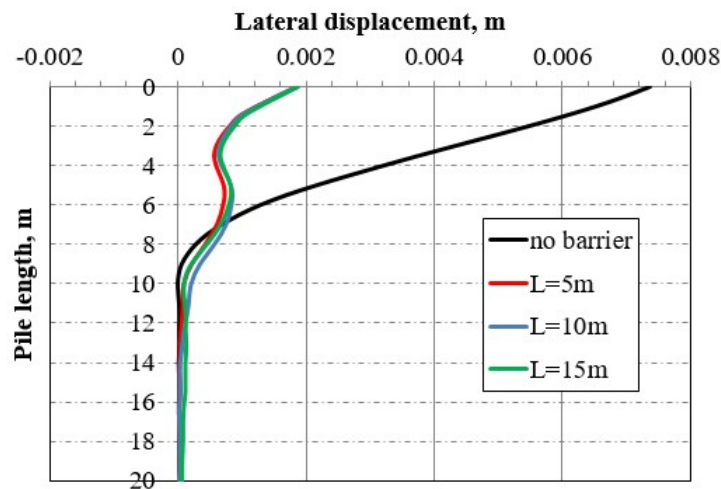


Figure 30. Lateral displacement of Pile No. 5 over its length at $t = 0.03$ seconds.

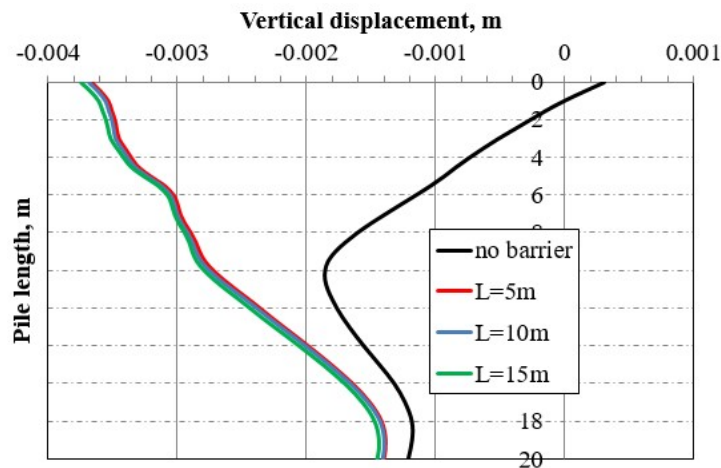


Figure 31. Vertical displacement of Pile No. 5 over its length at $t = 0.03$ seconds.

4. Conclusions

A finite element analysis using ABAQUS was conducted to study the effect of surface blast load on pile foundation considering different techniques in order to reduce the risk of the blast load. The pile foundation system consisted of nine 20-m length concrete piles encased in steel pipes with external diameter of 0.6 m and connected with a raft foundation of 10.0×10.0 m in plane dimensions and a thickness of 1.0 m. The soil profile consisted of upper layer of silty clay with a total thickness of 10 m. This layer was followed by 40-m thick stiff clay. The raft was loaded by 200 kN/m² to represent the load transferred from the structure. Explosive charge of 457 kg of TNT was assumed at a standoff distance 2.5 m from raft and at a height of 0.56 m above ground surface. Different techniques were considered in the study including using open trench before the pile foundation and wall barrier from different materials with a dimension of 10.0 m length, 0.25 m thickness and a

depth of 5.0 m with its top at the ground surface. According to the results, the following conclusions were obtained:

1. The open trench provides significant protection to the pile foundations under blast load effect. The enhancement in the response of the pile foundation upon using the open trench was better than all the wall barriers used.

2. Wall barriers can provide good enhancement of response of soil and pile foundation against surface blast load. However, the material of the wall barrier can play a vital role in this effect. Expanded Polystyrene (EPS) was the best material used for the wall barrier due to its hyperelastic and viscoelastic properties.

3. The protection provided by the wall barrier to the pile foundation against surface blast load is significantly affected by the thickness of the wall barrier. Larger thickness of wall barrier provides better enhancement and protection to the pile foundation. However, this should be considered with the cost of the wall barrier and the importance of the building and how susceptible to possible terrorist attack.

4. A depth of 5.0 m is sufficient for the wall barrier to provide significant protection to surface blast load threat. Larger depths provide slight enhancement that is not worthy compared to the increase in cost and construction challenges.

The study will be extended to investigate if similar results can be obtained when considering the effect of surface blast load on underground structures considering different parameters as the depth of underground structure, soil profile and various possible mitigation techniques.

5. Acknowledgement

The authors would like to express their thanks to Prince Sultan University for supporting in publishing the article.

References

- Ismail, M., Ibrahim, Y., Nabil, M., Ismail, M.M. Response of A 3-D reinforced concrete structure to blast loading. *International Journal of Advanced and Applied Sciences*. 2017. 4. 10. Pp. 46–53.
- Ibrahim, Y.E., Ismail, M.A., Nabil, M.A. Response of Reinforced Concrete Frame Structures under Blast Loading. *Procedia Engineering*. 2017. 171. Pp. 890–898.
- Fu, F. Dynamic response and robustness of tall buildings under blast loading, *Journal of Constructional Steel Research*. 2013. 80. Pp. 299–307.
- Choi, J., Choi, S., Kim, J. J. and Hong, K. Evaluation of blast resistance and failure behaviour of prestressed concrete under blast loading. *Construction and Building Materials*. 2018. 173. Pp. 550–572.
- Ritchie, C.B., Packer, J.A., Seica, M.V., Zhao, X. Behaviour and analysis of concrete-filled rectangular hollow sections subject to blast loading. *Journal of Constructional Steel Research*. 2018. 147. Pp. 340–359.
- Hadianfard, M.A., Malekpour, S., Momeni, M. Reliability analysis of H-section steel columns under blast loading, *Structural Safety*. 2018. 75. Pp. 45–56.
- Baker, W.E. *Explosions in Air*. Austin. 1973. Texas, University of Texas Press.
- ASCE. *Manual 42, Design of Structures to Resist Nuclear Weapons Effects*. New York City, New York. American Society of Civil Engineers, 1985.
- Cooper, P.W. *Explosives Engineering*. Hoboken, New Jersey: John Wiley & Sons, Inc., 1996.
- ABAQUS 6.14 User Documentation. Dessault Systems, 2018.
- ANSYS. *AUTODYN User's Manual*. Canonsburg, Pennsylvania: ANSYS Inc., 2018.
- LS-DYNA User's Manual. Livermore Software Technology Corporation, 2018.
- Lu, Y. Underground blast induced ground shock and its modeling using artificial neural network. *Computers and Geotechnics*, 2005. 32. Pp. 164–178.
- Gui, M.W., Chien, M.C. Blast-resistant analysis for a tunnel passing beneath Taipei Shongsan airport—a parametric study. *Geotechnical & Geological Engineering*. 2006. 24. Pp. 227–248.
- Wang, J.G., Sun, W., Anand, S. Numerical investigation on active isolation of ground shock by soft porous layers. *Journal of Sound and Vibration*. 2009. 321. Pp. 492–509.
- Shin, J.H., Moon, H.G., Chae, S.E. Effect of blast-induced vibration on exiting tunnels in soft rocks. *Tunnelling and Underground Space Technology*. 2011. 26. Pp. 51–61.
- Feldgun, V.R., Karinski, Y.S., Yankelevsky, D.Z. The effect of an explosion in a tunnel on a neighboring buried structure. *Tunnelling and Underground Space Technology*. 2014. 44. Pp. 42–55.
- De, A., Morgante, N., Zimmie, T.F. Numerical and physical modeling of geofoam barriers as protection against effects of surface blast on underground tunnels, *Geotextiles and Geomembranes*. 2016. 44. Pp. 1–12.
- DOD. *Structures to Resist the Effects of Accidental Explosions. Unified Facilities Criteria (UFC) 3–340–02*. Arlington, Virginia: Department of Defense, 2008.
- Zhang, Y, Chen, Y., Chen, S., Liu, H., Fu, Z. Experimental study on deformation of a sandy field liquefied by blasting. *Soil Dynamics and Earthquake Engineering*. 2019. 116. Pp. 60–68.
- DOD. *Fundamentals of Protective Design for Conventional Weapons. TM 5–855–1*. Arlington, Virginia. Department of Defense, 1986.

22. Larcher, M. Simulation of the Effects of an Air Blast Wave. JRC Technical Notes (JRC) 41337. Luxembourg: European Communities, 2007.
23. Kinney, G.F., Graham, K.J. Explosive Shocks in Air. Berlin, Germany: Springer-Verlag, 1985.
24. Krauthammer, T., Altenberg, A. Negative Phase Blast Effects on Glass Panels. International Journal of Impact Engineering. 2000. 24. Pp. 1–17.
25. Smith, P.D., Hetherington, J.G. Blast and Ballistic Loading of Structures. Oxford, England: Butterworth-Heinemann, 1994.
26. Wang, Z., Lu, Y., Bai, C. Numerical Analysis of Blast-Induced Liquefaction of Soil. Computers and Geotechnics. 2008. 35. 2. Pp. 196–209.
27. Ibrahim, Y., Nabil, M. Finite Element Analysis of Pile Foundations under Surface Blast Loads. 13th International Conference on Damage Assessment of Structures. Porto, Portugal, 2019. July 9–10.
28. Davies, M.C.R. Dynamic soil structure interaction resulting from blast loading. Proceeding of the International Conference on Centrifuge Modelling (Centrifuge 94). Singapore, 1994. Pp. 319–324.
29. De, A., Morgante, A.N., Zimmie, T.F. Numerical and physical modeling of geofoam barriers as protection against effects of surface blast on underground tunnels. Geotextiles and Geomembranes. 2016. 44. Pp. 1–12.
30. De, A., Zimmie, T.F. Centrifuge modeling of surface blast effects on underground structures Geotechnical Testing Journal. 2007. 30. Pp. 88–93.
31. Baziari, M.H., Shahnazari, H., Kazemi, H. Mitigation of surface impact loading effects on the underground structures with geofoam barrier: Centrifuge modeling. Tunneling and Underground Space Technology. 2018. 80. Pp. 128–142.
32. Gould, K.E. High explosive field tests: Explosion Phenomena and Environmental Impacts, DNA 6187F. 1981. Washington, DC: Defense Nuclear Agency.
33. NUREG/CR-7201: Characterizing Explosive, Effects on Underground Structures, Center for Nuclear Waste Regulatory Analyses. 2015. U.S. Nuclear Regulatory Commission Washington, DC 20555–0001.
34. Nagy, N., Mohamed, M., Boot, J.C. Nonlinear Numerical Modelling for the Effects of Surface Explosions on Buried Reinforced Concrete Structures. Geomechanics and Engineering. 2010. 2. Pp. 1–18.
35. Huang, T.K., Chen, W.F. Simple Procedure for Determining Cap-Plasticity-Model Parameters. Journal of Geotechnical Engineering. 1990. 116. 3. Pp. 492–513.
36. Chopra, A.K., Chakrabarti, P. The Koyna Earthquake and the Damage to the Koyna Dam, Bulletin of Seismological Society of America. 1973. 63. 2. Pp. 381–397.
37. Martin, O. Comparison of different Constitutive Models for Concrete in ABAQUS/Explicit for Missile Impact Analyses. JRC Scientific and Technical Reports. EUR 24151. European Commission, Joint Research Centre, Institute for Energy, 2010.
38. Johnson, G.R., Cook, W.H. Fracture characteristics of three metals subjected to various strains, strain rates, temperatures and pressures. Engineering Fracture Mechanics. 1985. 21. Pp. 31–48.
39. Jamil, Z.W., Guan, W.J., Cantwell, X.F., Zhang, G.S., Langdon G.S., Wang, Q.Y. Blast response of aluminum/thermoplastic polyurethane sandwich panels – experimental work and numerical analysis. International Journal of Impact Engineering. 2019. 127. Pp. 31–40.
40. Dassault Systems. ABAQUS/Standard; Theory Manual and Example Problems Manual; Release 6.12. Dassault Systems. Waltham, MA, USA, 2011.

Contacts:

Yasser Ibrahim, 00966553470474; yibrahim@vt.edu

Marwa Nabil, +201222694682; marwa_nabil_amin@yahoo.com

:

© Ibrahim, Y.E-H, Nabil, M., 2019



DOI: 10.18720/MCE.90.6

Behavior of two-way slabs subjected to drop-weight

R. Al-Rousan*

Jordan University of Science and Technology, Irbid, Jordan

* E-mail: rzalrousan@just.edu.jo

Keywords: engineering, materials science, technology, civil engineering, structural concrete

Abstract. Prediction of punching shear strength in RC two-way slabs with different fiber volume fractions, and freely drop weight heights (Impact load) is fundamental to propose structural design procedures for structures subjected to impact load. Moreover, the punching failure of two-way slabs subjected to impact can consider as a complex behavior in design. Thus, the punching shear capacity of reinforced concrete (RC) two-way slabs subjected to drop-weight impacts investigated in this paper by using Nonlinear Finite Element Analysis (NLFEA). Firstly, the simulated models were validated against fifteen RC slabs with Polypropylene Fiber (PF) volume (V_f) of 0, 0.3, 0.6, and 0.9 % and subjected to impact load at the height of 0, 1.2, and 2.4 m. Then, the simulated slabs were expanded to cover slabs not subjected to impact load (impact height (H_I) of 0 m) and slabs with V_f of 0 % to 1.2 % and subjected to impact load at the height of 1 m to 11m, resulting in a total of 182 RC slabs. The behavior of each slab evaluated in terms of the crack patterns, ultimate punching shear capacity, and deflection profile. The results showed that adding the PF at a dosage of 0.1 to 1.2 % by volume of concrete leads to significant enhancement in the overall structural behavior of the slabs and their resistance to impact loading. Attractively, after impact height of 10 m ($KE = 686.00$ J), the simulated RC slabs with PF volume fraction less than 0.7 % are failed. While all the simulated RC slabs subjected to impact load at the height of 11 m ($KE 754.26$ J) failed. Finally, NLFEA was also performed to provide a prediction for impact factor based on PF volume fraction and the impact load height.

1. Introduction

The response of reinforced concrete (RC) elements subjected to impact load is a hot topic in the previously published research work. Also, it still needs more elaboration to understand their complex behavior. This hot topic is significant especially in the area of RC nuclear facilities or military fortification structures that are used in high-hazard or high-threat applications as well as in the structures that are designed to resist the accidental impact loading due to falling rock and ship or vehicle collisions with offshore facilities, bridges, and buildings. Therefore, extensive work should be undertaken in an attempt to develop a design procedure for post-impact resistant and to improve the behavior of RC elements subjected to impact loads. Up to now, the establishing of empirical provisions for estimating the damage and structural capacity under specific impact loading is the most focused topic of the majority of the impact loading related research [1–8]. Nowadays two-way RC flat slabs can be considered as the excellent solution for residential, commercial, and office buildings because of the practical and economic issues such as the easy installation of electrical and mechanical infrastructures, the considerably simpler and reduced formwork, and faster site operations as well as the more comfortable and versatility space partitioning. Moreover, the punching failure considered as a complex behavior in the design of the RC two-way flat slab. Besides, the punching failure is typically brittle and considered as the ultimate load capacity of two-way RC slabs and can cause a sudden collapse of the entire structure [9–15].

Al-Rousan, R. Behavior of two-way slabs subjected to drop-weight. Magazine of Civil Engineering. 2019. 90(6). Pp. 62–71. DOI: 10.18720/MCE.90.6

Аль-Рушан Р. Поведение двухсторонних плит, подвергнутых падению груза // Инженерно-строительный журнал. 2019. № 6(90). С. 62–71. DOI: 10.18720/MCE.90.6



This open access article is licensed under CC BY 4.0 (<https://creativecommons.org/licenses/by/4.0/>)

Recently, utilizing fiber reinforced concrete has emerged as a practical approach for enhancing the performance of RC elements under impact loading. Numerous studies have shown that FRC elements (conventional steel reinforcing bars) demonstrate superior resistances to global impact behavior than local damage mechanism development and. As a result, acquire enhanced energy absorption capabilities under impact loading concerning RC elements [16]. Also, FRC is used to increase the punching shear capacity and the deformation capacity of RC flat slabs due to the capability of fibers in the bridging after the creation of the cracks [17, 18]. Based on the previous literature review, the punching shear strength of the RC two-way flat slabs after impact load omitted. Therefore, this paper presents the methodology and conclusions from a nonlinear finite element analysis (NLFEA) program in terms of the effect of impact load on the punching shear behavior of RC and polypropylene fiber reinforced (PFR) concrete two-way slabs. Highlighting was placed on assessing the impact of fiber volume fractions, and freely dropped weight heights on the RC two-way flat slab behavior in terms of ultimate load capacity, deflection profile, toughness or energy absorption as well as the mode of failure.

2. Methods

2.1. Description of the experimental program

The experimental program reported by Al-Rousan [19] included testing fifteen two-way reinforced concrete slabs as a simply supported system with an equally clear length and width of 1.0 m as well as slab thicknesses of 7 cm. The investigated parameters include the slab thicknesses, t_s (7 cm and 9 cm), fiber volume fractions (0 %, 0.3 %, 0.6 %, 0.9 %, and 1.2 %), and freely drop weight (10 cm in diameter and weighs 7 kg) heights, h_i (0, 1.2 m, and 2.4 m). The slabs reinforced with seven steel bars with a diameter of 5 mm in each direction which is equivalent to steel reinforcement ratios of 0.0018 and 0.0025 for the 9 cm and 8 cm slabs according to the ACI 318-14 Code. A dropped mass height of 1.2 m and 2.4 m represented impact velocity of 4.85 m/s and 6.86 m/s, respectively, as well as the kinetic energy of 82.32 J and 164.64 J, respectively.

The RC two-way slabs were tested firstly under impact load by using a special design setup consists of steel members with I-section joined together to provide a horizontal platform to give simply supported condition for the two-way slab. A steel ball of 7 kg mass with adjustable heights of 1.2 m to 2.4 m is allowed to fall freely through 150 mm in diameter hollow tube member placed vertically to stick the top surface of the tested two-way slabs at the center. After applying the impact load, all slabs tested as simply supported in both directions placed and were monotonically loaded up to failure using a hydraulic jack centrally positioned at the top of the slab. A square steel plate with a thickness of 50 mm and a side length of 200 mm was used to simulate the column with 200 mm sides. The applied load measured by using the load cell. Three linear variable differential transformers (LVDT) were placed at a specific location to measure the deflection profile of the tested slabs. Figure 1 shows the stress-strain diagrams for the concrete batches with different fiber volume fractions as well as the compressive strength, splitting tensile strength, and modulus of elasticity. Table 1 shows the results of tested slabs

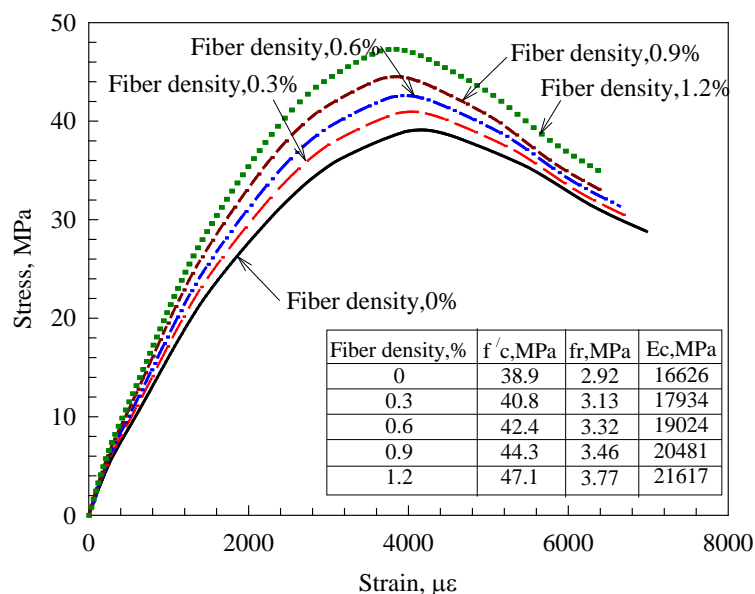


Figure 1. Stress-strain diagrams and mechanical properties of concrete [19].

2.2. Nonlinear Finite Element Analysis

Nonlinear finite element (NLFEA) is a very useful and efficient tool for the analysis of complex structures in terms of the significant savings in the time, cost of fabrication and experimental testing, changing any parameter, allowing for obtaining the stress and corresponding strain, as well as the load capacity and corresponding displacement at any location. Accordingly, the NLFEA program package (ANSYS) was used to simulate the actual behavior of the tested RC slabs (Table 1). Then NLFEA simulation models (Table 2) were expanded to provide a parametric study of 182 RC slabs in terms of PF volume fraction (0.0–1.2 %) and impact load height (0 (No Impact) to 11 m (Failure of all slabs)) or kinetic energy (68.69 J and 754.26 J), respectively.

Table 1. Specimens' details and tested [19] versus NLFEA results.

Slab	Percent of fibers by volume (V_f)	Height of the falling mass (H_i), m	Experimental- Ultimate punching shear load, kN	NLFEA-Ultimate punching shear load, kN
Sf0.0t0.07h0	0	None	88.9	88.9
Sf0.3t0.07h0	0.30 %		93.4	93.4
Sf0.6t0.07h0	0.60 %		96.1	96.1
Sf0.9t0.07h0	0.90 %		100.7	100.7
Sf1.2t0.07h0	1.2 %		108.4	108.4
Sf0.0t0.07h1.2	0	1.2	61.8	62.0
Sf0.3t0.07h1.2	0.30 %		67.8	68.4
Sf0.6t0.07h1.2	0.60 %		74.9	73.7
Sf0.9t0.07h1.2	0.90 %		83.0	81.1
Sf1.2t0.07h1.2	1.2 %		91.0	91.5
Sf0.0t0.07h2.4	0	2.4	58.1	58.1
Sf0.3t0.07h2.4	0.30 %		63.9	64.1
Sf0.6t0.07h2.4	0.60 %		70.4	69.2
Sf0.9t0.07h2.4	0.90 %		77.9	76.0
Sf1.2t0.07h2.4	1.2 %		85.5	85.8

Table 2. NLFEA RC slabs details and ultimate load capacity.

Impact Load	V_f , %														
	H_i , m	KE , J	0.0	0.1	0.2	0.3	0.4	0.5	0.6	0.7	0.8	0.9	1.0	1.1	1.2
0.0	0.00	88.9	91.0	92.4	93.4	94.3	95.1	96.1	97.3	98.8	100.7	102.9	105.5	108.4	
1.0	68.69	63.5	66.0	68.1	70.0	71.8	73.6	75.5	77.7	80.2	83.0	86.2	89.8	93.8	
1.2	82.33	62.0	64.5	66.5	68.4	70.1	71.8	73.7	75.9	78.3	81.1	84.2	87.7	91.5	
2.0	137.16	61.0	63.4	65.4	67.2	68.9	70.7	72.5	74.6	77.0	79.7	82.8	86.2	90.0	
2.4	164.71	58.1	60.4	62.4	64.1	65.7	67.4	69.2	71.1	73.4	76.0	78.9	82.2	85.8	
3.0	205.90	56.8	59.0	60.9	62.6	64.2	65.8	67.5	69.4	71.7	74.2	77.1	80.3	83.8	
4.0	274.13	52.9	55.0	56.7	58.3	59.8	61.3	62.9	64.7	66.8	69.1	71.8	74.8	78.1	
5.0	343.04	48.2	50.1	51.7	53.1	54.5	55.8	57.3	59.0	60.9	63.0	65.4	68.2	71.2	
6.0	411.27	43.5	45.2	46.7	48.0	49.2	50.4	51.8	53.2	54.9	56.9	59.1	61.6	64.3	
7.0	479.93	38.4	39.9	41.2	42.3	43.4	44.5	45.7	47.0	48.5	50.2	52.2	54.3	56.7	
8.0	548.63	29.3	30.4	31.4	32.3	33.1	33.9	34.8	35.8	37.0	38.3	39.7	41.4	43.2	
9.0	617.25	13.2	13.7	14.1	14.5	14.9	15.3	15.7	16.1	16.6	17.2	17.9	18.6	19.4	
10.0	686.00	F	F	F	F	F	F	F	0.9	2.4	4.2	6.5	9.1	11.9	
11.0	754.26	F	F	F	F	F	F	F	F	F	F	F	F	F	

Note: H_i : V_f : Percent of fibers by volume Impact load height, KE : Kinetic Energy, and F : Failure.

The SOLID65 element is capable of predicting the non-homogeneity, brittleness, and nonlinear behavior of concrete materials using a smeared crack approach with ultimate uniaxial tensile and compressive strengths (Figure 1). The detailed concrete properties in tension, compression, and modulus of elasticity are included earlier in Section 2.1. The Poisson's ratio is taken as 0.2. The shear transfer coefficient (β_t) taken as 0.8, which is nearly more than typical values for plain concrete since the fibers allow for the transfer of stress across the cracks. The efficiency of the PF in increasing the tensile and flexural strengths of the concrete based on the number and the orientation of PF per unit cross-sectional concrete area evaluated. The amount and orientation of PF per unit area were calculated based on the probability method proposed by Parviz and Lee [20]. LINK8 element was used to simulate the steel reinforcement bars with elastic-perfectly plastic behavior, Poisson's ratio of 0.3, yield strength of 460 MPa, and elastic modulus of 200 GPa. The Steel ball, steel plates at the loading and support locations were simulated using the SOLID45 element with linear elastic behavior; Poisson ratio and elastic modulus of 0.3 and 200 GPa, respectively.

Figure 2 shows the typical NLFEA meshing of the RC slab before and after the impact load. In NLFEA, the total applied load divided into a series of load steps or load increments. Newton-Raphson equilibrium iterations

provide convergence at the end of each load increment within tolerance limits equal five times the default tolerance limits of 0.5 % and 5 % for force and displacement checking to achieve the convergence of NLFEA solution.

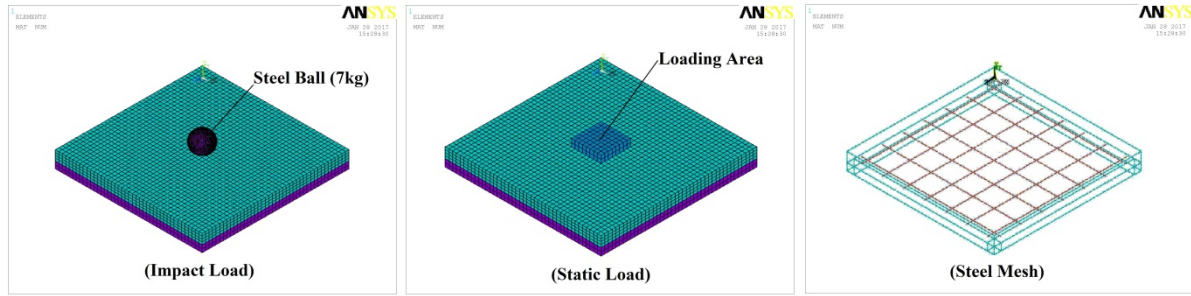


Figure 2. Typical finite element meshing of the RC slabs before and after impact.

3. Results and Discussion

3.1. Validation of NLFEA results

The tested RC slabs were simulated to validate the NLFEA, as shown in Table 2. The results from the experimental and NLFEA compared in terms of the load-deflection curves (Figure 3) and the ultimate load at failure (Table 2). Inspection of Figure 3 reveals that the NLFEA load-deflection curves had an excellent agreement with the experimental results. Moreover, Table 2 indicates that the NLFEA simulated RC slabs are very close to the tested ones in terms of the load-deflection behavior (Figure 3), ultimate load capacity (Table 2), and mode of failure (Figure 4).

For further illustration, the NLFEA models were expanded to cover the effect of PF volume fraction and impact load height or kinetic energy on the impact factor (b). Impact factor (b) calculated by dividing the ultimate load capacity of the slab subjected to impact load by the control slab (no impact) as shown in Table 3. Depending on the kinetic energy of the RC slabs having similar concrete compressive and tensile strength, Table 3 can be utilized to predict the required impact factor of a specific PF volume fraction. After an impact height of 10 m ($KE = 686.00$ J), the simulated RC slabs with PF volume fraction less than 0.7 % failed. While all the simulated RC slabs subjected to impact load at the height of 11 m ($KE 754.26$ J) failed.

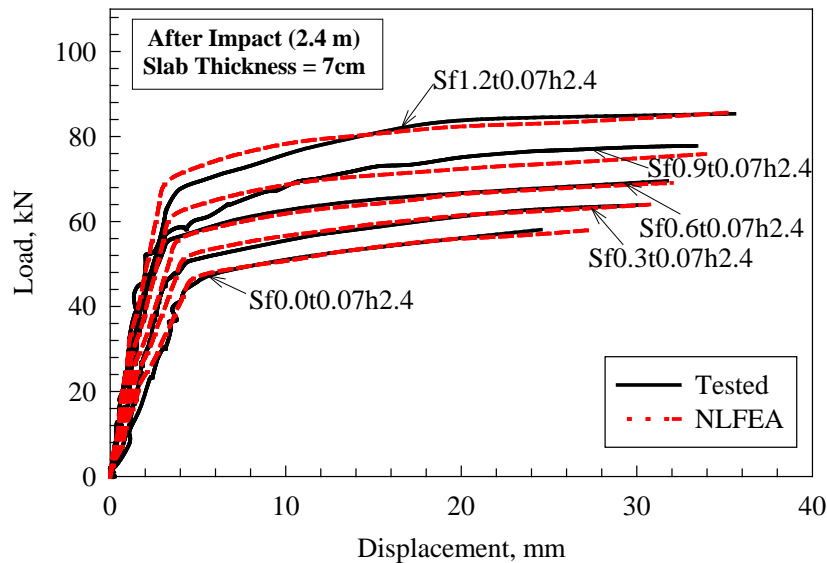
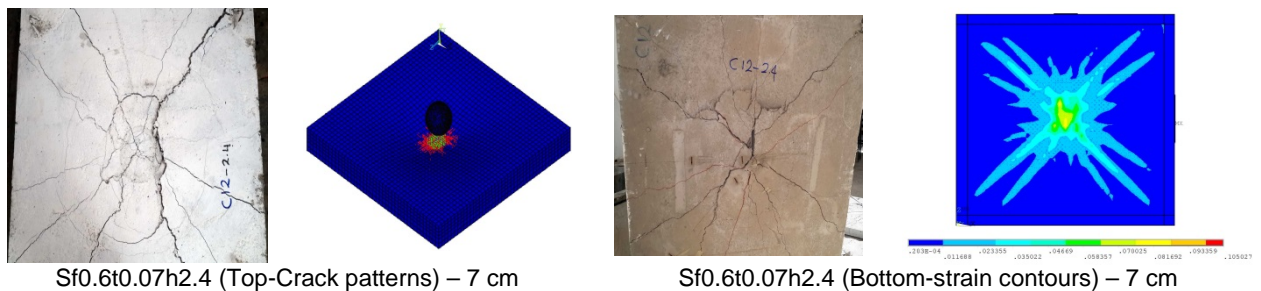


Figure 3. Typical tested [19] and NLFEA Load versus mid-span displacement curves.



Sf0.6t0.07h2.4 (Top-Crack patterns) – 7 cm

Sf0.6t0.07h2.4 (Bottom-strain contours) – 7 cm

Figure 4. Typical tested [19] and NLFEA results of RC slabs.

Table 3. Impact factor (b) using NLFEA.

Impact Load		<i>b</i>													
<i>H_i</i> , m	<i>KE</i> , J	0.0	0.1	0.2	0.3	0.4	0.5	0.6	0.7	0.8	0.9	1.0	1.1	1.2	
0.0	0.00	1.000	1.000	1.000	1.000	1.000	1.000	1.000	1.000	1.000	1.000	1.000	1.000	1.000	
1.0	68.69	0.714	0.726	0.738	0.749	0.762	0.774	0.786	0.799	0.812	0.825	0.838	0.852	0.866	
1.2	82.33	0.697	0.709	0.720	0.732	0.743	0.755	0.768	0.780	0.793	0.805	0.818	0.832	0.845	
2.0	137.16	0.686	0.697	0.708	0.720	0.731	0.743	0.755	0.767	0.779	0.792	0.805	0.818	0.831	
2.4	164.71	0.654	0.664	0.675	0.686	0.697	0.708	0.720	0.731	0.743	0.755	0.767	0.780	0.792	
3.0	205.90	0.638	0.649	0.659	0.670	0.680	0.691	0.703	0.714	0.725	0.737	0.749	0.761	0.773	
4.0	274.13	0.595	0.604	0.614	0.624	0.634	0.644	0.655	0.665	0.676	0.687	0.698	0.709	0.721	
5.0	343.04	0.542	0.551	0.560	0.569	0.578	0.587	0.597	0.606	0.616	0.626	0.636	0.646	0.657	
6.0	411.27	0.489	0.497	0.505	0.513	0.522	0.530	0.539	0.547	0.556	0.565	0.574	0.584	0.593	
7.0	479.93	0.432	0.439	0.446	0.453	0.460	0.468	0.475	0.483	0.491	0.499	0.507	0.515	0.523	
8.0	548.63	0.329	0.334	0.340	0.345	0.351	0.357	0.362	0.368	0.374	0.380	0.386	0.393	0.399	
9.0	617.25	0.148	0.151	0.153	0.155	0.158	0.160	0.163	0.166	0.168	0.171	0.174	0.177	0.179	
10.0	686.00	<i>F</i>	0.009	0.024	0.042	0.063	0.086	0.110							
11.0	754.26	<i>F</i>													

Note: *H_i*: *b*: Impact factor, *KE*: Kinetic Energy, and *F*: Failure.

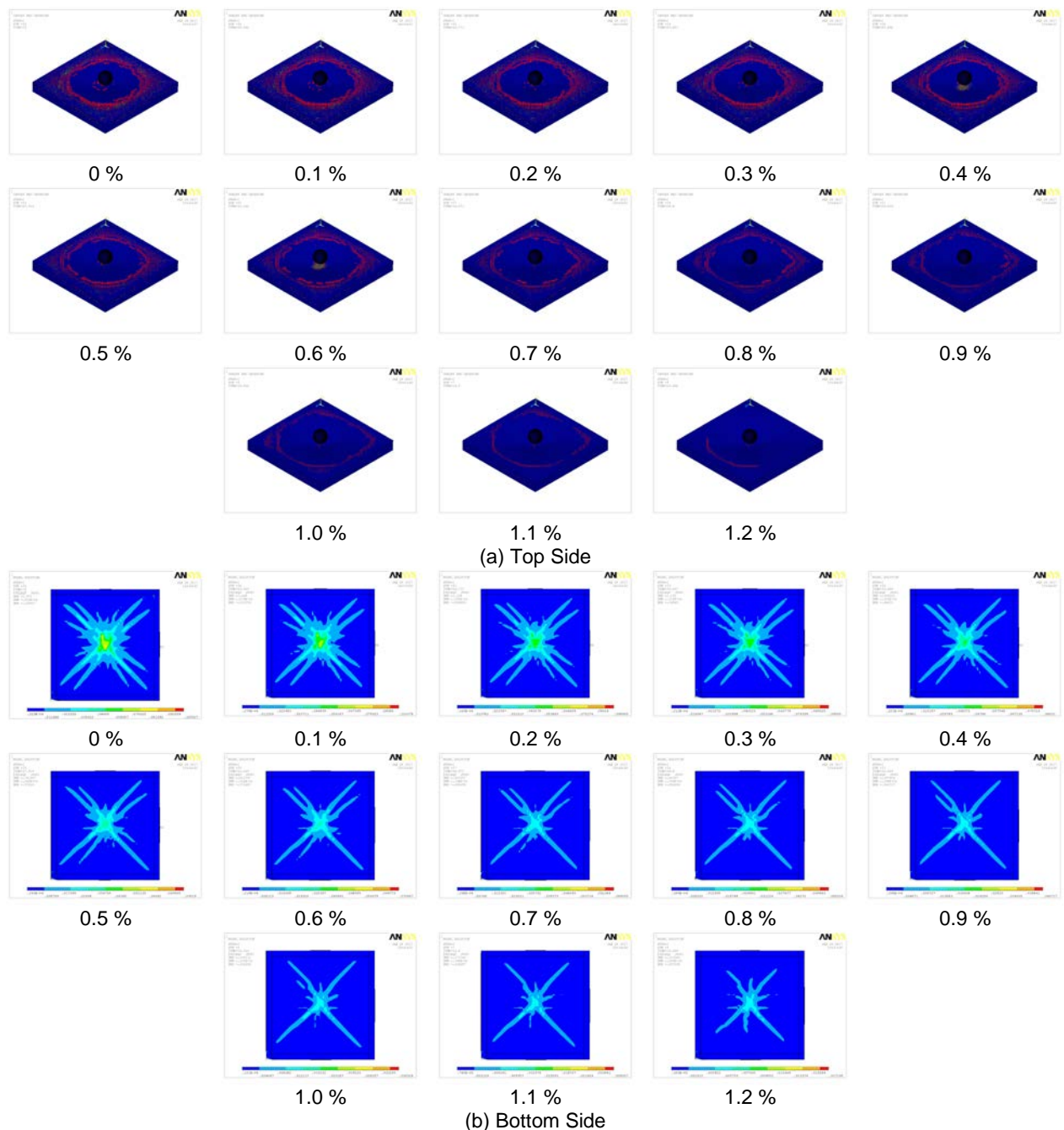


Figure 5. Typical crack patterns of the simulated models.

3.2. Mode of failure

Based on the NLFEA results, all simulated slabs failed in the punching shear mode, and flexural cracks started from the loading steel plate and extended until the edges of the tested slab. Punching shear mode of failure was a brittle that occurred near the loading steel plate (compression face or top surface) at the ultimate failure load. Followed by the development of a punching shear failure cone at the tensile face (Bottom surface). Figure 5 shows the typical punching shear failure on the compression face and tensile face. Inspection of Figure 5 shows that slabs subjected to impact had more flexural cracks and large punching shear cone than slabs not subjected to impact. Besides, Figure 5 shows the increase of fiber volume decreased the number of flexural cracks and the size of the punching shear cone. Because the fibers resist the applied forces until the fibers were pulled out from the concrete. Additionally, the occupation of fibers in stretching the failed bottom surface (tension face) of the slab away from the loading steel plate thus increased their punching shear capacity.

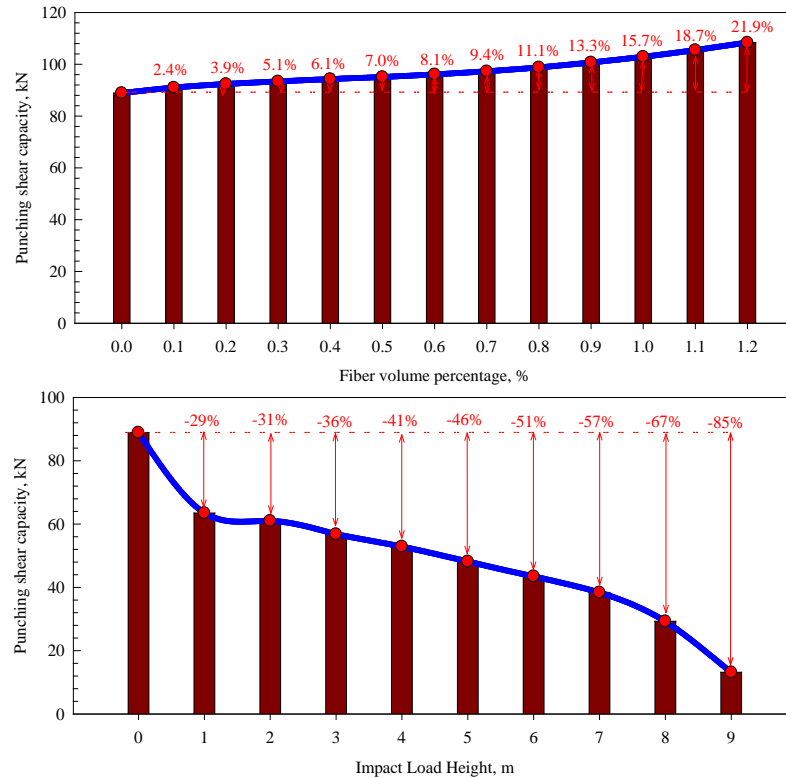


Figure 6. Effect of fiber volume percentage and impact load height on punching shear load.

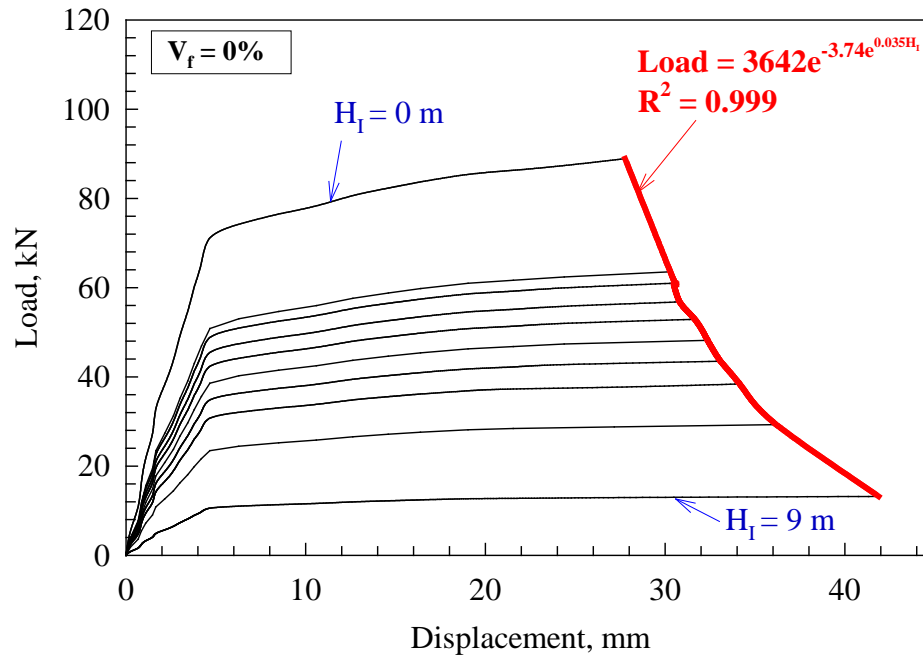
3.3. Ultimate load capacity

Table 2 and Figure 6 show the summarized results and the effect of fiber volume percentage and impact load on the punching shear load of the tested slabs. Inspection of Figure 6 reveals that the ultimate punching shear capacity of control slab (slabs not subjected to impact) generally increases. Also, the degradation in slab strength due to impact load decreases with the increasing fiber volume percentage. Adding V_f in 0.1 to 1.2 % by volume fraction increased the ultimate punching capacity for slab without V_f by about 2.4 to 21.9 %, respectively. Also, the impact load at the height of 1 m to 9 m created degradation in the ultimate punching shear capacity of 29 % to 85 %, respectively. As well as the efficiency of fiber in absorbing of impact load or decreasing the ultimate load capacity degradation increased with the increasing of V_f percentage.

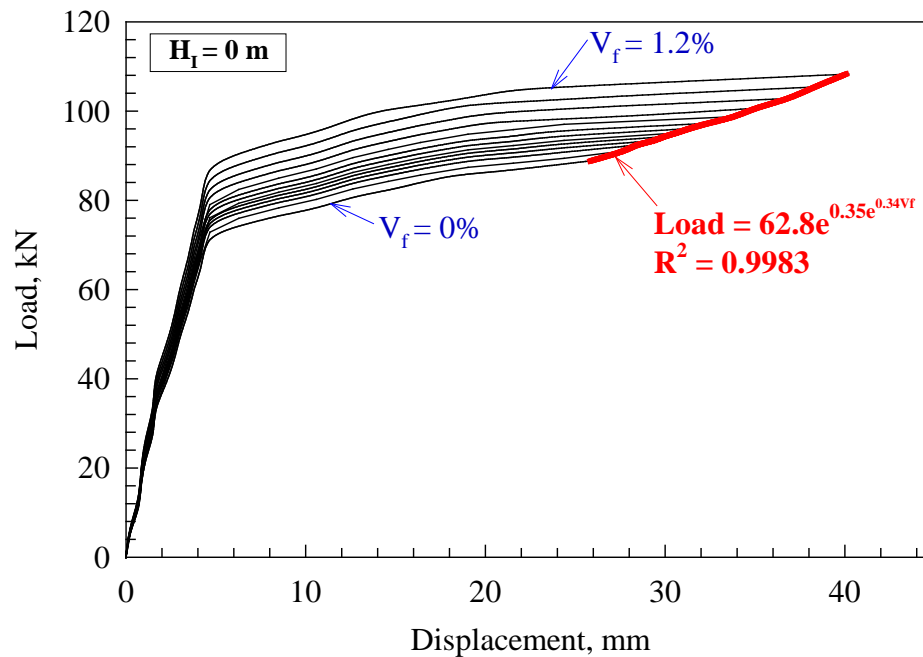
3.4. Load deflection behavior

Figure 7 shows the effect of the impact load and fiber volume on the load-displacement behavior, stiffness, and toughness. The stiffness defined as the slope of the curve from the initiation of the first crack (reaching the tensile strength of the concrete) to the displacement equal to 3 mm. The toughness defined as the area under the load-displacement behavior. The load-displacement behavior can be divided into two stages based on the crack growth and the shape of the load-displacement behavior, as shown in Figure 7. In the first stage (zero loadings to load at which the displacement equal to 3 mm), the behavior is approximately elastic liner before the initiation of the first crack (which is located at the center of the slab and close to the loading steel plate) and caused a reduction in the stiffness of the curve. Then, in the second stage, the stiffness was reduced suddenly, followed by the development of the punching shear cone. Inspection of Figure 7 reveals that the impact load height caused a higher reduction in stiffness and in toughness to control slab (no impact load) than fiber volume percentage. Besides, Figure 7 shows that the stiffness and toughness generally increase with the increasing fiber volume percentage. The adding of PFR assists in delaying and resisting the formulation and expanding of cracks, thus slab stiffness and toughness are

enhanced. Also, Figure 7 shows the proposed equation for predicting ultimate load capacity in terms of impact load height (Figure 7(a)) and fiber volume percentage (Figure 7(b)).



(a) Effect of impact load height (H_I)



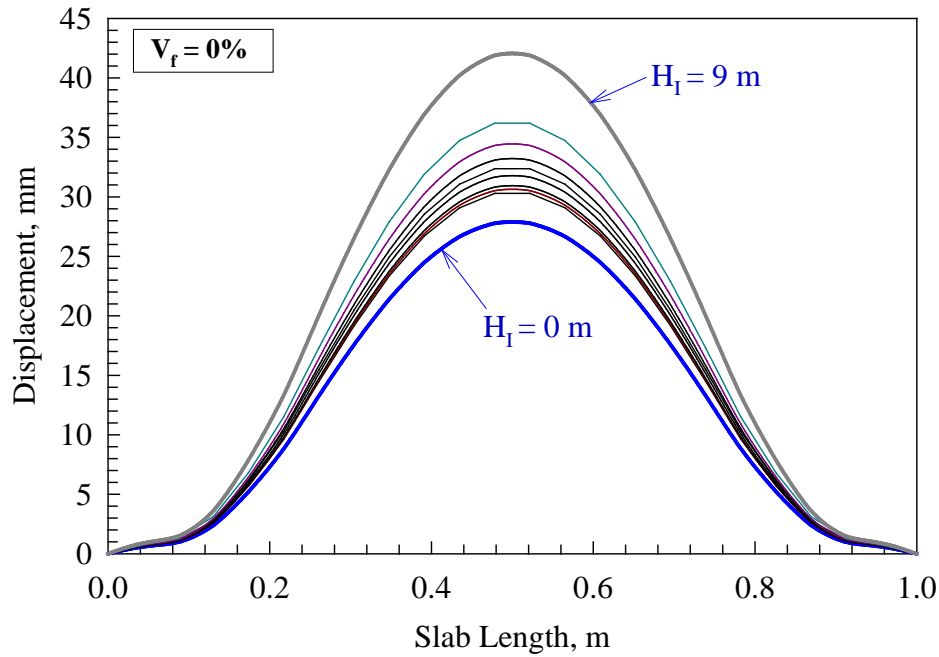
(b) Effect of fiber volume (V_f)

Figure 7. Typical load versus displacement curves.

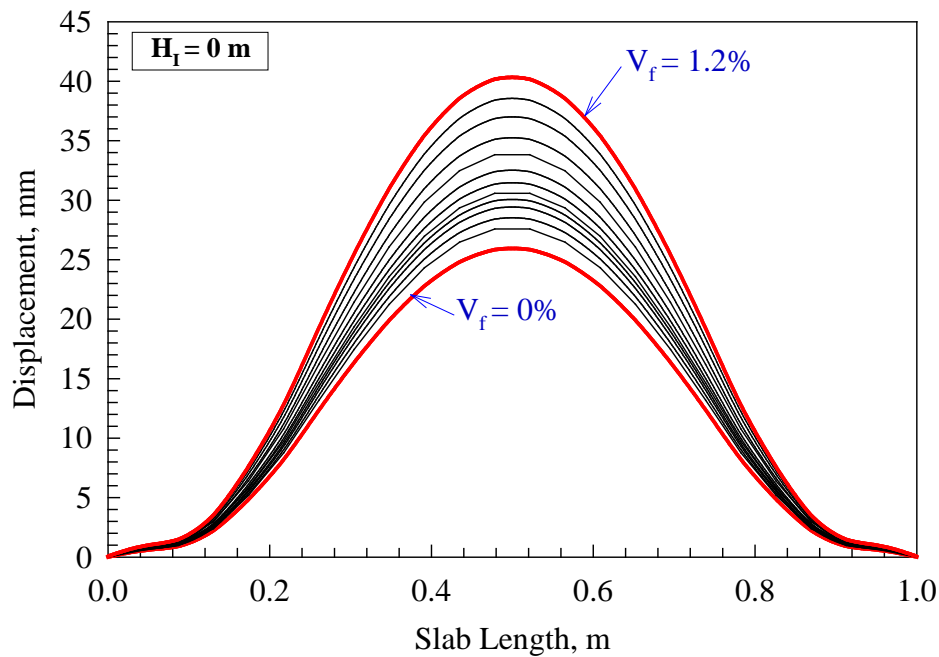
3.5. Deflection profile

Assessment of the displacement profile of the simulated slabs provides further information (quantitative measure) on the topic of the effect of tested parameters (Figure 8). The global structural behavior that is not directly obvious from studying the load-displacement behavior and ultimate mid-point displacement. Figure 8 shows the effect of the impact load and fiber volume on the displacement profile. Inspection of Figure 8 reveals that the impact load had the highest displacement profile, specifically at the mid-point comparing with the impact load at the lowest height. This mode of failure is observed the same in slabs subjected to impact at a higher height had more flexural cracks and large punching shear cone than slabs subjected to impact at the lowest height. While the displacement at the quarter-point is almost equal for both impact heights. It is seen that the PFR was successful in justifying the growth of localized failures in terms of the number of flexural cracks and the size of the punching shear cone. The PFR slabs exhibited displacement profile in which

displacement was more consistently distributed and, as a result, we're able to achieve more extensive displacement profile at failure.



(a) Effect of impact load height (H_I)



(b) Effect of fiber volume (V_f)

Figure 8. Typical displacement shapes,

3.6. Punching shear model for two-way RC slabs subjected to impact load

An empirical model was proposed to predict the punching shear strength of two-way RC slabs subjected to impact load as a function of tested parameters. Most models founded in the literature and design codes base their verifications on a critical section to find the punching shear strength of non-impacted RC slabs without shear reinforcement [9–20]. Equation (1) shows the ACI 318-14 expression for circular or square columns of two-way slab moderate relative to the concrete compressive strength and thickness of the slab.

$$V_R = 0.33b_o d \sqrt{f'_c}, \quad (1)$$

where V_R is the punching shear capacity of two-way slabs at critical section located at $d/2$ from the face of the square or circular column;

d is the effective depth of the slab;

f'_c is the concrete compressive strength at 28 days;

b_o is the perimeter of the critical section.

Based on the above equation, Equation (2) can be used to describe the punching shear capacity of RC two-way slabs subjected to impact with some modifications as following:

$$V_R = \alpha \beta b_o d \sqrt{f'_c}, \quad (2)$$

where α and β is a factor accounting for fiber volume fraction and impact load effects, respectively. Based on the regression analysis of the RC two-way slabs not subjected to impact load ($\beta = 1$) as shown in Figure 9 [19], Equation (3) presents the relationship between the fiber volume fraction and α factor.

$$\alpha = 0.321e^{0.1523V_f}, \quad (3)$$

where V_f is the fiber volume fraction percentage. Based on the analysis of the RC two-way slabs subjected to impact load Table 3 shows the β factor based on impact height and fiber volume fraction percentage. Thus the punching shear strength of the RC two-way slabs subjected to impact can be defined by the following equations

$$V_R = (0.321\beta e^{0.1523V_f}) b_o d \sqrt{f'_c}. \quad (4)$$

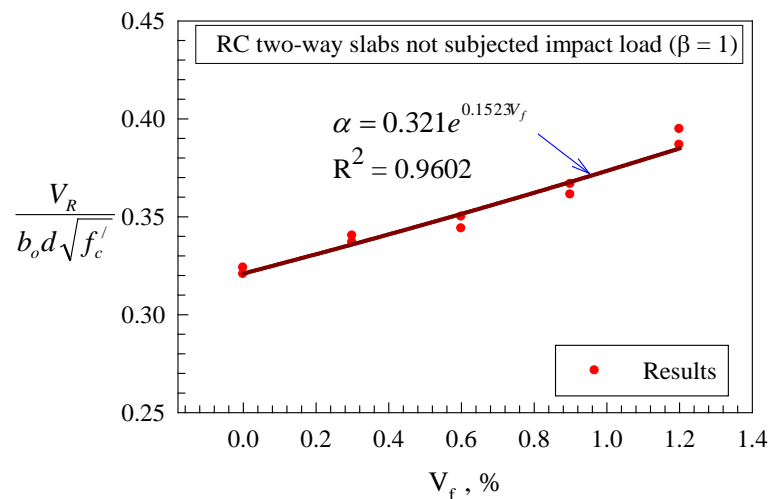


Figure 9. Relationships between fiber volume fraction percentage (V_f) and α factor for RC two way slabs not subjected impact load [19].

4. Conclusions

1. The increase in impact load and the fiber volume increased the number of flexural cracks and the size of the punching shear cone.

2. Adding fiber volume in 0.1 to 1.2 % by volume fraction enhanced the ultimate punching capacity with 2.4 to 21.9 % while the impact load at the height of 1 m to 9 m created degradation in the ultimate punching shear capacity of 29 % and 85 %.

3. After an impact height of 10 m, the simulated RC slabs with PF volume fraction less than 0.7 % failed. While all the simulated RC slabs subjected to impact load at the height of 11 m failed.

4. Based on innovative NLFEA verified with the experimental results, the impact factor (β) proposed for predicting the ultimate punching shear capacity of RC slabs at specific PF volume and kinetic energy.

5. Acknowledgments

The author acknowledges the technical support provided by the Jordan University of Science and Technology.

References

1. Kennedy, R.P.A. Review of Procedures for the Analysis and Design of Concrete Structures to Resist Missile Impact Effects. *Nuclear Engineering and Design*. 1976. 37(2). Pp. 183–203. DOI: 10.1016/0029-5493(76)90015-7.
2. Kishi, N., Mikami, J. Empirical Formulas for Designing Reinforced Concrete Beams under Impact Loading. *ACI Structural Journal*. 2012. 109(9). Pp. 509–519. DOI: 10.14359/51683870
3. Chen, Y., May, I.M. Reinforced Concrete Members under Drop Weight Impacts. *Proceedings of the Institution of Civil Engineers Structures and Buildings*. 2009. 162(1). Pp. 45–56. DOI: 10.1680/stbu.2009.162.1.45.
4. Hughes, G. Hard Missile Impact on Reinforced Concrete. *Nuclear Engineering and Design*. 1984. 77(1). Pp. 23–35. DOI: 10.1016/0029-5493(84)90058-X.
5. Sawamoto, Y., Tsubota, H., Kasai, Y., Koshika, N., Morikawa, H. Analytical Studies on Local Damage to Reinforced Concrete under Impact Loading by Discrete Element Method. *Nuclear Engineering and Design*. 1998. 179(2). Pp. 157–177. DOI: 10.1016/S0029-5493(97)00268-9.
6. Li, Q.M., Reid, S.R., Wen, H.M., Telford, A.R. Local Impact Effects of Hard Missiles on Concrete Targets. *International Journal of Impact Engineering*. 2005. 32(1–4). Pp. 224–284. DOI: 10.1016/j.ijimpeng.2005.04.005.
7. Saatci, S., Vecchio, F.J. Effects of Shear Mechanisms on Impact Behavior of Reinforced Concrete Beams. *ACI Structural Journal*. 2009. 106(1). Pp. 78–86. DOI: 10.14359/56286
8. Zamaliev, F.S., Zakirov, M.A. Stress-strain state of a steel-reinforced concrete slab under long-term. *Magazine of Civil Engineering*. 2018. 83(7). Pp. 12–23. DOI: 10.18720/MCE.83.2.
9. Tohid, Mousavi, Erfan, Shafei. Impact response of hybrid FRP-steel reinforced concrete slabs. *Structures*. 2019. 19. Pp. 436–448. DOI: 10.1016/j.istruc.2019.02.013.
10. Mastali, M., Ghasemi Naghibdehi, M., Naghipour, M., Rabiee, S.M. Experimental assessment of functionally graded reinforced concrete (FGRC) slabs under drop weight and projectile impacts. *Construction and Building Materials*. 2015. 95. Pp. 296–311. DOI: 10.1016/j.conbuildmat.2015.07.153.
11. Yilmaz, Tolga, Kirac, Nevzat, Anil, Özgür, Erdem, R. Tuğrul, Sezer, Ceyda. Low-velocity impact behaviour of two way RC slab strengthening with CFRP strips. *Construction and Building Materials*. 2018. 186. Pp. 1046–1063. DOI: 10.1016/j.conbuildmat.2018.08.027.
12. Wenjie, Wang, Nawawi, Chou. Experimental and theoretical studies of flax FRP strengthened coconut fibre reinforced concrete slabs under impact loadings. *Construction and Building Materials*. 2018. 171. Pp. 546–557. DOI: 10.1016/j.conbuildmat.2018.03.149.
13. Kumar, Vimal, Iqbal, M.A., Mittal, A.K. Impact resistance of prestressed and reinforced concrete slabs under falling weight indenter. *Procedia Structural Integrity*. 2017. 6. Pp. 95–100. DOI: 10.1016/j.prostr.2017.11.015.
14. Lorena, Francesconi, Luisa, Pani, Flavio, Stochino. Punching shear strength of reinforced recycled concrete slabs. *Construction and Building Materials*. 2016. 127. Pp. 248–263. DOI: 10.1016/j.engstruct.2015.09.010
15. Micael M.G. Inácio, André F.O. Almeida, Duarte M.V. Faria, Válder J.G. Lúcio, António Pinho Ramos. Punching of high strength concrete flat slabs without shear reinforcement. *Engineering Structures*. 2015. 103. Pp. 275–284. DOI: 10.1016/j.engstruct.2015.09.010.
16. Zhang, J., Maalej, M., Quek, S.T. Performance of Hybrid-Fiber ECC Blast/Shelter Panels Subjected to Drop Weight Impact. *Journal of Materials in Civil Engineering*. ASCE. 2007. 19(10). Pp. 855–863. DOI: 10.1061/(ASCE)0899-1561(2007)19:10(855).
17. Cheng, M.Y., Parra-Montesinos, G.J. Evaluation of steel fiber reinforcement for punching shear resistance in slab-column connections – Part I: Monotonically increased load. *ACI Structure Journal*. 2010. 107(1). Pp. 101–109. DOI: 10.14359/51663394.
18. Maya, L.F., Fernández Ruiz, M., Muttoni, A., Foster, S.J. Punching shear strength of steel fibre reinforced concrete slabs. *Engineering Structures*. 2012. 40. Pp. 83–94. DOI: 10.1016/j.engstruct.2012.02.009.
19. Al-Rousan, R.Z. Failure Analysis of Polypropylene Fiber Reinforced Concrete Two-Way Slabs Subjected to Static and Impact Load Induced by Free Falling Mass. *Latin American Journal of Solids and Structures*. 2018. 15(1). Pp. e19. DOI: 10.1590/1679-78254895.
20. Parviz, S., Cha-Don, L. Distribution and orientation of fibers in steel fiber reinforced concrete. *ACI Materials Journal*. 1990. 87(5). Pp. 433–439. DOI: 10.14359/1803.

Contacts:

Rajai Al-Rousan, +962799887574; rزالrouسان@just.edu.jo

© Al-Rousan, R., 2019



DOI: 10.18720/MCE.90.7

Resistance of cement stone in sanitation solutions

V.V. Strokovna, V.V. Nelubova*, M.D. Rykunova

V.G. Shukhov Belgorod State Technological University, Belgorod, Russia

** E-mail: nelubova@list.ru*

Keywords: concrete construction, cements, corrosion, biodegradation, chemical attack, acid resistance

Abstract. Biological corrosion is a type of effect that influences almost all possible construction projects. The primary measures for its prevention include sanitary and preventive work carried out using various chemicals. The shortcoming of buildings chemical treatment is the degradation effect on building composites with a significant reduction in the life of structures. The subject of the study was presented by the aggressive effect degree of sanitation treatment on various compositions of cement stone assessment. During the research Portland cement and aluminous cement, samples were exposed in two mediums – reagent solution (experimental medium) and tap water (control medium). The degree of medium influence on the cement stone samples was estimated according to the data on the main physic and chemical parameters of the process and phase-structural transformations of the stone after aging in an aggressive environment. There was an increase in the strength of samples after 6 months of exposure both for Portland cement stone and aluminous cement stone compared to the samples aged in pure water and original samples without exposure that showed the absence of the degradation effect of decontamination solution on the cement stone. The increase in the strength of materials occurred due to the intensification of carbonization processes in the sanitation agent medium resulting in the mud injection of pores and voids due to the crystallization of insoluble calcium carbonates. It was confirmed by the compaction of the micro-structure of cement stone expressed by the increase in the mass of samples and the total concentration of carbonate compounds in the volume of the material after 6 months of exposure.

1. Introduction

A significant increase of industrial impact on ecosystem associated with urbanization makes it necessary to monitor and control the process in terms of the harmful effects of production on the environment, as well as the degradation of buildings and structures as a result of the influence of various factors [1–6].

The corrosion of building materials, in the surroundings of which a person spends up to 80 % of his life, is one of the main problems in the context of the globalization of technological development. This is primarily due to the increase in the number of industrial enterprises; frequent disregard of building regulations in the process of waterproofing of certain parts of buildings and structures; the lack of proper ventilation. Biological corrosion is a type of effect that influences almost all possible construction objects [7–15]. At the same time it is obvious that in the case of agricultural enterprises, the problem of structural degradation as a result of the life of living organisms is especially acute, since it is aggravated by the annual increase in the number of farms and production facilities, as well as the number of various livestock farms.

Nowadays, the problem of biological deterioration of buildings and structures of the enterprises of agro-industrial complex is being solved using sanitary and preventive measures. This process covers a whole range of measures for the rehabilitation of buildings, in particular, disinfection, desinsection and disacidification, cleaning the area around an enterprise, as well as preventive treatment of equipment. The measures for the disinfection of buildings are planned in advance by zoo engineers in accordance with the technological map of livestock movement.

Strokovna, V.V., Nelubova, V.V., Rykunova, M.D. Resistance of cement stone in sanitation solutions. Magazine of Civil Engineering. 2019. 90(6). Pp. 72–84. DOI: 10.18720/MCE.90.7

Строкова В.В., Нелубова В.В., Рыкунова М.Д. Стойкость цементного камня в растворах санационных средств // Инженерно-строительный журнал. 2019. № 6(90). С. 72–84. DOI: 10.18720/MCE.90.7



This open access article is licensed under CC BY 4.0 (<https://creativecommons.org/licenses/by/4.0/>)

Despite the existing variety of methods for the control of pathogenic micro-flora (physical, mechanical, chemical, biological, as well as mixed), chemical methods are the most widely used. They include the use of substances of various compositions that provide a detrimental effect on pathogenic microorganisms [16–20]. It is necessary to note that the use of chemical control methods, despite obvious advantages (almost complete destruction of pathogenic micro-flora), is associated with significant disadvantages, since frequent surface treatment of structural elements of buildings and structures with caustic substances leads to their degradation due to the destruction under the influence of aggressive acids, leaching of soluble substances. As a result it leads to the formation of additional porosity of materials, micro-cracks and the development of various microorganisms on a surface.

The compliance with high-quality sanitary and prophylactic measures is an important part of technological process for the effective functioning of livestock, poultry, animal husbandry and crop production enterprises. The experience of the operation of enterprises of this type, characterized by a variety of technological features of production, showed that the existing set of measures to maintain the cleanliness of buildings does not provide the necessary degree of sterility, which allows reliable (in an adequate measure) prevention of «biological fatigue» of materials and structures.

It is necessary to note that in the development of building composites of increased durability, the tests in most cases are limited to studying the effects of biological corrosion on the properties of a composite [21–25], however, according experimental data on the influence of natural conditions on the properties and structural characteristics of cement stone, the authors revealed that microorganisms do not have time to fully form in bulk structures and on the surface of a material during the inter-recovery period, characterized by short periods of time [26, 27]. This approach shows that building composites of agricultural objects are more affected by the means used for processing of buildings than by the effects of bio-corrosion agents (bacteria and filamentous fungi, algae in some cases). In this regard, the assessment of the impact and contribution of each type of effect is an important task for the development of methods for prolonging the resistance and stability of materials and building objects as a whole.

According to the above mentioned aspects, the purpose of this study was to assess the impact of sanitation treatment (chemical corrosion) on the change in the physic and mechanical characteristics of cement stone of various compositions and its phase-structural transformations when simulating actual operating conditions.

2. Methods

Portland cement was used as the most spread and studied binder, as well as alumina cement with an initial higher corrosion resistance in relation to certain types of exposure. The researchers used Portland cement CEM I 42.5 N produced by Belgorodsky Cement Enterprise Belgorod, Belgorod Oblast, Russia) and GZ-50 aluminous cement produced by the Pashiiski Metallurgical Cement Plant (Pashiiia, Perm Region, Russia). Mineralogical and chemical composition are given in tables 1–4.

Table 1. Chemical composition of Portland cement clinker.

The content of oxides, wt. %								
CaO	SiO ₂	Al ₂ O ₃	Fe ₂ O ₄	CaO _{св}	SO ₃	MgO	R ₂ O	loss on ignition
65.22	21.48	4.75	4.35	0.20	1.87	0.43	0.20	1.5

Table 2. Mineralogical composition of Portland cement clinker.

Minerals, %			
C ₃ S	C ₂ S	C ₃ A	C ₄ AF
65.2	15.1	6.0	13.7

Table 3. Chemical composition of aluminous cement.

The content of oxides, wt. %				
CaO	SiO ₂	Al ₂ O ₃	Fe ₂ O ₃	other
40.5	10.4	40.10	2.65	6.35

Table 4. Mineralogical composition of aluminous cement.

Minerals, %			
CA	C ₂ AS	C ₁₂ A ₇	other
40	38	10	12

The compositions based on the investigated binders were prepared using a Matest E095 laboratory mortar mixer. The weigh-in of the components of the binder was carried out on an electronic weighting unit

with an accuracy of 0.01 g. All the samples were made in metal forms, pre-lubricated with a thin layer of machine oil. The cube samples were formed with an edge size of 20 mm based on Portland cement and alumina cement at a water-cement ratio of 0.3.

For the research of simulation media for each type of cement, 2 batches of sample cubes were formed with 6 cubes for each series of tests: 5 simulation media and 6 months of sample exposure. The cement stone samples that hardened for 28 days were obtained for control. Thus, 84 samples were molded for each type of cement.

After laying in the molds, the samples based on Portland cement hardened for 1 day in a bath with a hydraulic shutter in the molds, then they were redressed and continued to harden for 27 days under the same conditions.

In the case of aluminous cement, after production the molds with the samples were stored for (6 ± 0.5) hours in air-wet conditions at a relative humidity of 90 %, then they were placed in a bath with water. After (24 ± 2) hours from the time of production, the molds were removed from the water, the samples were formed and placed in a bath with water and stored in it for 90 days before the experiment. The period of 90 days was chosen in order to wait for the completion of the process of recrystallization of metastable phases into stable ones.

At the end of hardening process, the samples in the amount of 6 pieces from each type of binder were tested using a PGM-100 hydraulic press, the remaining samples were exposed in simulation media and tested for strength every month.

The researchers used as simulation media the following:

- Piped water. This series of samples was evaluated as control compositions for Portland cement and aluminous samples, respectively (pH = 6.8);

- An aqueous solution of a disinfectant used for the treatment of buildings during the rehabilitation of facilities of the Aldecol DEZ 25 (Germany) agricultural complex, which included: glutaric dialdehyde 12.5 %, formaldehyde 9.5 %, alkyl-dimethyl-benzyl-ammonium chloride 5 %, methanol up to 2.5 %. This product had the 3rd class of hazard and was water soluble. For research, the authors used a solution with an active substance concentration of 0.5 % (pH = 7.09), which corresponded to the recommendations of a producer.

The samples were placed in glass desiccators with a tight lid. They were arranged in such a way that all the faces of the cube were in contact with the simulation medium (Figure 1). For this purpose, a polyethylene net was placed between the samples. During the experiment, desiccators were kept closed and opened once a month for sampling and updating the simulation medium. At the same time the composition of simulation medium was updated every month, thus the medium had constant aggressive effect on the investigated samples.



Figure 1. System for laboratory exposure of samples in model environments.

The testing in all model media was simultaneous and lasted for 6 months, with sampling in order to control such parameters as: pH of the medium, appearance, mass variation, compressive strength, chemical resistance of samples, micro-structural and phase transformations of cement stone.

The pH of aqueous solutions was determined using an OYSTER-16 pH meter. The determination of the pH of the contents of each desiccator (simulation medium solution) was carried out by measuring the pH of the solution before immersion of the samples and after each month of exposure.

The degree of influence of the medium on cement stone was estimated according to the data on mass variation (defined in percents as the difference between the initial and final mass, referred to the initial mass of the sample), as well as the chemical resistance coefficient (the ratio of the strength of samples exposed in a simulation medium to the strength samples aged in piped water).

The analysis of micro-structural changes was carried out monthly throughout the experiment using a TESCAN MIRA 3 LMU high resolution scanning electronic microscope. The microstructure of all compositions was studied by analyzing a representative sample of images, by scanning the entire surface of the sample at magnifications of 200 to 50000 times, with a direct description during shooting. For the subsequent demonstration of the research results, the authors surveyed the areas typical for morpho-structure at identical magnifications for each sample: 350; 5000; 15000; 36000 times.

The phase composition of the initial and aggressive samples was evaluated using an ARL X'TRA X-ray diffractometer. Shooting conditions were: $CuK\alpha$ radiation, interval of diffraction angles $2\theta = 4-64^\circ$, scan step 0.02° , pulse acquisition time – 1.2 sec.

The method of full-profile quantitative X-ray diffraction analysis was used as the main analytical tool for the diagnosis and quantitative determination of weight concentrations of crystalline mineral formations in binders.

Full-profile quantitative X-ray diffraction analysis was performed using the DDMv.1.95e program in the DDM-algorithm version (Derivative Difference Minimization). The advantages of using this algorithm in the calculated full-profile procedures is that there is no need to clarify the parameters of the background line of the X-ray patterns.

During quantitative full-profile X-ray diffraction analysis of Portland cement stone, the main minerals of Portland cement clinker, as well as uniquely diagnosed minerals that reveals its hydration, were examined. For this, the following structural models were used from the structural data base of inorganic substances ICSD: alite (Ca_3SiO_5 triclinic) – 4331-ICSD, belite ($\beta-Ca_2SiO_4$) – 81096-ICSD, brownmillerite (C_4AF) (9197-ICSD), portlandite ($Ca(OH)_2$) – 202233-ICSD, calcite ($CaCO_3$) – 16710-ICSD and ettringite – 90823-ICSD.

For a quantitative calculation of the mineral composition, the phases with known crystal lattice parameters, characterized by a constant composition, were chosen. Therefore, C-S-H phases, which differed in inconsistent composition, did not participate in the calculations, which did not indicate their absence in the hydrated cement stone.

The following structural models from the structural data base of inorganic substances ICSD were used to obtain proved ideas about the mineral composition of samples of aluminous cement stone: CA (260-ICSD), CA_2 grossite (16191-ICSD), $C_{12}A_7$ mayenite (29212-ICSD), CA_6 gibonite 5H (34394-ICSD), $Ca_2MgSi_2O_7 - Ca_2Al_2SiO_7$ ackermanite-gelenite (67689-ICSD), $CaMg[CO_3]_2$ dolomite (31334-ICSD), $\beta-C_2S$ (81096-ICSD), $\alpha-C_2S$ (82997-ICSD), $CaSiO_3$ wollastonite 2M (201538-ICSD), $CaTiO_3$ perovskite (62149-ICSD). As structural models of hydrated phases the authors used: CAH_{10} (407150-ICSD), C_3AH_6 (66274-ICSD) and AH_3 gibbsite (6162-ICSD).

3. Results and Discussion

According to the results of a visual assessment of the appearance of cement stone samples aged in a 0.5 % Aldecol solution, it is possible to conclude that the medium has a slight effect on the change in color, surface and other attributes of both Portland cement (Figure 2, a) and aluminous stone (Figure 2, b). The solution of Aldecol was washed, as a result of which a thin white film was seen on the samples, which was easily erased upon contact with the sample (soapy coat).

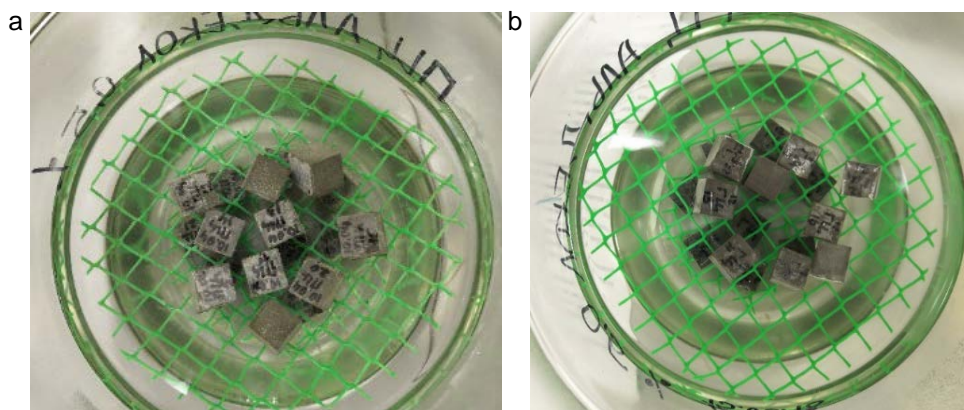


**Figure 2. Appearance of cement stone samples, aged in an Aldecol Based Medium:
a) Portland cement; b) aluminous cement.**

It is necessary to note that the dynamics of changes in the pH-medium with Portland cement stone almost completely coincides with the same indicators for the control (aqueous) medium, not only in character, but also in value (Figure 3, a). A jump was observed in the first month of aging, due to leaching, and then there was a gradual decrease in the value to the initial level when the samples were immersed in medium.

The exposure of samples based on aluminous stone in a control aqueous medium, as in the case of Portland cement, led to a jump in the pH medium in the first month of exposure with further flattening and lowering to the initial value, which was due to the natural processes of dissolution and crystallization in an aqueous medium (Figure 3, b). The change in the pH-medium of the solution of the sanitation agent practically coincided with pure water: at the initial stage, the value increased from 7 to 10, then gradually decreased to the initial value.

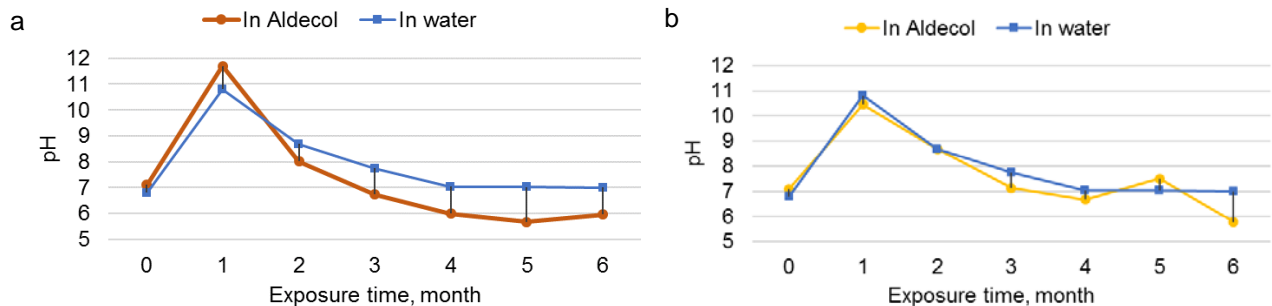


Figure 3. Correlation of changes in the pH-medium of cement stone samples aged in piped water and in Aldecol solution, depending on the exposure time: a) Portland cement stone; b) aluminous cement stone.

The analysis of the dynamics of the mass of cement stone samples depending on the medium and the time period of exposure allowed noting the following. In the case of Portland cement, the nature of the change in the mass of the samples during aging in a sanitation agent and clean water coincided (Figure 3, a): during the first three months there was a uniform increase in weight, the intensity of which further decreased and the mass practically did not change.

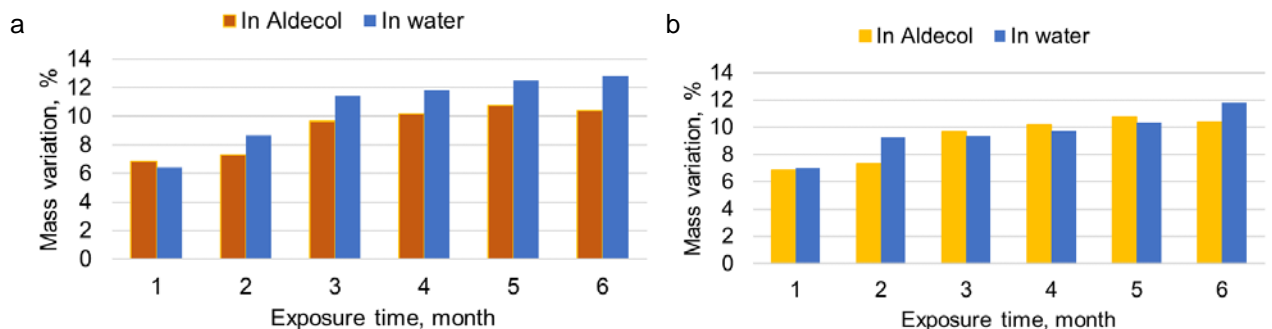


Figure 4. Correlation of changes in mass variation of samples of cement stone aged in piped water and in Aldecol solution, depending on the exposure time: a) Portland cement; b) aluminous cement.

From the point of hydration aluminous cement is a more complex system in comparison with classical Portland cement, the kinetics of structure formation of which are significantly influenced by the parameters of the hardening medium. The exposure of samples of aluminous cement stone in water led to the increase in their mass (Figure 4, b). In this case, the mass increase in the second month of exposure compared to the first month was only 2%. By the end of the experiment (6 months of aging), the total weight increase of the samples was 12%. A similar character was demonstrated by mass variation of samples in the control medium (Figure 4, b). In addition, the difference in weight increase compared to the control aqueous medium was insignificant regardless of the exposure time of the samples.

Since cement is a binder of hydration hardening, it is obvious that placing samples in an aqueous medium will provide the increase in the final strength of the samples, which is confirmed by the obtained data (Figure 5, a). The increase in exposure time in sanitation agent of Portland cement stone provides the increase in strength compared to the source material by 10% in the first month and 1.9 times after 6 months of exposure. At the same time, the strength of Portland cement samples is 10% lower than that for a stone aged in clean water. However, there is the excess of strength after the entire exposure time compared to the control medium. This aspect is determined by a number of factors: for example, the main active ingredient of Aldecol is glutaric aldehyde, which is distinguished by its ability to soften water and also reduce its overall acidity by reducing the amount of carbon dioxide. Probably, in this case, Aldecol acts as an intensifier of carbonization processes in terms of the increase of the amount of crystallized calcium carbonates, in particular, calcite, which acts as an effective colmatant [28]. This is expressed by the increase in the mass of samples noted earlier (Figure 4, a), as well as their strength in comparison with control materials.

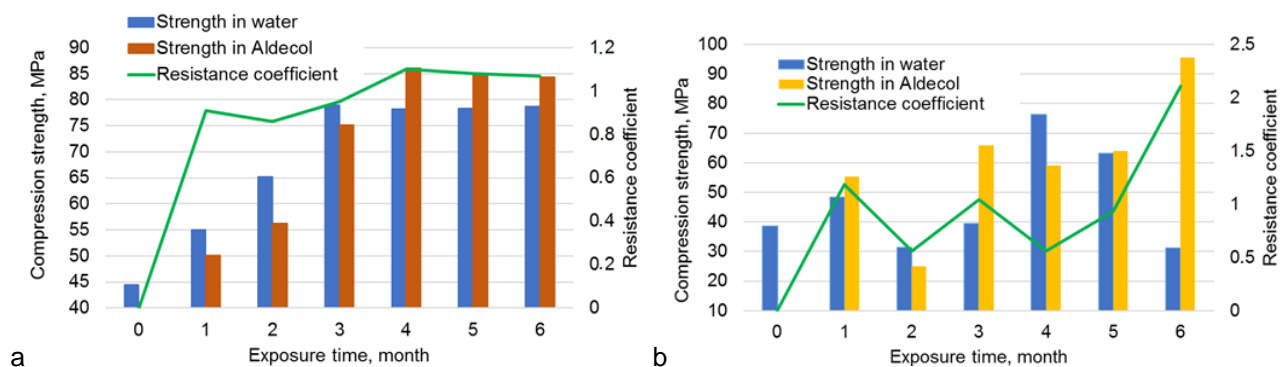


Figure 5. Change in compressive strength and resistance coefficient of cement stone samples aged in piped water and Aldecol solution, depending on the exposure time: a) Portland cement; b) aluminous cement.

The nature of the change in the strength of aluminous stone is distinguished by the absence of a strict dependence on the exposure time (Figure 5, b): after one month of exposure, the increase in strength in water medium (control solution) is 26 %. At the same time, already in the second month, a significant drop in strength is noted: 1.8 times and by 18 % compared to similar indicators after 1 month of exposure and at the age of 28 days, respectively. It can be explained by the hardening of aluminous cement. The initial hardening of the matrix of aluminous stone in the early stages is reasoned by the crystallization of hydro-aluminates of various compositions as a result of hydration processes. A possible explanation for the decrease in the strength of a stone based on aluminous cement after two months of hardening in water is recrystallization of meta-stable highly basic calcium hydro-aluminates into stable forms of hydrated compounds. On the one hand, it is accompanied by the increase in the density of new formations and, on the other hand, by a softening of the system due to the formation of additional voids associated with the decrease in the volume occupied by the crystalline substance.

A further increase in strength can be explained by the hardening of aluminous cement with the excess of water. Under such conditions, at the initial stage, a gel of hydration products is formed in the form of small lamellar X-ray amorphous crystals, which subsequently grow together and form a consolidated framework of the material.

It is necessary to note that the system of hardening aluminous cement is the most unstable due to constantly changing processes of primary crystallization and recrystallization of the formed substance. In this regard, the fluctuations in the strength of aluminous stone, due to the specifics of structure formation in water medium, do not contradict classical ideas about the theory of hydration and hardening of aluminous cement.

The nature of the change in the strength of samples of aluminous cement stone in the medium of the sanitation agent is comparable with the data obtained for a clean control medium (Figure 5, b). Nevertheless, it is possible to note some differences. Thus, as in the case of a clean medium, there is a drop in strength after two months, which, obviously, is associated with the transition of meta-stable compounds into stable and stable hydro-aluminate compounds. Further exposure for 3 months leads to the increase in strength by 1.7 and 2.6 times compared with samples exposed in a control medium of a similar age and two months in a simulation medium, respectively. In the next two months, strength does not change significantly. However, after 6 months, the increase in strength is 3 times in comparison with control materials at the age of 6 months and by 48 % compared to the samples aged 5 months in a simulation medium.

Similar dependences are noted in resistance coefficient, since its value is directly proportional to the strength indices of the samples during aging in simulation media (Figure 5). It is necessary to note that the chemical resistance of aluminous cement in a solution of a sanitation agent is high - the resistance coefficient of all samples, regardless of the exposure time, is more than 1. The following can present a possible explanation for the significant increase in the strength of the matrix of aluminous cement. As it is noted above, Aldecol is characterized by its ability to "accumulate" carbon dioxide in the system. Under such conditions, it is possible to form calcium carboaluminates in aluminous stone, which subsequently decompose into stable insoluble carbonate compounds, in particular, vaterite. This ensures the filling of free space in the stone matrix formed as a result of recrystallization of meta-stable hydroaluminates. As a result, the system is compressed, and the strength of the array increases.

The data on the carbonization of cement stone match the results of quantitative x-ray phase analysis. When analyzing the phases, only the crystalline phase of clearly fixed minerals is taken into account, since the composition of the X-ray amorphous substance, which is mainly represented by calcium hydrosilates of various mineral compositions, can not be identified. The degree of carbonization is estimated by the amount of portlandite as the most soluble phase, actively participating in chemical processes during corrosion, as well as calcium carbonates (calcite, aragonite, vaterite) as an indicator of the degree of carbon dioxide exposure.

The described properties are confirmed by the changes in the microstructure and mineral composition. Thus Portland cement stone samples aged in Aldecol solution are characterized by the increase in the total CaO concentration in the composition of portlandite, calcite, aragonite and vaterite after one month of exposure (Table 1, Figure 6). Later, the content is reduced to some extent and further significant fluctuations do not occur.

Table 1. Mineral composition of Portland cement stone exposed in Aldecol solution, mass %.

Mineral	Period of hardening, months						
	28 days	1	2	3	4	5	6
Alite	23.69	18.3	17.7	15.8	12.7	14.0	10.9
Belite	14.1	12.1	12.1	11.9	11.8	11.1	10.5
Brownmillerite	13.21	6	4.8	3.8	3.6	2.6	2
Portlandite	24.70	40.9	35.0	32.2	30.8	27.6	17.4
Calcite	4.29	19.8	26.5	29.0	35.3	43.2	57.8
Aragonite	18.36	–	–	–	–	–	–
Vaterite	1.65	–	–	–	–	–	–
Ettringite	–	2.9	3.9	7.3	5.8	1.5	1.4

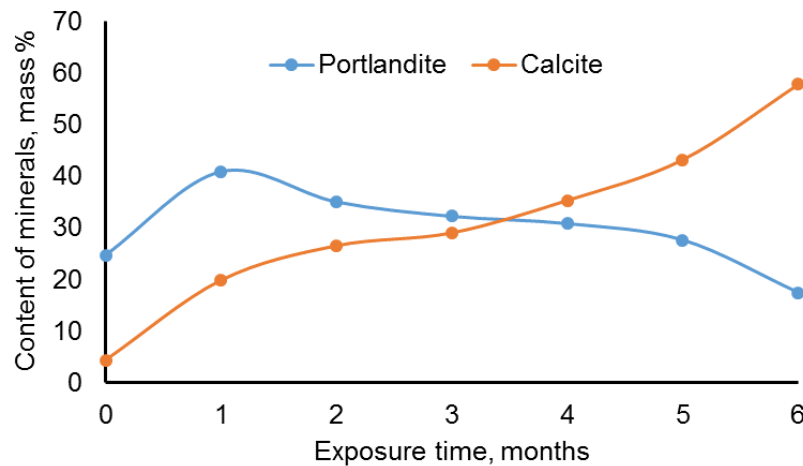


Figure 6. Dependences of Content of Portlandite and Calcite on exposure time of Portland cement samples aged in Aldecol solution.

At the same time, the increase in strength for all solutions is comparable, the maximum increase is observed after 6 months (Figure 5, a), which is characterized by the maximum concentration of calcite (Figure 6), crystallizing in pores and voids, thus filling the free space and compacting the array. In samples aged for 1 month in an Aldecol solution, sufficiently large tabular portlandite crystals reaching 60 mcm are identified (Figure 7 a). Hexagonal plates have clearly defined faces, which indicate growth structures. The crystals have cleavage, which is also confirmed by the layering of the structure for new formations (Figure 7, b). Elongated columnar crystals are typical of all samples exposed for no more than 4 months (Figure 7, c, d). They grow on the walls of the pores and grow through the tabular crystals. In samples of the exposure of 2 months and more tabular crystals continue to be found in cavities (Figure 7, b), the edges of which are covered with small new formations of later generations. The samples aged in Aldecol are characterized by the absence of elongated columnar crystals after 4 months of exposure (Figure 7, e, f).

To sum up the analysis of the microstructure of Portland cement stone samples exposed in a sanitation medium, it is necessary to note that dissolution structures are not identified in the samples. This, firstly, correlates to the kinetics of changes in strength and the change in the ratio of CaO content in portlandite and calcite, and secondly, indicates that Aldecol is not an aggressive agent and does not have a chemical effect on hydration products.

In the case of samples of aluminous cement stone, aged in a sanitation solution, the strength changes randomly. This correlates well to the data on changes in the main mineral phases of the stone (Table 2).

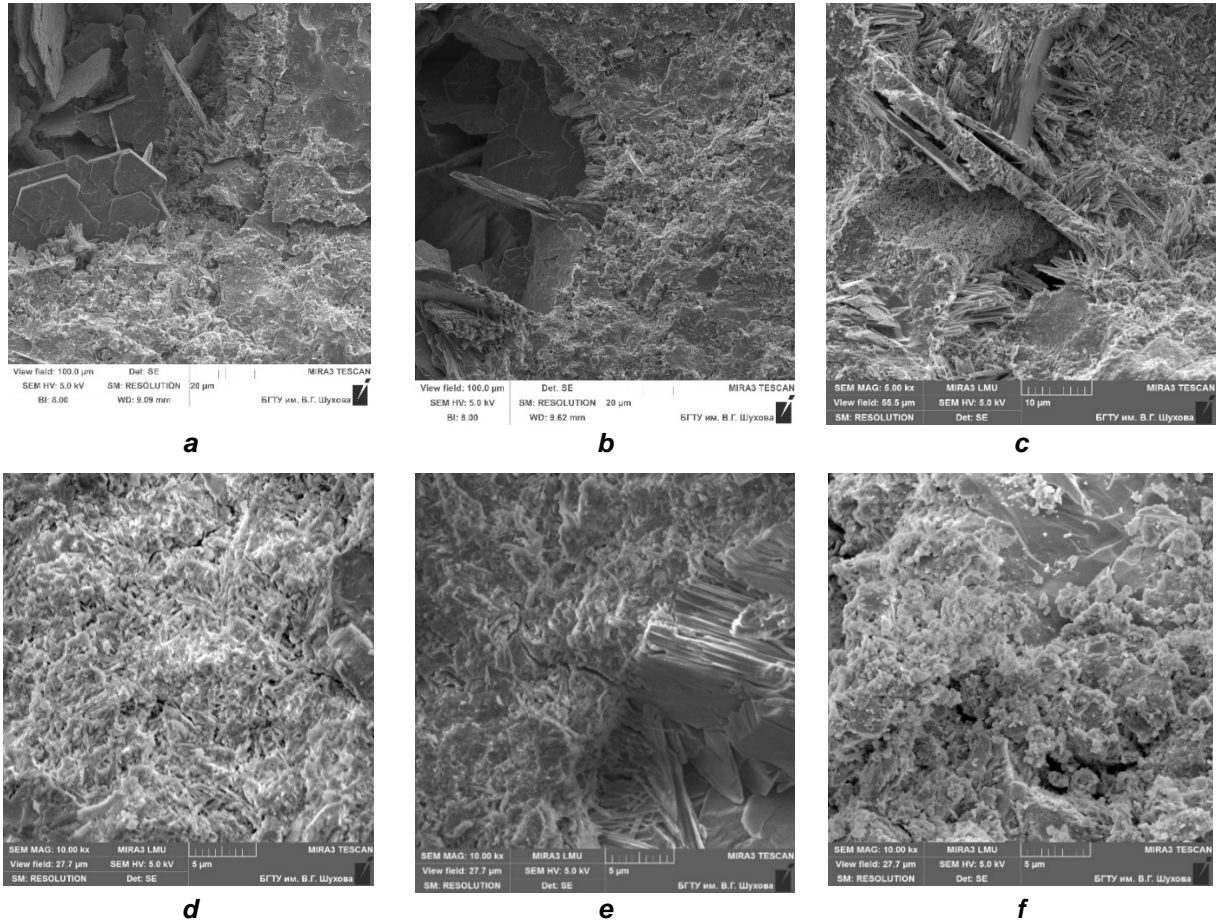


Figure 7. Microstructure of samples of Portland cement stone aged in Aldecol solution: a – one month; b – two months; c – three months; d – four months; e – five months; f – six months.

Table 2. Mineral composition of aluminous cement stone exposed in Aldecol solution, mass %.

Mineral	Period of hardening, months						
	28 days	1	2	3	4	5	6
CAH ₁₀	28.53	35.9	13.2	34.7	33.9	33.7	24.1
C ₃ AH ₆	0	1.6	4.5	0.0	6.4	4.0	7.3
AH ₃ Hydrargillite	5.76	14.1	24.9	14.8	16.9	14.5	20.8
Akermanite – Helenite	23.01	16.1	13.9	17.0	15.2	15.8	14.8
α-C ₂ S	4.42	3.0	2.3	3.1	3.1	2.8	3.2
CA	3.19	2.6	4.0	3.7	3.0	2.8	3.7
Vaterite	3.22	3.4	17.1	3.6	0.0	3.8	1.7
C ₄ AF	12.6	9.6	9.6	8.7	8.9	8.9	7.4
Perovskite	8.02	6.8	5.5	8.3	6.7	8.0	10.8
Wollastonite 2M	11.25	6.9	5.0	6.1	5.9	5.8	6.3

Significant differences in the variation kinetics of aluminate phases, which are responsible for the strength of aluminous cement composites, were not noted in comparison with the control medium: as in the case of pure water, CAH₁₀ recrystallized into stable forms C₃AH₆ and AH₃ (Figure 8).

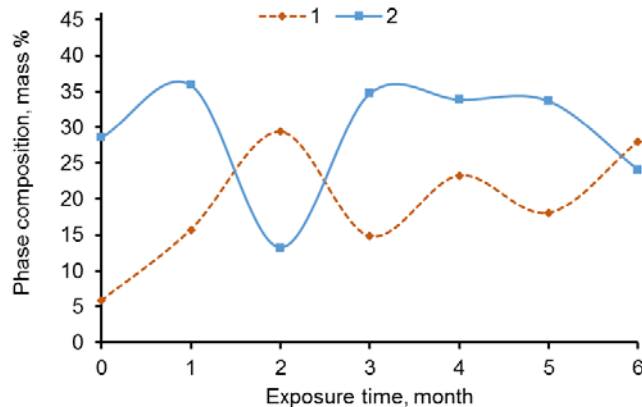


Figure 8. Dependences of phase changes C₃AH₆ + AH₃ (1) and CAH₁₀ (2) on exposure time for aluminous samples of cement stone aged in Aldecol solution.

During exposure in a sanitation agent, the concentration of carbonate compounds (vaterite) increased, which was due to the carbonization of the initially formed substance (Table 2). At the same time, its maximum value was noted after 3 months of exposure in a solution of a sanitation agent. It complied with the strength data: the strength after 3 months of exposure was two times higher than that for samples aged in water (Figure 5, b). In contact with Aldecol medium the concentration of vaterite increased, which was associated with the carbonization of calcium compounds of aldehydes (Table 2).

After 1 month of exposure in all types of solutions, the matrix of samples of aluminous cement stone was dense and composed of cryptocrystalline substance (Figure 9, a). With the increase in exposure time to 2 months, no significant changes in the microstructure were observed except decompaction and traces of dissolution (Figure 9, b). In samples exposed in Aldecol for 3 months in the zones of the pore space, new formations with atypical morphostructures for this system appeared. These were druses from intergrowths of lamellar crystals resembling "gypsum roses" (Figure 9, c). The size of individual druse reached 100 microns, the size of individual plates reached up to 30 microns. These aggregates were surrounded by fine crystalline columnar crystals not exceeding 3 microns in length. Such areas of the accumulation of idiomorphic crystals were quite often found in samples aged in Aldecol solution. After exposure for longer periods (4–6 months) in the Aldecol solution, both the structures of the formation of later generations and the structures of its dissolution were observed (Figure 9, d–f).

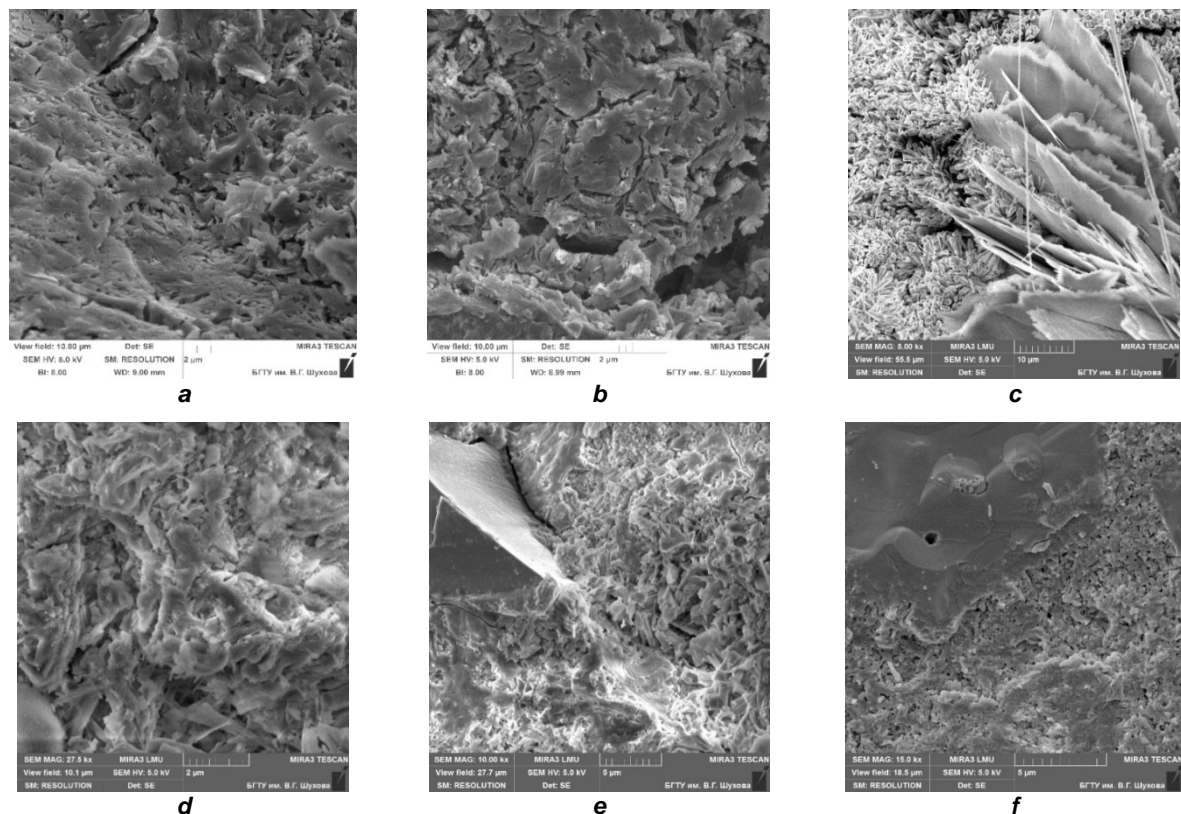


Figure 10. Microstructure of samples of aluminous cement stone aged in Aldecol solution: a –one month; b –two months; c –three months; d – four months; e – five months; f –six months.

4. Conclusion

Thus, the research showed the influence of the model environment, which was an imitation of the impact of the sanitation processing of the premises of agricultural enterprises. It was found that there was no obvious degradation effect of the sanitation solution on the cement stone.

1. The dependences of the strength of cement stone as the main indicator of the quality and resistance of the composite were established: after 6 months of exposure in sanitation solution the strength of the stone samples increased regardless of its composition.

2. For Portland cement stone, the increase in strength was 10 % compared to the samples aged in pure water, and 1.9 times compared to the original samples without exposure.

3. In the case of aluminous cement, there was a 2-times increase in strength compared to samples aged in pure water, and 1.6 times compared to the original samples without exposure.

4. It was shown that the increase in the strength of materials occurs due to the intensification of carbonization processes in the environment of sanitation product, which led to the colmatation of pores and voids due to crystallization of insoluble calcium carbonates. This was confirmed by compaction of the microstructure of cement stone, expressed by a 12 % increase in the mass of samples regardless of the type

of cement stone, as well as the increase in the total concentration of carbonate compounds in the volume of the material after 6 months of exposure.

Nevertheless, it is necessary to note that despite the obvious positive effect of the solutions of sanitation agent on the properties of cement stone, the real impact of such products during processing is probably characterized as a negative one. It is explained by the cyclical effect in terms of alternate wetting / drying of the surface of material, which will lead to the release of soluble calcium hydroxide to the surface and washing off during subsequent processing with the formation of additional porosity of products.

5. Acknowledgement

The research was conducted in the framework of State Task of the Russian Federation Ministry of Education and Science № 7.872.2017/4.6 Development of principles for the design of ecologically positive composite materials with prolonged biological resistance, 2017–2019. This work was realized using the laboratory platform of the High Technology Center at BSTU named after V.G. Shukhov.

References

1. Popova, O.N., Glebova, Y.M. Monitoring and quality assessment of urban development areas based on neural network modeling and GIS. *Construction of Unique Buildings and Structures*. 2017. 62(11). Pp. 47–59. DOI: 10.18720/CUBS.62.4.
2. Vengrinovich, V.L., Ryabtsev, V.N. Damage identification using the moving fractal method for automated monitoring. *Construction of Unique Buildings and Structures*. 2018. 68(5). Pp. 52–61. DOI: 10.18720/CUBS.68.5.
3. Manzhilevskaya, S.E. Environmental monitoring of ecological safety in areas of construction, reconstruction and operation of objects. *Construction Materials and Products*. 2019. Vol. 2. No. 3. Pp. 78–84. (rus)
4. Shatalov, V.V. Relevance of the reaction of artificial breathing atmospheres in terms of air pollution. *Construction Materials and Products*. 2019. Vol. 2. No. 3. P. 34–40. (rus)
5. Abramyan, S.G., Burlachenko, O.V., Oganessian, O.V. The use of composite materials in the reconstruction of floors of industrial buildings. *Construction Materials and Products*. 2019. Vol. 2. No. 3. P. 58–64. (rus)
6. Kalachuk, T.G., Kolmykova, I.V., Shin, E.R. Evaluation of the seismic inertia forces on the actual damage of bridges. *Construction Materials and Products*. 2019. Vol. 2. No. 3. P. 28–33. (rus)
7. Noeiaghahi, T., Mukherjee, A., Dhama, N., Chae, S.-R. Biogenic deterioration of concrete and its mitigation technologies. *Construction and Building Materials*. 2017. 149. Pp. 575–586. DOI: 10.1016/j.conbuildmat.2017.05.144.
8. Anikina, N.A., Smirnov, V.F., Smirnova, O.N., Zaharova, E.A. Protection of construction materials based on acrylates from biodeterioration. *Magazine of Civil Engineering*. 2018. 81(5). Pp. 116–124. DOI: 10.18720/MCE.81.12.
9. Tokach, Y.E., Goncharova, E.N. Creating Bioresistant Technogenic Waste Basted Coatings for Construction Materials. *Procedia Engineering*. 2016. 150. Pp. 1547–1552. DOI: 10.1016/j.proeng.2016.07.109
10. Estokova, A., Harbulakova, V.O., Luptakova, A., Kovalcikova, M. Analyzing the relationship between chemical and biological-based degradation of concrete with sulfate-resisting cement. *Polish Journal of Environmental Studies*. 2019. 28(4). Pp. 2121–2129. DOI: 10.15244/pjoes/91079.
11. Song, Y., Wightman, E., Tian, Y., Jack, K., Li, X., Zhong, H., Bond, P.L., Yuan, Z., Jiang, G. Corrosion of reinforcing steel in concrete sewers. *Science of the Total Environment*. 2019. 649. Pp. 739–748. DOI: 10.1016/j.scitotenv.2018.08.362.
12. Jiang, G., Sun, J., Sharma, K.R., Yuan, Z. Corrosion and odor management in sewer systems. *Current Opinion in Biotechnology*. 2015. 33. Pp. 192–197. DOI: 10.1016/j.copbio.2015.03.007.
13. Pires, J.F., Cardoso, L.S., Schwan, R.F., Silva, C.F. Diversity of microbiota found in coffee processing wastewater treatment plant. *World Journal of Microbiology and Biotechnology*. 2017. 33(12). DOI: 10.1007/s11274-017-2372-9.
14. Estokova, A., Harbulakova, V.O., Luptakova, A., Prascakova, M., Stevulova, N. Sulphur oxidizing bacteria as the causative factor of biocorrosion of concrete. *Chemical Engineering Transactions*. 2011. 24. Pp. 1147–1152. DOI: 10.3303/CET1124192.
15. Harbulakova, V.O., Estokova, A., Luptakova, A. An investigation of the bacterial influence of acidithiobacillus thiooxidans on concrete composites. *E3S Web of Conferences*. 452018.
16. Strigáč, J., Martauz, P., Eštoková, A., Številová, N., Luptáková, A. Bio-corrosion resistance of concretes containing antimicrobial ground granulated blastfurnace slag BIOLANOVA and novel hybrid H-CEMENT. *Solid State Phenomena*. 2016. 244. Pp. 57–64. DOI: 10.4028/www.scientific.net/SSP.244.57.
17. Jiang, G., Zhou, M., Chiu, T.H., Sun, X., Keller, J., Bond, P.L. Wastewater-Enhanced Microbial Corrosion of Concrete Sewers. *Environmental Science and Technology*. 2016. 50(15). Pp. 8084–8092. DOI: 10.1021/acs.est.6b02093.
18. Erich, S.J.F., Mendoza, S.M., Floor, W., Hermanns, S.P.M., Homan, W.J., Adan, O.C.G. Decreased bio-inhibition of building materials due to transport of biocides. *Heron*. 2011. 56(3). Pp. 93–106.
19. Gao, S.-H., Ho, J.Y., Fan, L., Richardson, D.J., Yuan, Z., Bond, P.L. Antimicrobial effects of free nitrous acid on *Desulfovibrio vulgaris*: Implications for sulfide-induced corrosion of concrete. *Applied and Environmental Microbiology*. 2016. 82(18). Pp. 5563–5575. DOI: 10.1128/AEM.01655-16.
20. Deshmukh, S.P., Patil, S.M., Mullani, S.B., Delekar, S.D. Silver nanoparticles as an effective disinfectant: A review. *Materials Science and Engineering C*. 2019. 97. Pp. 954–965. DOI: 10.1016/j.msec.2018.12.102.
21. Erofeev, V.T., Rodin, A.I., Kravchuk, A.S., Kaznacheev, S.V., Zaharova, E.A. Biostable silicic rock-based glass ceramic foams. *Magazine of Civil Engineering*. 2018. 84(8). Pp. 48–56. DOI: 10.18720/MCE.84.5
22. Chromková, I., Čechmánek, R. Influence of biocorrosion on concrete properties. *Key Engineering Materials*. 2018. 760 KEM. Pp. 83–90. DOI: 10.4028/www.scientific.net/KEM.760.83.
23. Erofeev, V.T., Bogatov, A.D., Smirnov, V.F., Bogatova, S.N., Rimshin, V.I., Kurbatov, V.L. Bioresistant building composites on the basis of glass wastes. *Biosciences Biotechnology Research Asia*. 2015. 12(1). Pp. 661–669. DOI: 10.13005/bbra/1710.
24. Li, G., Zhang, A., Song, Z., Shi, C., Wang, Y., Zhang, J. Study on the resistance to seawater corrosion of the cementitious systems containing ordinary Portland cement or/and calcium aluminate cement. *Construction and Building Materials*. 2017. 157. Pp. 852–859. DOI: 10.1016/j.conbuildmat.2017.09.175.

25. Nematzadeh, M., Dashti, J., Ganjavi, B. Optimizing compressive behavior of concrete containing fine recycled refractory brick aggregate together with calcium aluminate cement and polyvinyl alcohol fibers exposed to acidic environment. *Construction and Building Materials*. 2018. 164. Pp. 837–849. DOI: 10.1016/j.conbuildmat.2017.12.230.
26. Strokova, V., Nelyubova, V., Rykunova, M., Dukhanina, U. Strength and structure of cement stone exposed to domestic chicken coop. *Journal of Physics: Conference Series*. 2019. 1145 (1). DOI: 10.1088/1742-6596/1145/1/012015.
27. Strokova, V.V., Zhernovsky, I.V., Nelubova, V.V., Rykunova, M.D. Structural transformations of cement stone in conditions of development of the biocenosis of a poultry enterprise. *Materials Science Forum*. 2018. 945 MSF. Pp. 269–275. DOI: 10.4028/www.scientific.net/MSF.945.269.
28. Fedosov, S.V., Rumyantseva, V.E., Krasilnikov, I.V., Konovalova, V.S., Evsyakov, A.S. Mathematical modeling of the colmatation of concrete pores during corrosion. *Magazine of Civil Engineering*. 2018. 83(7). Pp. 198–207. DOI: 10.18720/MCE.83.18.

Contacts:

Valeria Strokova, +7(4722)55-87-85; vvstrokova@gmail.com

Victoria Nelubova, +7(910)368-76-69; nelubova@list.ru

Marina Rykunova, +7(4722)54-90-41; tumashova93@mail.ru

© Strokova, V.V., Nelubova, V.V., Rykunova, M.D., 2019



DOI: 10.18720/MCE.90.7

Стойкость цементного камня в растворах санационных средств

В.В. Строкова, В.В. Нелубова*, М.Д. Рыкунова

Белгородский государственный технологический университет им. В.Г. Шухова, г. Белгород, Россия

* E-mail: nelubova@list.ru

Ключевые слова: бетонная конструкция, цементы, коррозия, биодеструкция, химическая коррозия, кислотостойкость

Аннотация. Биологическая коррозия является видом воздействия, затрагивающим практически все возможные объекты строительства, что особенно остро касается предприятий агропромышленного комплекса. К основным мероприятиям по предотвращению коррозионного процесса конструкций относятся санитарно-профилактические работы, проводимые при помощи различных химических средств (биоцидов). Концентрацию рабочих растворов для санации определяют исходя из цели дезинфекции и степени устойчивости возбудителей, при этом не учитывается их влияние на физико-механические свойства поверхности материала. Химическая обработка помещений, несмотря на очевидные плюсы, связанные с уничтожением патогенной микрофлоры, характеризуется недостатками, главным из которых является деградационное воздействие на строительный композит и, как следствие, существенное сокращение жизненного срока конструкций. Предметом исследования являлась оценка степени агрессивного воздействия санационной обработки помещений на цементный камень различного состава. В качестве объектов исследования использовались портландцемент как наиболее распространенное изученное вяжущее и глиноземистый цемент как вяжущее с начальной более высокой коррозионной стойкостью. В качестве экспериментальной среды, моделирующей воздействие санационного средства на камень при реальной эксплуатации материала в натуральных условиях, использовался раствор реагента для санации. Контрольной средой выступала водопроводная вода. Оценку степени воздействия среды на цементный камень различного состава осуществляли на основании данных об основных физико-химических показателях процесса (изменение массы, водородного показателя среды, прочности на сжатие и коэффициента химической стойкости), а также фазово-структурные трансформации камня (минеральный состав, микроструктурные особенности матрицы цементного камня), выдержанного в агрессивной среде в зависимости от длительности экспонирования. Установлено отсутствие явного деградационного воздействия санационного раствора на цементный камень: отмечается рост прочности образцов после 6 месяцев экспозиции (для портландцементного камня: на 10 % по сравнению с образцами, выдержанными в чистой воде, и в 1,9 раза по сравнению с исходными образцами без выдержки; для глиноземистого цементного камня: в 2 раза по сравнению с образцами, выдержанными в чистой воде, и в 1,6 раза по сравнению с исходными образцами без выдержки) как основного показателя качества и резистивности композита и, как следствие, коэффициента химической стойкости. Рост прочности материалов происходит вследствие интенсификации карбонизационных процессов в среде санационного средства, что приводит к кольматации пор и пустот за счет кристаллизации нерастворимых карбонатов кальция. Это подтверждается уплотнением микроструктуры цементного камня, выражаемой ростом массы образцов на 12 % независимо от вида цементного камня, а также увеличением суммарной концентрации карбонатных соединений в объеме материала после 6 месяцев выдержки.

Литература

1. Попова О.Н., Глебова Ю.М. Мониторинг и оценка качества урбанизированных территорий на основе методов нейросетевого моделирования и ГИС // Строительство уникальных зданий и сооружений. 2017. № 11(62). С. 47–59. DOI: 10.18720/CUBS.62.4
2. Венгринович В.Л., Рябцев В.Н. Идентификация повреждений методом подвижного фрактала при автоматизированном мониторинге // Строительство уникальных зданий и сооружений. 2018. №5(68). С. 52–61. DOI: 10.18720/CUBS.68.5
3. Манжилевская С.Е. Экологический мониторинг экологической безопасности в зонах строительства, реконструкции и функционирования объектов // Строительные материалы и изделия. 2019. Т. 2. № 3. С. 78–84.

4. Шаталов В.В. Актуальность создания искусственных дыхательных атмосфер в условиях загрязнения атмосферного воздуха // Строительные материалы и изделия. 2019. Т. 2. № 3. С. 34–40.
5. Абрамян С.Г., Бурлаченко О.В., Оганесян О.В. Применение композитных материалов при реконструкции полов промышленных зданий // Строительные материалы и изделия. 2019. Т. 2. № 3. С. 58–64.
6. Калачук Т.Г., Колмыкова И.В., Шин Е.Р. Оценка сейсмичности сил инерции по фактическим повреждениям мостов // Строительные материалы и изделия. 2019. Т. 2. № 3. С. 28–33.
7. Noeiaghaei T., Mukherjee A., Dhami N., Chae S.-R. Biogenic deterioration of concrete and its mitigation technologies // Construction and Building Materials. 2017. 149. Pp. 575–586. DOI: 10.1016/j.conbuildmat.2017.05.144.
8. Аникина Н.А., Смирнов В.Ф., Смирнова О.Н., Захарова Е.А. Защита строительных материалов на основе акрилатов от биоповреждений // Инженерно-строительный журнал. 2018. № 5(81). С. 116–124. doi: 10.18720/MCE.81.12
9. Tokach Y.E., Goncharova E.N. Creating Bioresistant Technogenic Waste Based Coatings for Construction Materials // Procedia Engineering. 2016. Vol. 150. Pp. 1547–1552. DOI: 10.1016/j.proeng.2016.07.109
10. Estokova A., Harbulakova V.O., Luptakova A., Kovalcikova M. Analyzing the relationship between chemical and biological-based degradation of concrete with sulfate-resisting cement // Polish Journal of Environmental Studies. 2019. 28(4). Pp. 2121–2129. DOI: 10.15244/pjoes/91079.
11. Song Y., Wightman E., Tian Y., Jack K., Li X., Zhong H., Bond P.L., Yuan Z., Jiang G. Corrosion of reinforcing steel in concrete sewers // Science of the Total Environment. 2019. 649. Pp. 739–748. DOI: 10.1016/j.scitotenv.2018.08.362.
12. Jiang G., Sun J., Sharma K.R., Yuan Z. Corrosion and odor management in sewer systems // Current Opinion in Biotechnology. 2015. 33. Pp. 192–197. DOI: 10.1016/j.copbio.2015.03.007.
13. Pires J.F., Cardoso L.S., Schwan R.F., Silva C.F. Diversity of microbiota found in coffee processing wastewater treatment plant // World Journal of Microbiology and Biotechnology. 2017. 33(12). DOI: 10.1007/s11274-017-2372-9.
14. Estokova A., Harbulakova V.O., Luptakova A., Prascakova M., Stevulova N. Sulphur oxidizing bacteria as the causative factor of biocorrosion of concrete // Chemical Engineering Transactions. 2011. 24. Pp. 1147–1152. DOI: 10.3303/CET1124192.
15. Harbulakova V.O., Estokova A., Luptakova A. An investigation of the bacterial influence of acidithiobacillus thiooxidans on concrete composites // E3S Web of Conferences. 2018. 45.
16. Strigáč J., Martauz P., Eštoková A., Številová N., Luptáková A. Bio-corrosion resistance of concretes containing antimicrobial ground granulated blastfurnace slag BIOLANOVA and novel hybrid H-CEMENT // Solid State Phenomena. 2016. 244. Pp. 57–64. DOI: 10.4028/www.scientific.net/SSP.244.57.
17. Jiang G., Zhou M., Chiu T.H., Sun X., Keller J., Bond P.L. Wastewater-Enhanced Microbial Corrosion of Concrete Sewers // Environmental Science and Technology. 2016. 50(15). Pp. 8084–8092. DOI: 10.1021/acs.est.6b02093.
18. Erich S.J.F., Mendoza S.M., Floor W., Hermanns S.P.M., Homan W.J., Adan O.C.G. Decreased bio-inhibition of building materials due to transport of biocides // Heron. 2011. 56(3). Pp. 93–106.
19. Gao S.-H., Ho J.Y., Fan L., Richardson D.J., Yuan Z., Bond P.L. Antimicrobial effects of free nitrous acid on *Desulfovibrio vulgaris*: Implications for sulfide-induced corrosion of concrete // Applied and Environmental Microbiology. 2016. 82(18). Pp. 5563–5575. DOI: 10.1128/AEM.01655-16.
20. Deshmukh S.P., Patil S.M., Mullani S.B., Delekar S.D. Silver nanoparticles as an effective disinfectant: A review // Materials Science and Engineering C. 2019. 97. Pp. 954–965. DOI: 10.1016/j.msec.2018.12.102.
21. Erofeev V.T., Rodin A.I., Kravchuk A.S., Kaznacheev S.V., Zaharova E.A. Biostable silicic rock-based glass ceramic foams // Magazine of Civil Engineering. 2018. 84(8). Pp. 48–56. DOI: 10.18720/MCE.84.5
22. Chromková I., Čechmánek R. Influence of biocorrosion on concrete properties // Key Engineering Materials. 2018. 760 KEM. Pp. 83–90. DOI: 10.4028/www.scientific.net/KEM.760.83.
23. Erofeev V.T., Bogatov A.D., Smirnov V.F., Bogatova S.N., Rimshin V.I., Kurbatov V.L. Bioresistant building composites on the basis of glass wastes // Biosciences Biotechnology Research Asia. 2015. 12(1). Pp. 661–669. DOI: 10.13005/bbra/1710.
24. Li G., Zhang A., Song Z., Shi C., Wang Y., Zhang J. Study on the resistance to seawater corrosion of the cementitious systems containing ordinary Portland cement or/and calcium aluminate cement // Construction and Building Materials. 2017. 157. Pp. 852–859. DOI: 10.1016/j.conbuildmat.2017.09.175.
25. Nematzadeh M., Dashti J., Ganjavi B. Optimizing compressive behavior of concrete containing fine recycled refractory brick aggregate together with calcium aluminate cement and polyvinyl alcohol fibers exposed to acidic environment // Construction and Building Materials. 2018. 164. Pp. 837–849. DOI: 10.1016/j.conbuildmat.2017.12.230.
26. Strokova V., Nelyubova V., Rykunova M., Dukhanina U. Strength and structure of cement stone exposed to domestic chicken coop // Journal of Physics: Conference Series. 2019. 1145(1) DOI: 10.1088/1742-6596/1145/1/012015
27. Strokova V.V., Zhemovsky I.V., Nelubova V.V., Rykunova M.D. Structural transformations of cement stone in conditions of development of the biocenosis of a poultry enterprise // Materials Science Forum. 2018. 945 MSF. Pp. 269–275. DOI: 10.4028/www.scientific.net/MSF.945.269.
28. Федосов С.В., Румянцова В.Е., Красильников И.В., Коновалова В.С., Евсяков А.С. Математическое моделирование кольматации пор бетона при коррозии // Инженерно-строительный журнал. 2018. № 7(83). С. 198–207. doi: 10.18720/MCE.83.18.

Контактные данные:

Валерия Валерьевна Строчкова, +7(4722)558785; эл. почта: vvstrokova@gmail.com

Виктория Викторовна Нелюбова, +79103687669; эл. почта: nelubova@list.ru

Марина Дмитриевна Рыкунова, +7(4722)549041; эл. почта: tumashova93@mail.ru



DOI: 10.18720/MCE.90.8

Retrofitting of fire stations in cold climate regions

A. Borodinecs*, A. Prozuments, A. Zajacs, J. Zemitis

Riga Technical University, Riga, Latvia

* *E-mail: borodinecs@rtu.lv*

Keywords: buildings, energy efficiency, energy retrofit

Abstract. Most of the urban housing stock in European cities consists of multi apartment buildings. Improvement of energy efficiency of the existing building stock is the key priority across the world. As such, unclassified buildings including fire stations present a significant potential for application of innovative energy efficient measures. Despite the fact that fire stations account for a rather insignificant share on the scale of the total building stock, it is vitally important to ensure optimal thermal comfort as well as reduce energy consumption in those buildings. This in turn contributes in minimizing maintenance and running costs for municipalities. This paper analyses typology of Latvian fire stations and their energy consumption. Standardized IFC model was developed to evaluate effect of implementation of energy efficiency measures in a selected fire station. The study results showed that the proposed theoretical thermal energy consumption of developed standardised model correlates with the measured data. The measured average annual energy consumption including electricity for fire stations was 317 kWh/m² and thermal energy for space heating – 135.4 kWh/m². Based on theoretical model, different retrofitting scenarios were evaluated using IDA-ICE dynamic energy simulation software. The results of this study can be expanded and applied to other types of unclassified buildings (in countries with cold climate) such as police departments and prisons.

1. Introduction

Energy efficiency of buildings as well as sustainable development of construction sector has been put forward among major priorities in the European Union [1]. Moreover, countries such as USA, China and Russia are consistently improving and tightening their legislation on buildings energy performance [2–4]. For example, Russia has tightened its legislation with regards to heat resistance requirements for opaque elements of building envelope by 200 % [5]. Despite the increased focus on implementation of energy efficient measures in buildings, the world's energy consumption is increasing at a rate of approximately 10 % per year [6]. It should be noted that the main contributors to this dynamic are the developing countries. The main target group for implementation of energy efficiency measures in building sector are multi apartment and public buildings, which are major contributors to CO₂ emissions [7]. Meanwhile the energy efficiency in so called unclassified buildings is not being adequately addressed, as these buildings are not part of governmental subsidies. Unclassified buildings include army barracks, warehouses, police departments, fire depots, prisons etc. These buildings constitute approximately 1 % of the total building stock share. Nevertheless, when it comes to energy conservation, even this small building share should not be neglected. Unclassified buildings are typically occupied 24/7 and consume up to 5 times more energy than a regular apartment building per floor area. Retrofitting of such buildings would ensure not only reduction of energy consumption but also allow for an improvement of thermal comfort and indoor air quality. This is very important for occupants residing for an extended time in one building. For instance, when staying inside the fire stations, firefighters are exposed to polycyclic aromatic hydrocarbons [8]. The main reasons for that are insufficient (or in many cases non-existing) ventilation, poor quality of a building or improper retrofitting. It should be noted that it is mainly fire stations constructed before 1990s that are not well maintained and do not have energy efficient solutions [9]. While the residential sector in the EU countries has a high potential for saving energy by lowering the heating demand through properly insulating building envelope [10], the retrofitting packages for the fire stations should have a stronger focus on upgrading the mechanical systems and incorporating renewable energy sources. Modern fire fighter trucks have electric equipment that use 12 V batteries. These batteries are usually charged in between the emergency callouts through an electric grid. In

Borodinecs, A., Prozuments, A., Zajacs, A., Zemitis, J. Retrofitting of fire stations in cold climate regions. Magazine of Civil Engineering. 2019. 90(6). Pp. 85–92. DOI: 10.18720/MCE.90.8

Бородинец А., Проземент А., Заяц А., Земитис Ю. Реновация пожарных депо в условиях холодного климата // Инженерно-строительный журнал. 2019. № 6(90). С. 85–92. DOI: 10.18720/MCE.90.8



such cases installation of PV arrays could have a positive effect on overall energy performance profile of the fire stations.

A recent study analysed five typical mid-scale fire stations, whose lighting bills came out to 9500\$ annually per station [11]. The same study estimated that the potential energy saving due to an increased thermal insulation of external building envelope would be in the ballpark of 20 %. However, the application of thermal insulation may not be enough to ensure sustainable retrofitting. Such issues as poor indoor air quality, unsatisfactory thermal comfort and environmental impact should also be addressed when it comes to fire stations. Another study [12] analysed the use of green-rating system (LEED) to assess overall sustainability of fire stations. The results showed the importance of implementation of green-rating system which allows municipalities to take adequate design measures on future maintenance and retrofitting strategies.

A typical fire station is a low-rise building. There are several cost optimal solutions for the construction and retrofitting of low-rise buildings [13] which can be easily applied to fire stations. However, retrofitting of the fire stations is more complicated in comparison to residential and public buildings. This type of buildings have specific requirements on ventilation due to firefighting truck exhaust pipes and hot water consumption pattern, that has explicit peak loads on staff shifts change. This requires an installation of a more powerful hot water boiler. Retrofitting packages should also include measures for moisture control [14].

The main objective of this study is to evaluate current energy efficiency of non-renovated buildings and to perform an indoor air quality analysis in order to evaluate working parameters of heating, ventilation and air conditioning systems as well as airtightness of the building envelope. Based on acquired results standard energy retrofitting measures will be offered and analyzed in terms of both energy reduction and operation cost reductions. For this purpose, real fire stations under operation in Latvia were selected. Latvia is situated in Northern Europe along the Baltic sea region and represents a country with mildly cold climate. Several studies on buildings' energy efficiency in Baltic sea region [15, 16] have shown that estimations of energy reduction in Latvia can be used and adopted in this region. Other studies have shown that climatic conditions and building typology in Latvia are very similar to major Russian cities such as St. Petersburg, Leningrad district and Moscow.

2. Methods

Research methodology lies on the development of theoretical building model which was validated based on real on-site measurements. Validated model was used to evaluate different retrofitting scenarios. In addition, real indoor air parameter measurements were conducted to identify critical points.

The method of the energy consumption evaluation for unclassified buildings is based on the analysis of the real measured thermal energy consumption in fire stations. In total, the dataset on 40 fire stations was analysed. All analysed buildings were connected to district heating systems. Data was provided by the maintenance organizations of those buildings for the time period 2016–2019. In addition, on-site IAQ measurements and technical inspection was performed. EXTECH CO2/Humidity/Temperature dataloggers were used. These loggers have the following technical parameters:

- ✓ CO₂ range 0 to 4000 ppm; resolution 1ppm;
- ✓ Temperature range 0 to 50 °C; resolution 0.5 °C;
- ✓ Humidity range 10 to 90 %; resolution 0.1 %;

Dataloggers were installed in different rooms to evaluate indoor air quality.

For theoretical evaluation of energy consumption and effect of different retrofitting packages, the dynamic energy simulation tool Indoor Climate and Energy (IDA-ICE) 4.8 was chosen. This software allows to estimate energy consumption with one-hour interval and includes a detailed evaluation of heat balance, indoor air temperature, operative temperature etc. In addition, it takes into account human comfort level and metabolic rate.

IDA-ICE dynamic energy simulation tool was validated in accordance with ISO 13791:2012 [5] and [6]. Climate data was derived from ASHRAE 2013 which differs from ASHRAE 2017 data only by 2.5 % [15]. The accuracy of this software simulations was proved by studies [8, 9].

In general, calculations of the annual thermal energy demand for a prototype building can be determined by the equation adopted from [17]:

$$E_{annual} = \frac{(\sum U_i A_i + \sum \psi_j l_j + \sum \chi k + (V_{air} \cdot c)) \cdot 24 \cdot D_{heat} \cdot (T_{in} - T_{out})}{1000 \cdot A_b} - \eta \cdot (Q_{int} + Q_{sol}), \quad (1)$$

where U_i is heat transfer coefficient of the building construction element (W/(m²·K));

A_i is the area of the respective construction element of the building prototype model (m²);

ψ_i is heat transfer coefficient of the linear thermal bridge (W/(m·K));

l_i is length of the linear thermal bridge (m);

χ_k is heat transfer coefficient of the point thermal bridge (W/K);

V_{air} is ventilation air volumetric flowrate (m³/h);

c is air heat capacity per volume = 0.34 (Wh/(m³·°K));

D_{heat} is number of heating days;

T_{in} is average set-point temperature in the assessment (heating or cooling) period (°C);

T_{out} is average external temperature in the calculation period (°C);

A_b is total floor area of the building (m²);

η is gain use coefficient for heating in accordance with Paragraph 99 of this Regulation or Standard LVS EN ISO 13790:2009 L;

Q_{int} is interior gains of the whole building in the assessment period t (kWh/m²);

Q_{sol} is solar heat gains (kWh/m²).

$$Q_{sol} = \frac{\sum A_{sol} \cdot E_{sol}}{1000 \cdot A_b}, \quad (2)$$

where A_{sol} is area of collecting useful solar energy of the building (m²);

E_{sol} is solar irradiation in the assessment period t per area A_{sol} (Wh/m²).

3. Results and Discussion

3.1. Typology of fire stations

During the period before the year 1940, 15 % of buildings currently serving as fire stations were built (with the total area of 2553.7 m²). From 1945 to 1970, 45 % of all fire station buildings were built with the total area of 11251.1 m². From 1971 to 1990, 25 % of fire stations buildings were built with the total area of 8208.0 m². After 1991, the remaining 15 % of all fire stations buildings were built with the total area of 4098.1 m². A typological overview of several Latvian fire stations is provided in Figure 1.



Figure 1. A review of typical Latvian fire stations.

As shown in Figure 1, all fire stations were built according to individual projects. However, a typology of the analysed depots indicates to common construction principles. Namely, the first floor is used for parking fire-fighting vehicles whereas the second floor is used for staff needs and administration. For the purpose of this research a unified fire station building model was developed in Industry Foundation Classes (IFC) data model format (Figure 2) in order to evaluate different retrofitting scenarios. However it should be noted that theoretical estimations are not always achieved in practice, and therefore a certain degree of deviation may occur between the theoretical model and the actual fire stations [18].

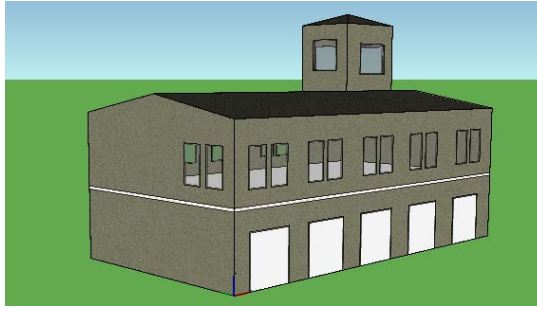


Figure 2. Industry Foundation Classes (IFC) data model for a typical Latvian fire station.

Using the 3D model, it is possible to evaluate the efficiency of various energy performance improvement measures and their conformity with the specific nature of fire stations. Similar layout and construction features can be found in many post-soviet countries including Russian Federation, where brick walls are historically widely used for such buildings.

3.2. Measurements of indoor air quality in a non-renovated fire station

The analysed building was constructed in 1910. There is not any mechanical ventilation and central hot tap water system installed. An exhaust ventilation system is installed to extract the exhaust gas from the firefighting truck exhaust pipes. Indoor air quality measurements were conducted in two different premises: a) a break room of a firefighting depot staff and b) a repair shop in the same building. Measurement results showed the diurnal changes of the indoor environmental parameters for the break room (Figure 3). In total 8000 measurements were recorded with 10-minute intervals.

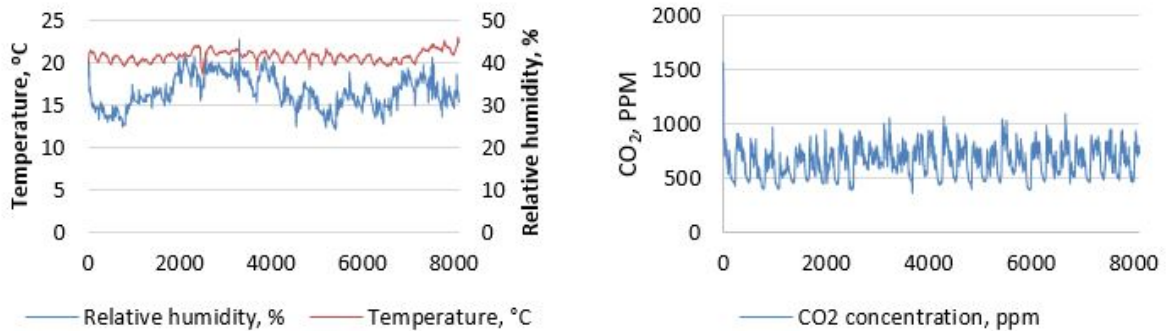


Figure 3. Indoor air quality measurements for the break room.

Analysis of the graphs in Figure 3 shows that the indoor air temperature ranges from 18 to 23 °C with an average of 20.7 °C. It can be concluded that the indoor air temperature fits the recommended temperature range for human thermal comfort set forth by Latvian Building Norms and commonly referred international industry recommendations, such as ASHRAE [19]. Changes in temperature follow a diurnal pattern with peaks in indoor air temperature during the second part of the day.

Relative humidity ranges from 25 to 45 % with an average of 33 %, which is below the recommended values for human comfort. Similarly to indoor air temperature, relative humidity peaks are observed primarily during the afternoon hours.

The average concentration values of carbon dioxide CO₂ came out to 662 ppm which is below the limit of 1000–1200 ppm set forth by industry standards. Concentrations of CO₂ peaks at around 900–1000 ppm during the second part of the day.

Results regarding the changes of indoor environmental parameters for the repair shop can be seen in Figure 4.

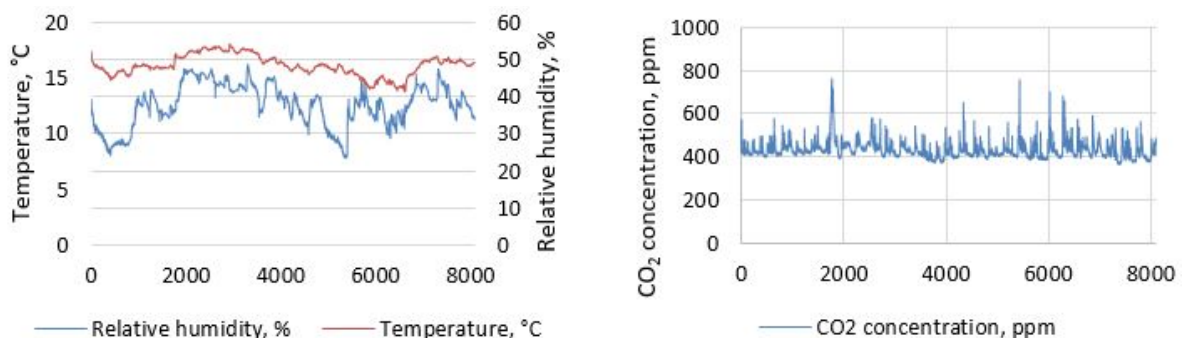


Figure 4. Indoor air temperature and relative humidity measurements for the repair shop.

The average concentration of carbon dioxide CO₂ came out to be 430 ppm which is below the limit set forth by industry standards. Concentrations of CO₂ ranges from 360–760 ppm during with peak during the second part of the day.

Given that the analyzed building didn't have any kind of controlled ventilation system, while CO₂ was kept within acceptable limits and the relative humidity was low, it can be concluded that the airtightness of the external building envelope was not sufficient.

3.3. Analysis of thermal energy consumption and technical conditions

The measured average annual energy consumption including electricity for fire stations was 317 kWh/m². The relationship curve showing the link between fire stations' energy consumption and the year they were constructed is shown in Figure. 5.

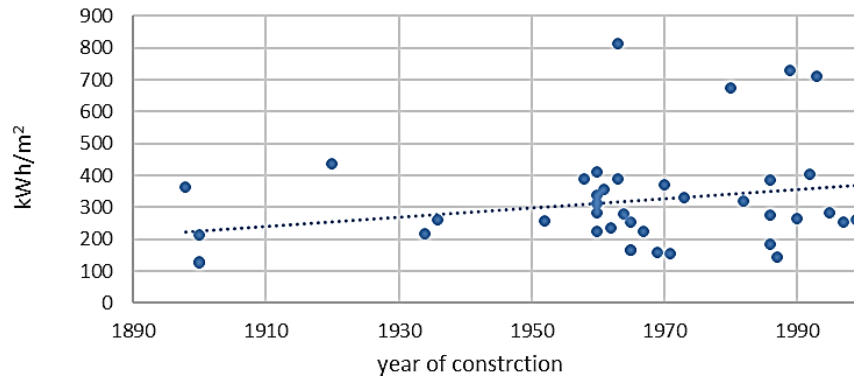


Figure 5. Measured average total annual energy consumption.

As it can be seen in Figure 5, there is no strict correlation between energy consumption of the building and its' year of construction. A more detailed analysis of thermal energy consumption in fire stations located in the City of Riga is shown in Figure 6.

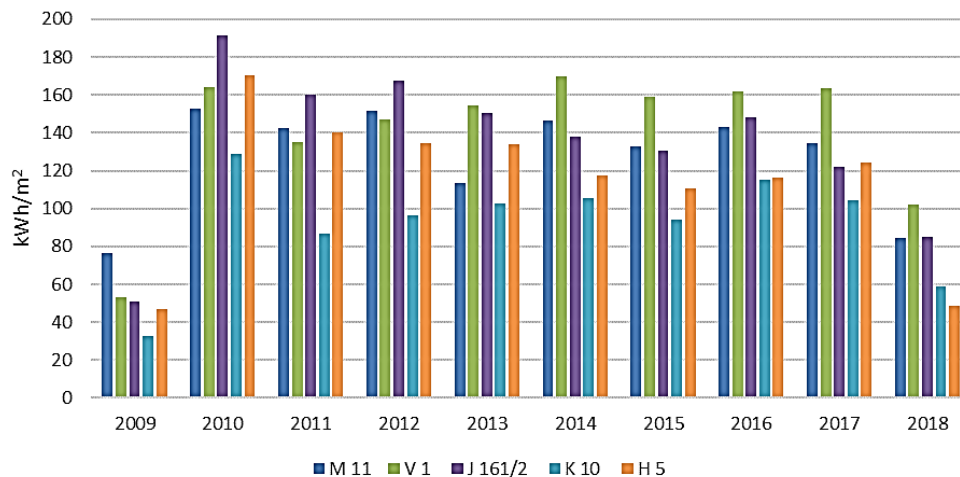


Figure 6. Annual heat energy consumption of fire station (address information is deliberately hidden).

The investigated buildings have poor thermal performance, which is due to the fact that those buildings were constructed before 1990 when the normative U-values stipulated by the national building code were not nearly as strict as they are today. The study results showed that the average annual heat consumption for fire departments is 135.4 kWh/m² within the timeline of 2010 to 2017. Data on the total annual energy consumption was not available for 2009 and 2018. Results are rather similar to typical Latvian multi apartment buildings, which annually consume 190 kWh/m² for heating and hot water preparation. It is also important to note that in contrast to residential buildings majority of the fire stations do not have central hot tap water systems. Instead, the electric hot water boilers are used.

During the energy audit, it was found that the existing hot tap water system is in poor technical condition and does not ensure sufficient supply of hot water.

3.4. Energy consumption estimation in different Latvian cities

In this chapter a theoretical estimation of energy consumption was performed for Latvian climatic conditions, which is similar in Baltic Region and in Western regions of Russian federation, in order validate dynamic energy calculations and to evaluate different retrofitting scenarios. For this purpose a typical Latvian fire station was selected (Figure 2). As a first step, a non-renovated building was analyzed. Table 1 presents data on Energy consumption of non-renovated buildings with the activity level of 2.0 MET, 1.4 CLO in garage and 1.2 MET, 0.85 CLO in office part. The energy consumption for hot tap water was not taken into consideration.

Table 1. Energy consumption of non renovated buildings, kWh/m².

	City of Riga	City of Liepaja	City of Gulbene	City of Daugavpils
HVAC electricity	0	0	0	0
District heating	136.2	123.2	160.7	151.5

As it can be seen in the table the obtained results for the City of Riga are in a good agreement with the measured data. The discrepancy is less than 10 %. It can be concluded that this model can be used for further estimation of the impact of retrofitting scenarios on final energy consumption.

In the scope of this study three retrofitting scenarios were analysed. Scenario 1 «basic» includes thermal insulation of building envelope in accordance to Latvian legislation [16] and installation of mechanical ventilation system without exhaust air heat recovery. Scenario 2 is similar to scenario 1, however, it is enhanced by the installation of the exhaust air heat recovery unit. Third scenario is a deep retrofitting approach which is suitable for Latvian climatic conditions [20, 21]. It includes installation of more efficient exhaust air heat recovery unit, better airtightness of building envelope and an extra thermal insulation that meets the passive house standard requirements.

Table 2. Description of retrofitting scenarios.

	U-values, W/m ² K	Ventilations rate, n ⁻¹	Exhaust air heat recovery, %	Airtightness of building envelopes q ₅₀ , m ³ /(m ² h)
Scenario 1 “basic”	Opaque elements – 0.2 Windows – 1.3 Doors 1.8	Garage – 2 Office part – 0.9	0	3.5
Scenario 2 – “basic plus”	Opaque elements – 0.2 Windows – 1.3 Doors 1.8	Garage – 2 Office part – 0.9	85	2
Scenario 3 “advanced”	Opaque elements – 0.10 Windows – 0.7 Doors 1.2	Garage – 2 Office part – 0.9	92	1

Table 3. Energy consumption of renovated buildings, kWh/m².

	Scenario 1				Scenario 2				Scenario 3			
	Riga	Liepaja	Gulbene	Daugavpils	Riga	Liepaja	Gulbene	Daugavpils	Riga	Liepaja	Gulbene	Daugavpils
HVAC electricity	25.7	25.7	25.7	25.7	25.1	25.1	25.1	25.1	25	25	25	25
District heating	229.0	215.1	265.9	252.9	63.2	54.5	83.9	80.1	46.1	39.1	64.7	62.14

Figure 7 shows annual comparison of thermal energy consumption before and after retrofitting.

The results of this study indicate that an installation of mechanical ventilation system without exhaust air heat recovery unit significantly increases energy consumption even for a well-insulated building. Installation of an exhaust air heat recovery unit, on the other hand, ensures a reduction of thermal energy consumption by 165.8 kWh/m² or by 72 %. However, there is a significant increase in electricity consumption to run an air handling unit which on average adds 25 kWh/m². The average district heating price in Riga is 62.8 Euro/MWh while the electricity price is 160 Euro/MWh. The economic benefit in this case would not be justified, as the financial benefit of energy saving measures of deep retrofit would not outweigh the cost of electricity consumption to run the AHU. Energy savings for thermal energy is 10.4 Euro/m² and increase for electricity use is 4 Euro/m². This would make an overall energy cost reduction 6.4 Euro/m².

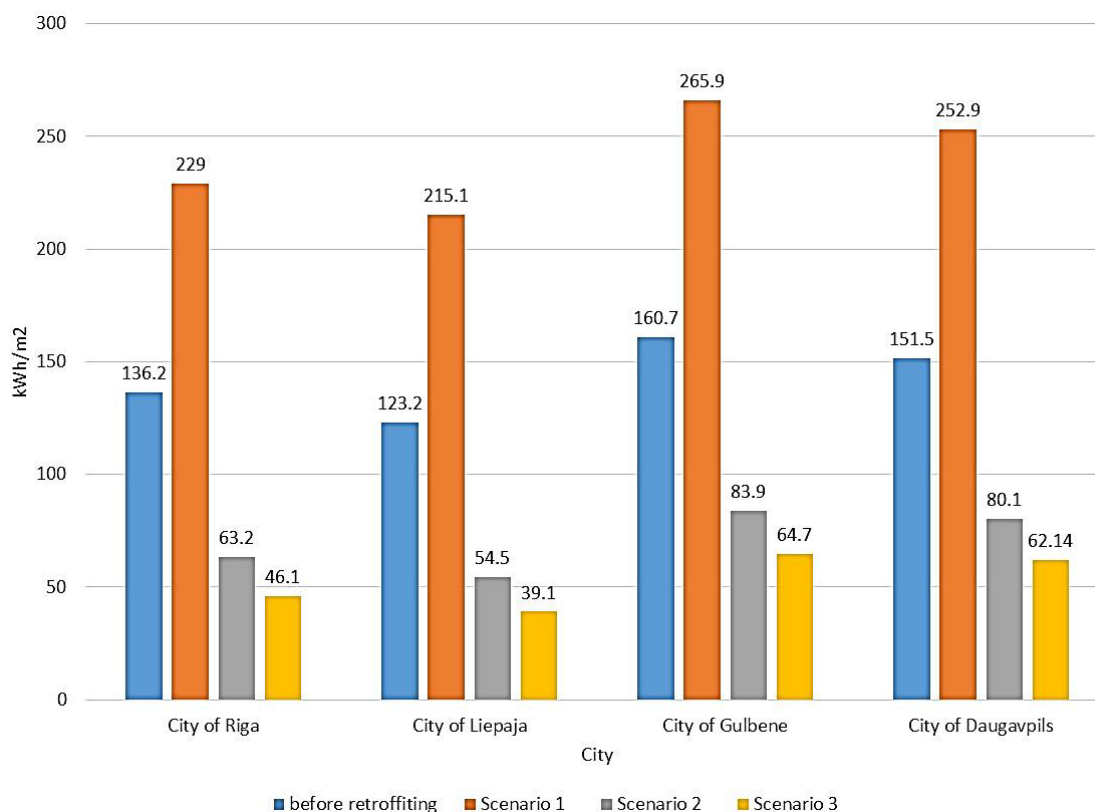


Figure 7. Comparison of energy consumption for heating before and after renovation.

4. Conclusions

In scope of this study a detailed analysis of indoor air quality and energy consumption for Latvian fire stations was performed. Acquired results can be expanded and applied in other countries and regions located in cold climate zone. Analysed buildings represent typical brickwork construction widely used before 1990ies not only in Latvia but in majority of the post-soviet countries.

1. Despite the increased focus on implementation of energy efficient measures in buildings, the world's energy consumption is constantly increasing. The main target group for implementation of energy efficiency measures in building sector are multi apartment and public buildings. Meanwhile the energy efficiency in so called unclassified buildings is not adequately addressed, as these buildings are not part of governmental subsidies. However, energy consumption of such buildings as fire stations should not be neglected. Firstly, majority of these buildings were constructed before 1990ies without substantial thermal insulation. Secondly, fire stations are operating 24/7 and should provide an adequate thermal comfort and indoor air quality for their personnel. Currently, the thermal comfort conditions can be ensured only in renovated airtight buildings

2. In scope of this study the indoor air quality measurements were performed in non-renovated fire station depot which is located in City of Riga, representing cold climate zone. Analysis had shown that the average indoor air temperature was 20.7 °C, average relative humidity – 33 % and CO₂ concentration 662 ppm. It can be concluded that non renovated external building envelope can be characterized by a high uncontrolled air infiltration rate. Extra air infiltration is compensated by extra heating load.

3. The paper presents the results of calculated and measured data of the energy consumption for fire stations that were built before 1990s. The measured data for these buildings show that average measured total thermal energy consumption is 135.4 kWh/m² while the total energy consumption including electricity was about 317 kWh/m².

4. Dynamic energy simulation for typical fire station has shown a good correlation with measured data. Based on the dynamic energy simulation the theoretical energy savings were evaluated for three different scenarios. Typical deep retrofitting package allows for 66 % reduction of thermal energy for space heating. Installation of mechanical ventilation system without heat recovery increases energy consumption by 72 % in comparison to renovated building without any mechanical ventilation.

5. Acknowledgements

This study was supported by the European Regional Development Fund project Nr.1.1.1.1/16/A/048 "Nearly zero energy solutions for unclassified buildings".

This work also has been partly supported by the European Regional Development Fund within the Activity 1.1.1.2 “Post-doctoral Research Aid” of the Specific Aid Objective 1.1.1 “To increase the research and innovative capacity of scientific institutions of Latvia and the ability to attract external financing, investing in human resources and infrastructure” of the Operational Programme “Growth and Employment” (1.1.1.2/VIAA/2/18/344)

References

1. D'Agostino, D., Mazzarella, L. What is a Nearly zero energy building? Overview, implementation and comparison of definitions. *Journal of Building Engineering*. 2019.
2. Shaffer, B., Flores, R., Samuelsen, S., Anderson, M., Mizzi, R., Kuitunen, E. *Urban Energy Systems and the Transition to Zero Carbon – Research and Case Studies from the USA and Europe*. Energy Procedia, 2018.
3. (DOE) US Department of Energy. *An Assessment of Energy Technologies and Research*, 2015.
4. Amecke, H., Deason, J. *Buildings Energy Efficiency in China, Germany and the United States*. Clim. Policy Initiat., 2013.
5. Gorshkov, A.S. The energy efficiency in the field of construction: questions of norms and standards and solutions for the reduction of energy consumption at buildings. *Magazine of Civil Engineering*. 2010. 11(1). Pp. 9–13.
6. Rueda, R., Cuéllar, M.P., Pegalajar, M.C., Delgado, M. Straight line programs for energy consumption modeling. *Appl. Soft Comput.* J. 2019.
7. Karatasou, S., Santamouris, M. Socio-economic status and residential energy consumption: A latent variable approach. *Energy Build.* 2019.
8. Oliveira, M. et al. Polycyclic aromatic hydrocarbons at fire stations: firefighters' exposure monitoring and biomonitoring, and assessment of the contribution to total internal dose. *J. Hazard. Mater.* 2017.
9. McCormac, Declan. *Dublin City Council Fire Brigade Survey. Display Energy Certificate: Advisory Report*. Dublin, 2011.
10. Aydin, E., Brounen, D. The impact of policy on residential energy consumption. *Energy*, 2019.
11. K. Forward, D. Nahill, and Jeffrey Stokes, «City of Boston's Firehouse Energy Efficiency» 2011.
12. Rokde, P., Valdes-Vasquez, R., Mosier, R. *The Green Status of Fire Stations in the United States: An Analysis of LEED-NC V3*. *J. Green Build.*, 2019.
13. Golova, T.A., Denisova, A.P. Energy efficiency of the Rural Wall multi-layer structure in low-rise building design. *Magazine of Civil Engineering*. 2014.52(8). Pp. 9–19. (rus). DOI: 10.5862/MCE.52.2.
14. Peregrine Energy Group. *Energy Efficiency Opportunities For Fire Department Facilities West Ossipee, New Hampshire*. Boston, 2011.
15. Baranova, D., Sovetnikov, D., Borodinecs, A. The extensive analysis of building energy performance across Baltic sea-region. *Sci. Technol. Built Environ.* 2018. Pp. 1–45, Apr.
16. Borodinecs, A., Zemitis, J., Sorokins, J., Baranova, D.V., Sovetnikov, D.O. Renovation need for apartment buildings in Latvia. *Magazine of Civil Engineering*. 2016. 68(8). Pp. 58–64. DOI: 10.5862/MCE.68.6
17. Danilevsky, L.N., Danilevsky, S.L. The algorithm and accuracy of definition of heattechnical indicators of buildings. *Magazine of Civil Engineering*. 2017. 73(5). Pp. 49–61. doi: 10.18720/MCE.73.5.
18. Korniyenko, S. Analysis of energy consumption levels for energy efficiency estimation in buildings. *Energy-Safety and Energy-Economy*, 2017.
19. ASHRAE. *ANSI/ASHRAE STandard 62.1 – 2007: Ventilation for acceptable indoor air quality*, 2010.
20. Kalamees, T. et al. What kind of heat loss requirements NZEB and deep renovation sets for building envelope? *CESB 2016 – Central Europe Towards Sustainable Building 2016: Innovations for Sustainable Future*, 2016.
21. D'Agostino, D., Mazzarella, L. Data on energy consumption and Nearly zero energy buildings (NZEBs) in Europe. *Data Br.*, 2018.

Contacts:

Anatolijs Borodinecs, +37126079655; anatolijs.borodinecs@rtu.lv

Aleksejs Prozuments, 26079655; aleksejs.prozuments@rtu.lv

Aleksandrs Zajacs, 003719874677; aleksandrs.zajacs@rtu.lv

Jurgis Zemitis, +37128369940; jurgis.zemitis@rtu.lv

© Borodinecs, A., Prozuments, A., Zajacs, A., Zemitis, J., 2019



DOI: 10.18720/MCE.90.9

Maturity sensors placement based on the temperature transitional boundaries

Ye.B. Uteпов^{1*}, A. Aniskin², A.P. Ibrashov³, A. Tulebekova¹

¹ L.N. Gumilyov Eurasian National University, Nur-Sultan, Kazakhstan

² University North, Koprivnica, Croatia

³ CSI Research & Lab, LLP, Nur-Sultan, Kazakhstan

* E-mail: utepov-elbek@mail.ru

Keywords: reinforced concrete, hydration, temperature, sensors, positioning, interpolation, heat map

Abstract. The way in which the maturity sensors are placed determines their number required for a particular monolithic building skeleton. Previous studies scarcely address this aspect, providing only logical assumptions. Therefore, this study proposes an alternative placement strategy for maturity sensors based on transitional boundaries of concrete curing temperature distribution. The transitional boundaries may be determined using the heat map representation of temperature distribution, where the unknown values are computed by the Inverse Distance Weighting method. Based on the experimentally poured concrete slab and randomly embedded maturity sensors revealed that the transitional boundaries form elliptical shapes. The temperature distributions along the largest diameter of ellipses were plot on a single graph, which created regular and reverse parabolas. As a result, the distance between the closest opposite intersections of the parabolas is assumed as the maximum acceptable step to set the maturity sensors. The proposed placement strategy may be applicable for the sensors that measure various continuous phenomena, for example the relative humidity.

1. Introduction

There are many methods to control the concrete compressive strength. Some of them are clustered as destructive, some as nondestructive [1]. The traditional destructive control of concrete strength is based on the tests of standard concrete specimens by compression using the press machines. In the field conditions the standard specimens are prepared from the freshly arrived concrete mixture in parallel with the pour of concrete structure. Usually for each batch of the concrete mixture, at least 9 specimens are prepared. It is supposed that the specimens cure at the same ambient conditions as the concrete structure. At the curing ages of 3, 7 and 28 the specimens are tested. Three specimens are tested at each testing day. The load of squeezing corresponding to the moment when the specimen starts breaking, or the cracks appear on it, is fixed as the value of the strength. The average of strengths of the three specimens is taken as a value of concrete compressive strength at a certain day of curing [2]. This method of strength control is widely accepted worldwide as the more robust method. However, due to several circumstances and human factor the testing procedure is not always precisely followed in the constructing sites. These circumstances may include wrong sequence and timing of the preparation of specimens (e.g. the structure is poured too late after the specimens are prepared), confusing the batch of concrete mixture, and the difference of curing conditions (e.g. after preparation the specimens are hold at the laboratory). Moreover, it is worth noting the difference of sizes between the specimens and a real structure. Massive structures cure slower than the smaller ones. All of this makes the test results more unreliable. Nevertheless, the method is still extensively used, since it is regulated by the actual construction standards of almost each country all over the world [1, 2]. The traditional nondestructive concrete-control mostly refers to the shock-impulse method implemented in a special equipment. The mechanism of shock-impulse method is based on the energy appearing at the hit of hammer of the corresponding equipment. According to the preliminary calibrations, the obtained energy is converted into the value of compressive strength. The shock-impulse method is also regulated by the construction standards in many countries. Its main advantage is that it gives the result immediately. The equipment is mostly portable and easy to handle [3]. Although it has certain advantages, the method has its own disadvantages. The method enables

Uteпов, Ye.B., Aniskin, A., Ibrashov, A.P., Tulebekova, A. Maturity sensors placement based on the temperature transitional boundaries. Magazine of Civil Engineering. 2019. 90(6). Pp. 93–103. DOI: 10.18720/MCE.90.9

Утепов Е.Б., Анискин А., Ибрашов А., Тулебекова А. Размещение датчиков зрелости в зависимости от границ температурного перехода // Инженерно-строительный журнал. 2019. № 6(90). С. 93–103. DOI: 10.18720/MCE.90.9



obtaining the compressive strength at a certain point where the hammer hits. Therefore, referring the obtained value of compressive strength to the whole structure would be a wrong decision. Since in reality, every part of the structure cures differently. This is why the several points of the structure must be tested. In general, both traditional methods imply the human involvement, labor-intensive, cost-inefficient, and disable real time measurements [4].

The concrete curing refers to the exothermal process [5], where the cement hydration releases heat. This is why at early ages of concrete curing the internal temperature of concrete intensively increases and slowly decreases afterwards [6]. The continuous strength gain of the concrete throughout many years indicates that the chemical reaction in it is long-lasting. Measuring the internal temperature over time opens great opportunities during concrete works. It helps making proper decisions on unmolding the formwork and loading the structures, and influences the pace of construction [7]. This feature of concrete is studied in many previous works [6, 8–11]. It is proven that the combined effect of time and temperature enables estimating the actual compressive strength of the concrete. To refer to this effect, [12] introduced the terms «maturity index» or «temperature-time factor». There are two maturity functions, enabling concrete strength estimation: Nurse-Saul and Arrhenius functions. The Nurse-Saul function assumes that there is a linear relationship between the maturity and hydration temperature history. The Arrhenius function assumes that there is an exponential relationship between the compressive strength and hydration temperature [12]. The maturity method is effective by means of embedded temperature sensors that can be either wired or wireless in terms of control [13, 14]. The sensors enable continuous monitoring of internal parameters of concrete (not only the temperature) as long as they are powered by electricity [15–17]. The manufacturers of such sensors are the Canadian company «Giatec» [18, 19], American company «ConcreteSensors» [20] and some others are widely discussed in [5]. The advantages and disadvantages of these sensors are thoroughly discussed by [21], who proposed the less expensive sensor prototype with improved features (Figure 1).



Figure 1. Sensor prototype [21].

In [21] it is argued that the economic impact for construction sites may be reached due to the timely knowledge about the concrete strength, which saves overhead expenses. However, using too many sensors is quite costly [5]. Because the expenses to purchase many sensors may leave no savings at all. Therefore, it is important to define a necessary number of sensors to be used for a certain monolithic building skeleton in advance. The number of sensors needed depend on the location where the sensors must be installed. Currently, the optimal location of the concrete maturity sensors has not been well studied, but there are studies on optimal placement strategies of other types of sensors [22–24], mainly used for modal tests [25] proposed the sensor placement strategy based on the finite element simulations, where the case of heat transfer problem in the concrete slab was considered. Due to the specificity of the internal temperature behavior of concrete curing, none of the considered above strategies seems appropriate for maturity sensor placement. However, some techniques proposed by [25], such as representing the heat transfer in a colored heat map, may be helpful [26] suggests to consider three aspects when selecting the installation locations of the concrete maturity sensors, such as critical weather locations on the structural element, concrete mixture pour schedule, and the structurally critical locations. The environmental phenomena, such as wind, rain, and shadow may influence the internal temperature of concrete to some extent, which eventually affects its strength gain [21] proposed a cross-correlation matrix that shows how the concrete parameters influence each other at laboratory and field conditions. According to this matrix for the studied mixture, in the ambient conditions the effect of internal temperature on the strength gain is only 14 %. The rest of 86 % goes to the ambient temperature (33 %), internal relative humidity (25 %) and ambient relative humidity (29 %). The pour schedule is also important. Since one huge structure may require several pours until it is filled completely, and the interval between the pours may fluctuate up to several hours. In this case [26] proposes a mandatory installation of the sensor in the location of the last pour. Due to the concrete at this location will most likely gain the necessary strength later than the concrete at the previously poured locations. Probably the most important locations to install the sensors are the critical locations, where the highest negative and positive design moments are observed. Commonly, in the monolithic building skeleton the maximum positive moment

is located at a mid-span, and a maximum negative moment is located at a slab-column boundary. These locations are considered the most responsible when conducting the design of spatial skeleton of the building [26]. Other aspects that need to be considered are the power of the network (if the sensor is wireless) and the safety from accidental damage. The existing analogs of maturity sensors [18, 20] use Bluetooth data transfer protocol. Because of the short operating distance of Bluetooth, it is important to install the sensors at easy-accessible locations, to ease the future data retrieval. To eliminate this shortcoming, [21] proposed to change the Bluetooth into the Narrow Band IoT network. The safe locations to install the sensors would be those with low workers traffic. The concrete pouring may also damage the sensors. Therefore, it is necessary to install them in a distance from the pouring location [26].

Previous studies propose only logically assumed locations to install the sensors without providing justifications. Considering the importance of the sensor positioning, current study proposes an alternative approach for allocation of the embedded sensors. As per [27], the temperature is a continuous phenomenon. This means its values change smoothly throughout the surface until the border (hereinafter – transitional boundary) where the influence of other phenomena begins to prevail. If considering the internal temperature during the concrete curing process, the same behavior may be observed. This study anticipates that such behavior of the internal temperature of concrete gives understanding of at which step the maturity sensors must be set. Hypothesized that the transitional boundaries most likely occur around the reference points, where the values of the temperature are known, and creates elliptical shapes. Therefore, it is assumed that the maximum setting step of maturity sensors must be less than the largest diameter of each elliptical shape of transitional boundary. The suitable approach to define and measure the transitional boundaries could be the colored heat map representation of temperature distribution as used in [25], which enables visualizing the change over the surface somewhat clearly. In the light of the aforementioned assumptions, this study aims to develop and justify an alternative strategy of concrete maturity sensor placement. Thus, the concrete curing temperature distribution is considered as the object of study and the transitional boundaries of temperature values – as the subject of study. Further chapters enclose the proposed hypothesis more in detail based on the experimental studies conducted.

2. Methods

To create the heat maps of temperature distribution and determine the transitional boundaries, at least the values of temperature at the reference points must be predefined. The rest of temperature values throughout the whole surface can be determined using the interpolation technique. Laying out all the temperature values at the corresponding positions in the 2D plane and assigning scaled colors to them generates a heat map. Moreover, the more reference points involved, the more precisely the interpolation calculates the temperatures at each position in the plane. To avoid unrealism, the reference points must be randomly distributed across the plane. The heat map may give a proper justification of the maximum setting step of maturity sensors. To investigate the hypothesis, a reinforced concrete slab experimentally taken as the 2D plane. The slab had the rectangular shape with the dimensions of 12×6×0.2 m and poured outdoor. Conducted the following sequence of operations:

1) Before the pour of the slab by the concrete, 5 maturity sensors developed by [21] were mounted on the rebar of the slab in random locations in the plane, as shown in the Figure 2 below. The sensors were located in the center of the slab thickness.

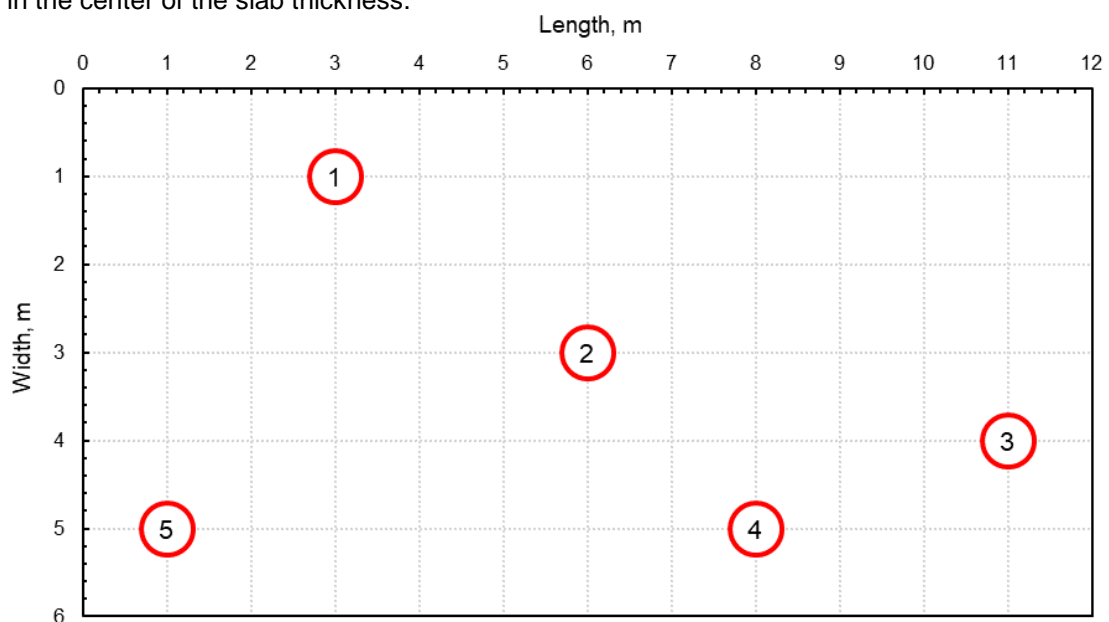


Figure 2. Locations of the maturity sensors.

2) The slab was poured by the concrete B25 M350 in 6 approaches of a skip by around 14 m³ of concrete mixture from one batch. Total time spent for the pouring process was less than an hour. The ambient temperature was between 10÷12 °C. The slab had no thermal insulation. The particleboard was used as a formwork of the slab. The thermos-physical properties of the formwork were not considered, since it was expected that its effect would be insignificant due to the similarity of the ambient temperature and the initial temperature of the concrete mixture.

3) Immediately after the pour, with the interval of one hour the sensors measured the internal temperature of concrete for 28 days (i.e. each sensor had 672 readings).

4) The readings of each sensor were transferred to the computer and converted into Excel format.

5) In the Excel document, 672 sheets were created, each containing the readings of corresponding hour of measurements.

6) In each sheet, 2D planes were created with the size of 1200×600 cells (i.e. the size of each cell was equivalent to 10×10 cm in regard to the size of the concrete slab). The values of temperature at reference points (existing readings) were laid in the corresponding cells of each of the planes (Figure 2).

7) The unknown values of temperature in the 2D planes were interpolated using the Inverse Distance Weighting (IDW) method. IDW is a spatial interpolation method that enables estimating the unknown values based on the weighted average of the known values [28, 29]. Thus, each cell on the 2D plane was assigned by the equation, where the weights represented the distances from each cell to the locations of reference points. The equation is as followed:

$$t_c = \frac{\sum_{i=1}^n \frac{t_i}{d_i^p}}{\sum_{i=1}^n \frac{1}{d_i^p}}, \quad (1)$$

where t_c is unknown value of temperature in the cell;

i is number of reference point;

t_i is known value of temperature at the reference point i ;

d_i is search distance from the cell to the reference point i ;

p is power of IDW ($p = 2$) [29].

8) To generate the hourly heat maps, the cells on the 2D plane were color-scaled using the Excel conditional formatting feature based on the values of temperature that the cells contained. The choice of Excel to create heat maps is justified by its flexibility in the implementation of custom method for estimating unknown values of temperature based on existing ones. Existing software to estimate temperature field are adapted to solve specific tasks such as thermal design. They are based on certain methods, which cannot be customized and do not cover the needs of this study. Thereby, they considered the influence of ambient temperature on a particular object, which temperature is initially stable. In case of concrete mixture, its temperature is instable and fluctuating over time. Moreover, there is no need to consider the ambient temperature when the sensors measure the actual internal temperature of concrete.

9) All the hourly heat maps were combined into one average in order to define the averaged transitional boundaries and the shaded elliptical shapes that they surround. Then there were drawn the cross-section lines passing through the reference points and coinciding in the orientation of the largest diameters of elliptical shadings.

10) Temperature distribution graphs were created in the cross-sections, and the distance between the opposite intersections of the graphs enabled determining the acceptable setting step of sensors.

3. Results and Discussion

As planned, the measurement of temperature in the body of reinforced concrete slab was carried out by the embedded sensors for 28 days with the interval of 1-hour. The sensors collected 672 readings each. When displaying all the obtained readings onto the chart, observed the following behavior of the concrete curing temperature presented in Figure 3 below.

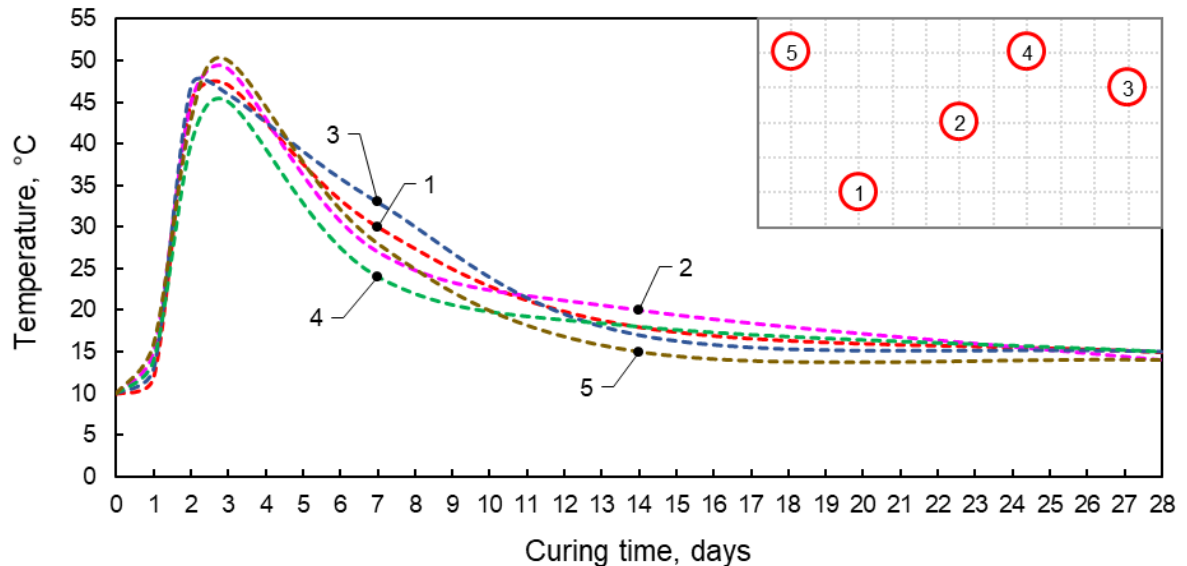


Figure 3. Temperature mode of concrete curing.

From the figure above it is seen that although the initial temperature of concrete mixture when pouring was uniform (around 10 °C), at further concrete curing observed the difference between the values of temperature at all reference points (i.e. sensor locations). This indicates that the concrete gained its strength unevenly throughout the whole period. Some parts of the slab gained strength faster than other parts. There could be many reasons of this consequence, such as poor quality of concrete mixture and its rheological structure, influence of environmental phenomena or simply human error while taking care of the concrete. However, it is impossible to achieve a perfectly even curing of concrete, especially when it comes to the extended and flat structures. In general, it is shown that at the second and third days the internal temperature reached its peak. This is due to the exothermal reaction during the cement hydration. Thus, the highest temperature of 50 °C reached on the third day at the location of sensor Number 5. Little earlier, on the second day the temperature at the location of sensor No. 3 reached its peak at 47 °C. The temperature peak at other sensor locations fluctuated between 45–49 °C. The notable variation of the temperature between 24–33 °C is observed on the 7th day, which is probably most like is caused by the influence of external phenomena. Furthermore, the temperatures at the sensor locations smoothly decreased up to the 28th day and reached the ambient temperature of around 14–15 °C. The small variation of temperature at the 28th day may indicate that the strength of concrete at all the reference points became more or less uniform.

To enable smooth transition of scaled colors in the heat maps, the 2D plane was split into the grid of cells with the size of 10 cm. A smaller cell size, such as 1 cm, would make the transition even smoother. Thus, 672 heat maps were obtained for each hour within 28 days. The heat maps of the most important ages of 1, 2, 3, 7, 14 and 28 days of the concrete curing are presented in Figure 4 a), b), c), d), e) and f) respectively.

The figures above demonstrate how the temperature changed during the 28 days of concrete curing. The heat maps were generated based on the values of temperature at each cell of 2D planes. Here some values were known (at reference points), some were unknown and interpolated using IDW method, as planned. The heat maps used three scaled colors to demonstrate the change of the temperature values on the plane: blue, white and red. The cells colored in blue and red represents the lower and the higher values of temperature respectively. The white color is selected to indicate the transitional boundaries between the lower and higher values of temperature and vice versa. It should be noted that the scale of the colors at each heat map of a certain period is assigned between the lowest and the highest values of temperature within the corresponding heat map. For note, if scaling the colors between the lowest and highest values of temperature within the whole period of 28 days of concrete curing (e.g. between 10–50 °C), the change of the temperature values in majority of heat maps would be indistinguishable. The obtained heat maps colorfully emphasize the dynamics of changes in the internal temperature of concrete, which can eventually provoke a variation in the strength gain in different parts of the concrete structure. In this regard, it helps better understanding the hydration reaction in the concrete structure to make proper decisions on preventive measures.

To gain a general picture on the reasonable setting step of the sensors, the average heat map were generated based on the values of temperature at all the cells of all 672 hourly heat maps. The resulting heat map is shown in Figure 5 below.

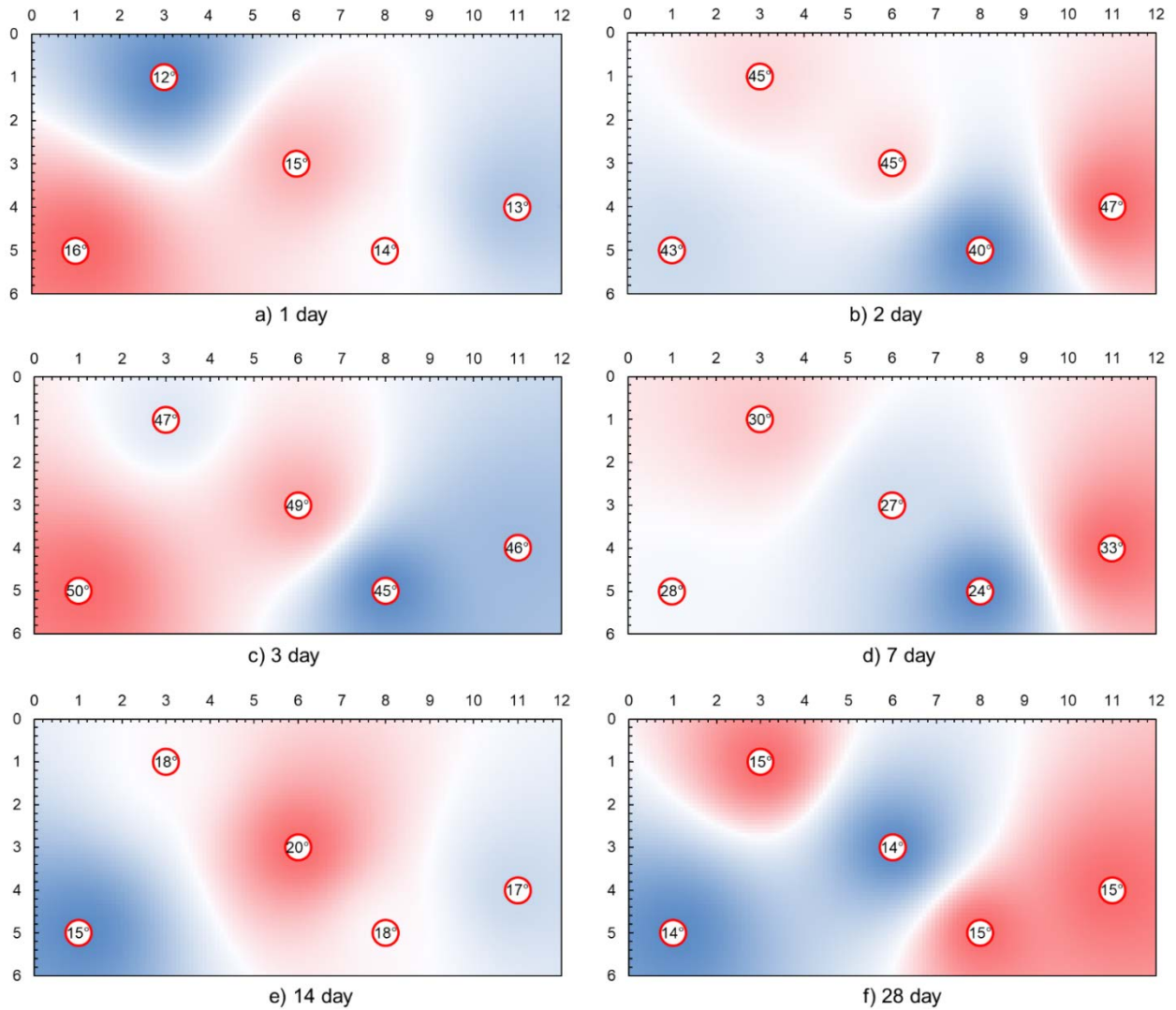


Figure 4. Heat maps of temperature distribution.

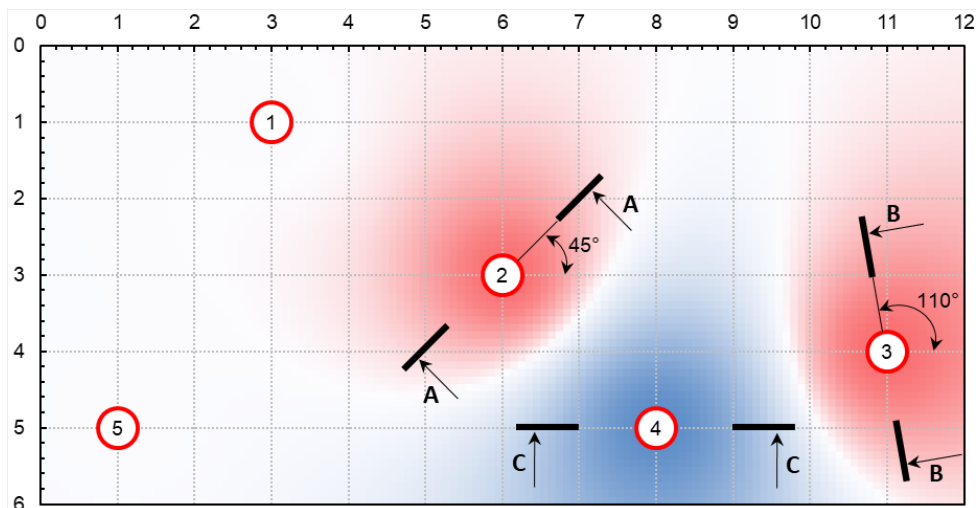


Figure 5. Heat map of average temperature distribution.

The obtained heat map depicted distinct shadings with ellipsis shapes around three reference points. Here the lowest temperature values in the cells colored in blue are observed around the sensor No. 4 and the highest – around the sensors No. 2 and 3 in the cells colored in red. Other sensor locations fell on to the mean values of the temperature distribution. Such a picture is a consequence of higher instability of the values of internal temperature at the reference points No. 2, 3 and 4, than at the reference points No. 1 and 4, based on the readings during 28 days of concrete curing. However, it is this picture that gives basis for further reasoning and justification of the acceptable sensor setting step. Thereby, according to the last operation of this study, the temperature distribution graphs were created at the cross-sections A-A, B-B and C-C that pass

through the reference points. For the location of sensor No. 2, 3 and 4, the cross-sections were selected at the angles of 45, 110 and 0 degrees to the horizontal axis respectively, and the graphs of temperature distribution were drawn, as presented in Figure 6 below.

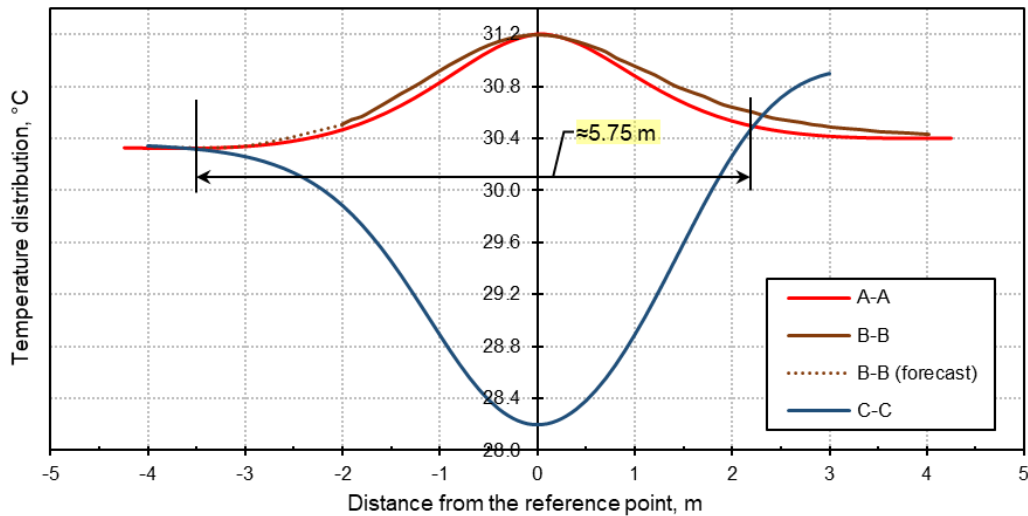


Figure 6. Distribution of temperature at cross-sections.

From the figure above it is seen that the values of temperature at cross-sections fell within the range of 28.2–31.2 °C. The graphs took a parabolic shape with the peaks on the vertical axis. The higher peaks are observed at the reverse parabolic graphs A-A and B-B, where the highest values of temperature was identified (Figure 5). Conversely, the lower peak is observed at the regular parabolic graph C-C. Since the lower part of the cross-section B-B rests close on the border of the 2D plane, its temperature distribution graph was prolonged through the forecast of its trend (marked with dotted line), in order to enable its intersection with the graph C-C having the lower peak. If considering the graphs A-A and B-B, it may be noticed that their transitional boundaries start in an average distance of 3.5 m from their reference points. In case of the graph C-C, from one side (left) the transitional boundary starts in a distance of 4 m, while from the other side (right), it starts in a distance of 3 m from the reference point. To retrieve the combined effect of all the temperature distribution graphs, suggested to pay attention onto the intersection of the graphs on both sides. Such intersections may create several new asymmetrical shapes, depending on the number of cross-sections taken. Proposed that the distance between the closest opposite intersections of the temperature distribution graphs represented by regular and reverse parabolas may be considered as the maximum acceptable setting step of maturity sensors. In addition, to ease the selection of the intersections, proposed to consider the asymmetrical shape with the smallest area that lays more inward compared to other asymmetrical shapes. This study revealed the distance of 5.75 m between the two opposite intersections of the temperature distribution graphs, based on three considered cross-sections. Thus, the setting step of maturity sensors suggested to be set less than this distance.

Similar results may be obtained if using a thermal imaging camera instead of the maturity sensor. However, it should be noted that the thermal imaging camera enable reading the temperature only on the surface of concrete structure, and therefore this equipment is not appropriate to replicate this study. It is important to have the readings of internal temperature of concrete structure. Current study involved the wireless maturity sensors. However, to replicate the study one may use wired temperature sensors as well.

4. Conclusion

1. Previous studies proved the effectiveness of the embedded maturity sensors for monitoring the reinforced concrete structures compared to the traditional destructive and nondestructive methods in terms of labor-intensity, portability and comfortableness, as well as ability of real time measurements. However, the cost-efficiency of the embedded sensors depends on their number used for a certain volume of concrete structure or the whole building skeleton due to their relatively high purchase price. Therefore, it is worth paying particular attention to the way the sensors are placed in the concrete structure when using them. Since the more efficient the positioning of the sensors, the less they can be used.

2. It is revealed that the existing methods to establish locations of concrete maturity sensors are weakly substantiated and based solely on logical assumptions, not considering the possible variation of curing intensity at different parts of the concrete structure. Therefore, in this study proposed the alternative method to position the maturity sensors underpinned by the dynamics of transitional boundaries of temperature distribution during the whole concrete curing period.

3. Experimentally identified that the transitional boundaries surround the patterns with more or less similar (or clustered) values of temperature. Moreover, these patterns most likely have the elliptical shapes.

The temperature distribution throughout the whole dimension of concrete structure may be obtained using the Inverse Distance Weighting interpolation method, using the known values from the sensor measurements and their locations. Thereby, in current study defined the convenience of heat map representation to clearly demonstrate the transitional boundaries and the pattern of temperature distribution. The heat map enables expressing the patterns by the color-scaled shadings of each point at the concrete structure, where the intensity of the colors are dependent of the values of temperature at the points. It was established that the suitable color scheme of the heat maps may consist of three different colors, that correspond to the values of low, medium and high temperatures on a certain heat map. In this study selected the color scheme that consists of blue, white and red colors. In this study 672 hourly heat maps were created that give clear visual interpretation of the dynamics of temperature distribution throughout the 28-day period. To enable defining their combined effect, it is proposed to create the consolidated heat map, based on the sum of values of all the heat maps at each respective points.

4. The study identified that the combined plotting of temperature distribution along the lines that coincide with the direction of the largest diameter of formed in the consolidated heat map elliptical shadings creates the asymmetrical shapes. These shapes are composed of the regular and reverse parabolas. Depending on the number of shadings selected to the plot, there may occur several asymmetrical shapes. It is suggested to consider the distance between the intersection of regular and reverse parabolas that create the asymmetrical shape with the smallest area as the maximum acceptable setting step of the maturity sensors. As a result of the experiments conducted, it is not recommended to exceed the setting step of the maturity sensor above 5.75 m.

References

1. Kibar, H., Ozturk, T. Determination of concrete quality with destructive and non-destructive methods. *Computers and Concrete [Online]*. 2015. 15(3). Pp. 473–484. DOI: 10.12989/cac.2015.15.3.473. URL: <http://koreascience.or.kr/journal/view.jsp?kj=KJKHDQ&py=2015&vnc=v15n3&sp=473>
2. Malek, J., Kaouther, M. Destructive and non-destructive testing of concrete structures [Online]. *Jordan Journal of Civil Engineering*. 2014. 8(4). Pp. 432–441. URL: <https://pdfs.semanticscholar.org/75e7/564faf6e1f4e83a0d73a3418236df16515d2.pdf>
3. Erdal, H., Erdal, M., Simsek, O., Erdal, H.I. Prediction of concrete compressive strength using non-destructive test results. *Computers and Concrete*. 2018. 21(4). Pp. 407–417. DOI: 10.12989/cac.2018.21.4.407.
4. Helal, J., Sofi, M., Mendis, P. Non-destructive testing of concrete: A review of methods [Online]. *Electronic Journal of Structural Engineering*. 2015. 14(1). Pp. 97–105. URL: <http://www.ejse.org/Archives/Fulltext/2015-1/2015-1-9.pdf>
5. Taheri, S. A review on five key sensors for monitoring of concrete structures [Online]. *Construction and Building Materials*. 2019. 204. Pp. 492–509. DOI: 10.1016/j.conbuildmat.2019.01.172. URL: <https://linkinghub.elsevier.com/retrieve/pii/S0950061819302090>
6. Ge, Z., Wang, K. Modified heat of hydration and strength models for concrete containing fly ash and slag [Online]. *Computers & concrete*. 2009. 6(1). Pp. 19–40. DOI: 10.12989/cac.2009.6.1.019. URL: <http://koreascience.or.kr/journal/view.jsp?kj=KJKHDQ&py=2009&vnc=v6n1&sp=19>
7. Zemajtis, Je.Z. Role of Concrete Curing. Portland Cement Association. Skokie, 2014.
8. Anwar Hossain, K.M. Influence of extreme curing conditions on compressive strength and pulse velocity of lightweight pumice concrete [Online]. *Computers & concrete*. 2009. 6(6). Pp. 437–450. DOI: 10.12989/cac.2009.6.6.437. URL: <http://koreascience.or.kr/journal/view.jsp?kj=KJKHDQ&py=2009&vnc=v6n6&sp=437>
9. Chen, H.-J., Yang, T.-Y., Tang, C.-W. Strength and durability of concrete in hot spring environments [Online]. *Computers & concrete*. 2009. 6(4). Pp. 269–280. DOI: 10.12989/cac.2009.6.4.269. URL: <http://koreascience.or.kr/journal/view.jsp?kj=KJKHDQ&py=2009&vnc=v6n4&sp=269>
10. Zhang, B., Cullen, M., Kilpatrick, T. Spalling of heated high performance concrete due to thermal and hygric gradients [Online]. *Advances in concrete construction*. 2016. 4(1). Pp. 1–14. DOI: 10.12989/acc.2016.4.1.001. URL: <http://koreascience.or.kr/journal/view.jsp?kj=TPTPR5&py=2016&vnc=v4n1&sp=1>
11. Farzampour, A. Temperature and humidity effects on behavior of grouts. *Advances in concrete construction*. An international journal. 2017. 5(6). Pp. 659–669. DOI: 10.12989/acc.2017.5.6.659.
12. ASTM C1074. Standard Practice for Estimating Concrete Strength by the Maturity Method, West Conshohocken, Pennsylvania, USA, 1998.
13. Lee, H.-S., Cho, M.-W., Yang, H.-M., Lee, S.-B., Park, W.-J. Curing Management of Early-age Concrete at Construction Site using Integrated Wireless Sensors [Online]. *Journal of Advanced Concrete Technology*. 2014. 12(3). Pp. 91–100. DOI: 10.3151/jact.12.91_100. URL: https://www.jstage.jst.go.jp/article/jact/12/3/12_91/_article
14. Kwon, S.H., Jang, K.P., Bang, J.-W., Lee, J.H., Kim, Y.Y. Prediction of concrete compressive strength considering humidity and temperature in the construction of nuclear power plants [Online]. *Nuclear Engineering and Design*. 2014. 275. Pp. 23–29. DOI: 10.1016/j.nucengdes.2014.04.025. URL: <https://linkinghub.elsevier.com/retrieve/pii/S0029549314002507>
15. Ashteyat, A.M., Ismeik, M. Predicting residual compressive strength of self-compacted concrete under various temperatures and relative humidity conditions by artificial neural networks. *Computers and Concrete*. 2018. 21(1). Pp. 47–54. DOI: 10.12989/cac.2018.21.1.047.
16. Hannan, M.A., Hassan, K., Jern, K.P. A review on sensors and systems in structural health monitoring: Current issues and challenges. *Smart Structures and Systems*. 2018. 22(5). Pp. 509–525. DOI: 10.12989/sss.2018.22.5.509.
17. Ranz, J., Aparicio, S., Fuente, J.V., Anaya, J.J., Hernández, M.G. Monitoring of the curing process in precast concrete slabs: An experimental study [Online]. *Construction and Building Materials*. 2016. 122. Pp. 406–416. DOI: 10.1016/j.conbuildmat.2016.06.041. URL: <https://linkinghub.elsevier.com/retrieve/pii/S0950061816309680>
18. Walsh, D. IoT Hero from Giatec Develops «SmartRocks» with Bluetooth [Online]. URL: https://www.silabs.com/community/blog.entry.html/2016/01/18/iot_hero_from_giatec-Av1P (date of application: 25.08.2019).
19. Giatec, S. Real-time temperature and maturity monitoring of concrete [Online]. URL: <https://www.giatecscientific.com/products/concrete-sensors/smartrock-maturity-meter/> (date of application: 25.08.2019).

20. ConcreteSensors. Durable wireless concrete sensor for concrete strength, temperature, RH [Online]. URL: <https://concret esensors.com/concrete-strength-and-temperature-monitoring-platform/wireless-concrete-sensor/> (reference date: 25.08.2019).
21. Utepov, Y.B., Khudaibergenov, O.A., Kabdush, Y.B., Kazkeev, A.B. Prototyping an embedded wireless sensor for monitoring reinforced concrete structures. *Computers and Concrete*. 2019. 24(2). Pp. 95–102. DOI: 10.12989/cac.2019.24.2.095.
22. Liu, K., Yan, R.-J., Guedes Soares, C. Optimal sensor placement and assessment for modal identification [Online]. *Ocean Engineering*. 2018. 165. Pp. 209–220. DOI: 10.1016/j.oceaneng.2018.07.034. URL: <https://linkinghub.elsevier.com/retrieve/pii/S0029801818305584>
23. Yin, H., Dong, K., Pan, A., Peng, Z., Jiang, Z., Li, S. Optimal sensor placement based on relaxation sequential algorithm [Online]. *Neurocomputing*. 2019. 344. Pp. 28–36. DOI: 10.1016/j.neucom.2018.03.088. URL: <https://linkinghub.elsevier.com/retrieve/pii/S0925231219301742>
24. Zhang, J., Maes, K., De Roeck, G., Reynders, E., Papadimitriou, C., Lombaert, G. Optimal sensor placement for multi-setup modal analysis of structures [Online]. *Journal of Sound and Vibration*. 2017. 401. Pp. 214–232. DOI: 10.1016/j.jsv.2017.04.041. URL: <https://linkinghub.elsevier.com/retrieve/pii/S0022460X1730370X>
25. Nath, P., Hu, Z., Mahadevan, S. Sensor placement for calibration of spatially varying model parameters [Online]. *Journal of Computational Physics*. 2017. 343. Pp. 150–169. DOI: 10.1016/j.jcp.2017.04.033. URL: <https://linkinghub.elsevier.com/retrieve/pii/S0021999117303042>
26. Giatec, S. Practical Installation Applications for Wireless Maturity Sensors [Online]. URL: <https://www.giatecscientific.com/education/practical-installation-applications-for-wireless-maturity-sensors/> (reference date: 25.08.2019).
27. Kessler, F.C., Battersby, S.E. *Working with Map Projections: A Guide to Their Selection*. CRC Press, 2019. Pp. 65.
28. Jing, M., Wu, J. Fast image interpolation using directional inverse distance weighting for real-time applications [Online]. *Optics Communications*. 2013. 286. Pp. 111–116. DOI: 10.1016/j.optcom.2012.09.011. URL: <https://linkinghub.elsevier.com/retrieve/pii/S0030401812009595>
29. GISGeography. Inverse Distance Weighting (IDW) Interpolation [Online]. URL: <https://gisgeography.com/inverse-distance-weighting-idw-interpolation/> (date of application: 25.08.2019).

Contacts:

Yelbek Utepov, +7(700)2101733; utepov-elbek@mail.ru
Aleksej Aniskin, +3(8592)304-94-06; aaniskin@unin.hr
Azamat Ibrashov, +7(701)7676673; a.ibrashov@csi.kz
Assel Tulebekova, +7(701)6481866; krasavka5@mail.ru

© Utepov, Ye.B., Aniskin, A., Ibrashov, A.P., Tulebekova, A., 2019



DOI: 10.18720/MCE.90.9

Размещение датчиков зрелости в зависимости от границ температурного перехода

Е.Б. Утепов^{1*}, А. Анискин², А. Ибрашов³, А. Тулебекова¹

¹ Евразийский национальный университет им. Л.Н. Гумилева, Нур-Султан, Казахстан,

² Университет Север, Копривница, Хорватия,

³ TOO CSI Research & Lab, Нур-Султан, Казахстан

* E-mail: utepov-elbek@mail.ru

Ключевые слова: железобетон, гидратация, температура, датчики, размещение, интерполяция, тепловая карта

Аннотация. От способа размещения датчиков зрелости зависит их количество, необходимое для определенного каркаса монолитного здания. Прежние исследования слабо освещают данный аспект, приводя лишь логические предположения. Поэтому в данном исследовании предлагается альтернативная стратегия размещения датчиков, основанная на переходных границах распределения температуры твердения бетона. Переходные границы могут быть определены с помощью построения тепловой карты распределения температуры, где неизвестные значения рассчитываются методом обратного взвешивания расстояния. На основе экспериментально залитой бетонной плиты с произвольно встроенными датчиками зрелости установлено, что переходные границы образуют эллиптические формы. Распределение температур по наибольшему диаметру эллипсов было нанесено на график, что привело к созданию правильных и обратных парабол. В результате, расстояние между ближайшими противоположными точками пересечения парабол принято в качестве максимально допустимого шага для установки датчиков зрелости. Предлагаемая стратегия размещения может быть применима к датчикам, которые измеряют различные непрерывные явления, например, относительную влажность.

Литература

1. Kibar H., Ozturk T. Determination of concrete quality with destructive and non-destructive methods // Computers and Concrete. 2015. № 3(15). Pp. 473–484. DOI:10.12989/cac.2015.15.3.473.
2. Malek J., Kaouther M. Destructive and non-destructive testing of concrete structures // Jordan Journal of Civil Engineering. 2014. № 4(8). Pp. 432–441.
3. Erdal H., Erdal M., Simsek O., Erdal H.I. Prediction of concrete compressive strength using non-destructive test results // Computers and Concrete. 2018. № 4(21). Pp. 407–417. DOI:10.12989/cac.2018.21.4.407.
4. Helal J., Sofi M., Mendis P. Non-destructive testing of concrete: A review of methods // Electronic Journal of Structural Engineering. 2015. № 1(14). Pp. 97–105.
5. Taheri S. A review on five key sensors for monitoring of concrete structures // Construction and Building Materials. 2019. № 204. Pp. 492–509. DOI:10.1016/j.conbuildmat.2019.01.172.
6. Ge Z., Wang K. Modified heat of hydration and strength models for concrete containing fly ash and slag. Computers & concrete. 2009. № 1(6). Pp. 19–40. DOI:10.12989/cac.2009.6.1.019.
7. Zemajtis J.Z. Role of Concrete Curing. Portland Cement Association. Skokie, 2014.
8. Anwar Hossain K.M. Influence of extreme curing conditions on compressive strength and pulse velocity of lightweight pumice concrete // Computers & concrete. 2009. № 6(6). Pp. 437–450. DOI:10.12989/cac.2009.6.6.437.
9. Chen H.-J., Yang T.-Y., Tang C.-W. Strength and durability of concrete in hot spring environments // Computers & concrete. 2009. № 4(6). Pp. 269–280. DOI:10.12989/cac.2009.6.4.269.
10. Zhang B., Cullen M., Kilpatrick T. Spalling of heated high performance concrete due to thermal and hygric gradients // Advances in concrete construction. 2016. № 1(4). Pp. 1–14. DOI:10.12989/acc.2016.4.1.001.
11. Farzampour A. Temperature and humidity effects on behavior of grouts // Advances in concrete construction, An international journal. 2017. № 5(6). Pp. 659–669. DOI:10.12989/acc.2017.5.6.659.
12. ASTM C1074. Standard Practice for Estimating Concrete Strength by the Maturity Method, West Conshohocken, Pennsylvania, USA, 1998.
13. Lee H.-S., Cho M.-W., Yang H.-M., Lee S.-B., Park W.-J. Curing Management of Early-age Concrete at Construction Site using Integrated Wireless Sensors // Journal of Advanced Concrete Technology. 2014. № 3(12). Pp. 91–100. DOI:10.3151/jact.12.91_100.

14. Kwon S.H., Jang K.P., Bang J.-W., Lee J.H., Kim Y.Y. Prediction of concrete compressive strength considering humidity and temperature in the construction of nuclear power plants // Nuclear Engineering and Design. 2014. № 275. Pp. 23–29. DOI: 10.1016/j.nucengdes.2014.04.025.
15. Ashteyat A.M., Ismeik M. Predicting residual compressive strength of self-compacted concrete under various temperatures and relative humidity conditions by artificial neural networks // Computers and Concrete. 2018. № 1(21). Pp. 47–54. DOI:10.12989/cac.2018.21.1.047.
16. Hannan M.A., Hassan K., Jern K.P. A review on sensors and systems in structural health monitoring: Current issues and challenges // Smart Structures and Systems. 2018. № 5(22). Pp. 509–525. DOI:10.12989/sss.2018.22.5.509.
17. Ranz J., Aparicio S., Fuente J.V., Anaya J.J., Hernández M.G. Monitoring of the curing process in precast concrete slabs: An experimental study // Construction and Building Materials. 2016. № 122. Pp. 406–416. DOI: 10.1016/j.conbuildmat.2016.06.041.
18. Walsh D. IoT Hero from Giatec Develops “SmartRocks” with Bluetooth. [Электронный ресурс]. URL: https://www.silabs.com/community/blog.entry.html/2016/01/18/iot_hero_from_giatec-Av1P (дата обращения: 25.08.2019).
19. Giatec, S. Real-time temperature and maturity monitoring of concrete. [Электронный ресурс]. URL: <https://www.giatecscientific.com/products/concrete-sensors/smartrock-maturity-meter/> (дата обращения: 25.08.2019).
20. ConcreteSensors. Durable wireless concrete sensor for concrete strength, temperature, RH. [Электронный ресурс]. URL: <https://concretesensors.com/concrete-strength-and-temperature-monitoring-platform/wireless-concrete-sensor/> (дата обращения: 25.08.2019).
21. Uteпов Y.B., Khudaibergenov O.A., Kabdush Y.B., Kazkeev A.B. Prototyping an embedded wireless sensor for monitoring reinforced concrete structures // Computers and Concrete. 2019. № 2(24). Pp. 95–102. DOI:10.12989/cac.2019.24.2.095.
22. Liu K., Yan R.-J., Guedes Soares C. Optimal sensor placement and assessment for modal identification // Ocean Engineering. 2018. № 165. Pp. 209–220. DOI: 10.1016/j.oceaneng.2018.07.034.
23. Yin H., Dong K., Pan A., Peng Z., Jiang Z., Li S. Optimal sensor placement based on relaxation sequential algorithm // Neurocomputing. 2019. № 344. Pp. 28–36. DOI: 10.1016/j.neucom.2018.03.088.
24. Zhang J., Maes K., De Roeck G., Reynders E., Papadimitriou C., Lombaert G. Optimal sensor placement for multi-setup modal analysis of structures // Journal of Sound and Vibration. 2017. № 401. Pp. 214–232. DOI: 10.1016/j.jsv.2017.04.041.
25. Nath P., Hu Z., Mahadevan S. Sensor placement for calibration of spatially varying model parameters // Journal of Computational Physics. 2017. № 343. Pp. 150–169. DOI: 10.1016/j.jcp.2017.04.033.
26. Giatec S. Practical Installation Applications for Wireless Maturity Sensors. [Электронный ресурс]. URL: <https://www.giatecscientific.com/education/practical-installation-applications-for-wireless-maturity-sensors/> (дата обращения: 25.08.2019).
27. Kessler F.C., Battersby S.E. Working with Map Projections: A Guide to Their Selection. CRC Press, 2019. Pp. 65.
28. Jing M., Wu J. Fast image interpolation using directional inverse distance weighting for real-time applications // Optics Communications. 2013. № 286. Pp. 111–116. DOI: 10.1016/j.optcom.2012.09.011.
29. GISGeography. Inverse Distance Weighting (IDW) Interpolation. [Электронный ресурс]. URL: <https://gisgeography.com/inverse-distance-weighting-idw-interpolation/> (дата обращения: 25.08.2019).

Контактные данные:

Елбек Бахитович Утепов, +7(700)2101733; utepov-elbek@mail.ru

Алексей Анискин, +3(8592)3049406; aaniskin@unin.hr

Азамат Ибрашов, +7(701)7676673; a.ibrashov@csi.kz

Асель Тулебекова, +7(701)6481866; krasavka5@mail.ru

© Утепов Е.Б., Анискин А., Ибрашов А., Тулебекова А., 2019



DOI: 10.18720/MCE.90.10

Ductility and moment redistribution capacity of two-span RC beams

R. Ehsani, M.K. Sharbatdar*, A. Kheyroddin

Semnan University, Semnan, Iran

**E-mail: msharbatdar@semnan.ac.ir*

Keywords: high performance fiber reinforced cement composites, two span concrete beam, ductility, moment redistribution, steel fibers

Abstract. The particular weaknesses of concrete buildings are brittle fracture and lack of material ductility, so using steel reinforcements and discrete fibers are an attempt to overcome this weakness. Strain hardening behavior under tensile force has made new material, High Performance Fiber Reinforced Cement Composite “HPFRCC” as a high performance material with high energy absorption capability and high cracking ability before failure. Therefore the structural application of this composite material in the structural members such as continuous beams to control cracks width and formation of multiple cracks, improve ductility, moment redistribution capacity have been investigated. In this paper, the effect of using HPFRCC containing 2 % steel fibers on the flexural performance of four large two-span reinforced concrete beams with similar dimensions and similar longitudinal reinforcement ratios has experimentally been investigated. Two beams were ordinary concrete with two different arrangements of stirrups in the middle support (hogging) and mid span (sagging) area and two other beams were companion but made with full HPFRCC composites. The specimens have rectangular cross section of 250 mm (height)×200 mm (width) and are continuous over two spans of 1800 mm each and two concentrated equal statically monotonic loads (from zero to the failure) are applied at the mid-span of each beam. The experimental results showed that using HPFRCC layers in section beams and reducing the spacing of the stirrups, increased the ultimate load, ductility ratio, plastic hinge characteristics and moment redistribution capacity of these beams compare to reference beam. The greatest load carrying capacity values 42 % were observed in FHPS compared to RCN beam. Maximum moment redistribution values of around 23.31 % was observed in FHPS beam and maximum displacement ductility ratio 1.8 was observed in FHPS beam compare to reference beam. In HPFRCC beam, the sufficient shear strength is provided in beam without local shear cracks. This allows the formation of plastic hinge in beams and plastic hinge zone.

1. Introduction

One of the high performance materials that has been prominent in recent years is the high performance fiber reinforced cement composites (HPFRCC). Strength, stiffness, toughness (the area under the stress-strain curve) and durability are the main characteristics of a High Performance Material. researchers investigated Durability of an Ultra High Performance Fiber Reinforced Concrete (UHPRFC) [1]. HPFRCC were classified in a way, which was separated from fiber reinforced Concrete (FRC), so HPFRCC were a special type of FRC composites whose characteristic sign was the strain hardening behavior under tensile force after the first cracking, which was accompanied by multiple cracks to reach high strains [2]. Researcher have recently looked at the applications of high performance fiber- reinforced cement composites [3]. At present, the most widely used micro and nanomodifiers of cement composites and simultaneously components of the cement stone are the finely dispersed active mineral additives such as silica foam and metakaolin [4–8]. It is known that concrete is a heterogeneous material, it has the low tensile strength to compressive strength ratio, and is prone to formation of microcracks in the process of shrinkage during hardening. These peculiarities determine the necessity of the solution of specific problems to identify the optimal combination of the

Ehsani, R., Sharbatdar, M.K., Kheyroddin, A. Ductility and moment redistribution capacity of two-span RC beams. Magazine of Civil Engineering. 2019. 90(6). Pp. 104–118. DOI: 10.18720/MCE.90.10

Эхсани Р., Шарбатдар М.К., Хайруллин А. Пластичность и способность перераспределения моментов двухпролётных железобетонных балок // Инженерно-строительный журнал. 2019. № 6(90). С. 104–118. DOI: 10.18720/MCE.90.10



This open access article is licensed under CC BY 4.0 (<https://creativecommons.org/licenses/by/4.0/>)

concrete matrix with different types of reinforcing fibers which technical characteristics may be varied within wide limits. The use of a fiber reinforcement allows to improve the tensile strength and tensile strength in bending, impact and fatigue strength, reduce the shrinkage the deformations, prevent the cracking, increase the flexibility, impact, and abrasive resistance, increase frost resistance, water resistance, etc. By applying the disperse reinforcing fibers of different types and sizes, we can adjust characteristics of concrete thereby ensuring required performance properties and durability [8–12].

Many structural applications of HPFRCC material are concentrated on simple beams, continuous beams (moment redistribution as effective parameters in RC structures), and beam-column connections, so the related researches are given following. Hemmati et al. (2015), performed experimental parametric studies to evaluate the impact of compressive strength, loading type and tensile reinforcement ratio on the characteristics of the final deformation of simplified support beams HPFRCC. It showed that, if concentrated loading in the middle of the span were changed to uniform loading, the plastic hinge rotation capacity would increase and examined the flexural behavior of high performance fiber reinforced concrete beams with the effect of the thickness of the HPFRCC layer at the height of the beam's cross section under a two-point flexural test also Researcher conducted research on increasing the bearing capacity in reinforced concrete frame using HPFRCC materials by numerical methods. In these models, the panel zone material was replaced by HPFRCC, which had different tensile and compressive strengths, and then complete concrete frames and complete HPFRCC frame were compared. The results showed that the use of these materials increased the bearing capacity and ductility of these frames [13–16].

Maghsoudi et al. (2010), investigated of reinforced high strength concrete continuous beams strengthened with fiber reinforced polymer. Experimental program was focused on flexural behavior and moment redistribution in continuous HSC beams. It was concluded that, as the number of CFRP sheet layers increases, the ultimate strength becomes higher, but the ductility, moment redistribution and ultimate strain of the CFRP sheet decrease. An analytical model for moment–curvature and load capacity were developed and used for the tested specimens. Good agreement between experiment and prediction values was reported [17].

And also Carmo et al. (2008) studied analytically factors affecting moment redistribution in continuous RC structures which are ignored in design codes. The studied parameters are structural type, load type, concrete strength, and beam slenderness. The main objective of the study was to understand better the capacity of forces redistribution in reinforced concrete beams [18–21]. Moreover, Holschemacher et al. (2012) investigated continuous two-layer reinforced concrete beam. 5 Models and full-scale statically determinate two-layer beams (TLB), made of steel fiber high strength concrete (SFHSC) in the compression zone and normal strength concrete (NSC) in the tensile zone, have been tested by the Researchers. As in the previous research stages, interaction of the concrete layers in a CTLB was studied to demonstrate the efficiency of such beams for real structures. No cracks between the SFHSC and NSC layers were observed up to the ultimate limit state of the tested beam, which demonstrates proper interaction between the layers. The results obtained in the present study enable a recommendation of CTLB for practical application as effective and economical continuous bending elements [23–25].

Mostofinejad et al. (2007) conducted a parametric study on moment redistribution in continuous RC beams with equal spans under uniform loading was performed. First, the governing equation for the allowable percent of moment redistribution was extracted using ductility demand and ductility capacity concepts. The effects of different parameters such as the concrete compressive strength, the amount and the strength of reinforcing steel, the magnitude of elastic moment at the support and the ratio of the length to the effective depth of the continuous beam on moment redistribution were then investigated. The results showed that, whereas the permissible moment redistribution in continuous reinforced concrete beams based on the relevant rules in the current codes is not in a safe margin in some cases, it is rather conservative in most cases [26]. Visintin et al (2018) investigated the moment redistribution in ultra-high performance fiber reinforced concrete beams. The results of the experimental investigation show that for beams where the hinge formed at the support, the observed moment redistribution was greater than the code predictions. However for the beam where the hinge formed under the load points, observed moment redistribution was significantly less than codes predictions. Hence, the results of this study show current design guidelines do not always provide a conservative prediction of moment redistribution in UHPFRC beams [27].

Bagge et al (2014) investigated the moment redistribution in RC beams, study of the influence of longitudinal and transverse reinforcement ratios and concrete strength. Evaluation of the experimental study indicated a highly nonlinear structural behavior of the tested beams with the distribution of moment differing from linear elastic analysis, even for low load levels. The evolution of moment redistribution and the moment redistribution at the ultimate limit state (ULS) were appreciably dependent on the arrangement of longitudinal reinforcement, whilst the transverse reinforcement ratio had a marginal impact up to yielding of the longitudinal reinforcing steel, with the concrete strength slightly reducing the degree of moment redistribution [28, 29].

Saghafi et al. (2018) investigated enhancement of seismic performance of beam-column joint connections using high performance fiber reinforced cementitious composites. The test results revealed that HPFRCC connections considerably enhanced shear and flexural capacity as well as deformation and damage

tolerance behavior at post-cracking stage compared to those of normal concrete at ultimate stages. Moreover, the failure mode of HPFRCC specimens changed from shear mode to flexural mode compared to the failure mode of concretes without required seismic details [30, 31].

A survey of literature shows that more experimental work is needed to investigate the use of HPFRCC material instead of normal concrete in continuous concrete beams and a research program must be established for investigating the structural behavior of a RC beam with HPFRCC. A great amount of researches in recent years, focused on the durability and steel corrosion of these composite beams and it is necessary to evaluate the structural behavior of these hybrid members. Furthermore, very limited research studied the effect of HPFRCC and confinement of concrete in compression on the rotational capacity, ductility and the capacity of redistributing stresses and moments between positive and negative regions of reinforced continuous concrete beams.

This paper examines the complete nonlinear response of a RC continuous beam and HPFRCC continuous concrete beams tested under monotonically increasing loads. From a different perspective, an important issue in designing HPFRCC continuous beams is the requirement of appropriate ductility and the capacity of redistributing stresses and moments between positive and negative regions. Given the collapsing flexural modes in these beams, the analysis of stress and moment redistribution calls for special investigation.

2. Methods

2.1. Materials properties of experimental program

In this research, the components of the materials and the mixing design used for constructing High Performance Fiber Reinforced Cement Composite (HPFRCC) were result of testing the specimens with different proportions of materials to achieve hardening behavior. So that the best mixing design based on Weight ratio was presented in Table 1. The cement amount used in the construction of beams was Portland cement with density of 3.05 g/cm^3 and the sand used in HPFRCC concrete had a diameter of 0.1 mm to 2.4 mm. In the construction of Normal Strength Concrete (NSC). Aggregates with a maximum diameter of 10 mm were used and the sand was smaller than 4.75 mm (sieve number 4). Sand and gravel had a specific density of 2.65 g/cm^3 . Silica fume with density of 2.2 g/cm^3 and grain size $0.1 \mu\text{m}$ and super plasticizer based poly-carboxylate with a density of about 1.07 g/cm^3 were used in the construction of concrete beams. Hook-end steel fibers with 30 mm length, 0.6 mm diameter, aspect ratio (l/d) of 50, tensile strength 1100 MPa, modulus of elasticity 200 GPa and density 7.85 gm/cm^3 were employed in this study. The density of this steel fiber is 7850 kg/m^3 and the weight of 0.01 m^3 of this fiber is 7850, so the volume fraction equal 2 % means that from 100 percentage of total volume of each cubic meter of concrete, 2 % equal 0.02 m^3 and 157 kg filled with steel fiber.

Table 1. Mixture proportions of HPFRCC and NSC.

Name of material	Concrete Components							
	Cement (Kg/m ³)	Sand (kg/m ³)	Gravel (kg/m ³ *)	Water (kg/m ³)	Super plasticizer (kg/m ³)	Silica fume (kg/m ³)	Steel fiber (kg/m ³)	Fiber volume fraction V_f (%)
HPFRCC*	850	1062	–	257	13.77	85	157	2
NSC**	450	597	1083	210	–	–	–	–

* High performance fiber reinforced cement Composite, ** normal strength concrete

Six cube samples with dimensions of $150 \times 150 \times 150 \text{ mm}$ were used to determine the compressive strength of normal strength concrete (NSC) and HPFRCC. The mean values of the 28 day compressive strengths of cubic samples for NSC and HPFRCC were 42.62 and 82.94 MPa, which were equal to 36.22 and 70.50 MPa in compressive strength cylindrical samples, respectively. The typical setup for the uniaxial tensile test is shown in Figure 1. To avoid fractures outside the measurement area, both ends of the specimens were made in the shape of a dog-bone. The elongation of the specimen was measured using two linear variable displacement transducers placed on two opposite sides of the specimen with a gauge length of 100 mm. The load was applied using displacement control hydraulic jack at a constant rate of 0.1 mm/min. Tensile Stress-strain responses of specimens was shown in Figure 1. The measured stress–strain curves are presented in Figure 1. The maximum tensile strain exceeded 0.71 % and the maximum tensile strength was approximately 6.7 MPa.

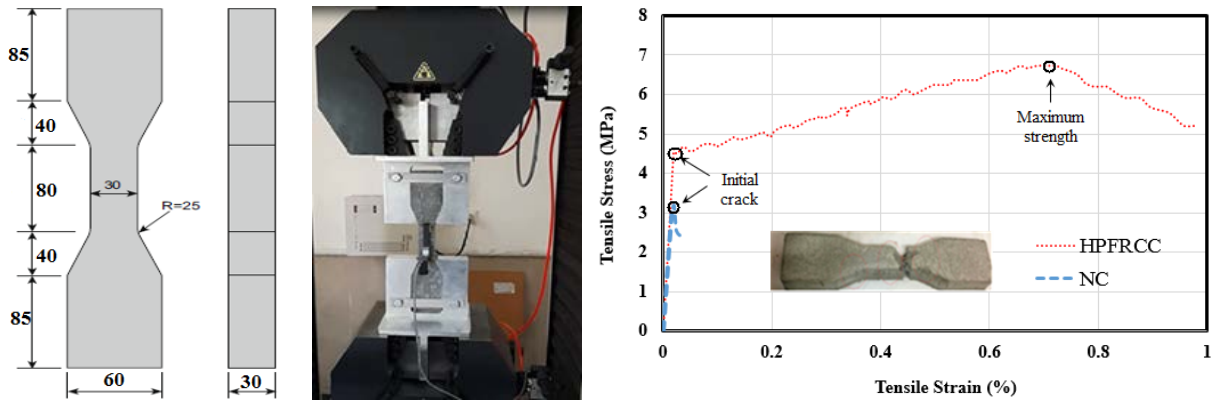


Figure 1. Dog-bone specimen configuration for uniaxial tensile tests (Units: mm).

In Table 2. Some important characteristics associated with the reinforcing steel are shown for all dimensions used for reinforcing the beams. The yield strength (f_y), yielding strain (ϵ_{sy}), ultimate strength (f_u) and ultimate strain (ϵ_{su}) are presented as mean values from standardized material tests.

Table 2. Reinforcing steel characteristics.

Type of rebar	Diameter Φ (mm)	Yielding strength f_y (MPa)	Yielding strain ϵ_{sy} (%)	Ultimate strength f_u (MPa)	Ultimate strain ϵ_{su} (%)	Modulus of elasticity E_s (MPa)
Longitudinal rebar	14	520	0.25	640	16	210
Longitudinal rebar	10	530	0.24	663	16	210
Transverse rebar	8	510	0.20	780	14	210

2.2. Test setup and instrumentation

In order to study the flexural behavior of two-span continuous beams with conventional concrete and HPFRCC composite, specimens had been selected that were as close to half-scale as possible to achieve reliable results. The general test set-up was shown in Figures 2 and 3, the beams consisted of two equal spans with two roller supports at both ends and one hinged support at the middle. A 1000 kN hydraulic actuator was used to apply a monotonic concentrated load on the mid-point of a rigid steel spreader beam. And also three load cells were used to measure the reaction at the supports. To measure the applied total load by hydraulic jack, a Load cell with a capacity of 1000 kN was used. Moreover, deflection was measured, using Linear Variable Differential Transformers (LVDTs), at three different locations in each span: at the midpoint, one-quarter, and three-quarters of the span length. Considering the distance of the experimental rigid frames and considering this limitation, the beams were 4000 mm long with two equal spans (1800 mm each span) to which two concentrated forces were applied at mid span. The beams were rectangular 250 mm \times 200 mm (height \times width) and this cross section was constant in all tests, as was the slenderness, $L/h = 7.2$ (L is the span length and h is the beam height) as shown in Figure 4.

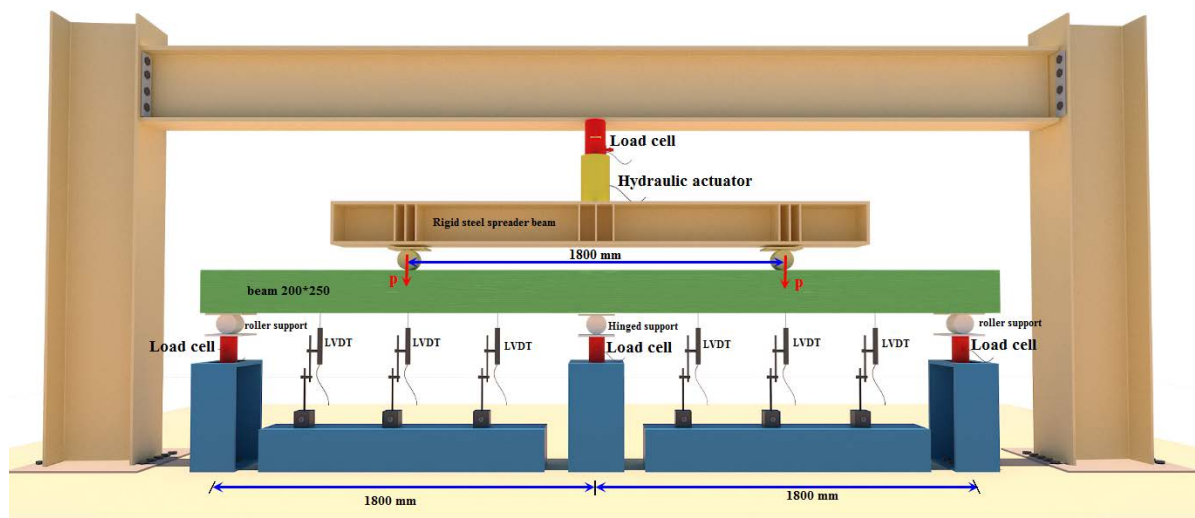


Figure 2. Test setup and instruments used in experiment of the beams.



Figure 3. General view of the test setup.

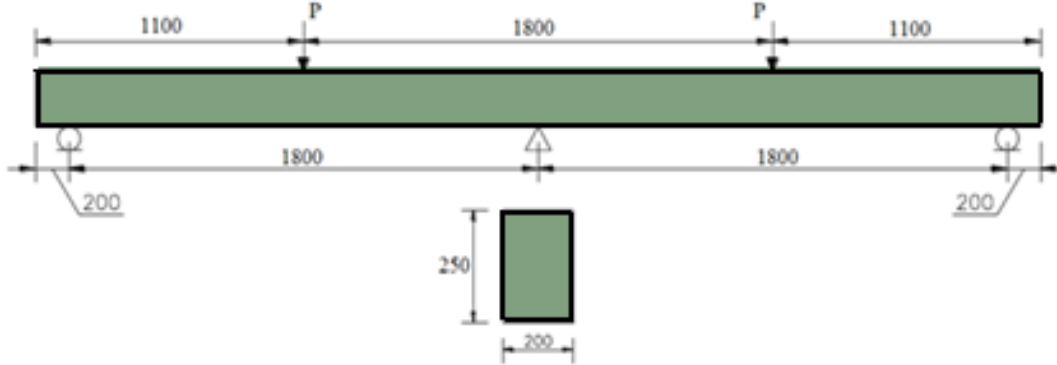


Figure 4. General Dimension of test specimens (unit: mm).

The reinforcement ratio (ρ_1, ρ_2) consumed in these beams was selected in such a way that the area section of bars was not more than balance reinforcement ratio (ρ_b) so the flexural failure occurred, this assumption was shown in Figure 5. As shown in Figure 6, two and three bars of 14 mm in diameter were used as the bottom and top longitudinal reinforcement negative moment at middle support and two bars of 14 mm in diameter as top and three bars of 14 mm and one bar of 10 mm were used at the maximum positive moment in the middle of the span. At the middle support section, the reinforcement ratio (ρ_1) was 0.01 and at mid-span section (ρ_2) was 0.012. This means that the longitudinal reinforcement ratio the mid – span section was 1.2 times that at the middle support section to allow plastic moment redistribution. In addition, the ratio of the bars used was more than Minimum amount and brittle failure did not occur in specimens. The area of the Stirrups used in these experimental samples was chosen in a way that was more than the minimum shear reinforcement. Therefore, the shear failure in these beams did not occur and the flexural behavior was dominant. After cracking of critical sections in a continuous steel-reinforced concrete beam, the difference between actual and predicted linear- elastic moment distribution in such beams can be identified in two stages. The first stage is caused by difference in concrete cracking in critical regions, and the second stage is caused by plastic deformation of steel reinforcement. Also, for beams with constant cross-section, flexural stiffness after cracking was found to be approximately proportional to tensile reinforcement ratio. Consequently, the distribution of bending moment after cracking will change according to the provided reinforcement as demonstrated in Figure 5. Electrical Strain Gauges (ESG) with a length of 30 mm and the electrical resistance of 120 ± 0.3 ohms were attached to the reinforcement and concrete surface at the three critical locations: middle support and two mid-span sections, as shown in Figures 6-a and 6-b. The details of all specimens are given in Table 3.

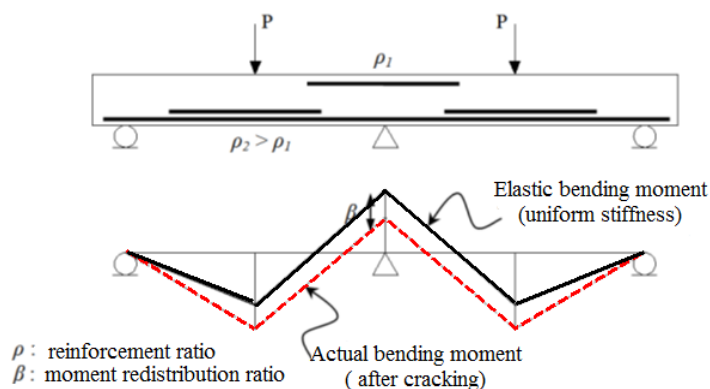


Figure 5. Elastic and actual bending moment in a continuous beam.

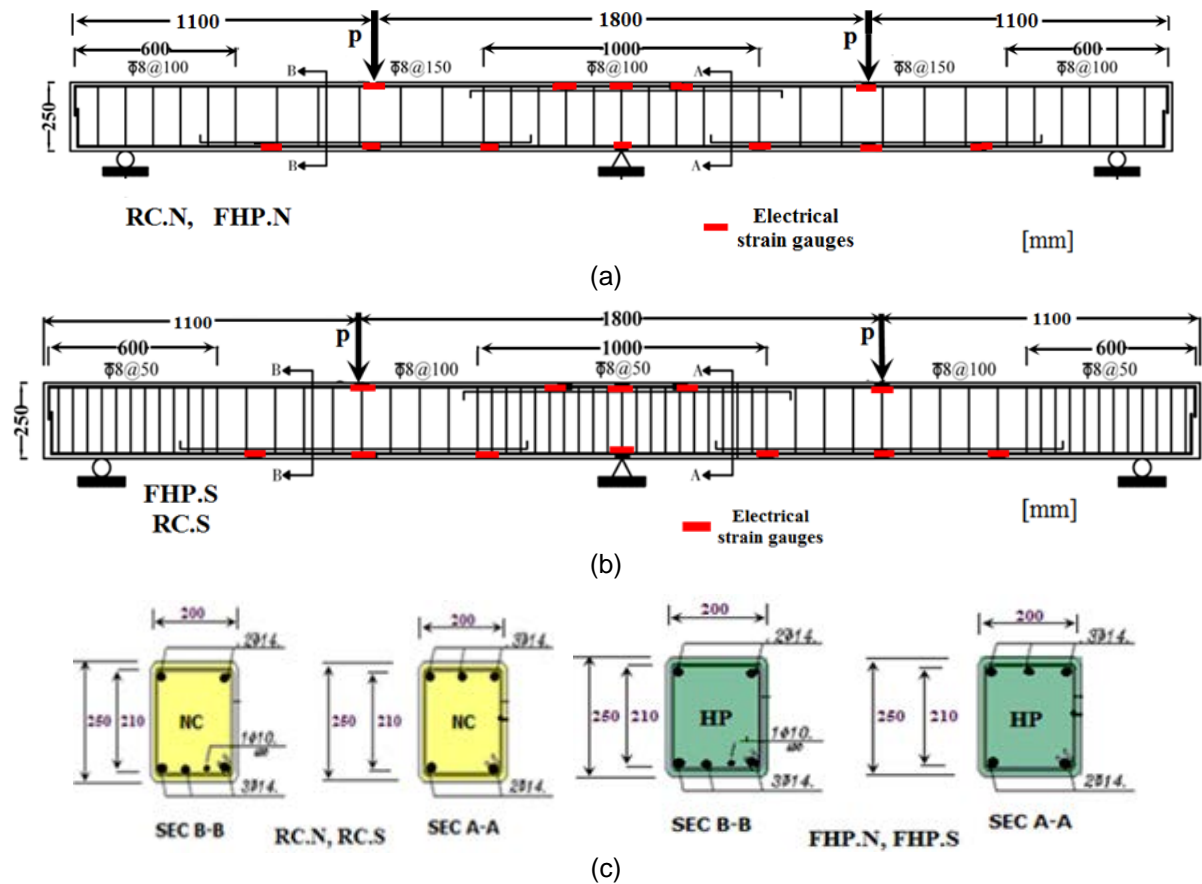


Figure 6. Reinforcement details of the beams: a) Reinforcement arrangement, FHP.N and RC.N Specimens. b) Reinforcement arrangement, FHP.S and RC.S Specimens. c) Typical Cross sections of beams in sagging (M^+) and hogging (M^-) region.

Table 3. Reinforcement Details and Concrete Properties of Tested Beam.

Specimen name	Cross section $b \times h$ (mm)	(NSC) and (HPFRCC) Compressive strength (MPa)	(NSC) and (HPFRCC) tensile strength (MPa)	Longitudinal bars at positive moment (M)	Longitudinal bars at negative moment (M^+)	Stirrups at the supports	Transverse reinforcement ratio (ρ_v) at the supports (%)	Stirrups in the middle of the span	Transverse reinforcement ratio (ρ_v) at middle of the span (%)
RCN*	200x250	36.22	3.44	3 \varnothing 14+1 \varnothing 10 (540.35)	3 \varnothing 14(462) mm ²	\varnothing 8@100	0.5	\varnothing 8@150	0.33
RCS**	200x250	36.22	3.44	3 \varnothing 14+1 \varnothing 10 (540.35) mm ²	3 \varnothing 14(462) mm ²	\varnothing 8@50	1	\varnothing 8@100	0.5
FHPN***	200x250	70.50	6.90	3 \varnothing 14+1 \varnothing 10 (540.35) mm ²	3 \varnothing 14(462) mm ²	\varnothing 8@100	0.5	\varnothing 8@150	0.33
FHPS****	200x250	70.50	6.90	3 \varnothing 14+1 \varnothing 10 (540.35) mm ²	3 \varnothing 14(462) mm ²	\varnothing 8@50	1	\varnothing 8@100	0.5

* Reinforced Concrete and Normal spacing stirrups, ** Reinforced concrete and special spacing stirrups, *** Reinforced HPFRCC and normal spacing stirrups, **** Reinforced HPFRCC and special spacing stirrups.

The stirrups and reinforcement ratios are accordance with the provision of American Concrete Institute [32], therefore the amount of transverse reinforcement was variable in this experimental study. Two beams, RC.S and FHP.S, were provided with transverse reinforcement ratio ($\rho_v = A_v / bs$) equal 2 higher than beams RC.N and FHP.N at the supports and approximately 1.5 higher than beams RC.N and FHP.N at middle of span. A bar of 8 mm was used, which its center-to-center distance was 100 mm. In addition, in the middle of the span and at a distance of 50 mm in the shear area, a bar of 8 mm was used, which its center-to-center distance was 150 mm. In non-closed space samples, in the middle of the span, bars of 8 mm were used, which its center-to-center distance was 150 mm and in the shear area its distance was about 100mm in order to set stirrups. Before loading the beams, all strain gauges were installed and the load cell performed completely during loading.

3. Results and Discussion

Mode of failure, load-deflection, load-strain, moment and load capacity, moment redistribution and ductility are the obtained results to be presented and discussed in following sections.

3.1. Failure mode and general behavior

Generally, the experimental results showed that the initiation and propagation of cracks in beams were depended on the tensile strength of the concrete mix, and the type of the reinforcement. Moreover the first cracks were vertical flexural at the middle support section followed by similar vertical cracks at mid-span, good agreement with the elastic bending moment distribution in continuous beams resulting in higher moment at middle support compared with that at mid span. Therefore the cracking pattern of specimens RCN and RC.S was similar that the first cracks in these two beams were in the negative moment region at the internal support. By increasing load, the new vertical and diagonal flexural cracks were observed in the positive and negative moment regions of both spans. The number of cracks at the middle support in beams with smaller stirrup spacing was more than those beams with wider spacing, the stirrups act as crack initiator and affect the flexural crack spacing and longitudinal reinforcement ratio at critical sections was effective factor to control the width of flexural cracks [31].

3.2. Load-deflection response and failure mode

The ultimate loads measured by the load cells of specimens are given in Table 4 and the load- deflection (in the middle of each span) curves of all the tested beams are shown in Figure 7. Ultimate load and corresponding vertical deflection of beam RCN were respectively 163.70 kN and 50.71 mm and these amounts for RCS with more transverse reinforcement were 186.94 kN and 79.00 mm. The ultimate loads of HPFRCC beams FHPN and FHPS were 205.63 kN and 229.88 kN, and their corresponding deflections were 83.27 mm and 98.66 mm, respectively.

Table. 4. Load and displacement of the tested beams.

Specimen notation	At Cracking		At yielding		At ultimate		$\frac{P_u}{P_{u(RC.N)}}$	Failure mode
	P_{cr} (kN)	Δ_{cr} (mm)	P_y (kN)	Δ_y (mm)	P_u	Δ_u		
RCN	31.25	1.76	147.48	11.28	161.85	50.71	1.0	Concrete crushing, Longitudinal steel bars rupture
RCS	35.93	1.63	160.21	14.27	186.94	78.99	1.15	Longitudinal steel bars rupture
FHPN	41.32	1.52	184.15	12.19	205.63	93.63	1.27	Longitudinal steel bars rupture
FHPS	46.27	1.41	198.73	12.84	229.88	104	1.42	Longitudinal steel bars rupture

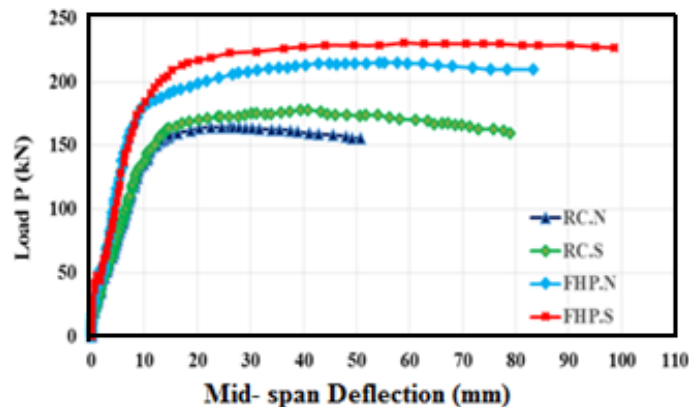


Figure 7. Load-deflection relationships for tested beams.

A comparison of the cracking load, yielding load, ultimate load, and corresponding deflection, and for all samples was shown in Figure 8. Further increase in cracking load in FHPS and FHPN beams compared to RCN and RCS beams was due to the hardening effects of HPFRCC composites. This could also be cited for yielding load, and maximum loads in beams, which were made with HPFRCC composite. Moreover, the beams constructed with closed space stirrups in comparison to beams with non-closed space stirrups showed an increase in cracking load, yielding load and maximum loads due to reducing and limiting the width of the crack and the non-extension of the shear and flexural cracking. Increased load was considerable in the beams made with HPFRCC composite. In the case of observed cracks in HPFRCC composite beams, it could be concluded that the fibers in the tensile section of these beams could control the width of the cracks and create more cracks. On the other hand, the force drop in these beams was lower than that of conventional concrete beams, so the HPFRCC composite beams exhibited a more ductile behavior. Considering the operability and ensuring the satisfaction of service of the flexural member, the generated deformation in the beams under the working

load would be ranging from $\frac{l}{480}$ to $\frac{l}{180}$ (3.75 mm to 10 mm for the mentioned beams) in accordance with

the allowable value according to the ACI 318M-08, depending on the type and function of the structure. According to the results of the experiments, the deformations generated in the load operation were in the satisfactory range of codes.

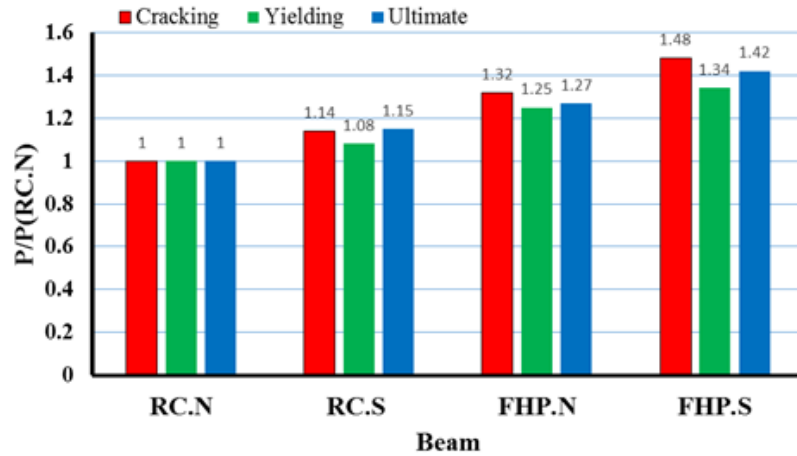


Figure 8. Comparison of loads ratio in cracking, yielding and ultimate modes.

The tested beams behavior before cracking was linear load-deflection. Upon cracking, stiffness was reduced as the load increased. Control beam, RCN, The tensile steel yielded ($P_y = 147.48$ kN) prior to concrete crushing at both the central support ($P_u = 161.85$ kN) and mid-span section as shown in Figure 9a. The new wider flexural cracks were occurred at the mid-span and center support and extended to the compressive regions. The tensile steels at central support of beam RCS were yielded at a load of 160.21 kN and the beam failed over the central support at the load 186.94 kN shown in Figure 9-b. The yielding loads of beams FHPN and FHPS were 184.15 and 198.73 kN prior to concrete crushing at both the center support and mid – span section as shown in Figures 9c and d. The beam failed by tensile rupture of the reinforcing bars prior to concrete crushing at both the central support and mid-span section as shown in Figure 9c. All beams exhibited three stage responses up to failure: representing the concrete pre cracking stage. Concrete post cracking to tension steel pre yield stage, tension steel post yield stage to failure.

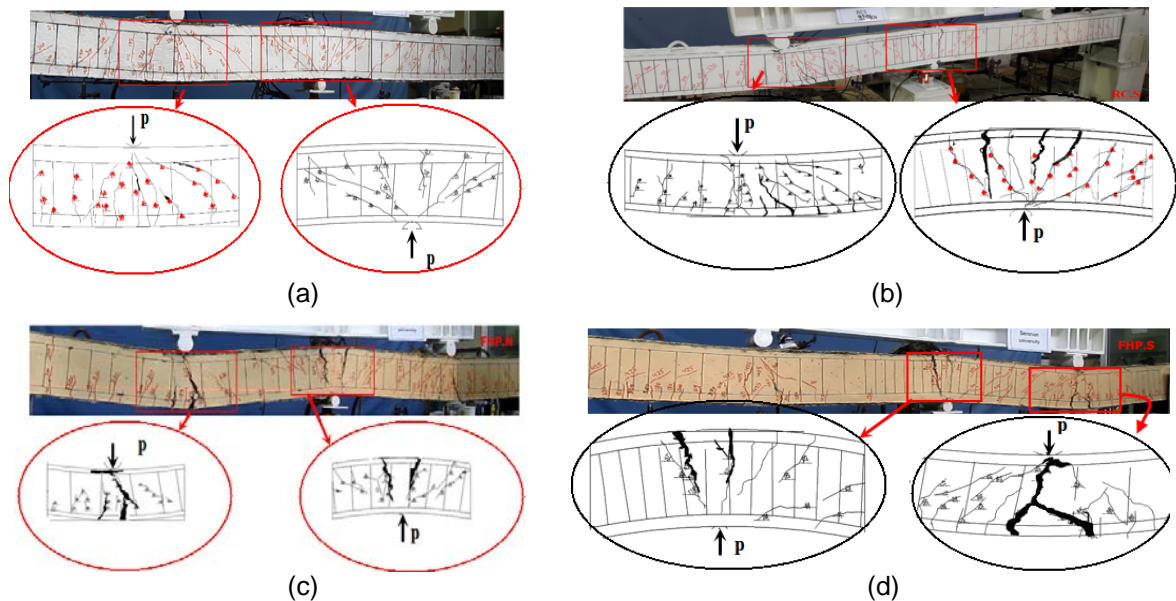


Figure 9. Failure shape and cracking pattern of tested beams: (a) RCN, (b) RCS, (c) FHPN, (d) FHPS.

Increasing the transvers reinforcement, as in beams RC.S compared with RC.N, resulted in improved ultimate load capacity and less deflection at any particular applied load. The transverse reinforcement ratio (ρ_v) of beam RC.S was twice of that of beam RC.N at the supports, resulting in 15 % increase in the ultimate load and 8 % reduction in mid-span deflection. Comparison of load-displacement curves of FHPN and FHPS beams in Figure 7 shows that the ultimate load capacity of specimen with closer stirrup spacing was improved and also its mid-span deflection was reduced. Therefore this issue had a positive effect on rotation capacity and moment redistribution at critical sections.

By observing the load-displacement response curves, it was shown that the FHPS and FHPN beams were ductile and the absorption capacity of energy had improved considerably and dramatically. The ultimate load in the FHPS sample increased by 42 % and the ductility coefficient of displacement was 80 % higher than RCN sample. By comparing the failure modes in Figure 9, the load-displacement response curve showed that FHPN and FHPS and RCS samples exhibited more ductile behavior than RCN samples, the first cracks started in the tested beams from the central support. When the load was applied to the beams, at the beginning of the loading, the severity of the load was low, the structure behaved as a linear elastic and the structure response was linear

and it was proportional to the load applied. At the critical zone (central support), when the load reached to P_{cr} , the hardness decreased in the cross section, so elastic re-distribution occurred, i.e. the critical section (central support) transferred some moment to the sections that had not yet been cracked (mid-span). In FHPFRCC beams with closed space shear reinforcement, crack width was less than RCN. The reason was the reinforcing effect of HPFRCC in preventing the expanding of cracks. In addition, by comparing the load – displacement response of the samples in Figure 7 and the presented results in Table 4, it could be seen that in the beams containing HPFRCC, the resistance against cracking and initial hardness of the samples had been increased. The increase in cracking load in HPFRCC samples, compared to RCN, was attributed to the role of HPFRCC composites in limiting the expansion of the cracks.

3.3. Ductility

The ductility of a beam can be defined as its ability to sustain inelastic deformation without loss of its load carrying capacity prior to failure. Ductility is more important for statically indeterminate structures, such as continuous beams, as it allows for moment redistribution through the rotation of plastic hinges. Ductility has generally been measured by a ratio called the ductility index or factor (μ). The ductility index is usually expressed as a ratio of rotation (θ), curvature (ϕ), deflection (Δ), and absorbed energy (E) at failure (peak load) divided by the corresponding property when the steel starts yielding. The displacement ductility index is defined by Equation

$\mu_{\Delta} = \frac{\Delta_u}{\Delta_y}$. Where Δ_u is the mid-span deflection at ultimate beam load and Δ_y is the mid-span deflection at

yielding load of the tensile steel reinforcement at the central support. The mid-span deflection at beam ultimate load (Δ_u) and yielding load (Δ_y), and the deflection ductility index (μ_{Δ}) are given in Table 5. As can be seen from Table 5, increasing the transverse reinforcement and closer stirrup spacing, in beams RCS and FHPS compared with RCN and FHPN resulted in improved displacement ductility. Comparing RCN with FHPN and RCS with FHPS, it can be seen that using HPFRCC allowed for more displacement ductility in the ultimate failure load beams. Figure 10 shows this positive effect on available rotation capacity and moment redistribution at critical sections. Another way of defining ductility was based on the concept of energy. Therefore, the energy density index μ_E , was the ratio of the absorbed energy of the beam of the ultimate load to the absorbed energy at the

yielding load. The quantity of energy was defined as $\mu_E = \frac{E_u}{E_y}$, in which, the energy absorbed by the E_u was

the beam in the ultimate load and E_y was the energy absorbed in the yielding load. In the present study, ductility was obtained based on displacement and absorbed energy methods. The energy density index μ_E are given in Table 5. As can be seen from Table 5, increasing the transverse reinforcement and closer and smaller spacing stirrup spacing, in beams RC.S and FHP.S compared with RC.N and FHP.N resulted in increased in energy density index (μ_E). Comparing RCN with FHPN and RCS with FHPS in Figure 11, it can be seen that using HPFRCC resulted in increasing in energy density index (μ_E).

Table 5. Energy and displacement ductility of the beams.

Specimen	$\mu_{\Delta} = \frac{\Delta_u}{\Delta_y}$	$\frac{\mu}{\mu_{(RC.N)}}$	E_y (kN.mm)	E_u (kN.mm)	$\mu_E = \frac{E_u}{E_y}$	$\frac{\mu_e}{\mu_e(RC.N)}$
RCN	4.5	1.0	737	7137	10	1
RCS	5.5	1.2	801	8921	11.1	1.2
FHPN	7.7	1.7	822	10706	13	1.3
FHPS	8.1	1.8	920	13454	14.6	1.5

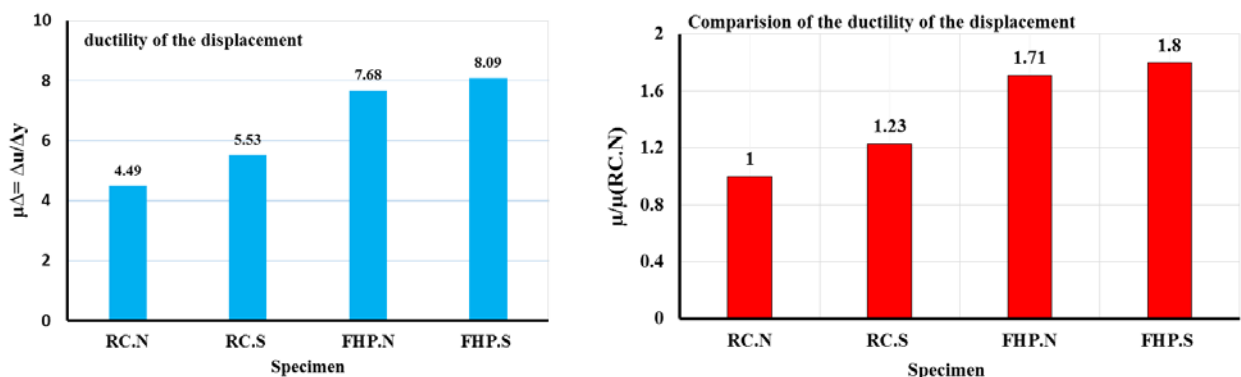


Figure 10. Displacement ductility of specimens.

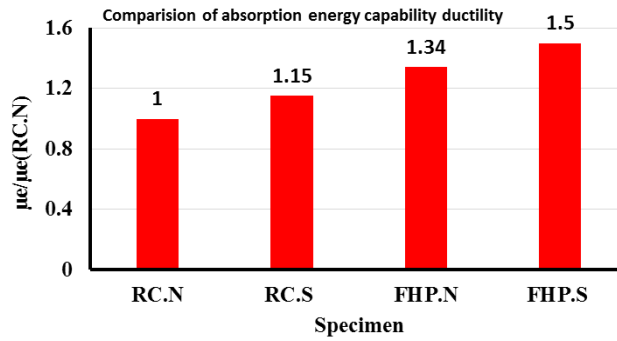
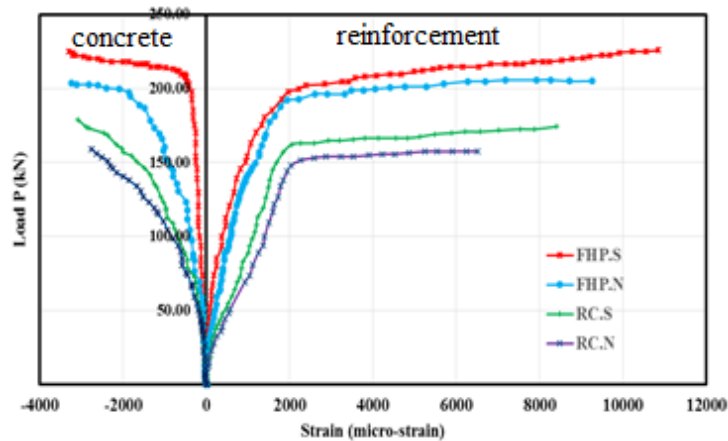


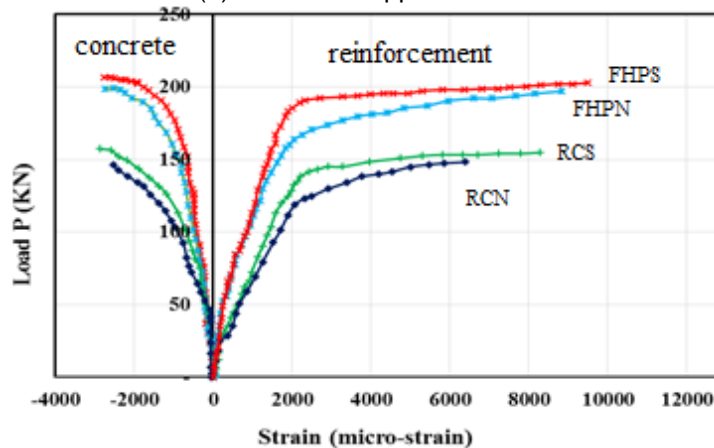
Figure 11. Energy ductility of specimens.

3.4. Load-strain response

The maximum measured strains of steel bars and concrete at the critical sections (mid-span and middle support) against the applied load are shown in Figure 12, indicating that the compressive strains in concrete at failure reached or exceeded the maximum compressive strain of 0.003. The section at middle support in all tested beams were cracked prior to the mid-span section. The measured strains in the top reinforcement over the middle support was about 1.2 times that in the bottom reinforcement at mid-span in all reinforced beams. In the FHPS sample, due to the greater confinement effect of closed- space stirrups, as well as the strain hardening effect on HPRCC, and because the fibers had maintained integrity, they could tolerate larger deformations and reinforcement had experienced larger strains. In the RCN beam under increasing loading, the cracks expanded faster and pressure concrete was crushed. Therefore, due to damage of the compressive concrete, the balance of the conventional reinforced concrete section collapsed and the applied force was falling down. Thus, the ductility of the NSC beams was less than that of the HPRCC beams.



(a) At middle support section



(b) At mid-span section

Figure 12. Load-strain curves.

3.4. Moments – curvature in critical section

Experimental moment – curvature response at sagging and hogging sections for tested beams are shown in Figure 13. The forces applied to the mid-span of the beams and the supports were measured by the load cell to calculate the moment at critical sections. The tensile strain values of the tensile reinforcements, which were also used to calculate the curvature of the beam, measured by the strain gauge connected to the

tensile reinforcement in the critical sections. The curvature at central support or mid – span is calculated by dividing the concrete strain ε_c by a distance to the neutral axis depth, c and given as $\varphi = \frac{\varepsilon_c}{c}$. In Figure 13a, it was clear that the ultimate moment value for the RCN beam was 45.78 kN.m. For example, ultimate moment value for RC.S, FHP.N and FHP.S were 51.57, 55.20 and 59.65 kN.m, respectively. The greatest increase in flexural strength in the central support of the FHP.S sample was found to be about 1.30 times more than the RC.N sample. According to Figure 13b, the ultimate moment capacity in the mid-span for the RC.N sample was 50.84 kN.m, while for RCS, FHPN and FHP.S samples, it was 58.33, 64.93 and 73.62 kN.m, respectively. The greatest increase in flexural capacity was observed in the mid-span of the FHP.S sample, which was about 1.44 times more than the RCN sample.

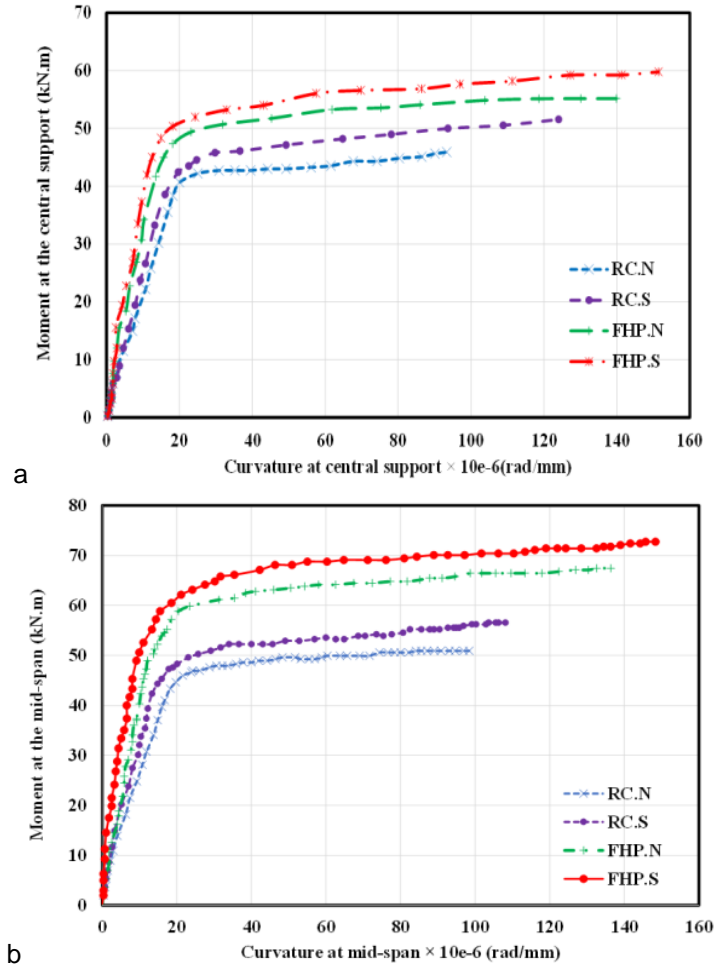


Figure 13. Moment-Curvature: a) at the central support b) at the mid-span.

In the Table 6, a summary of flexural capacity in the mid-span and central support for the specimens was recorded, as well as the increase of the flexural capacity in the critical sections for RC.S, FHP.N and FHP.S beams were compared with the RC.N beam. In this table, M_m^+ and M_C^- were respectively the positive moments in the central support and the negative moment in central support of the beams. In addition, φ_u and φ_y , respectively, were curvature in the ultimate state and curvature in the yielding state of the sections.

$\left(\frac{\varphi_u}{\varphi_y}\right)_m$, $\left(\frac{\varphi_u}{\varphi_y}\right)_c$ were the curvature ductility factor in the central support and mid-span.

Table 6. Flexural strength of samples in the central support and mid-span, and the ratio of increasing flexural strength and curvature ductility factor of beams.

Beams	M_C^- (kN.m)	M_m^+ (kN.m)	$\frac{M_C^-}{M_{C(RC.N)}}$	$\frac{M_m^+}{M_{M(RC.N)}}$	$\left(\frac{\varphi_u}{\varphi_y}\right)_c$	$\left(\frac{\varphi_u}{\varphi_y}\right)_m$
RC.N	45.78	50.84	1.00	1.00	4.75	4.72
RC.S	51.57	58.33	1.12	1.14	5.54	5.50
FHP.N	55.20	64.93	1.20	1.27	6.27	6.20
FHP.S	59.65	73.62	1.30	1.44	6.59	6.50

3.5. Moment redistribution

Since beams were statically indeterminate, the calculation of actual internal forces were based on the measured reactions. The variation of reactions versus the applied load for all tested beams are shown in Figure 14. The elastic end reaction with the value $R_1 = 0.312P$ and the elastic central support reaction with the value $R_2 = 1.376P$ was also plotted to evaluated the amount of load redistribution. Where R_1 and R_2 are the end and middle support reaction respectively. As shown in Figure 14, at the beginning of loading, the reaction force of the central and lateral support was similar to that obtained by linear analysis. In loads greater than the yielding load of tensile steel, at the same load level, the experimental reactions at the lateral supports were greater than the calculated reaction of the elastic relations. The experimental bending moments at both the middle support and mid-span were calculated using the measured reactions. The amount of moment redistribution can be obtained by comparing the actual and elastic bending moment. Diagrams of moment-load were also shown in the positive area (mid-span) and the negative (central support) for the tested beams in Figure 15. The moment in the mid-span and central support was calculated from the static equation and also based on the reaction of the center and lateral supports. As shown in Figure 15, in loads greater than the yielding load of tensile load, at the same load level, the moments in the central supports and the mid-span (under load) were less and more than the moments calculated from the elastic relations, respectively. The diagrams for moment were shown in both ultimate elastic and experimental modes for the tested beams in Figure 15. As shown in Figure 7, in the ultimate load, the difference between the experimental and elastic moment was due to moment redistribution. The amount redistribution ratio (β) given in Table 7 was calculated for the sagging and the hogging bending moment at mid-span and at the central support at failure load. The ratio was calculated by $\beta = \frac{M_e - M_{exp}}{M_e} \times 100 \%$, which

M_{exp} is the actual moment at an applied load; and M_e is elastic moment corresponding to the applied load. As indicated in Table 9, beam RCN had a moment redistribution ratio of 16.42 % at central support and 9.9 % at mid-span. The moment redistribution ratio of RCS, FHPN and FHPS beams was significantly increased due to smaller spacing stirrup and HPFRCC in beams. Actual versus elastic bending moment curves at failure are shown in Figure 16.

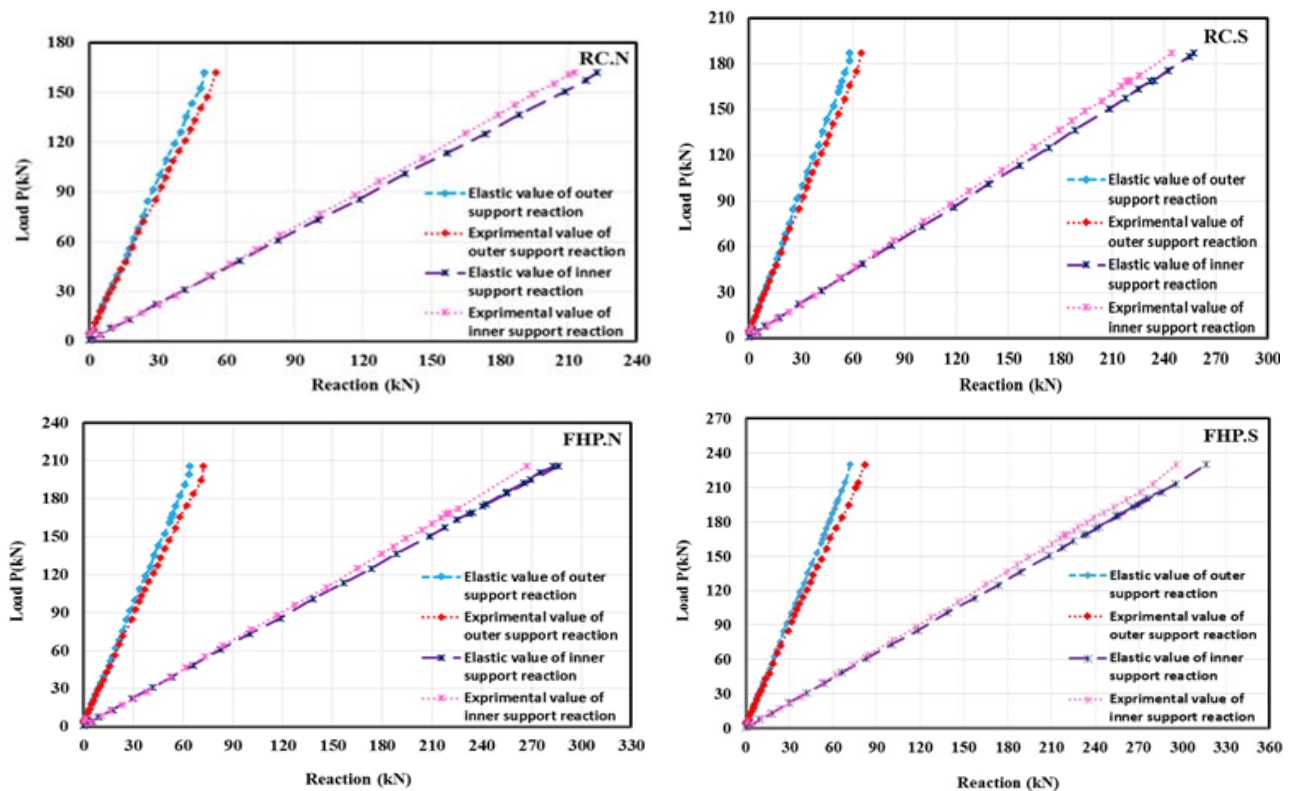


Figure 14. Load versus end and central support reactions of the tested beams.

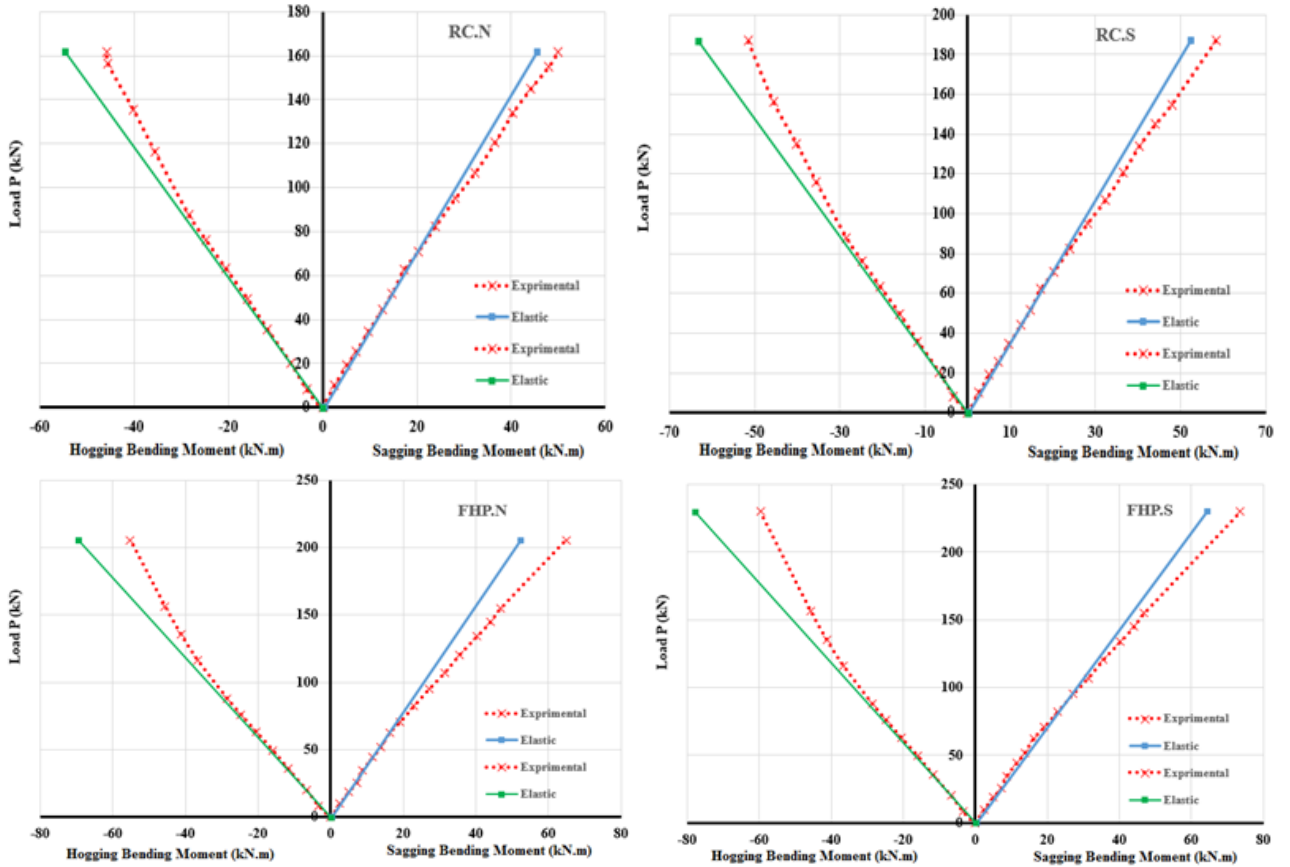


Figure 15. Applied load versus bending moment of tested beams.

Table 7. The amount of the reaction force of the lateral support, central support, the moment, and moment redistribution of the tested beams.

Beam	Ultimate load P_U (kN)	Reaction force of lateral support (kN)	Reaction force of central support (kN)	Central support			Mid-span		
				Elastic moment (kN.m)	Experimental moment (kN.m)	%MR β	Elastic moment (kN.m)	Experimental moment (kN.m)	%MR β
RC.N	161.85	55.49	212.72	54.78	45.78	16.42	45.44	49.94	-9.9
RC.S	186.94	64.82	244.24	63.27	51.57	18.49	52.49	58.33	-11.12
FHP.N	205.63	72.15	266.96	69.59	55.20	20.67	59.88	64.93	-12.47
FHP.S	229.88	81.80	296.16	77.79	59.65	23.31	64.54	73.62	-14.06

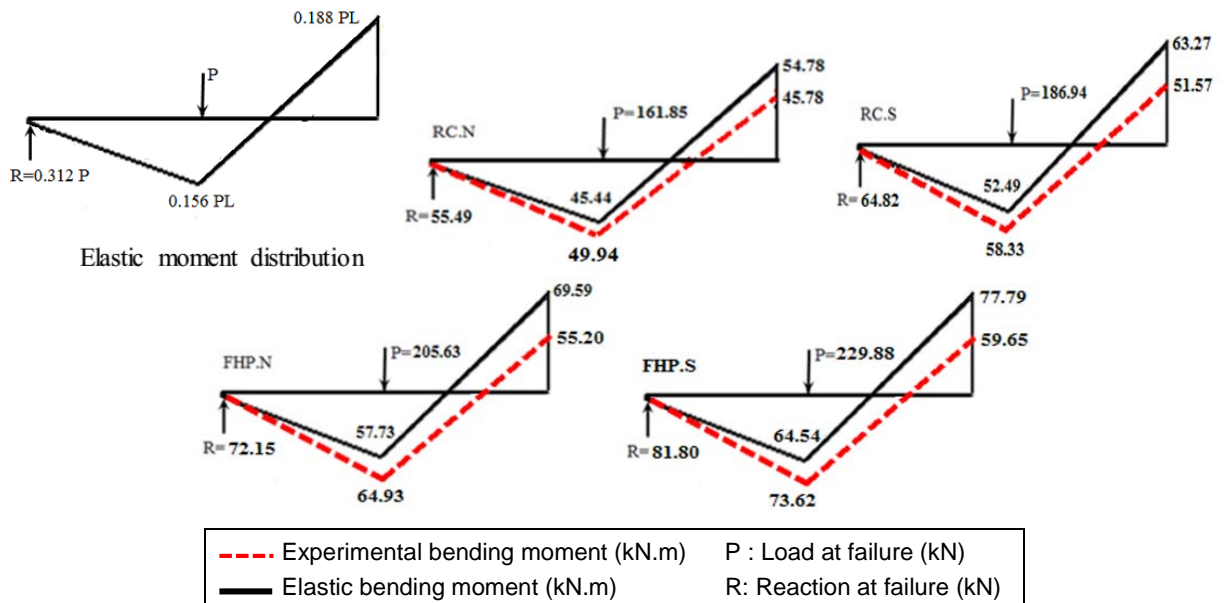


Figure 16. Actual versus elastic bending moment at failure.

4. Conclusion

In this research, the effect of HPFRCC and closed-space stirrups on flexural behavior of two-span reinforced concrete beams was studied and the following important results were concluded:

1. The experimental results showed that using HPFRCC and reducing the spacing of the stirrups and concrete confinement, increased the ultimate load, ductility ratio, energy absorption, plastic hinge characteristics and moment redistribution capacity of these beams compare to reference beam.

2. Comparison of curves of load – displacement of samples of RCN and FHPS showed that the toughness of FHPS improved by 1.82 times more than the RCN. Toughness mechanisms such as bridging the fibers increased tensile strength and reduced the brittle fracture after maximum load.

3. Comparison of the cracking pattern in the plastic zones of the beams showed that the cracking rate in the beams with HPFRCC and closed-space stirrups was more than the RCN beam and As a result, Energy dissipation became more.

4. Unlike beams with regular concrete, in which an initial crack is mostly dominant, HPFRCC beams shows a pseudo-strain hardening behavior with finely distributed multiple cracks. This multiple cracking process occurs in sequence as the applied tensile load increases, after tensile stress reaches the maximum affordable tensile stress of the weakest section, the crack at the weakest section is localized.

5. The displacement ductility and the energy ductility index of FHPS beam was about 1.80 and 1.50 times more than RCN beam respectively.

References

1. Wang, W., Liu, J., Agostini, F., Davy, C.A., Skoczylas, F., Corvez, D. Durability of an Ultra High Performance Fiber Reinforced Concrete (UHPFRC) under progressive aging. *Cement and Concrete Research*. 2014. 55. Pp. 1–13
2. Naaman, A.E. Setting the Stage, Toward Performance Based Classification of FRC Composites. *High Perform Fiber Reinforce Cement Compos (HPFRCC 4)*, Proc 4th Int RILEM Work 2003, 2003.
3. Khatana, S. A review on the use of fibers in reinforced cementitious concrete. *Journal of Industrial Textiles*. 2015. 45(2). Pp. 239–264.
4. Nizina, T.A., Ponomarev, A.N., Balykov, A.S., Pankin, N.A. Fine-grained fibre concretes modified by complexed nanoadditives. *International Journal of Nanotechnology*. 2017. 14(7/8). Pp. 665–679.
5. Nizina, T.A., Balykov, A.S., Volodin, V.V., Korovkin, D.I. Fiber fine-grained concretes with polyfunctional modifying additives. *Magazine of Civil Engineering*. 2017. 72(4). Pp. 73–83. doi: 10.18720/MCE.72.9.
6. Nizina, T.A., Balbalin, A.V. Vliyaniye mineralnykh dobavok na reologicheskie i prochnostnyye arakteristiki cementnykh kompozitov [Influence of mineral additives on the rheological and strength characteristics of cement composites]. *Vestnik TGASU [Bulletin of the Tomsk State University of Architecture and Construction]*. 2012. No. 2. Pp. 148–153. (rus)
7. Nizina, T.A., Balbalin, A.V. 'Mekhanicheskaya aktivatsiya cementnykh smesey spolifunktsionalnymi dobavkami [Mechanical activation of cement mixtures with polyfunctional additives]'. *Regionalnaya arhitektura i stroitelstvo [Regional Architecture and Construction]*. 2013. No. 2. Pp. 36–42. (rus)
8. Selyaev, V.P., Nizina, T.A., Balbalin, A.V. Mnogofunktsionalnye modifikatory cementnykh kompozitov na osnove mine-ralnykh dobavok i polikarboksilatnykh plastifikatorov [Multifunctional modifiers of cement composites based on mineral admixtures and polycarboxylate plasticizers], *Vestnik Volgogradskogo gosudarstvennogo arhitekturnostroitel'nogo uni-versiteta. Seriya: Stroitelstvo i arhitektura [Bulletin of Volgograd State University of architecture and construction. Series: Construction and architecture]*. 2013. No. 31, Part 2. Pp. 156–163. (rus)
9. Rabinovich, F.N. *Dispersno armirovannye betony [Disperse reinforced concretes]*, Stroyizdat, Moscow, 1989. 176 p. (rus)
10. Rabinovich, F.N. *Kompozity na osnove dispersno armirovannykh betonov. Voprosy teorii i proektirovaniya tekhnologiya konstrukcii [Composites based on disperse reinforced concretes. Questions of theory and design, technology, constructions]*. Moscow: Publishing house ASV, 2004. 560 p. (rus)
11. Zagorodnyuk, L.Kh., Shakarna, M., Shchekina, A.Y. Classification of Additives for the Reinforcement of Particulate Composites, GISAP (Global International Scientific Analytical Project), 2013. [Online]. URL: <http://gisap.eu/ru/node/23874>, free, Title from the screen, Language Russian, English.
12. Nizina, T.A., Balykov, A.S. Analiz kompleksnogo vliyaniya modifiziruyushchih dobavok i dispersnogo armirovaniya na fiziko-mekhanicheskie harakteristiki melkozernistykh betonov [Analysis of the combined effect of the modifier additives and particulate reinforcement on the physico-mechanical characteristics of fine-grained concretes]. *Regionalnaya arhitektura i stroitelstvo [Regional Architecture and Construction]*. 2015. No. 4. Pp. 25–33. (rus)
13. Hemmati, A., Kheyroddin, A., Sharbatdar, M.K. Increasing the flexural capacity of RC beams using partially HPFRCC layers. *Comput Concr*. 2015. 16. Pp. 545–568. DOI: <http://dx.doi.org/10.12989/cac.2015.16.4.000>.
14. Hemmati, A., Kheyroddin, A., Sharbatdar, M., Park, Y., Abolmaali, A. Ductile behavior of high performance fiber reinforced cementitious composite (HPFRCC) frames. *Constr Build Mater*. 2016. 115. Pp. 681–9. DOI: 10.1016/j.conbuildmat.2016.04.078.
15. Hemmati, A., Kheyroddin, A., Sharbatdar, M.K. Proposed equations for estimating the flexural characteristics of reinforced HPFRCC beams. *Iran J Sci Technol Trans Civ Eng*. 2014. 38. Pp. 395.
16. Hemmati, A., Kheyroddin, A. and Sharbatdar, M.K. Plastic hinge rotation capacity of reinforced HPFRCC beams. *J. Struct. Eng*. 2014. 141(2). 04014111. DOI: 10.1061/(ASCE)ST.1943-541X.0000858.
17. Akbarzadeh, H., Maghsoudi, A.A. Experimental and analytical investigation of reinforced high strength concrete continuous beams strengthened with fiber reinforced polymer. *Materials and Design*. 2010. 31. Pp. 1130–1147.
18. do Carmo, R., Lopes, S. Required plastic rotation of RC beams. *Proceedings of the Institution of Civil Engineers 2006 structures and Buildings*. 2006. 159(SB3). Pp. 77–86.
19. do Carmo, R., Lopes, S. Ductility and linear analysis with moment redistribution in reinforced high strength concrete beams. *Canadian Journal of Civil Engineering*. 2005a. 32(1). Pp. 194–203. DOI: 10.1139/104-080.

20. do Carmo, R., Lopes, S. Influence of the shear force and transversal reinforcement ratio on plastic rotation capacity Structural Concrete. 2005b. 6(3). Pp. 107–117. DOI: 10.1680/stco.2005.6.3.
21. do Carmo, R. Rotac,ãõ pla'stica e redistribuic,ãõ de esforç,os em vigas de betaõ de alta resistê'ncia "Plastic Rotation and Moment Redistribution in High Strength Concrete Beams"). Ph.D thesis, Universidade de Coimbra, Coimbra, Portugal, 2004. [In Portuguese].
22. Lou, T., Lopes, S.M.R., Lopes, A.V. Evaluation of Moment Redistribution in Normal-Strength and High-Strength Reinforced Concrete Beams. J Struct Eng. 2014. 140. 04014072. DOI: 10.1061/(ASCE)ST.1943-541X.0000994.
23. Iskhakov, I., Ribakov, Y. A design method for two-layer beams consisting of normal and fibered high strength concrete. Mater Des. 2007. 28. Pp. 1672–1677. DOI: 10.1016/j.matdes.2006.03.017.
24. Holschemacher, K., Mueller, T., Ribakov, Y. Effect of steel fibers on mechanical properties of high-strength concrete [Online]. Mater. Des. 2010. 31(5). Pp. 2604–2615. URL: <http://dx.doi.org/10.1016/j.matdes.2009.11.025>.
25. Holschemacher, K., Iskhakov, I., Ribakov, Y., Mueller, T. Laboratory Tests of Two-Layer Beams Consisting of Normal and Fibered High Strength Concrete: Ductility and Technological Aspects. Mech Adv Mater Struct. 2012. 19. Pp. 513–22. DOI: 10.1080/15376494.2011.556840.
26. Mostofinejad, D., Farahbod, F. Parametric study on moment redistribution in continuous RC beams using ductility demand and ductility capacity concept. Iran J Sci Technol. 2007. 31. Pp. 459.
27. Visintin, P., Ali, M.A., Xie, T., Sturm, A.B. Experimental investigation of moment redistribution in ultra-high performance fibre reinforced concrete beams. Construction and Building Materials. 2018. 166. Pp. 433–444.
28. Saghafi, M.h., Shariatmadar, H. Enhancement of seismic performance of beam-column joint connections using high performance fiber reinforced cementitious composites. Construction and Building Materials. 2018. 180. Pp. 665–680.
29. Saghafi, M.h., Shariatmadar, H., Kheyroddin, A. Experimental evaluation of mechanical properties of high performance fiber reinforced cementitious composites. Concr. Res. (JCRE). 2017. 9(2). Pp. 29–42.
30. Bagge, N., O'Connor, A., Elfgrén, L., Pedersen, C. Moment redistribution in RC beams-A study of the influence of longitudinal and transverse reinforcement ratios and concrete strength. Eng Struct. 2014. 80. Pp. 11–23. DOI: [org/10.1016/j.engstruct.2014.08](http://dx.doi.org/10.1016/j.engstruct.2014.08).
31. Bagge, N., O'Connor, A., Pedersen, C. Rotation capacity and plastic redistribution of forces in reinforced concrete beams. Bridge Concr Res Ireland 2012:517–23.
32. American Concrete Institute (ACI). ACI 318M-14: Building Code Requirements for Structural Concrete. 2014.

Contacts:

Ramin Ehsani, 00989121316379; raminehsani1350@gmail.com

Mohammad Sharbatdar, 0098-23-33654070; msharbatdar@semnan.ac.ir

Ali Kheyroddin, 0098-23-33654070; kheyroddin@semnan.ac.ir

© Ehsani, R., Sharbatdar, M.K., Kheyroddin, A., 2019



DOI: 10.18720/MCE.90.11

Kerman collapsible clay amendment by lime, bentonite, and nano silica

A. Firoozfar*, M. Dousti

University of Zanjan, Iran

* E-mail: firoozfar@znu.ac.ir

Keywords: collapsible soil, lime, nano silica, bentonite, treatment

Abstract. This paper presents an experimental study to understand the effects of selected additives on Kerman collapsible soil behavior which is dominated with such clay and is semi-arid province in the south-east of Iran. Collapsible soils, known as problematic soils, are materials with a relatively high porosity and demonstrate a potential for sudden and large decrease in their volume under water content changes with or without change in the applied stress level. In this study, soil samples are obtained from a project site in Kerman city and the collapse potential tests were performed on the prepared samples in accordance with ASTM as double oedometer consolidation test. Initially, the undisturbed level of collapsibility. Next, samples are treated with three kinds of additives namely: lime and bentonite in the 3, 5 and 8 percent and nano silica in 0.4, 0.7 and 1 percent of dry soil weight. For each percentage of additive, one sample was created and the results demonstrated that 5 % of Lime, 3 % of Bentonite and 1 % of nano silica are the optimum percentage of additives for decreasing the collapsibility. The collapsibility of Kerman clay is reduced significantly after treating with lime and nano silica in comparison to bentonite.

1. Introduction

There are various types of problematic soils such as dispersive soils, collapsible soils, expansive soils, etc. Collapsible soils are unsaturated soils, which show volume decrease in confronting increased moisture content under constant stress. Collapsible soils are scattered all around the world in a great volumes and they can be found in the United States, Europe, China and South Africa. It has been estimated that about 10 % of the surface area of the Earth is covered by these soils [1, 2]. Collapse phenomena have been reported in an extensive rate in many arid areas around the world, and all of them are happened due to wetting [3]. Several methods currently exist for improving the characteristics of collapsible soils such as dynamic compaction, chemical stabilization, inundation, and piling [4, 5]. Chemical stabilization is one of the most common methods for stabilization of the soil. This method is a process for enhancing the characteristics of soil by using additives such as lime, bentonite, Portland cement, fly ash and recently Nano-particles [6, 7, 8, 9]. Lime's reaction with soil is categorized in two different processes of short and long term reactions. Cation exchange and flocculation occur immediately within the soil, rapidly increase soil's pH level. This is regarded as a result of the dissolution of $\text{Ca}(\text{OH})_2$. Pozzolanic and carbonation reactions are categorized as the long-term reactions. The Pozzolanic reaction is actually a slow reaction which is mainly controlled by time, temperature and moisture. This reaction produces calcium silicate and calcium aluminate, which gradually enhances strength and durability in days or weeks after adding lime to the soil. Carbonation reaction is a damaging reaction which decreases the number of free ions in the mixture for cation exchange and pozzolanic reactions [6, 10]. The influence of lime on the collapsibility of tropical residual soils was investigated and the results showed a significant reduction in comparison with untreated soil samples [10]. A comprehensive study was conducted on the soil stabilizing effect of lime and made an estimation of the initial lime consumption (ICL) showing that, 5 % lime is sufficient for ICL [6]. The impact of lime on the strength of soil mixture was investigated in road construction and the result indicated that all

Firoozfar, A., Dousti, M. Kerman collapsible clay amendment by lime, bentonite, and nano silica. Magazine of Civil Engineering. 2019. 90(6). Pp. 119–129. DOI: 10.18720/MCE.90.11

Фироозфар А., Дусти М. Керманская просадочная глина, модифицированная оксидом кальция, бентонитом и нанокремнеземом // Инженерно-строительный журнал. 2019. № 6(90). С. 119–129. DOI: 10.18720/MCE.90.11



This open access article is licensed under CC BY 4.0 (<https://creativecommons.org/licenses/by/4.0/>)

tested samples reach a significant strength level when enough amount of lime is provided [11]. Another material which is commonly used for soil stabilization is bentonite. One of the most important features of bentonite is its usability in both granular and cohesive soils by determining the required amount of bentonite. It has been found that in cohesive and well-graded soils, less than 6 % and in the uniformly sized sands, 10 to 15 % of bentonite is sufficient, where compressibility and shear strength of the soil was investigated [12, 13, 14]. Besides, bentonite can improve the hydraulic conductivity of soils to meet the technical requirements of compacted clay liner (CCL). This was investigated using different percentages of bentonite and the result showed a considerable reduction in permeability caused mostly by swelling characteristics of bentonite, meeting most of the worldwide standards [9,15]. Over the last two decades, nanotechnology has been significantly used in many fields of science and using materials with the sizes smaller than 100 nm is defined as nanotechnology. In geotechnical engineering, nanotechnology is used in two different approaches: first, to have a better understanding of soil structure by studying the soil in nanoscale and secondly, soil stabilization using nano-size additives [16]. Despite previously conducted studies on the utilization of nanotechnology in soil mechanics, there are still numerous untouched analytical and experimental subjects. Experimental works were done to show the effect of nanomaterial on soil stabilization and soil permeability. It was found that the addition of nanomaterials decreases the permeability of soils [17]. The addition of nanomaterial to the sand affects the cyclic behavior of the soil. The inter-particle siloxane bonds due to collisions between nanoparticles forms the silica solution gel. This gel contains the individual sand particles together and maintains the soil structure under the dynamic loading [16,18, 19]. Kerman is a province located in the south-east of Iran. It has a number of notable sites such as the Bam Citadel and the ruined city of Arg-e-Bam made entirely of mud bricks, clay, straw and the trunks of palm trees (224–637 AD) (Figure 1). This province covers an area of 175,069 square kilometers including 11 % of the total area of Iran. The geographical diversity of this province causes a varying climate. Geologically, alluvial and aeolian sediments form most of the top layer of the Kerman plain [20]. The land of the City of Kerman, geographically located in the north west of the Kerman province, is mostly made up of the collapsible soils. This availability has resulted in the prevalence of these soils utilization in various projects due to the economic reasons. As an under-structure basement, these collapsible soil covers cause serious problems to the building structures and urban infrastructures such as water and gas pipelines, and embankment dams. Therefore, soil treatment can be a beneficial preconstruction operation in almost all projects in Kerman.



Figure 1. Kerman Province and city of Kerman.

This study considers the Kerman collapsible soil and suggests different approaches to amend this problematic soil which would address a major need in this province. This paper aims to explore the effect of different types of additives on the collapsibility of Kerman clay.

2. Materials

In this section, we discuss and elaborate on the materials used in this study.

Soil: soil samples are taken from a 5-meter depth of a construction site. In order to determine the physical and chemical properties of the soil, such as particle size, Atterberg limits, dry unit weight, and optimum moisture content, different tests are conducted according to ASTM. More than 90 % of the soil passed the sieve, which indicates no. 200 grain size distribution curve of the soil according to ASTM D422 Standard [21], see Figure 2. With reference to unified soil classification system (USCS), this soil is categorized as CL. Physical and chemical properties of the disturbed soil are shown in Tables 1 and 2:

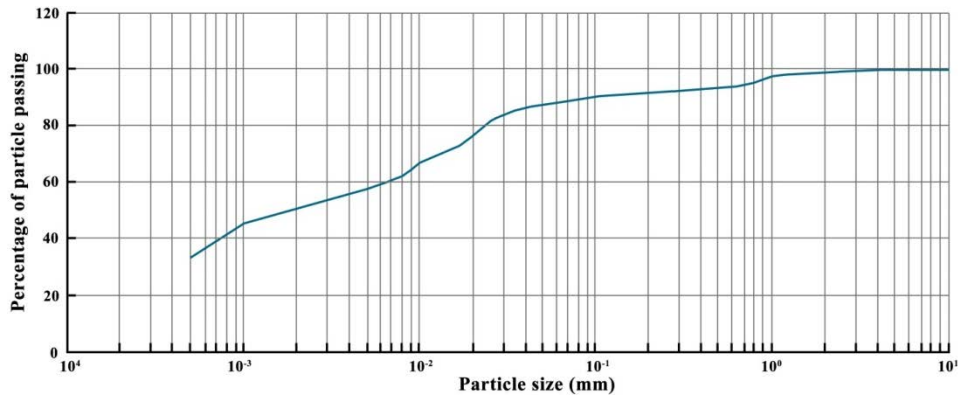


Figure 2. Particle size distribution of the Kerman collapsible soil.

Table 1. Physical characteristics of the soil used in the tests.

Characteristics	Value and Description
Density(gr/cm^3)	1.74
Liquid Limit (%)	33
Plastic Limit (%)	21
Clay content (%)	32
Passing no. 200 sieve (%)	90
Specific gravity (G_s)	2.77
Unified classification system	CL

Table 2. Chemical compositions of the soil and bentonite used in the tests.

Characteristics	Soil	Bentonite
SiO_2	45.01	55.35
CaO	13.62	1.09
Al_2O_3	11.95	14.07
Fe_2O_3	4.91	2.79
MgO	3.93	3.86
K_2O	2.49	0.21
Other	18.09	15.2

Additives: three additives namely lime, bentonite and Nano-silica are investigated in this study. These additives are readily available and their interaction with clay is clearly known.

Lime: The hydrated lime used for this project is a product of the Lorestan Lime Company and is a high-quality lime passes through an $80\mu\text{m}$ sieve opening, with 56.7 % of $\text{Ca}(\text{OH})_2$.

Bentonite: Sodium bentonite from Arak Poodr Factory is the other additive in this study. The chemical property of the bentonite and its physical analysis is shown in Tables 2 and 3.

Table 3. Physical characteristic of bentonite used in the tests.

Characteristics	Value and Description
Water absorption (%)	100–110
Absorption of montmorillonite (%)	>75
Liquid limit (%)	230
Plastic limit (%)	110
PH	9
Percent finer than No. 200	99.08

Nano-Silica: Silica nanoparticle is a white color powder. We use the Nano-silica from Pasargad Novin Company. A further discussion on the main properties of the Nano-silica is provided in the subsequent sections in this paper.

Permeants: For all tests, tap water was used.

3. Experimental Methods

Sample preparation: To achieve a homogeneous soil sample, dry soil and additives have to be mixed, and then water should be added to the mixture. Accordingly, the soil is air dried at the normal laboratory

temperature. All the specimens in this experiments are prepared with optimum moisture content and compacted at the maximum dry density. Next, lime and bentonite are added to the soil in the proportions of 3, 5, and 8 percent, respectively, and hand mixed together to obtain a homogeneous soil-additive mixture. Next, tap water is gradually spray-added to the mixture. Lime-soil reactions begin when the PH of the mixture reaches 12.4. By adding additional 2 percent or more of lime to the soil, PH reaches to 12.4. This also facilitates the long-term pozzolanic reactions [11, 22]. Nano-silica is added to the soil in 0.4, 0.7 and 1 % ratios with respect to the soil dry weight. Specific surface area (SSA) is an important parameter in nanomaterial’s reaction with soil. At nanoscale, a higher ratio of surface to volume causes intense interaction. Therefore, even small amounts of nanoparticles yield considerable effects on mechanical properties of the soil [8, 23]. For each percentage of additive, one sample is created.

Testing Procedure: As double odometer consolidation test (ASTM D 5333-03) is commonly performed on samples to determine their collapse potential. The significance of one dimensional collapse that occurs when unsaturated soils are flooded with water is covered by this test. Initially, undisturbed soil samples at natural water content are tested. Double odometer test examines collapsibility of soil samples regarding the void ratio variation resulted by the inundation of the sample. The collapse potential can be calculated as follows [24]:

$$I_c = \frac{\Delta e}{1 + e_0} \times 100, \tag{2}$$

where I_c stands for the collapse potential;

Δe is the change in void ratio upon flooding;

e_0 represents the void ratio before flooding.

Figure 3 shows the result of a double odometer test on an undisturbed sample. According to [11] and considering the results of the laboratory experiments, the base soil is classified as moderate collapsible clay exhibiting a collapse potential value of 5.9. Table 4 categorizes I_c from none to severe in degree of collapse potential.

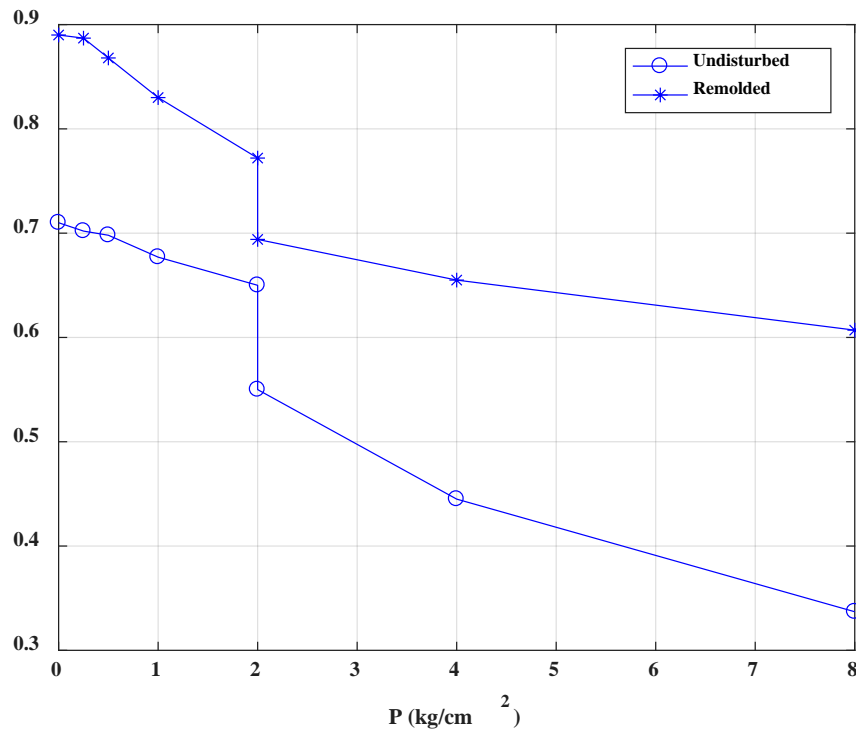


Figure 3. Result from double oedometer test on undisturbed and remolded specimen.

Table 4. Classification of Collapse potential [24].

Degree of collapse	Collapse potential (%)
None	0
Slight	0.1 to 2.0
Moderate	2.1 to 6.0
Moderately severe	6.1 to 10.0
Severe	>10

The double odometer test is re-applied on remolded samples under natural moisture without any additives. This test also is conducted on soil samples combined with additives to understand the effects of the additives on collapse potential. Double odometer tests are conducted on all the additive-amended samples with the optimum moisture content and at 100 % of maximum standard proctor dry unit weight.

4. Result and Discussion

In order to determine the collapsibility of an undisturbed soil sample, the specimen is tested according to ASTM regulation [25]. The result is shown in Figure 3. Considering Figure 3, the collapse potential of the undisturbed soil, i.e., I_c , is 5.9 which indicates a relatively high collapse potential. Up to a loading of 2 (Kg/cm²), the sample shows a slight rate of settlement. At the vertical stress of 2 (Kg/cm²) and after 24 hours, a significant change in strain observed, as a result of inundation. This severe change is due to the loss of the resistance factor binding the soil particles. This can cause serious problems the projects that use this type of soil. To prevent these phenomena, soil stabilization is one of the most effective and economic approaches. In the process of stabilization, soil inevitably remolded. Therefore, additionally the collapse potential test is also carried out on a remolded specimen to have a better understanding of the effect of different additives on soil behavior. The results from the experiment on the remolded sample without any additives are presented in Figure 3. The remolded specimen demonstrated a collapse potential equal to 4.17 and is categorized as moderate in the degree of collapse according to Table 4. As it can be seen, an anticipated reduction occurs in the collapse potential. This reduction is attributed to the impact of mechanical compaction of the soil under which the open structure of the collapsible soil breaks in comparison with the undisturbed sample. A comparison between the undisturbed and the remolded specimens reveals that the collapse potential decreases by 28 % under standard compaction. The Scanning Electron Microscopic (SEM) observation of the remolded sample, as presented in Figures 5 and 6, shows pores which can yield in a collapsible soil fabric. Thus, collapse under wetting should clearly occur by the densification of the areas where grains are clean with large pores around them

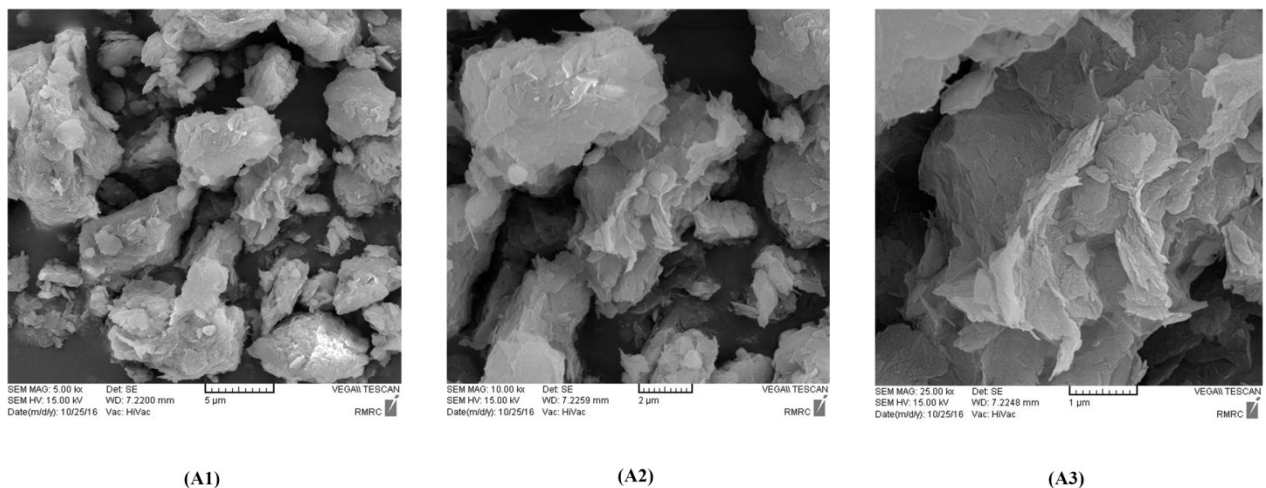


Figure 4. Microstructure observation of remolded collapsible soil sample at different magnification (A1-A2-A3).

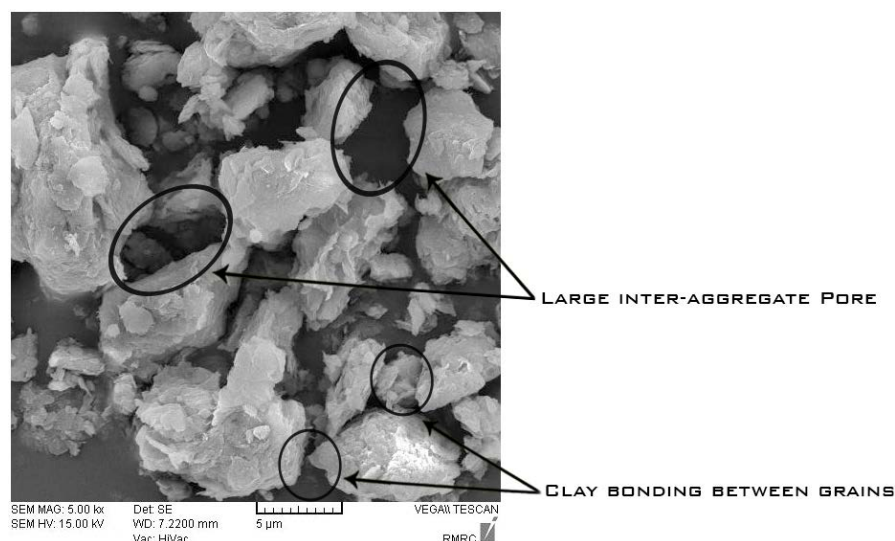


Figure 5. Large inter-aggregate pores and unstable clay bonding between grains in remolded collapsible soil.

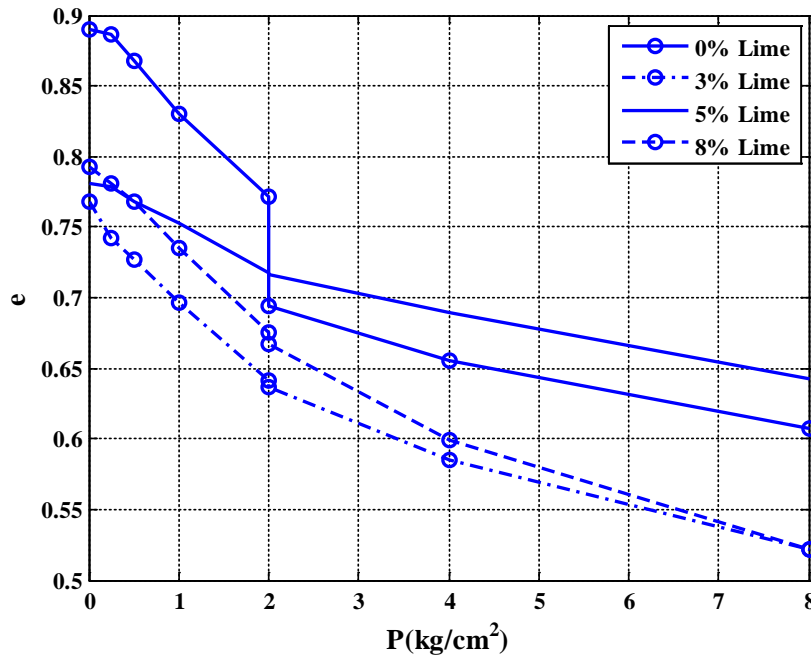


Figure 6. Comparison between results from double oedometer tests on three different lime-soil mixtures and remolded soil specimen.

4.1. Effects of lime on soil collapsibility

Lime-soil mixtures is treated for 18 days at a constant temperature and then the collapse potential test is conducted on the samples. In Figure 7 and Table 5, the results of the tests conducted on the lime-soil mixtures are presented. In all three different samples prepared by different percentages of additives, collapse potential decreases (from 4.17 to 0.12) drastically which shows lime can act as a proper additive for stabilization of Kerman collapsible clay. In all three lime-soil samples the degree of collapse decreases and mixtures with less than 5 % lime show a decreasing trend in the amount of strain and after that, the trend shows a gently sloping increase: therefore, it can be concluded that the most significant decrease in collapse potential occurs with 5 % of lime. Collapse potential decrease 97 percent in the 5 % lime treated samples compared with remolded pure soil samples. This result is in line with those of the previous studies [10, 26].

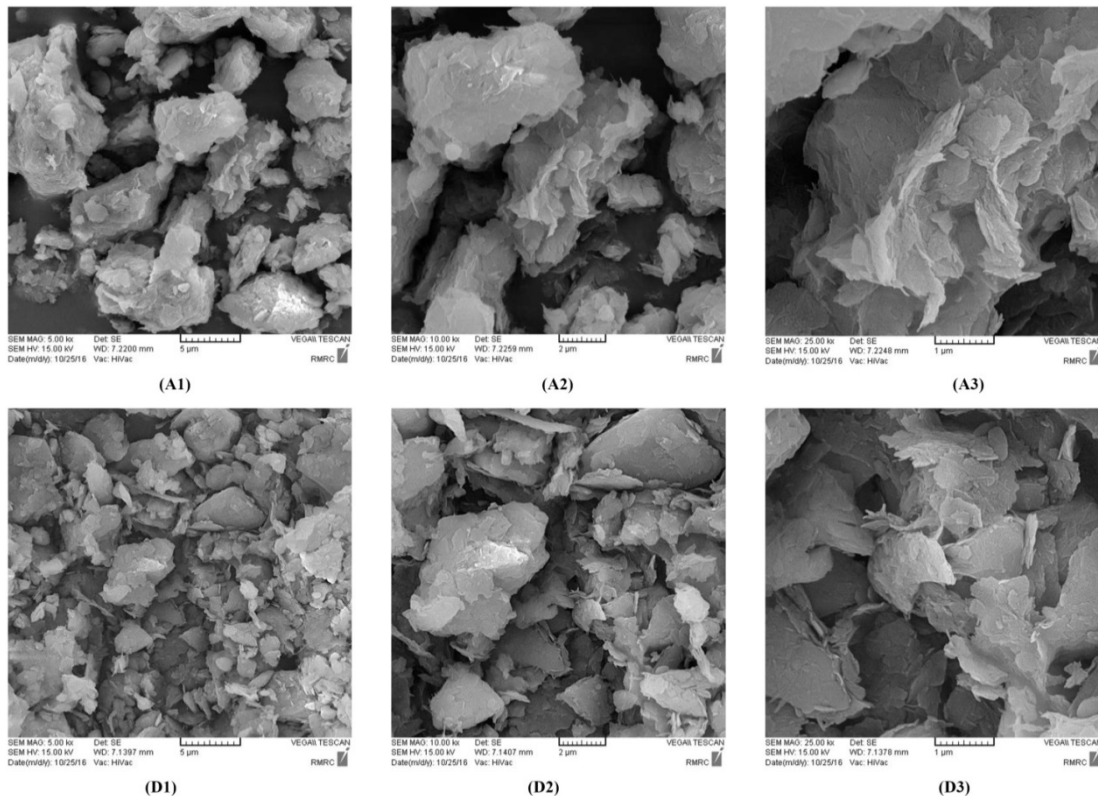


Figure 7. Microstructure observation of the effect of 5 % lime on collapsible soil (D1-D2-D3) in comparison to remolded raw specimen (A1-A2-A3) at different magnification.

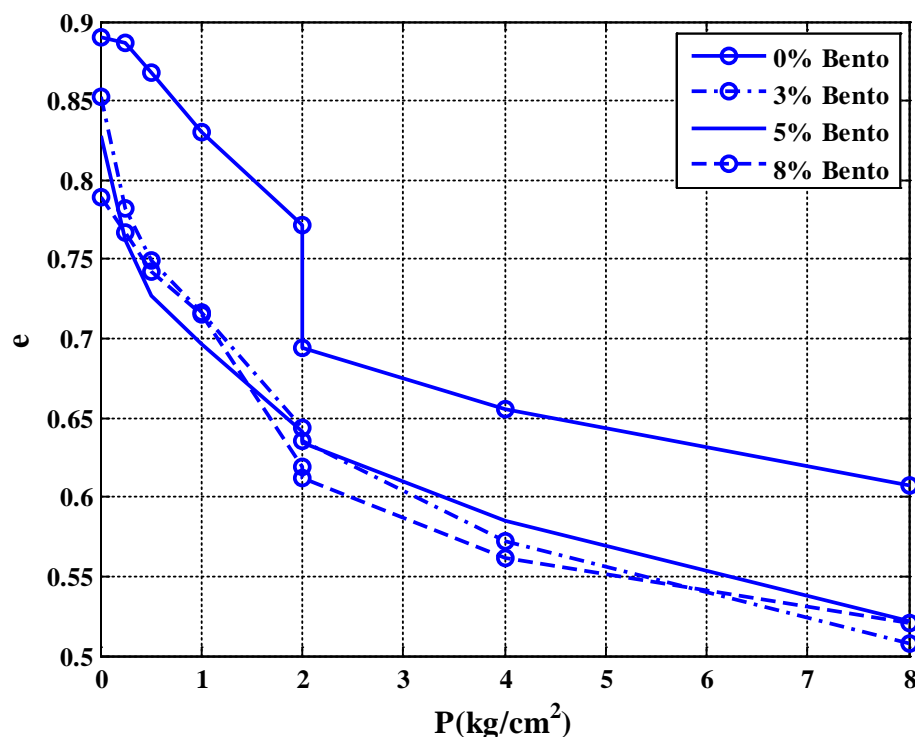
Table 5. Comparison between results from double odometer tests on three different lime-soil mixtures and remolded soil specimen.

Parameter	Soil	3 % Lime	5 % Lime	8 % Lime
Δe at vertical stress 2 (Kg/cm ²)	0.0788	0.004	0.002	0.008
Initial void ratio (e_0)	0.89	0.768	0.781	0.793
Collapse potential (%)	4.17	0.23	0.12	0.45
Degree of collapse	Moderate	Slight	Slight	Slight

The reactions between lime and soil are highly dependent on the time of curing hence, curing time significantly affects the results of the collapse potential test. The decrease in collapse potential in lime amended soil samples is attributed to three different procedures:

- Addition of moisture during the mixing process
- Compaction of the mixture which breaks the open structure of the collapsible soil
- Pozzolanic reaction between soil and lime which causes inter-particle bonding and flocculation of the soil particle leading to stabilize soil structure

The Scanning Electron Microscopy (SEM) images of 5 % lime-soil mixture as presented in different magnifications in Figure 8, indicate that the porous collapsible structure of soil, shown in Figure 8-A1, are filled in through the flocculation and, cation exchange reactions between lime and soil, which obviously decrease the volume of the inter-aggregate pores. Furthermore, the pozzolanic reactions happen between soil and lime strengthening the weak bonding between the particles in the soil. These reactions create a homogenous microstructure in the soil which is quite evident in Figures 8 D1, D2 and D3.

**Figure 8. Comparison between results from double oedometer tests on three different bentonite-soil mixtures and remolded soil specimen.**

4.2. Effects of bentonite on soil collapsibility

Bentonite-soil mixtures are left to rest for two days, and then the collapse potential tests are conducted on the samples. In Figure 9 and Table 6, the results of the tests on bentonite-soil mixtures are depicted. According to Table 4, in all three different samples, the degree of collapsibility decreases from the moderate level in the remolded soil sample to the slight level in treated samples. Although in all bentonite-soil mixture samples the collapse potential decreases, the maximum decline is observed by adding 3 % bentonite and with further addition, a minor increase is observed. Below 3 % bentonite addition, the amount of strain and consequently, the settlement showed a decreasing trend and after that, the trend is reversed showing a slight increase. Previous researches showed that the addition of bentonite up to 6 %, decreases the settlement of the mixture [27]. This differs from the findings of the present study. This inconsistency may be due to three different reasons: type of the used soil and bentonite, and the differences in the test procedure.

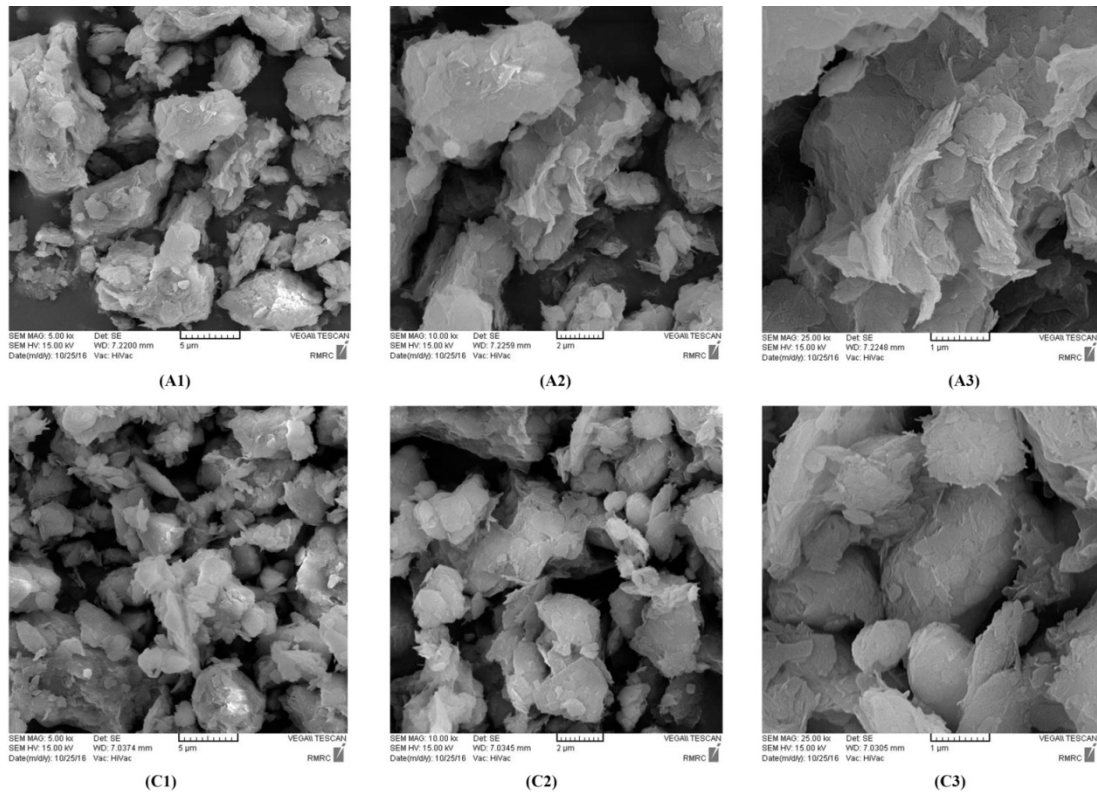


Figure 9. Microstructure observation of the effect of 3% bentonite on collapsible soil (C1-C2-C3) in comparison to remolded soil specimen (A1-A2-A3) at different magnification.

Table 6. Comparison between results from double oedometer tests on three different bentonite-soil mixtures and remolded soil specimen.

Parameter	Soil	3 % Bentonite	5 % Bentonite	8 % Bentonite
Δe at vertical stress 2 (Kg/cm ²)	0.0788	0.0047	0.0073	0.0092
Initial void ratio (e_0)	0.89	0.853	0.827	0.789
Collapse potential (%)	4.17	0.27	0.39	0.51
Degree of collapse	Moderate	Slight	Slight	Slight

The Scanning electron microscopy (SEM) observation of 3 % bentonite-soil mixture as presented in different magnifications in Figure 10 shows that, the inter-particle pores demonstrated (Figures 10 A1, A2 and A3) are supplied with the additive through the swelling characteristic of bentonite. In addition, high water absorption capability of bentonite forms a kind of gel which fills the pores (Figures 10 C1, C2 and C3). Moreover, expanded particles of bentonite act as filling materials of the pores and reduce the collapse potential of the soil. A comparison between lime and bentonite induced change shows that, although both of them decrease the collapsibility, it seems that the, lime creates a more homogenous microstructure which is more useful in collapsibility reduction of Kerman clay.

4.3. Effects of Nano-silica on soil collapsibility

Nano silica amended soil samples are packed and isolated for 48 hours and then the collapse potential tests are conducted on the samples. In Figure 11 and Table 7, the results of the collapse potential tests on Nano-silica soil mixtures are presented. In all the three different samples, collapse potential decreased revealing that Nano-silica can be an effective additive for stabilization of the Kerman collapsible soil. Regarding the obtained results, the collapsibility of the used clay is treated with adding 1 % Nano silica by dry weight of the soil. Nano silica is known as a pozzolanic material and is frequently used to improve soil properties. It is believed that the enhancement mechanism of colloidal silica is bonding between the gel and the clay particles. Gel encapsulates the individual clay particles and it is widely held view that this bonding and encapsulation improve soil structure [19].

The SEM images of the soil samples mixed with 1 % Nano-silica is depicted in different magnification in Figure 12 and shows changes in the basic structure where the inter-particles pores (Figures 12 A1, A2 and A3) are filled with CSH gel which is created by reaction between CaO and Al_2O_3 . Furthermore, this gel strengthens the bonding between soil particles and results in a homogenous microstructure (Figures 12 B1, B2 and B3) and consequently, decreases the collapse potential of the soil. These results match those observed in previous studies [8, 28].

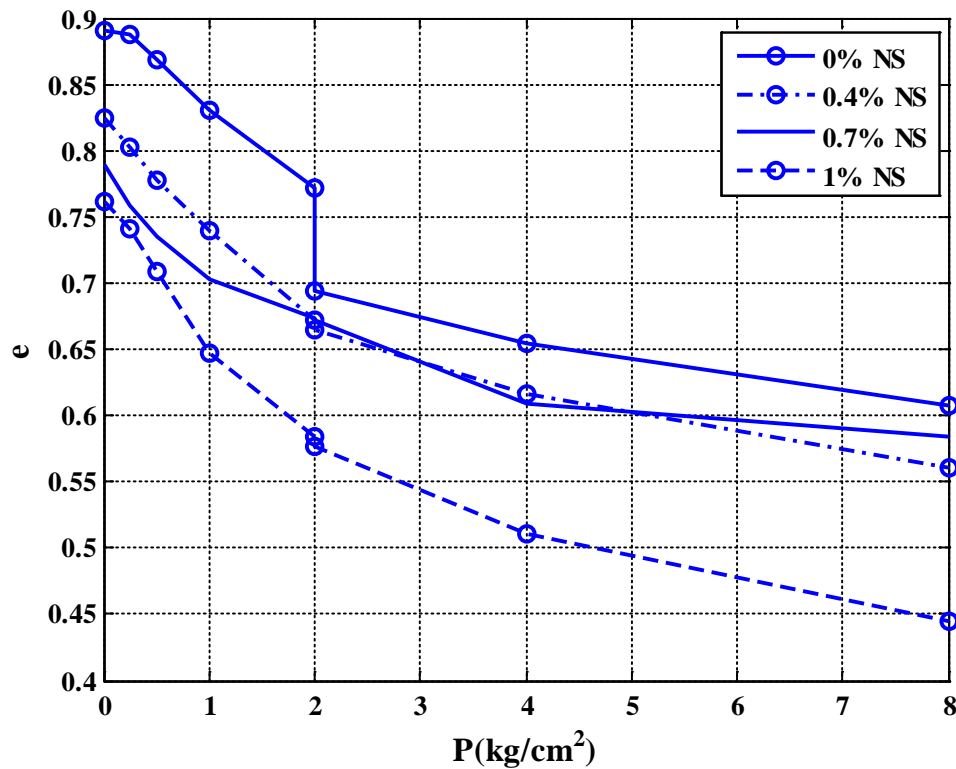


Figure 10. Comparison between results from double oedometer tests on three different Nano-silica-soil mixtures and remolded soil specimen.

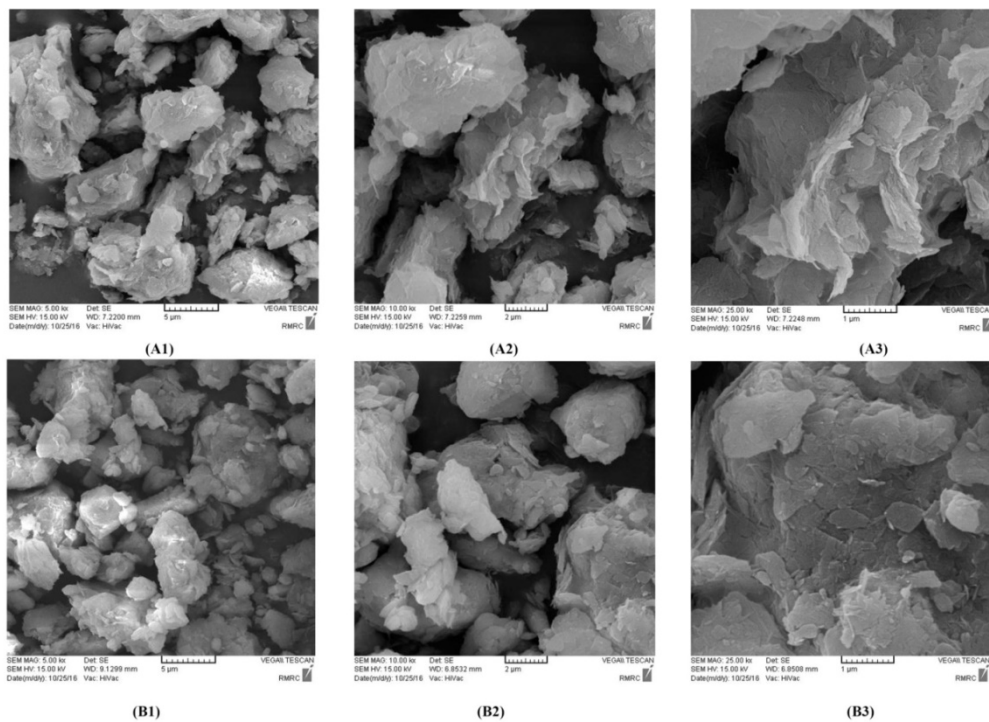


Figure 11. Microstructure observation of the effect of 1 % Nano-silica on collapsible soil (B1-B2-B3) in comparison to remolded soil specimen (A1-A2-A3) at different magnification.

Table 7. Comparison between results from double oedometer tests on three different Nano-silica-soil mixtures and remolded soil specimen.

Parameter	Soil	0.4 % Nano-silica	0.7 % Nano-silica	1 % Nano-silica
Δe at vertical stress 2 (Kg/cm ²)	0.0788	0.007	0.007	0.002
Initial void ratio (e_0)	0.89	0.82	0.79	0.76
Collapse potential (%)	4.17	0.39	0.38	0.12
Degree of collapse	Moderate	Slight	Slight	Slight

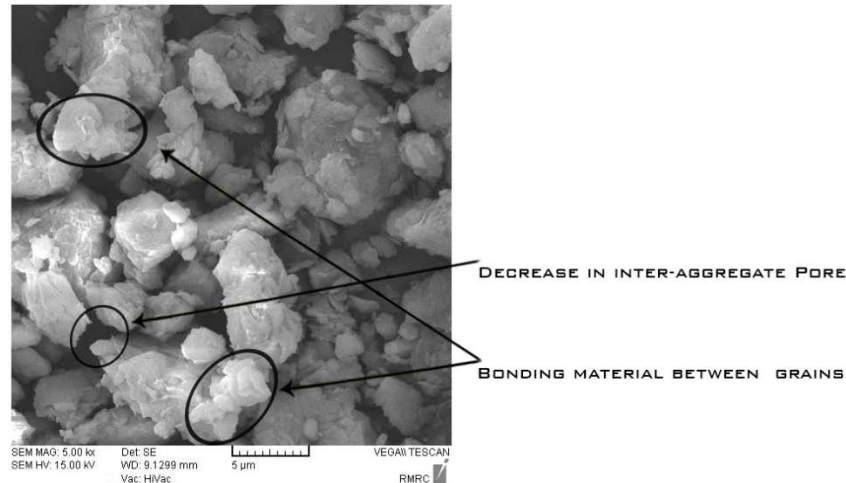


Figure 12. Effect of Nano-silica in filling the inter-aggregate pore and strengthening the unstable bonding between grains.

The SEM images of the soil samples mixed with 1 % Nano-silica is depicted in different magnification in Figure 12 and shows changes in the basic structure where the inter-particles pores (Figures 12 A1, A2 and A3) are filled with CSH gel which is created by reaction between CaO and Al_2O_3 . Furthermore, this gel strengthens the bonding between soil particles and results in a homogenous microstructure (Figures 12 B1, B2 and B3) and consequently, decreases the collapse potential of the soil. These results match those observed in previous studies [8, 28].

Figures 10 C1 and 12 B1 prove the lesser impact of the bentonite swelling property on filling the collapsibility of the specimens. At last, the differences in Figures 8 D1 and 12 B1, exhibit the sufficiency of both additives in decreasing the collapsibility of the Kerman clay.

The results demonstrated that 5 % of Lime, 3 % of Bentonite and 1 % of Nano silica are the optimum percentage of additives for decreasing the collapsibility. Both lime and Nano-silica demonstrate positive effects on reducing the Kerman clay collapsibility as the collapse potential diminished considerably in both specimens treated by these additives which is shown in Figures 7 and 11. In comparison of bentonite and Nano silica treated soil specimens in Figures 9 and 11, the reduction of the inter-particles in Nano silica treated specimens are evident. Also, the structure of the soil seems to be more homogenous.

5. Conclusions

The structure of a particular soil has a significant influence on its behavior in engineering particles. An open structure and weak inter-particle bonding may result in a higher collapsibility which requires a careful attention to factors affecting the collapse potential of the soils. A safe and applicable method to treat collapsible soils is using additives. The mixture of the soil and the additives is very sensitive to the quantity and the quality of its components. Thereby, finding the optimum additive ratio is important. In this research, three additives, namely lime, bentonite, and Nano-silica are selected and their effects on the collapse potential of the Kerman clay are investigated. Additive-soil mixture samples are tested and the results show that all of them decrease the collapsibility potential. The optimum additive percentage for lime, bentonite, and Nano-silica are determined as: 5 %, 3 and 1 % by the dry weight of soil, respectively. The collapsibility of Kerman clay is reduced significantly after treating with Lime and Nano silica in comparison to Bentonite. Although, both lime and Nano-silica had similar impacts on the collapse potential of the Kerman soil, Nano-silica is more recommended due to the shorter curing time of the specimens which is attributed to the great specific surface of the Nano-silica, leading to a lesser required material. Thus, it is recommended to consider Nano-particles as soil stabilizers. They do not need a long time of curing and small volume of minute volume of Nano-particle can effectively improve soil properties.

References

- Gao, G. The distribution and geotechnical properties of loess soils, lateritic soils and clayey soils in China. *Engineering Geology*. 1996. 42(1). Pp. 95–104. DOI: 10.1016/0013-7952(95)00056-9.
- Nouaouria, M., Guenfoud, M., Lafifi, B. Engineering properties of loess in Algeria. *Engineering Geology*. 2008. 99(1). Pp. 85–90. DOI: 10.1016/j.enggeo.2008.01.013.
- Lutenegger, A., Hallberg, G. Stability of loess. *Engineering Geology*. 1988. 25(2-4). Pp. 247–261. DOI: 10.1016/0013-7952(88)90030-0.
- Li, P., Vanapalli, S., Li, T. Review of collapse triggering mechanism of collapsible soils due to wetting. *Journal of Rock Mechanics and Geotechnical Engineering*. 2016. 8(2). Pp. 256–274. DOI: 10.1016/j.jrmge.2015.12.002.
- Rollins, K.M., Rogers, G.W. Mitigation measures for small structures on collapsible alluvial soils. *Journal of Geotechnical Engineering*. 1994. 120(9). Pp. 1533–1553. DOI: 10.1061/(ASCE)0733-9410(1994)120:9(1533).

6. Al-Mukhtar, M., Lasledj, A., Alcover, J.-F. Behaviour and mineralogy changes in lime-treated expansive soil at 20 C. Applied clay science. 2010. 50(2). Pp. 191–198. DOI: 10.1016/j.clay.2010.07.023.
7. Bozbey, I., Guler, E. Laboratory and field testing for utilization of an excavated soil as landfill liner material. Waste Management. 2006. 26(11). Pp. 1277–1286. DOI: 10.1016/j.wasman.2005.10.014.
8. Iranpour, B. The influence of nanomaterials on collapsible soil treatment. Engineering Geology. 2016. 205. Pp. 40–53. DOI: 10.1016/j.enggeo.2016.02.015.
9. Morandini, T.L.C., do Lago Leite, A. Characterization and hydraulic conductivity of tropical soils and bentonite mixtures for CCL purposes. Engineering Geology. 2015. 196. Pp. 251–267. DOI: 10.1016/j.enggeo.2015.07.011.
10. de Brito Galvão, T.C., Elsharief, A., Simões, G.F. Effects of lime on permeability and compressibility of two tropical residual soils. Journal of environmental engineering. 2004. 130(8). Pp. 881–885. DOI: 10.1061/(ASCE)0733-9372(2004)130:8(881).
11. Zukri, A. Pekan Soft Clay Treated with Hydrated Lime as a Method of Soil Stabilizer. Procedia Engineering. 2013. 53. Pp. 37–41, DOI: 10.1016/j.poeng.2013.02.006.
12. Hadi, M., Ajalloeian, R., Sadeghpour, A.H. Evaluation of Effect of Bentonite Addition on Fine-grain, s Behaviour Properties. Journal of Engineering Geology. 2014. 8(3). Pp. 2363–2388.
13. Sällfors, G., Öberg-Högsta, A.-L. Determination of hydraulic conductivity of sand-bentonite mixtures for engineering purposes. Geotechnical and Geological Engineering. 2002. 20(1). Pp. 65–80. DOI: 10.1023/A:1013857823676.
14. Slimani, R., Oxarango, L., Sbartai, B., Tinet, A.-J., Olivier, F., Dias, D. Leachate flow around a well in MSW landfill: Analysis of field tests using Richards model. Waste Management. 2016. DOI: 10.1016/j.wasman.2016.07.048.
15. Firoozfar, A., Khosroshiri, N. Kerman Clay Improvement by Lime and Bentonite to Be Used as Materials of Landfill Liner. Geotechnical and Geological Engineering. 2016. Pp. 1–13. DOI: 10.1007/s10706-016-0125-4.
16. Majeed, Z.H., Taha, M.R. A Review of Stabilization of Soils by using Nanomaterials. Australian Journal of Basic and Applied Sciences. 2013. 7(2). Pp. 576–581.
17. Noll, M.R., Bartlett, C., Dochat, T.M. In situ permeability reduction and chemical fixation using colloidal silica. Proceeding of the Sixth National Outdoor Action Conference on Aquifer Restoration, Ground Water Monitoring, and Geophysical Method, National Ground Water Association, 1992.
18. Huang, Y., Wang, L. Experimental studies on nanomaterials for soil improvement: a review. Environmental Earth Sciences. 2016. 75(6). Pp. 1–10. DOI: 10.1007/s12665-015-5118-8.
19. Langroudi, A.A., Jefferson, I., O'hara-Dhand, K., Smalley, I. Micromechanics of quartz sand breakage in a fractal context. Geomorphology. 2014. 211. Pp. 1–10.
20. Kangi, A., Khatibi, D. Evaluation of liquefaction potential in the kerman city based on spt, 2012.
21. Standard, A.D. D422–63, Standard test method for particle-size analysis of soils. ASTM International, West Conshohocken, 2007. DOI: 10:1520.
22. Bailey, J., Stevens, R., Kilpatrick, D. A rapid method for predicting the lime requirement of acidic temperate soils with widely varying organic matter contents. I. Development of the lime requirement model. Journal of soil science. 1989. 40(4). Pp. 807–820. DOI: 10.1007/978-94-011-3438-5_27.
23. Taha, M.R., Taha, O.M.E. Influence of nano-material on the expansive and shrinkage soil behavior. Journal of Nanoparticle Research. 2012. 14(10). Pp. 1190. DOI: 10.1007/s11051-012-1190-0.
24. Jennings, J., Pells, P., Robertson, A., Knight, K. A guide to construction on or with materials exhibiting additional settlement due to "Collapse" of grain structure, 1975.
25. Standard, A.D. D5333, Standard Test Method for Measurement of Collapse Potential of Soils. ASTM International, West Conshohocken, PA, 2003.
26. Naema, A. Improvement of collapsible soils. The eighth Alexandria international conference on Structural and Geotechnical Engineering, Department of Structural Engineering, Faculty of Engineering, Alexandria University, Egypt, 2014. DOI: 10.13140/RG.2.1475.2486.
27. Yeo, S.-S., Shackelford, C.D., Evans, J.C. Consolidation and hydraulic conductivity of nine model soil-bentonite backfills. Journal of Geotechnical and Geoenvironmental Engineering. 2005. 131(10). Pp. 1189–1198. DOI: 10.1061/(ASCE)1090-0241(2005)131:10(1189).
28. Gallagher, P.M., Conlee, C.T., Rollins, K.M. Full-scale field testing of colloidal silica grouting for mitigation of liquefaction risk. Journal of Geotechnical and Geoenvironmental Engineering. 2007. 133(2). Pp. 186–196. DOI: 10.1061/(ASCE)1090-0241(2007)133:2(186).

Contacts:

Alireza Firoozfar, 09121414177; firoozfar@znu.ac.ir

Majid Dousti, +989122426030; dousti.mj@gmail.com



ПОЛИТЕХ
Санкт-Петербургский
политехнический университет
Петра Великого

Инженерно-строительный институт
Центр дополнительных профессиональных программ

195251, г. Санкт-Петербург, Политехническая ул., 29,
тел/факс: 552-94-60, www.stroikursi.spbstu.ru,
stroikursi@mail.ru

Приглашает специалистов проектных и строительных организаций,
не имеющих базового профильного высшего образования
на курсы профессиональной переподготовки (от 500 часов)
по направлению «Строительство» по программам:

П-01 «Промышленное и гражданское строительство»

Программа включает учебные разделы:

- Основы строительного дела
- Инженерное оборудование зданий и сооружений
- Технология и контроль качества строительства
- Основы проектирования зданий и сооружений
- Автоматизация проектных работ с использованием AutoCAD
- Автоматизация сметного дела в строительстве
- Управление строительной организацией
- Управление инвестиционно-строительными проектами. Выполнение функций технического заказчика

П-02 «Экономика и управление в строительстве»

Программа включает учебные разделы:

- Основы строительного дела
- Инженерное оборудование зданий и сооружений
- Технология и контроль качества строительства
- Управление инвестиционно-строительными проектами. Выполнение функций технического заказчика и генерального подрядчика
- Управление строительной организацией
- Экономика и ценообразование в строительстве
- Управление строительной организацией
- Организация, управление и планирование в строительстве
- Автоматизация сметного дела в строительстве

П-03 «Инженерные системы зданий и сооружений»

Программа включает учебные разделы:

- Основы механики жидкости и газа
- Инженерное оборудование зданий и сооружений
- Проектирование, монтаж и эксплуатация систем вентиляции и кондиционирования
- Проектирование, монтаж и эксплуатация систем отопления и теплоснабжения
- Проектирование, монтаж и эксплуатация систем водоснабжения и водоотведения
- Автоматизация проектных работ с использованием AutoCAD
- Электроснабжение и электрооборудование объектов

П-04 «Проектирование и конструирование зданий и сооружений»

Программа включает учебные разделы:

- Основы сопротивления материалов и механики стержневых систем
- Проектирование и расчет оснований и фундаментов зданий и сооружений
- Проектирование и расчет железобетонных конструкций
- Проектирование и расчет металлических конструкций
- Проектирование зданий и сооружений с использованием AutoCAD
- Расчет строительных конструкций с использованием SCAD Office

П-05 «Контроль качества строительства»

Программа включает учебные разделы:

- Основы строительного дела
- Инженерное оборудование зданий и сооружений
- Технология и контроль качества строительства
- Проектирование и расчет железобетонных конструкций
- Проектирование и расчет металлических конструкций
- Обследование строительных конструкций зданий и сооружений
- Выполнение функций технического заказчика и генерального подрядчика

По окончании курса слушателю выдается диплом о профессиональной переподготовке
установленного образца, дающий право на ведение профессиональной деятельности

